UNDERSTANDING THE EFFECTS OF TEMPERATURE ON THE BEHAVIOUR OF CLAY

by

David Robert Kurz

A Thesis
Submitted to the Faculty of Graduate Studies of
The University of Manitoba
in Partial Fulfillment of the Requirement for the Degree of

DOCTOR OF PHILOSOPHY

Department of Civil Engineering
University of Manitoba
Winnipeg, Manitoba

Thesis Approval Form

This is a placeholder page.

In printed copies of the thesis, this page will be replaced with the official form provided by the University of Manitoba and signed by the examiners and chair of the PhD defense.

Abstract

There is a growing need to better understand the relationship between time, strain rate, and temperature on the load-deformation behaviour of clay soils in engineering applications. These applications may include: infrastructure constructed in northern regions where climate change is a growing concern; disposal of nuclear waste; and, industrial structures, such as furnaces, foundries, and refrigeration plants. Temperature variations may induce changes in internal pressure in the soil, swelling and shrinkage, and affect the mechanical properties of the soil.

This thesis presents thermal numerical modeling for two instrumented field sites in northern Manitoba. Thermal conductivity testing on samples from these sites and field data are used to calibrate these thermal numerical models. Various boundary conditions are examined. The capabilities of the models are evaluated to determine if the models adequately simulate and predict changes in temperature in geotechnical structures. A discussion is presented on the strengths and weaknesses in the models and the predictive capabilities of the models.

The thesis then shifts into understanding the concepts of thermoplasticity and viscoplasticity and the mathematics relating these concepts. Mathematical models that describe these concepts are examined and compared with traditional soil mechanics approaches. The concepts of thermoplasticity and viscoplasticity are combined in an encompassing elastic thermo-viscoplastic (ETVP) model using a semi-empirical framework. A sensitivity analysis is used to evaluate quantitatively the response of the model. The model is then validated qualitatively against published laboratory data. Applications of the ETVP model are discussed.

Acknowledgements

I would like to express my deepest gratitude to my co-advisors, Dr. Marolo Alfaro and Dr. Jim Graham for their guidance, encouragement, patience, and knowledge throughout this research program. Without them this research would not have been completed.

I would also like to thank my other advisory committee members, Dr. Jitendra Sharma and Dr. Scott Ormiston for their time, guidance, and insight. I extend my appreciation to Dr. Curtis Kelln for his time, assistance, and wisdom in helping me understand his model.

I extend my appreciation to all professors and support staff in the Department of Civil Engineering and my fellow graduate students for their friendship, discussions, and assistance during this research program. I would like to specifically acknowledge Mr. Kerry Lynch for his advice and technical assistance in the laboratory and my former colleague Dr. Hamid Batenipour for his collaboration during this research. Our respective programs were parallel but separate.

Financial support is acknowledged from the University of Manitoba, the National Science and Engineering Research Council of Canada, the Canadian Geotechnical Society, and the friends and family in support of the Neil Burgess Memorial Scholarship.

Finally, I wish to express my gratitude to my family for their unending support every step of this arduous journey.

Table of Contents

Abstract ii

Acknowledgements iii

Table of Contents iv

List of Figures vii

List of Tables vii

List of Copyrighted Material for which Permission was Obtained xv

Chapter 1: Introduction 1

1.1 Background 1
1.2 Research Objectives 4
1.3 Scope of Thesis 5
1.4 Organization of Thesis 5

Chapter 2: Literature Review 7

2.1 Introduction 7
2.2 Thermal Modeling 8
2.3 Elastic Plastic vs. Non-linear Functions 11
2.4 Cam-clay: An Elastic-plastic Model 14
2.4.1 Origins 14
2.4.2 Terminology 15
2.4.3 Validity of Assumptions 15
2.4.4 Extensions of Cam-clay 21
2.5 Thermoplasticity 22
2.6 Viscoplasticity 26
2.7 Expansion to an elastic thermo-viscoplastic model 33
2.7.1 Similarities between time and temperature 33
2.7.2 Existing Mechanics-based Models 35

2.7.3 A new semi-empirical approach 37
2.8 Justification for Research 38

Chapter 3: Laboratory Testing: Thermal Conductivity 53

3.1 Introduction 53
3.2 Apparatus and Procedure 54
3.3 Description of Soil Samples 61
3.4 Testing Procedures 64
3.5 Results 68
3.6 Comparison with Empirical Relationships 72
3.7 Commentary 74
3.8 Summary 75

Chapter 4: Case Histories: Thermal Numerical Modeling 86

4.1 Introduction 86
4.2 PR391 86
4.2.1 Site Description 86
4.2.2 Geotechnical Material Properties 88
4.2.3 Thermal Numerical Modeling 91
4.2.4 Modeling Results and Forward Prediction 98
4.2.5 Commentary 102
4.2.6 Concluding Comments 104
4.3 Radisson-Churchill Transmission line 104
4.3.1 Site Description 104
4.3.2 Geotechnical Material Properties 105
4.3.3 Thermal Numerical Modeling 106
4.3.4 Modeling Results 110
4.3.5 Commentary 113
4.3.6 Concluding Comments 115

Chapter 5: An ETVP Framework 141

5.1 Introduction 141
5.2 Elastic thermo-viscoplastic modeling 141
5.2.1 Terminology 143
5.2.2 Kelln's EVP Framework 144
5.2.3 Incorporation of T in ETVP 147
5.3 Sensitivity Analysis 156
5.4 Commentary 160
5.5 Summary 161

Chapter 6: Analysis and Discussion 178

6.1 Introduction 178
6.2 An Analysis of the ETVP Model 178
6.2.1 Terminology 179
6.2.2 Critical State 179
6.2.3 Interpretation of CI$\bar{U}$ tests 180
6.2.4 Interpretation of CID tests 184
6.2.5 Model Validation 189
6.3 Application of the ETVP Model 194
6.4 Commentary 198
6.5 Summary 201

Chapter 7: Closure 224

7.1 Summary 224
7.2 Conclusions 225
7.3 Recommendations for future work 227

References 229

Appendix I 240

List of Tables

Table 3.1: Thermal Conductivity for PR391 76

Table 3.2: Thermal Conductivity for PR373 76

Table 3.3: Thermal Conductivity for Manitoba Hydro Samples 76

Table 3.4: Measured vs. Estimated Thermal Conductivity 77

Table 4.1: Thermal Material Properties (PR391) (after Batenipour 2012) 116

Table 4.2: Revised Thermal Material Properties (PR391) 116

Table 4.3: n-Factors 116

Table 4.4: Revised Thermal Material Properties (MB Hydro) 116

Table 5.1: Soil parameters used to simulate $CI\bar{U}$ and CID triaxial tests 162

Table 6.1: Critical State ratios for $CI\bar{U}$ NC tests 202

Table 6.2: Critical State ratios for $CI\bar{U}$ LOC tests 203

Table 6.3: Summary for $CI\bar{U}$ NC values 204

Table 6.4: Summary for $CI\bar{U}$ LOC values 205

Table 6.5: Summary for $CI\bar{U}$ HOC values 206

Table 6.6: Summary for CID NC values 207

Table 6.7: Summary for CID LOC values 207

Table 6.8: Summary for CID HOC values 208

List of Figures

Figure 2.1: Effect of temperature variation on volume change (Campanella and Mitchell 1968) (Used with permission)..... 40

Figure 2.2: Effect of temperature on pore water pressure in saturated illite specimens under undrained conditions (Campanella and Mitchell 1968) (Used with permission)..... 40

Figure 2.3: Effect of temperature on isotropic consolidation behaviour of saturated illite (Campanella and Mitchell 1968) (Used with permission)..... 41

Figure 2.4: An elastic perfectly plastic model 41

Figure 2.5: An elastic-plastic model with strain hardening 42

Figure 2.6: Volumetric hardening of the yield surface for a state of stress, A, moving to C in q-p' stress space..... 42

Figure 2.7: Compression space V-ln(p') in the Cam-clay model..... 43

Figure 2.8: A general state of stress..... 43

Figure 2.9: Observed yielding behaviour in (a) p' vs. volume strain and (b) q vs. shear strain (Graham, Noonan, and Lew 1983) (Used with permission)..... 44

Figure 2.10: Typical Oedometer results (Batenipour 2012) (Used with permission)..... 44

Figure 2.11: The associated flow rule concept 45

Figure 2.12: Representation of the yield surface (a) at constant temperature, T, (b) at variable thermoplastic volumetric strain, ε_v^{tp}, and variable temperature, ΔT, and (c) at constant ε_v^{tp} and variable ΔT (Hueckel and Baldi 1990) (Used with permission) 45

Figure 2.13: Representation of Tanaka's TEP model showing the relationship between thermally induced volumetric strains and mean effective stress (Graham et al. 2001) (Used with permission)..... 46

Figure 2.14: Definition of 'instant' and 'delayed' compression compared with 'primary' and 'secondary' compression (Bjerrum 1967) (Used with permission) 46

Figure 2.15: The time-line model (Bjerrum 1967) (Used with permission)..... 47

Figure 2.16: Measured and predicted results from consolidated-undrained tests on Hong Kong marine deposits (a) axial strain ε_a vs. q and (b) effective stress paths normalized with preconsolidation pressure, σ'_c (Yin et al. 2002) (Used with permission)..... 48

Figure 2.17: Inadmissible development of viscoplastic volumetric strains with constant stress for a stress state that resides inside a current yield locus which has its size defined by p'_o on the isotropic normal compression line (iso-ncl) (Kelln 2007) (Used with permission)..... 49

Figure 2.18: Admissible development of viscoplastic volumetric strains with constant stress for a stress state that resides outside a current yield locus which has its size defined by p'_o that does not fall on the isotropic normal compression line p'_n. The locus of p'_o in the V-p' compression plane forms the viscoplastic limit line (vpl) parallel with the isotropic normal compression line (Kelln 2007) (Used with permission)..... 50

Figure 2.19: Computed and measured surface settlement beneath the south shoulder of the embankment near Limavady (Kelln 2007) (Used with permission)..... 51

Figure 2.20: Computed and measured inclinometer profile (Kelln 2007) (Used with permission)..... 51

Figure 2.21: Stress-strain behaviour in oedometer tests at different temperatures (Eriksson 1989) (Used with permission) 52

Figure 2.22: Description of 'primary consolidation', 'secondary compression', 'delayed compression' and the material constant, ψ, in V-ln(t) space (Kelln 2007) (Used with permission)..... 52

Figure 3.1: TP08 Thermal Probe and Storage Cap 78

Figure 3.2: Campbell Scientific CR23X micrologger 78

Figure 3.3: GT01 Guiding Tubes..... 79

Figure 3.4: Stainless Steel Cell (base plate, cylinder, top cap)..... 79

Figure 3.5: Schematic of test cell with specimen and thermal probe inserted..... 80

Figure 3.6: A 4.0% Concentration Agar-Water Gel 80

Figure 3.7: Location of project sites and permafrost in Manitoba..... 81

Figure 3.8: SEM micrograph for weakly decomposed peat sample at x50 magnification . (Image provided courtesy of Mr. Cory Jay Pyziak, unpublished) 82

Figure 3.9: SEM micrograph for moderately decomposed peat sample at x50 magnification (Image provided courtesy of Mr. Cory-Jay Pyziak, unpublished).... 82

Figure 3.10: Example analysis of the tests performed on each sample 83

Figure 3.11: Thermal conductivity vs. temperature; PR391 specimens with assumed relationships 83

Figure 3.12: Thermal conductivity vs. temperature; selected PR373 specimens with assumed relationships 84

Figure 3.13: Thermal conductivity vs. temperature; Manitoba Hydro specimens with assumed relationships 84

Figure 3.14: Unfrozen Silt and Clay; re-plotted after Harlan and Nixon (1978) (Used with permission)..... 85

Figure 3.15: Frozen Silt and Clay; re-plotted after Harlan and Nixon (1978) (Used with permission)..... 85

Figure 4.1: Photograph of PR391 site (provided courtesy of Dr. H. Batenipour) 117

Figure 4.2: Soil stratigraphy of PR391, 'unstable' section..... 117

Figure 4.3: Unfrozen Water Content vs. Temperature (PR391)..... 118

Figure 4.4: Thermal Conductivity vs. Temperature (PR391)..... 118

Figure 4.5: Model Cross Section for PR391 Unstable Section with materials, finite element mesh, boundary conditions, and thermistor string locations..... 119

Figure 4.6: Sensitivity of PR391 2D model to selected mesh sizes (Fine: 0.15-0.30 m; Original: 0.25-0.50 m; Coarse: 0.50 m) at the mid-slope of the embankment 120

Figure 4.7: Sensitivity of PR391 2D model to location of the far (right hand) no heat flux boundary at the mid-slope of the embankment..... 120

Figure 4.8: Approximately 2-year Mean Daily Temperature; Climate data and fitted sine function 121

Figure 4.9: 25-year Mean Daily Temperature; sine function fitted to CCCma data and linear trendline 121

Figure 4.10: Comparison of thermistor, *'Assumed'*, *'Batenipour'* and *'Kurz'* below the (a) toe and (b) mid-slope of the embankment 122

Figure 4.11: Comparison of thermistors to a mid-slope boundary condition of *'Point'* and *'Line'*. Temperatures below the (a) toe and (b) mid-slope of the embankment..... 123

Figure 4.12: Comparison of thermistors to *'Kurz'*, *'Sine'*, and *'CCCma'* below the toe of the embankment (see also related data in Figure 4.13)..... 124

Figure 4.13: Comparison of thermistors to *'Kurz'*, *'Sine'*, and *'CCCma'* below the toe of the embankment (see also related data in Figure 4.12)..... 125

Figure 4.14: Comparison of thermistors to *'Kurz'*, *'Sine'*, and *'CCCma'* below the mid-slope of the embankment (see also related data in Figure 4.15)..... 126

Figure 4.15: Comparison of thermistors to *'Kurz'*, *'Sine'*, and *'CCCma'* below the mid-slope of the embankment (see also related data in Figure 4.14)..... 127

Figure 4.16: Temperature versus Time for (a) 0.0 m and (b) 1.0 m at the toe of the embankment (see also related data in Figure 4.17)..... 128

Figure 4.17: Temperature versus Time for (a) 4.0 m, and (b) 8.0 m at the toe of the embankment (see also related data in Figure 4.16)..... 129

Figure 4.18: Temperature versus Time for (a) 2.0 m and (b) 5.0 m at the mid-slope of the embankment (see also related data in Figure 4.19)..... 130

Figure 4.19: Temperature versus Time for (a) 8.0 m at the mid-slope of the embankment (see also related data in Figure 4.18) 131

Figure 4.20. Temperature versus Time for 10 years; (a) 1.0 m below the toe of the embankment and (b) 2.0 m below the mid-slope of the embankment. 132

Figure 4.21: Photograph of a transmission tower in the 138 kV Radisson-Churchill transmission line (provided courtesy of Dr. Marolo Alfaro) 133

Figure 4.22: Typical foundation design 133

Figure 4.23: Unfrozen Water Content vs. Temperature (Hydro)..... 134

Figure 4.24: Model Cross Sections (truncated at 5 m depth, 10 m radius) for transmission tower (a) deep foundation (showing steel) and (b) shallow foundation (no steel) 135

Figure 4.25: Measured Thermocouple data from Tower 3 at (a) 0.6 m (2.0 ft) and (b) 6.0 m (20.0 ft) from the tower..... 136

Figure 4.26. Measured Thermocouple data from Tower 45 at (a) 0.6 m (2.0 ft) and (b) 6.0 m (20.0 ft) from the tower 137

Figure 4.27: Modeled Temperature profile for the Shallow Foundation and short insulation at (a) 0.6 m (2.0 ft) and (b) 6.0 m (20.0 ft) from the tower 138

Figure 4.28: Modeled Temperature profile for the Deep Foundation at 0.6 m (2.0 ft) from the tower (a) without steel and (b) with steel 139

Figure 4.29: Temperature versus Time above and below the footing for 15 years in the Deep Foundation; (a) without steel (b) with steel 140

Figure 5.1: Compression space (V:ln(p')) showing a point a_0 proceeding to a_1 after time t (after Kelln 2007) (Used with permission) 163

Figure 5.2: Linear and exponential relationships for the creep parameter versus temperature anchored at a temperature of 28°C (301.15K) for given values of ψ 163

Figure 5.3: Response of the ETVP model on a CIŪ test for NC soil at a strain rate of 15.0%/day and (ψ_1:T_1) = (0.006:28.0°C): (a) stress space (q:p'); (b) deviatoric stress versus shear strain (q:ε_q) 164

Figure 5.4: Comparison of temperature and preconsolidation pressure for CIŪ NC test at a strain rate of 15.0%/day for a stress-strain plot normalized to preconsolidation pressure 165

Figure 5.5: Response of the ETVP model on a CIŪ test for NC soil at a strain rate of 15.0%/day and (ψ_1:T_1) = (0.006:28.0°C): (a) stress space (q:p'); (b) compression space (V:p'); (c) viscoplastic volumetric strain rate versus isotropic mean effective stress ($\dot{\varepsilon}_p^{vp}$:p'_m); (d) deviatoric stress versus shear strain (q:ε_q); (e) pore water pressure versus shear strain (u:ε_q) 166

Figure 5.6: Response of the ETVP model on a CIŪ test for NC soil at a strain rate of 0.15%/day and (ψ_1:T_1) = (0.006:28.0°C): (a) stress space (q:p'); (b) compression space (V:p'); (c) viscoplastic volumetric strain rate versus isotropic mean effective stress ($\dot{\varepsilon}_p^{vp}$:p'_m); (d) deviatoric stress versus shear strain (q:ε_q); (e) pore water pressure versus shear strain (u:ε_q) 167

Figure 5.7: Response of the ETVP model on a CIŪ test for LOC soil at a strain rate of 15.0%/day and (ψ_1:T_1) = (0.006:28.0°C): (a) stress space (q:p'); (b) compression space (V:p'); (c) viscoplastic volumetric strain rate versus isotropic mean effective stress ($\dot{\varepsilon}_p^{vp}$:p'_m); (d) deviatoric stress versus shear strain (q:ε_q); (e) pore water pressure versus shear strain (u:ε_q) 168

Figure 5.8: Response of the ETVP model on a CI$\bar{U}$ test for LOC soil at a strain rate of 0.15%/day and (ψ_1:T_1) = (0.006:28.0°C): (a) stress space (q:p'); (b) compression space (V:p'); (c) viscoplastic volumetric strain rate versus isotropic mean effective stress ($\dot{\varepsilon}_p^{vp}$:p'_m); (d) deviatoric stress versus shear strain (q:ε_q); (e) pore water pressure versus shear strain (u:ε_q)..... 169

Figure 5.9: Response of the ETVP model on a CI$\bar{U}$ test for HOC soil at a strain rate of 15.0%/day and (ψ_1:T_1) = (0.006:28.0°C): (a) stress space (q:p'); (b) compression space (V:p'); (c) viscoplastic volumetric strain rate versus isotropic mean effective stress ($\dot{\varepsilon}_p^{vp}$:p'_m); (d) deviatoric stress versus shear strain (q:ε_q); (e) pore water pressure versus shear strain (u:ε_q)..... 170

Figure 5.10: Response of the ETVP model on a CI$\bar{U}$ test for HOC soil at a strain rate of 0.15%/day and (ψ_1:T_1) = (0.006:28.0°C): (a) stress space (q:p'); (b) compression space (V:p'); (c) viscoplastic volumetric strain rate versus isotropic mean effective stress ($\dot{\varepsilon}_p^{vp}$:p'$_m$); (d) deviatoric stress versus shear strain (q:ε_q); (e) pore water pressure versus shear strain (u:ε_q)..... 171

Figure 5.11: Response of the ETVP model on a CID test for NC soil at a strain rate of 15.0%/day and (ψ_1:T_1) = (0.006:28.0°C): (a) stress space (q:p'); (b) compression space (V:p'); (c) viscoplastic volumetric strain rate versus isotropic mean effective stress ($\dot{\varepsilon}_p^{vp}$:p'_m); (d) deviatoric stress versus shear strain (q:ε_q); (e) specific volume versus shear strain (V:ε_q)..... 172

Figure 5.12: Response of the ETVP model on a CID test for NC soil at a strain rate of 0.15%/day and (ψ_1:T_1) = (0.006:28.0°C): (a) stress space (q:p'); (b) compression space (V:p'); (c) viscoplastic volumetric strain rate versus isotropic mean effective stress ($\dot{\varepsilon}_p^{vp}$:p'_m); (d) deviatoric stress versus shear strain (q:ε_q); (e) specific volume versus shear strain (V:ε_q)..... 173

Figure 5.13: Response of the ETVP model on a CID test for LOC soil at a strain rate of 15.0%/day and (ψ_1:T_1) = (0.006:28.0°C): (a) stress space (q:p'); (b) compression space (V:p'); (c) viscoplastic volumetric strain rate versus isotropic mean effective stress ($\dot{\varepsilon}_p^{vp}$:p'_m); (d) deviatoric stress versus shear strain (q:ε_q); (e) specific volume versus shear strain (V:ε_q)..... 174

Figure 5.14: Response of the ETVP model on a CID test for LOC soil at a strain rate of 0.15%/day and (ψ_1:T_1) = (0.006:28.0°C): (a) stress space (q:p'); (b) compression space (V:p'); (c) viscoplastic volumetric strain rate versus isotropic mean effective stress ($\dot{\varepsilon}_p^{vp}$:p'_m); (d) deviatoric stress versus shear strain (q:ε_q); (e) specific volume versus shear strain (V:ε_q)..... 175

Figure 5.15: Response of the ETVP model on a CID test for HOC soil at a strain rate of 15.0%/day and (ψ_1:T_1) = (0.006:28.0°C): (a) stress space (q:p'); (b) compression space (V:p'); (c) viscoplastic volumetric strain rate versus isotropic mean effective stress ($\dot{\varepsilon}_p^{vp}$:p'_m); (d) deviatoric stress versus shear strain (q:ε_q); (e) specific volume versus shear strain (V:ε_q)..... 176

Figure 5.16: Response of the ETVP model on a CID test for HOC soil at a strain rate of 0.15%/day and (ψ_1:T_1) = (0.006:28.0°C): (a) stress space (q:p'); (b) compression space (V:p'); (c) viscoplastic volumetric strain rate versus isotropic mean effective stress ($\dot{\varepsilon}_p^{vp}$:p'_m); (d) deviatoric stress versus shear strain (q:ε_q); (e) specific volume versus shear strain (V:ε_q)..... 177

Figure 6.1: CIU NC deviator stress at (a) Peak, (b) EOT, (c) Ratio of EOT/Peak..... 209

Figure 6.2: CI$\bar{U}$ NC pore water pressures at (a) Peak, (b) EOT 210

Figure 6.3: CI$\bar{U}$ NC pore water pressure parameter, A at (a) Peak, (b) EOT..... 211

Figure 6.4: CI$\bar{U}$ LOC deviator stress at (a) Peak, (b) EOT, (c) Ratio of EOT/Peak 212

Figure 6.5: CI$\bar{U}$ LOC pore water pressures at (a) Peak, (b) EOT..... 213

Figure 6.6: CI$\bar{U}$ LOC pore water pressure parameter, A at (a) Peak, (b) EOT 214

Figure 6.7: CI$\bar{U}$ HOC deviator stress at (a) Peak, (b) EOT, (c) Ratio of EOT/Peak..... 215

Figure 6.8: CI$\bar{U}$ HOC pore water pressures at (a) Peak, (b) EOT 216

Figure 6.9: CI$\bar{U}$ HOC pore water pressure parameter, A at (a) Peak, (b) EOT..... 217

Figure 6.10: CID NC at the EOT for (a) deviator stress and (b) specific volume..... 218

Figure 6.11: CID LOC at the EOT for (a) deviator stress and (b) specific volume..... 219

Figure 6.12: CID HOC deviator stress at (a) Peak, (b) EOT, (c) Ratio of EOT/Peak.... 220

Figure 6.13: CID HOC specific volume, V at (a) Peak, (b) EOT..... 221

Figure 6.14: CID LOC tests at OCRs 1.20, 1.67, 2.00 illustrating an interpretation of κ(T) 222

Figure 6.15: Temperature vs. Volumetric Strain for various OCRs..... 223

Figure 6.16: Temperature vs. Volumetric Strain for various OCRs during CID Shearing with temperature increase 223

List of Copyrighted Material for which Permission was Obtained

Figure 2.1: Effect of temperature variation on volume change (Campanella and Mitchell 1968) (With permission from the American Society of Civil Engineers) 40

Figure 2.2: Effect of temperature on pore water pressure in saturated illite specimens under undrained conditions (Campanella and Mitchell 1968) (With permission from the American Society of Civil Engineers) 40

Figure 2.3: Effect of temperature on isotropic consolidation behaviour of saturated illite (Campanella and Mitchell 1968) (With permission from the American Society of Civil Engineers) 41

Figure 2.9: Observed yielding behaviour in (a) p' vs. volume strain and (b) q vs. shear strain (Graham, Noonan, and Lew 1983) (With permission from the NRC Research Press) 44

Figure 2.10: Typical Oedometer results (Batenipour 2012) (With permission from Dr. H. Batenipour) 44

Figure 2.12: Representation of the yield surface (a) at constant temperature, T, (b) at variable thermoplastic volumetric strain, ε_v^{tp}, and variable temperature, ΔT, and (c) at constant ε_v^{tp} and variable ΔT (Hueckel and Baldi 1990) (With permission from the American Society of Civil Engineers) 45

Figure 2.13: Representation of Tanaka's TEP model showing the relationship between thermally induced volumetric strains and mean effective stress (Graham et al. 2001) (With permission from the NRC Research Press) 46

Figure 2.14: Definition of 'instant' and 'delayed' compression compared with 'primary' and 'secondary' compression (Bjerrum 1967) (With permission from ICE Publishing) 46

Figure 2.15: The time-line model (Bjerrum 1967) (With permission from ICE Publishing) 47

Figure 2.16: Measured and predicted results from consolidated-undrained tests on Hong Kong marine deposits (a) axial strain εa vs. q and (b) effective stress paths normalized with preconsolidation pressure, σ'_c (Yin et al. 2002) (With permission from the NRC Research Press) 48

Figure 2.17: Inadmissible development of viscoplastic volumetric strains with constant stress for a stress state that resides inside a current yield locus which has its size defined by p'_o on the isotropic normal compression line (iso-ncl) (Kelln 2007) (With permission from Dr. C. Kelln)..... 49

Figure 2.18: Admissible development of viscoplastic volumetric strains with constant stress for a stress state that resides outside a current yield locus which has its size defined by p'_o that does not fall on the isotropic normal compression line p'_n. The locus of p'_o in the V-p' compression plane forms the viscoplastic limit line (vpl) parallel with the isotropic normal compression line (Kelln 2007) (With permission from Dr. C. Kelln)..... 50

Figure 2.19: Computed and measured surface settlement beneath the south shoulder of the embankment near Limavady (Kelln 2007) (With permission from Dr. C. Kelln) 51

Figure 2.20: Computed and measured inclinometer profile (Kelln 2007) (With permission from Dr. C. Kelln)..... 51

Figure 2.21: Stress-strain behaviour in oedometer tests at different temperatures (Eriksson 1989) (With permission from Taylor-Francis)..... 52

Figure 2.22: Description of 'primary consolidation', 'secondary compression', 'delayed compression' and the material constant, ψ, in V-ln(t) space (Kelln 2007) (With permission from Dr. C. Kelln)..... 52

Figure 3.8: SEM micrograph for weakly decomposed peat sample at x50 magnification . (Image provided courtesy of Mr. Cory Jay Pyziak, unpublished)..... 82

Figure 3.9: SEM micrograph for moderately decomposed peat sample at x50 magnification (Image provided courtesy of Mr. Cory-Jay Pyziak, unpublished) ... 82

Figure 3.14: Unfrozen Silt and Clay; re-plotted after Harlan and Nixon (1978) (With permission from the McGraw-Hill Companies, Inc.)..... 85

Figure 3.15: Frozen Silt and Clay; re-plotted after Harlan and Nixon (1978) (With permission from the McGraw-Hill Companies, Inc.)..... 85

Figure 4.1: Photograph of PR391 site (provided courtesy of Dr. H. Batenipour)..... 117

Figure 4.21: Photograph of a transmission tower in the 138 kV Radisson-Churchill transmission line (provided courtesy of Dr. Marolo Alfaro)..... 133

Figure 5.1: Compression space (V:ln(p')) showing a point a_0 proceeding to a_1 after time t (after Kelln 2007) (With permission from Dr. C. Kelln)..... 163

Chapter 1: Introduction

1.1 Background

Northern Canada is rich in mineral, petrocarbon, and hydroelectric energy resources and is home to many First Nations communities. Road, rail, and air communications are essential in developing this area to maintain connections to these communities and to extract natural resources. Thawing of summer ice in the Arctic Ocean is expected to lead to increased shipping into the port of Churchill. Additional infrastructure, such as roads and railways, will be needed in northern Manitoba to accommodate a growing demand. Design and maintenance of this new infrastructure will have to take account of climate change and degradation of the engineering properties of soil over the expected life of these projects.

Design and construction of infrastructure in these regions, or in other scenarios where temperatures fluctuate over a wide range, are prime examples of where understanding the effects of time and temperature on the behaviour of foundation soils is necessary. This is important where permafrost exists or where the ground experiences many freeze-thaw cycles. Climatic and anthropogenic changes are leading to increases in ground temperatures and, in some areas, thawing of permafrost. This can result in differential settlements and non-recoverable shear deformations (Brown 1967).

Construction of highway fills in Northern Manitoba currently follow similar practices to those used in warmer regions. Fill materials typically have higher thermal conductivity than the native soil. In addition, construction of roadways and other infrastructure removes vegetation cover, alters drainage patterns, affects snow cover, and

increases heat transfer. As a result, construction of infrastructure contributes significantly to disturbance of the discontinuous permafrost currently encountered in the northern half of Manitoba. The disturbance lies approximately north of an isotherm with a current mean annual air temperature of 0.0°C. Observations and studies have suggested that the mean annual surface temperatures in northern Manitoba may increase upward of 4.0°C in the next hundred years (IPCC 2007). (The author's research sites discussed later in Chapters 3 and 4 are located in Northern Manitoba.) Thus, there is a need to improve our understanding of the performance of civil engineering infrastructure as temperatures change with time. In addition, variations in other meteorological conditions such as, precipitation, solar radiation, and wind speed may induce temperature changes in the ground and may alter soil behaviour.

Projects involving northern infrastructure and climate change have sparked greater interest in the fields of science and engineering into understanding the effects of temperature on infrastructure. Researchers are investigating ways to mitigate the potentially negative impact on infrastructure, some of which involve preserving permafrost. In turn, this increased interest may help to improve communications between geoscientists and geotechnical engineers as problems such as these are approached from different perspectives.

In engineering, there is a growing need to better understand the effects of time, strain rate, and temperature on soil behaviour in a broader sense. Time-dependent stress-strain behaviour of clayey soils has been observed (e.g. Tavenas et al. 1978; Graham, Crooks, and Bell 1983; Leroueil et al. 1985). This behaviour is now supported in mathematical soil models (e.g. Yin 1990, Kutter and Sathialingam 1992, Hinchberger and

Rowe 1998, 2005, and Kelln 2007) which can explain deformations of embankments and foundations that were not described well by traditional soil mechanics approaches.

The effects of temperature are not limited to infrastructure impacted by climate. Disposal of nuclear waste and industrial structures such as furnaces and refrigeration plants, also involve understanding the effects of heat transfer on soil behaviour. Nuclear waste, for example, produces temperature and pressure variations, swelling and shrinkage, and stress-strain changes in the materials involved in the projects (Graham et al. 2001). In addition, temperature variations induce changes in the diffuse double layers (DDLs) in clay soils, and in turn, mechanical properties such as compressibility, pore water pressures, strength and hydraulic conductivity (Tanaka 1995).

The DDLs have a direct interaction on viscoplastic behaviour as they influence particle distributions and interparticle forces. Some thermal behaviour observed in the laboratory has also been developed into mathematical models (e.g. Hueckel and Borsetto 1990, Tanaka 1995).

Current semi-empirical soil models describe, separately, time- (viscoplastic) and temperature- (thermoplastic) dependent soil behaviour as extensions to traditional elastoplasticity. The challenge now is to develop these concepts - viscoplasticity and thermoplasticity - in an encompassing elastic-plastic model capable of reproducing soil behaviour that is commonly observed in the laboratory and the field. Background research on viscoplasticity and thermoplasticity is dealt with more completely in Chapter 2, which provides a review of the literature related to the author's project.

1.2 Research Objectives

This thesis examines the following hypotheses:

(1) Thermistors installed in field projects provide useful data for calibrating thermal numerical models for simulating and predicting temperature changes in clay soils.

(2) Existing viscoplastic and thermoplastic models can be combined into an encompassing elastic thermo-viscoplastic model using a semi-empirical framework.

The objective of (1) is to produce a numerical model that can be used as a predictive tool for determining changes in temperature in geotechnical structures. The objective of (2) is to develop a constitutive model that will reproduce the combined effects of temperature- and time-dependent mechanical behaviour of soil observed in laboratory and field tests.

Fulfillment of the first hypothesis will be attained through developing thermal numerical models using commercially available software calibrated using field measurements. Two projects will be examined; an unstable section of road embankment, and foundations for electrical transmission towers. The models will use thermal material properties determined from laboratory testing and will be validated against measured field data from both sites.

Fulfillment of the second hypothesis will be attained by examining the impact of temperature on the creep parameter, ψ, introduced in the elastic viscoplastic (EVP) model developed by Kelln (2007), such that $\psi = \psi(T)$. This is consistent with a suggestion by Kelln (2007). Laboratory testing for this hypothesis was not included in the project; therefore, published laboratory data is examined and setting the creep parameter as a function of temperature is explored quantitatively through a sensitivity analysis. The model is validated qualitatively using published data.

1.3 Scope of Thesis

The field sites included in this thesis were part of the programs of other postgraduate students at the University of Manitoba. There is no separate field component for this thesis, which is based on original research by the author into data collected by others from the field sites.

Provincial Road 391 (PR391) was the research site for the doctoral thesis published by the author's colleague, Dr. H. Batenipour (Batenipour 2012). The Radisson-Churchill transmission line was part of a project initiated by Manitoba Hydro. Data provided came from reports by technicians of Manitoba Hydro and thermistors monitored on site between 1987 and 1990. The author has not visited this site personally.

Thermal numerical modeling of both sites was performed by the author using data provided by Batenipour et al. (2010), Batenipour (2012), Manitoba Hydro, the author's laboratory program, and empirical relationships found in the literature. For this thesis, the laboratory program tested for thermal conductivity on samples from PR391, the Manitoba Hydro site, and PR373 (The results are not yet published at the time of writing).

The development of the ETVP model is confined to temperature variations above 0.0°C to avoid the added complexities surrounding phase changes of water in the soil matrix. The model is developed in a spreadsheet and has not been implemented in commercially available software as an add-in function.

1.4 Organization of Thesis

Following this Introduction in Chapter 1, Chapter 2 reviews literature pertinent to the

research study. The chapter explores the effect of temperature on soil, discusses the development of elastic-plastic models, examines the concepts of viscoplasticity and thermoplasticity, and concludes with a discussion on mathematical similarities that may allow these concepts to be combined into an elastic thermo-viscoplastic (ETVP) model.

Chapter 3 presents laboratory testing for thermal properties on soil. The theory, procedures, and apparatuses used in obtaining thermal properties are described and a discussion on the results is presented. These thermal properties are then used in the numerical modeling presented in Chapter 4.

Chapter 4 describes two case histories for which thermal numerical modeling was developed: (i) a section of the PR391 road embankment near Thompson, Manitoba and (ii) the design and performance of tower foundations for the Radisson-Churchill transmission line. Modeling and field results from both sites are discussed.

Chapter 5 presents the framework for the new ETVP model. Relevant formulations from previous EVP, TEP, and ETP models are outlined. Terminology related to the new ETVP model is introduced and described. A sensitivity analysis is presented with results from simulated drained and undrained triaxial tests. A discussion is included on the parameters used in the analysis.

Chapter 6 analyzes quantitatively the response of the ETVP model by exploring how the parameters in the sensitivity analysis affect the results. Trends and anomalies in the data are identified and discussed. The model is then validated qualitatively and the practical applications of the ETVP model are presented.

Chapter 7 provides a summary of the work presented in this thesis, presents the author's conclusions, and offers recommendations for future work.

Chapter 2: Literature Review

2.1 Introduction

A discussion regarding the implications of temperature changes in soil, clays in particular, is presented along with a brief examination of climate change and the importance of understanding temperature through improved thermal modeling. The chapter then examines relationships between temperature and load-deformation behaviour.

Elastic-plastic behaviour of soils is explored and various approaches to this concept are presented. A semi-empirical model, Cam-clay, is chosen and key features and assumptions in the model are explained. Discussion continues with strengths and weaknesses of the model and its ability to be easily expanded to include aspects of temperature and time, among others.

An introduction to thermoplasticity includes a critique of two existing models. Viscoplasticity is then presented, with descriptions of contrasting theories and developed solutions. A discussion on the similarities between thermoplasticity and viscoplasticity provides a bridge between these concepts. An overview of existing elastic thermo-viscoplastic (ETVP) models based on mechanics provides additional insight into combining concepts from separate semi-empirical models into an encompassing model. This provides a foundation for implementing temperature effects in the model developed in Chapter 5 and justifies proceeding with an examination of the two hypotheses presented in Chapter 1.

2.2 Thermal Modeling

Understanding the effects of temperature on the behaviour of clay soils plays an important role in various engineering applications. These include construction in northern regions, areas experiencing variations in meteorological conditions (e.g. solar radiation, precipitation, temperature), and disposal of nuclear waste to name a few. A large portion of earlier research at the University of Manitoba explored the effects of high temperature and pressure on a bentonite-sand 'buffer' used in nuclear waste disposal (Lingnau 1993, Yarechewski 1993, Tanaka 1995, and Crilly 1996). One of the primary focuses in understanding the effect of temperature on soil has been at temperatures above the freezing point of water (0.0°C).

Effects of Temperature:

Farouki (1986) summarizes research on the relationship between thermal properties (e.g. thermal conductivity, heat capacity, thermal diffusivity) and various physical properties (including density, water content, degree of saturation). Campanella and Mitchell (1968) discuss a number of studies that establish the significance of temperature on the physical and mechanical behaviour of saturated soil. Extensive literature reviews on the temperature effects on clay are presented by Lingnau (1993) and Tanaka (1995). Only a summary of the principal effects is provided here. It is important to note that a large portion of research pertaining to the effects of temperature on clay has tested specimens at temperatures above 20.0°C to upwards of 100.0°C and not at near zero temperatures.

Campanella and Mitchell (1968), among others, report constant effective stress tests with open drainage lines experience a decrease in volume (expelling water) with an

increase in temperature and an increase in volume (absorbing water) with a decrease in temperature. The volume changes are irrecoverable for a first increase in temperature and partially recoverable for temperature cycles less than the magnitude of the first temperature increase. Figure 2.1 shows this behaviour and suggests a parallelism to overconsolidated behaviour (Campanella and Mitchell 1968). The volumetric strains for the recoverable and irrecoverable portions of this behaviour are termed thermo-elastic and thermo-plastic, respectively (Tanaka 1995).

Temperature increases lead to higher pore water pressures when drainage is restricted (undrained conditions). Under constant isotropic total pressures, Campanella and Mitchell (1968) show that pore water pressures induced by temperature changes are reversible and that small changes in temperature result in substantial changes in pore pressure. This results in reduction of effective stresses. Figure 2.2 shows pore water pressures as a function of temperature. Campanella and Mitchell (1968) also report that the compression indices (C_c) of remolded illitic clay were unaffected by temperature (Figure 2.3). Demars and Charles (1982) and Crilly (1996) report similar results.

Tanaka (1995) provides a full discussion regarding the discrepancies in the literature pertaining to the strength of soils. In short, for an increase in temperature, some researchers show a decrease in strength (Hueckel and Baldi 1990) whereas others show an increase in strength (Lingnau 1993). Graham et al. (2001) explain that the discrepancy in the results does not imply faulty experiments, but rather different overconsolidation ratios, drainage conditions, and changes in temperature. They further explain that the different results may also be due to differences in the dielectric constant for different clay minerals. This implies that procedures used in laboratory testing must be carefully

considered before comparing the results with those from other researchers and from proposed numerical models.

Further discussion into thermoplasticity is provided in Section 2.5, which discusses the models produced by Hueckel and Baldi (1990) and Tanaka (1995) in more detail. Section 2.7 presents additional information and compares similarities between viscous and thermal behaviour.

The excellent laboratory work of Côté and Konrad (2005*a* and *b*, 2006, 2007) has not been related to the concept of thermoplasticity. Their research is primarily experimental and related to methods for determining and predicting thermal conductivities and improving design approaches. The research provides valuable insights into heat transfer and the rate at which thermal strains develop.

Effects of Climate and Infrastructure:

Currently, permafrost is encountered within the northern half of Canada. It corresponds approximately to an isotherm with a current mean annual air temperature (MAAT) of 0.0°C. Observations and studies have suggested that the mean annual surface temperatures for the author's research sites (presented in later Chapters) may increase upward of 4.0°C in the next hundred years (IPCC 2007). As a result, there is a need to improve our understanding of the performance of civil infrastructure as temperatures change with time in these northern regions.

It is evident that ground in northern Canada is thawing due to both climatic (meteorological) and anthropogenic causes (e.g. Brown 1997). Variations in meteorological conditions such as, precipitation, solar radiation, and wind speed induce

temperature changes in the ground and will eventually alter thermal behaviour of the soil. The anthropogenic causes mentioned here refer to civil infrastructure and alterations to the terrain and natural vegetation, not to emissions and other greenhouse gases. These anthropogenic causes all affect settlement, drainage patterns, soil moisture, and insolation, such that ground temperatures, and potentially thermal properties, are affected. This conclusion arises from earlier research outlining the effect of water, density, and degree of saturation and their importance to thermal properties of soils (Farouki 1986).

2.3 Elastic Plastic vs. Non-linear Functions

A linear-elastic material experiences a reversible increment of strain, $\Delta\varepsilon$, proportional to an applied (or removed) increment of stress, $\Delta\sigma$. The ratio of (normal) stress-to-strain remains constant at Young's modulus, E, and obeys Hooke's Law. A nonlinear elastic material experiences a variable ratio between stress and strain such that at different stress levels, σ_i and σ_j, $\Delta\sigma$ produces different reversible strain increments $\Delta\varepsilon_i$ and $\Delta\varepsilon_j$, respectively. This type of material generally experiences a loss of stiffness with an increase in load, although some materials may stiffen with strain.

An elastic-plastic material does not fully recover all strains upon unloading, thus resulting in non-recoverable plastic deformations. Clay and other soils can often be modeled successfully as elastic-plastic materials. Various types of models have been developed out of a need to describe the behaviour of soil commonly observed in the laboratory under diverse testing conditions. Some of these models are described below.

Elastic-perfectly plastic Model:

An elastic-perfectly plastic model is defined by an elastic region and a plastic region separated by a yield locus. The elastic region may follow either linear or nonlinear elasticity and may be isotropic or anisotropic; however straining takes place in the plastic region at a constant load (or stress level) as shown in Figure 2.4. This implies that the material will behave elastically below a certain stress. At this stress, it will deform plastically until the load (stress) is removed. Some residual deformation will be experienced after unloading. This material model is a non-strain hardening model, meaning additional strength is not gained as the material continues to strain. For example, Bolton and Whittle (1999) apply an elastic-perfectly plastic material model to experimental results obtained from a pressuremeter.

Hyperbolic Model:

Kondner (1963) and Duncan and Chang (1970) showed that the stress-strain behaviour of clay can be approximated by a hyperbola. Their models are capable of modeling non-linear, stress-dependent, inelastic behaviour of clay. The model relies on a locally variable tangent modulus of elasticity, E_t, Poisson's ratio, v, and the Mohr-Coulomb failure criterion; cohesion, c, and friction angle, φ. Yin (1990) points out that the Duncan-Chang hyperbolic model is limited because it does not "account for volumetric strains produced by shear strains and shear strains produced by effective mean stresses." It also requires considerable calibration because the parameters of the hyperbolic function vary with stress level in sands and preconsolidation pressure in clays.

Elastic-Plastic Hardening Models:

An elastic-plastic soil with strain hardening, as shown in Figure 2.5, gains strength (load resistance) with additional straining. Upon unloading, the material recovers only a portion of the strain applied as a result of the previous plastic deformations, but has an enlarged elastic region should reloading occur.

A volumetric hardening model limits elastic behaviour to stresses and stress increments inside a yield surface. When applied mean and shear stresses attempt to exceed the current yield surface, plastic strains begin to develop and the yield surface becomes enlarged to include the new stress state. This enlargement of the elastic region is usually accompanied by compression and decreasing specific volume. Figure 2.6 illustrates expanding elliptical yield surfaces as a result of volumetric hardening. 'Original' and 'Modified' Cam-clay (Roscoe and Schofield 1963; Roscoe and Burland 1968) are examples of volumetric hardening elastic-plastic models. Fundamentals of Cam-clay are discussed in Section 2.4. A deviatoric hardening model (e.g. Pietruszczak and Niu 1992) alters the yield surface by allowing a variation in the friction angle. A deviatoric hardening model can be applied to potentially unstable materials or material experiencing dynamic loading. More detailed discussion on the differences between the volumetric hardening and deviatoric hardening model is not presented in this thesis.

Geomechanical/Physics-based models:

Geomechanical models are complex mathematical models that rely on continuum mechanics and physics. They employ series of matrices and differential equations that satisfy force equilibrium and the laws of conservation of mass and energy, and at the

same time define relationships such as stress-strain behaviour, fluid flow, degree of saturation, thermodynamics, boundary conditions, among others. Models such as these can have elements defined in any coordinate system (e.g. planar, cylindrical or spherical) depending on symmetry. Zhou et al. (1998*a*, *b* and *c*) present models that describe the effects of temperature, pore pressure, saturation, deformation, and volume change.

Geomechanical models can contain a few to tens of variables. Graham et al. (1997) suggest that a concern with these models lies in the inability to determine the various parameters reliably in laboratory testing. Despite considerable work at a number of institutions, it is still unclear how some parameters can be determined and whether resulting solutions are unique.

2.4 Cam-clay: An Elastic-plastic Model

2.4.1 Origins

Cam-clay was originally developed as a model that helped the understanding of 'triaxial' compression and the relationship between stresses and strains in clay soils (Roscoe and Schofield 1963). Roscoe and his colleagues published papers (e.g. Roscoe et al. 1958; Roscoe et al. 1963) that describe the yielding of clays, stress paths, and critical state soil mechanics. 'Original' Cam-clay assumes partial (non-linear) recovery of volumetric strains and was developed based on work and energy theories and a conceptual material–not real soil (Schofield and Wroth 1968).

'Modified' Cam-clay (MCC) was introduced by Roscoe and Burland (1968) with a revision of the yield surface to better account for shear distortion that occurs on stress paths with a low stress ratio ($\eta = q/p'$) within the state boundary surface. Mean effective

stress is defined as $p' = p - u$; $p = (\sigma_1 + \sigma_2 + \sigma_3)/3$; deviatoric stress is defined as $q = q' = \sigma_1 - \sigma_3$, where σ_1, σ_2, σ_3 are principal stresses, and u is pore water pressure.

2.4.2 Terminology

When Cam-clay was redefined by Roscoe and Burland (1968), it was named 'modified' Cam-clay to differentiate it from the original model described by Roscoe and Schofield (1963). Discussions in the literature conclude that the physical and mathematical capabilities of MCC, in conjunction with experimental results, indicate that it is the superior model. Gens and Potts (1987) and Wood (1990) suggest dropping the 'modified' qualifier since most literature indicates that 'modified' Cam-clay was the more commonly used non-linear effective stress model. This is still the case and has led to the adoption of the terms 'original Cam-clay' and 'Cam-clay', deleting 'modified' in the latter. Many publications continue to use 'modified' Cam-clay and Cam-clay (implying 'modified') interchangeably while differentiating from the original Cam-clay model through the use of the 'original' qualifier or by the abbreviation, OCC. The use of Cam-clay or MCC herein implies 'modified' Cam-clay.

2.4.3 Validity of Assumptions

The definition of an elastic plastic model must be guided by four main assumptions of the material behaviour (Wood 1990). These include knowledge of (1) elastic properties, (2) a yield criterion, (3) a plastic potential (flow rule), and (4) a hardening rule. Strictly speaking, a failure criterion is not required but is convenient and commonly included. Cam-clay was based on the following fundamental assumptions:

(1) The elastic behaviour is isotropic and non-linear; volumetric and shear strains are uncoupled; and, stress-strain behaviour is straight with slope κ in V-ln(p') space, where V is the specific volume;

(2) Yield surfaces are elliptical;

(3) An associated flow rule applies;

(4) The plastic hardening law is constant and is straight with a slope λ in V-ln(p') space;

(5) Large strain failure is controlled by the Mohr-Coulomb criterion where $(\sigma_1'/\sigma_3')_{max}$ remains constant in q-p' space.

Each assumption and the associated terminology are addressed in more detail below. Figures 2.6 and 2.7 outline the basics of Cam-clay that are discussed in the following sections. A three dimensional 'state boundary surface' can be constructed from this figure. Behaviour inside this surface is elastic, whereas behaviour on the surface, has both elastic and plastic components.

(1) Elasticity and Plasticity:

Strains resulting from stress increments can be partitioned into two components; elastic and plastic. These components can be added together to give the total strain. By definition, elastic strains are considered instantaneous and recoverable, whereas plastic strains are permanent and non-recoverable. Plastic deformation represents a physical rearranging of soil particles. In clays, physical rearrangement requires volumetric expansion or compression, movement of pore water, and time dependency.

Given the complexities of clay (e.g. anisotropic, multi-phase, viscous, etc), 'recoverable' is a relative term; nonetheless Hooke's Law is applied when linear isotropic

behaviour is assumed. This means that stress and strain are related through the elastic constant, Young's Modulus, *E*, and the relationship between axial and radial strains, and Poisson's ratio, *v*. Alternatively, in soil mechanics, the bulk, *K*, and shear, *G*, moduli are commonly used. They are related to E and ν by:

[Eq. 2.1] $$K = \frac{E}{3(1 - 2v)}$$

[Eq. 2.2] $$G = \frac{E}{2(1 + v)}$$

Any combination of two parameters from *E*, *v*, *K*, and *G* are the only requirements in defining isotropic elasticity. In matrix form, the relationship between stress and strain for isotropic materials is defined as:

[Eq. 2.3] $$\begin{bmatrix} p' \\ q \end{bmatrix} = \begin{bmatrix} K' & 0 \\ 0 & 3G \end{bmatrix} \begin{bmatrix} \varepsilon_v \\ \varepsilon_s \end{bmatrix}$$

where $p' = p - u$; $p = (\sigma_1 + \sigma_2 + \sigma_3)/3$; $q = q' = \sigma_1 - \sigma_3$; $\varepsilon_v = \varepsilon_1 + \varepsilon_2 + \varepsilon_3$; and $\varepsilon_s = 2(\varepsilon_1 - \varepsilon_3)/3$ and p is mean stress, q is deviatoric stress, u is pore water pressure, ε_v is volumetric strain, ε_s is shear strain, and σ_i and ε_i are principal stresses and strains (Figure 2.8).

Evidence for elasticity is commonly examined through laboratory tests and a graphical representation of the results. As mentioned earlier, 'recoverability' is not usually complete, so 'elasticity' should be qualified. Typical graphs show a stress-strain (σ_i-ε_i) relationship; however in soil mechanics it is also common to see p'-e, p'-V, p'-ε_v, q-ε_s graphs, where '*e*' is the void ratio and '*V*' is specific volume, (*1 + e*). Specific volume, *V*, is the volume occupied by unit volume of solids. Graham, Noonan, and Lew (1983) show the stress-strain relationships, p'-ε_v and q-ε_s, between samples of Winnipeg (Agassiz) clay (Figure 2.9). (Note that recoverability was not explored.) The discontinuities represent a

change in behaviour from primarily elastic behaviour to a combination of elastic and plastic behaviour and is thought to be yielding (Graham, Noonan, and Lew 1983).

Typical oedometer results show distinct elastic and plastic behaviour with repeatable results. Figure 2.10 illustrates elastic behaviour (C_r, recompression index) and plastic behaviour (C_c, compression index) and indicates that the rate of either elastic or plastic deformation can be modeled approximately as constant with respect to log(stress). Various methods (e.g. the method illustrated in Figure 2.10) exist for calculating C_r and C_c, but these methods are not discussed in this thesis.

Many argue (e.g. Jardine et al. 2004, Clayton and Heymann 2001) that true elasticity is only seen when strains are very small, of the order 10^{-3} or less. Unloading-reloading cycles, as shown in Figure 2.10, usually show some hysteresis that may be associated with viscous effects and not just elasticity.

(2) Yielding and Yield Loci:

Yielding, first observed in metals, was initially defined by the Tresca, and subsequently the von Mises, criteria. These criteria are well suited for metals, but are less suited to represent yielding in soils. Regardless, the principle of yielding remains the same.

In its simplest definition, yielding is behaviour observed during loading (or reloading) when a material deviates from a stiffer elastic response into a plastic response. This occurs when the reloading exceeds the previous maximum stress, also known as the yield stress. The new maximum loading becomes the new yield stress should the material be unloaded and later reloaded. In one-dimensional compression, soil mechanics more commonly refers to yield stresses as preconsolidation pressures, σ'_{zc} (see Figure 2.10).

Yielding is also observed along more general stress paths plotted in *p'-q* planes. The locus of separate yield stresses is known as a yield locus.

Yielding is more readily observed in natural clays due to the microstructure that developed following deposition (Wood 1990). Graham, Noonan and Lew (1983) discuss testing on Winnipeg clay from different depths and preconsolidation pressures. The paper notes that preconsolidation pressure decreased with depth in this clay due to atmospheric weathering and glacial activity at shallow depths.

(3) Flow Rule:

The flow rule defines the ratio between the volumetric and shear components of plastic strain (ε_v^p, ε_s^p). Generally, it is related to the respective state of stress (p'_y, q_y) on the yield surface. Schofield and Wroth (1968) defined the flow rule as:

[Eq. 2.4] $$\nu\dot{\varepsilon}_{ij}^{p} = \frac{\partial F}{\partial \sigma'_{ij}}$$

where ν is a scalar factor proportional to the amount of work used and F is the yield function. Chen and Baladi (1985) use Q for the plastic potential and $d\Phi$ as the scalar function describing expansion or contraction of the yield surface.

An associated flow rule concept is illustrated in Figure 2.11 and assumed in Cam Clay. At each state of stress, the plastic strain increments can be plotted as vectors. A curve joining these vectors such that they are normal to the curve is termed the plastic potential. In cases where the yield function and the plastic potential are different, the flow rule is termed non-associated. An associated flow rule occurs when the yield function and plastic potential are identical. This simplifies calculations within a model.

(4) Hardening Law:

Prager (1959) described two variations of a hardening law in his discussion on the movement of a yield surface. These hardening laws are isotropic and kinematic. In isotropic hardening, the yield surface can change size but not its shape or alignment; that is successive yield surfaces remain centred on the original axes. In kinematic hardening, the yield surface remains a constant size but can change position. Isotropic hardening is easier to describe mathematically. Volumetric hardening is similar, mathematically, to isotropic hardening, except that, as shown in Figure 2.6, there is a common point and only one common axis for all yield surfaces.

Wood (1990) discusses how a normalized yield loci (q/σ'_{zc} vs. p'/σ'_{zc}) demonstrates volumetric hardening. The shape of the yield locus remains constant regardless of preconsolidation pressure; thus volumetric hardening can be assumed. The elasticity, however, is anisotropic (Graham and Houlsby 1983).

(5) Failure Criterion:

The Mohr-Coulomb failure criterion is widely used to describe failure in soil mechanics. This criterion has been adopted within the Cam-clay model although it is not required to fully define the model itself. The criterion describes the relationship between normal stress, σ'_n, and shear stress, τ_f, through cohesion, c', and a friction angle, φ, or angle of shearing resistance. This relationship is defined as:

[Eq. 2.5] $$\tau_f = c' + \sigma'_n \tan\varphi'$$

In Cam-clay, the cohesion term is assumed to be zero and in this case the Mohr-Coulomb failure criterion becomes $(\sigma'_1/\sigma'_3)_{max}$.

Strengths and Weaknesses of Cam-clay:

The strength of the Cam-clay model lies with its relative simplicity. The equations can be broken down into linear, logarithmic, and elliptical functions that can be manipulated easily. The input parameters required for the model can be obtained through standard oedometer and conventional triaxial tests. These parameters have a physical meaning that can be readily understood. Cam-clay also has the capability to model realistically the stress-strain behaviour of isotropically consolidated clays and can handle both compression and shear behaviour (Perić et al. 2006).

A disadvantage in Cam-clay is the assumption of perfect elasticity within the yield surface; however, this can be compensated with the formulations discussed later that account for viscous behaviour. Another disadvantage of Cam-clay is that for both drained and undrained analyses only effective stress strength parameters (such as φ') are used as inputs. Thus, results can be difficult to compare with other analyses that use undrained shear strength, s_u. Natural clays have also been shown to exhibit anisotropic behaviour (e.g. Graham and Houlsby 1983) and although the model does not handle anisotropy at all, valuable insights into soil behaviour can still be gained.

2.4.4 Extensions of Cam-clay

The framework describing Cam-clay can be manipulated easily. Studying one known aspect of soil behaviour with respect to a new variable can lead to the development of a new form of the basic Cam-clay model as described in Sections 2.5 and 2.6. Cam-clay, by itself, is one of a large family of elastic-plastic models that can reasonably predict soil behavior in a number of applications that include effects of changes in temperature,

viscosity, loading duration, degree of saturation and pore fluid chemistry (e.g. Hueckel and Borsetto 1990, Yin 1990, Tanaka 1995, Wheeler and Sivakumar 1995, Hueckel 1997, Tamagnini 2004, Kelln 2007, among others).

2.5 Thermoplasticity

Thermoplasticity describes non-recoverable temperature-dependent behaviour. This behaviour primarily includes deformations as a result of expansion or contraction of a specimen. Thermoplastic behaviour is not only dependent on temperature, but is affected by the presence of water and whether drainage is permitted. It is also affected by stress history and mineralogy. Modeling temperature effects in soil involves understanding this behaviour and the mechanics of heat flow. This section focuses on two models describing the effects of temperature on clays above the freezing point of water (0.0°C).

A Semi-Empirical Mechanics Approach:

Hueckel and his colleagues introduced a thermoplastic model in the companion papers Hueckel and Borsetto (1990) and Hueckel and Baldi (1990) that builds on the Cam-clay model to include temperature effects. The focus in this model is on thermo-mechanical behaviour of the soil skeleton in drained conditions. Therefore, the model leans toward a mechanics-based approach yet is still based on a semi-empirical framework.

The elastic domain, defined by the three-dimensional elliptical surfaces in Figure 2.12, in this model is defined as thermal softening. That is, the yield surface will shrink during heating and expand during cooling. To sustain constant effective stress during drained heating, thermal softening must be compensated by plastic strain hardening.

Thus, heating implies compressive plastic strains or thermal consolidation (Hueckel and Baldi 1990). Cooling then results in elastic deformation and does not produce plastic strains.

Another aspect of the thermoplastic model is the assumption of "nonassociativity". Hueckel and Borsetto (1990) state that thermoplastic strain depends on strain and temperature history and that it cannot be expressed through effective stress and temperature but instead must be related to stress rate and temperature rate. They conclude by stating that for the solely mechanical part of soil behaviour, a more sophisticated model should be used over MCC.

This model has been used to examine the thermomechanical failure due to pore water pressure on various samples subjected to heating and cooling (Hueckel and Pellegrini 1991, 1992). Tanaka (1995) argues that this model does not extend significantly the understanding of soil behaviour in V-ln(p') compression space, which is an important feature of the Cam-clay model. He also argues that the rules outlined for elastic and plastic straining in compression space have not been fully defined.

Tanaka's TEP Model:

Tanaka (1995) developed a new thermo-elastic-plastic (TEP) model based on the MCC critical state framework. This model describes behaviour of soil at different temperatures; however, only rate-independent soil is considered (that is, no creep behaviour is included). Tanaka built six assumptions into his model:

(1) Elastic properties (shear (G) and bulk (K) moduli) depend on temperature, where lower values of the moduli result from higher temperatures. This means the slope of the unload-reload lines, κ, in V-ln(p') space increases with temperature, $\kappa = \kappa(T)$;

(2) Yield loci shrink with increasing temperature but remain elliptical in q-p' space;

(3) Normal compression (hardening) curves in V-ln(p') space have slopes, λ, that are independent of temperature, though lines are at successively lower values of specific volume, V, at higher temperatures;

(4) Large-strain strength envelopes are independent of temperature in q-p' space and the slope $M = (q_f/p'_f)$ is a unique value in q-p' space at all temperatures;

(5) The flow rule is associated at all temperatures;

(6) The coefficient of undrained thermal expansion is independent of temperature.

Similarities between Tanaka's TEP model and the model presented by Hueckel and colleagues are evident though there are also some differences. Both models follow assumptions (2), (3), and (4) but the model presented by Hueckel and colleagues assumes a non-associated flow rule. Tanaka, Graham, and Crilly (1995) comment that a large amount of experimental evidence suggest that an associated flow rule can be assumed without serious error. Hueckel and Pellegrini (1992) present a discussion related to (6) but the concept is not formally added to their model.

Figure 2.13 illustrates the framework of Tanaka's model in V-ln(p') compression space. The figure shows κ_1, λ_1 for temperature T_1 (unload-reload line (url) M_1P_1); constant volume heating resulting in κ_2, λ_2 for T_2 (url M_2P_2); and drained heating resulting in κ_2, λ_2 for T_2 with a url $M'_2P'_2$ at a different position. At a lightly overconsolidated position N_1,

or heavily overconsolidated position P_1, drained heating from T_1 to T_2 would result in compression to N_2 or expansion to P_2 and is referred to as temperature-induced incremental elastic volumetric strain, $d\varepsilon_v^{Te}$.

The key assumption in Tanaka's model is in (1) where he states that the unload-reload lines are a function of temperature such that κ increases with temperature. For this reason, Tanaka's model is a TEP model as opposed to an elastic thermoplastic (ETP) model. Tanaka (1995) argues that some experimental evidence for this phenomenon is limited and has not been formally presented. Crilly (1996) tested this theory in a series of oedometer tests with constant load durations and concluded that the unload-reload lines are independent of temperature. Graham et al. (2001) use $\kappa = \kappa(T)$ despite Crilly's results, to allow the calculation of $d\varepsilon_v^{Te}$.

The problem may relate to how thermo-plastic strains are accounted for in Tanaka's model. Kelln (2007) clarified that the reason why κ in the Bjerrum (1967) model and in constant strain rate tests (Graham, Crooks, and Bell 1983) apparently varies with strain rate is because measurements include viscoplastic strains. It is possible that the variable κ required in Tanaka's model, and observed in some laboratory data, also includes thermo-plastic strains at different temperatures. This is examined in Chapter 6.

Equations and more detailed discussions for Tanaka's TEP model can be found in Tanaka (1995), Tanaka et al. (1995*a*), Tanaka et al. (1995b), Lingnau et al. (1995), Lingnau et al. (1996), Tanaka et al. (1997) and Graham et al. (2001.)

2.6 Viscoplasticity

Viscoplasticity describes (strain) rate-dependent non-recoverable behaviour. For example, a constant load applied to any material will, with time, lead to permanent plastic deformation (In clays, this involves rearrangement of soil particles). This is commonly referred to as creep or secondary compression. Kelln (2007), however, suggests that creep is simply time-dependent plasticity and that the term ‘creep’ is, in itself, redundant since creep is a result of time and plastic straining.

The effects of time on the stress-strain behaviour of clay have been observed in the laboratory (e.g. Graham, Crooks, and Bell 1983; Leroueil et al. 1985) and have led to the development of elastic viscoplastic (EVP) soil models. These models help explain mathematically the physical evidence for rate-dependent behaviour. In the process of formulating an EVP model, several approaches have been proposed. They can be summarized by two hypotheses that are identified in the literature as Hypothesis A and Hypothesis B (Ladd et al. 1977).

Hypothesis A and Hypothesis B:

Ladd and his colleagues proposed these hypotheses as a summary of consolidation theories. Hypothesis A separates consolidation into two components; 'primary consolidation' and 'secondary compression' (sometimes incorrectly called 'secondary consolidation'). 'Primary consolidation' occurs as a result of changes in pore water pressure (hydraulic gradients) while 'secondary compression' is due to creep (viscosity) of clay structures (Yin et al. 1993). The basis for this hypothesis is Terzaghi's 1-D consolidation theory which assumes that the relationship between effective stress and

void ratio is independent of time and that changes in void ratio are due to changes in excess pore water pressures (Mesri 1973). Terzaghi's consolidation theory is used to calculate time-dependent primary settlement at the end-of-primary (EOP) consolidation. Once primary settlement has been completed, then a C_α coefficient (discussed further in Section 2.7) is introduced to estimate the 'secondary compression'. The implication of Hypothesis A is that a unique stress-strain relationship exists at EOP consolidation and that creep only begins after primary consolidation has been completed. Laboratory results (e.g. Kabbaj et al. 1988) indicate that the assumption of a unique relationship at EOP is incorrect. Thus Hypothesis A is invalid.

Hypothesis B assumes that creep (viscous) behaviour occurs during the whole consolidation process. This is consistent with approaches adopted in rheology and viscoplastic theories and used in continuum mechanics (Yin et al. 1995). Linear rheological models using elastic springs and viscous dashpots provided a foundation for describing time-dependent stress-strain behaviour. However, these models, being linear, were unable to adequately express non-linear soil behaviour. Nevertheless, Hypothesis B is the correct hypothesis. The concept behind Hypothesis B has been explored by Perzyna (1963); Olzsak and Perzyna (1964); Bjerrum (1967); Yin (1990); Hinchberger and Rowe (1998); and Kelln (2007), among others.

Perzyna's viscoplastic framework (and recent developments):

The original framework for an EVP model was proposed by Perzyna (1963) and Olszak and Perzyna (1964). Perzyna's framework assumes that total strain rates are the sum of elastic and ‘anelastic’ (sic) components. Perzyna uses the term 'anelastic' to imply rate-

dependent deformation but with no obvious relationship between stress and strain. In more recent literature, the term 'anelastic' is replaced with 'viscoplastic', implying rate-dependent inelastic behaviour. The viscoplastic strain rate is partitioned into viscous and plastic components:

[Eq. 2.6] $$\dot{\varepsilon}_{ij} = \dot{\varepsilon}_{ij}^{e} + \dot{\varepsilon}_{ij}^{vp}$$

The viscoplastic strain rates are defined by the flow rule:

[Eq.2.7] $$\dot{\varepsilon}_{ij}^{vp} = \gamma\langle\Phi(F)\rangle\frac{\partial Q}{\partial\sigma_{ij}}$$

where γ is a fluidity parameter, F is the yield function, Q is the plastic potential, and Φ is a scalar function where:

[Eq. 2.8] $$\langle\Phi(F)\rangle = \Phi(F)\ for\ F > 0$$

$$\langle\Phi(F)\rangle = 0 \qquad for\ F \leq 0$$

If $Q \equiv F$, an associated flow rule applies, if $Q \neq F$, the flow rule is non-associated. This function implies that a change of stress within the yield surface ($F \leq 0$) results in only time-independent elastic deformations. A change of stress resulting in a position outside the yield surface ($F > 0$) results in time-dependent plastic deformations in addition to the elastic deformations. This is the reason the original framework is also known as overstress viscoplasticity.

The original framework established by Perzyna has provided a foundation for understanding time-dependent stress-strain behaviour. Several EVP models have been developed using this framework (e.g. Zienkiewicz and Cormeau 1974; Adachi and Oka 1982; Kutter and Sathialingam 1992; Hinchberger and Rowe 1998). In recent years, success in modeling has been achieved by Hinchberger and Rowe (2005), Gnanendran et

al. (2006), Li and Rowe (2007), and Hinchberger and Qu (2009), among others. These models are offshoots of the EVP cap model developed in Hinchberger and Rowe (1998).

Yin (1990) argues that many models, such as Zienkiewicz and Cormeau (1974) and Adachi and Oka (1982), define separate scalar functions to suit their modeling and that determination of the model parameters is difficult and unclear. Yin (1990) and Kelln (2007) comment that it is unclear why the scalar multiplier (Φ) is a function of the yield function (F). Despite success in EVP modeling, the models using Perzyna's framework still require a change in stress (overstressing) to begin viscoplastic straining. Models such as Yin (1990), Yin et al. (2002), and Kelln (2007) show this is unnecessary.

Bjerrum's time line model (and recent developments):

Bjerrum (1967) developed a conceptual model in which total compression is divided into 'instant' and 'delayed' compression, essentially different words for what are now called ‘elastic’ and ‘viscoplastic’ compression. He felt that Terzaghi's separation of compression into 'primary' and 'secondary' was arbitrary and he aimed at improving the understanding of time-dependent stress-strain behaviour. Figure 2.14 demonstrates the difference between Bjerrum's and Terzaghi's approaches.

Bjerrum (1967) also proposed a system of time lines that represent a unique relationship between void ratio (vertical strain), overburden pressure (vertical stress), and time, technically, the duration of loading. This system of parallel time lines (Figure 2.15) describes delayed compression in e-log(σ'_z) space and the relationship between vertical load, void ratio, and loading durations. The time lines begin with an 'instant' time line to describe first-time compression (lowest value of e for a given initial load). Bjerrum

(1967) argued "for a given value of the overburden pressure and void ratio there corresponds an equivalent time of sustained loading and a certain rate of delayed consolidation, independent of the way in which the clay has reached these values." Bjerrum used p-stress (Figure 2.15) to indicate effective overburden pressure (vertical stress) more commonly defined as σ'_z. In this thesis, "p" will be reserved for mean stress.

Yin (1990) criticized Bjerrum's model (which remained qualitative), stating that Bjerrum's understanding of the 'instant time line' was flawed and in conflict with observations of high constant rate of strain tests. The error in Bjerrum's understanding was that the 'instant time line' should be associated with the κ-line, not the λ-line. Yin commented further that Bjerrum's time lines were obtained from single-stage consolidation tests and that the method for finding 'equivalent time' is ill-defined. Nevertheless, Bjerrum's definition of 'instant' and 'delayed' compression and his time line model have provided a better understanding of the effects of time (or better, strain rate) on consolidation. Laboratory results (e.g. Graham, Crooks, and Bell 1983) support Bjerrum's model and demonstrate parallelism with the 'delayed' compression lines in e-log(σ'_z) space. Parallels also exist between Bjerrum's model and Yin's development of an EVP model (Yin and Graham 1989; Yin 1990; Yin and Graham 1994; Yin and Graham 1999; Yin et al. 2002).

Yin's EVP Models:

The models presented in Yin and Graham (1989), Yin (1990), and Yin and Graham (1994) introduced a new creep function within the MCC framework. These models were partially based on Bjerrum's time line model (1967) and the viscoplasticity mechanics

introduced by Perzyna (1963, 1966). Aspects of Bjerrum's model such as the 'instant time line' and 'equivalent time' were redefined and new terms such as a 'reference time line' and a 'viscoplastic limit line' were introduced to cope with other aspects of the model. The flow rule defined by Perzyna (1963, 1966) was used to calculate viscoplastic strain rates; however, Yin and his colleagues defined the scaling function as $S = \gamma <\Phi F>$ (refer to Equations 2.7 and 2.8) and present an approach for determining S in Yin (1990) and Yin and Graham (1999).

Yin et al. (2002) redefined the creep function and reformulated the model based on the framework outlined in Yin and Graham (1999) to accommodate both normally consolidated and overconsolidated clays in a general stress state. Yin and Zhu (1999) and Yin et al. (2002) demonstrate the model's ability to reproduce observed soil behaviour from triaxial tests for Hong Kong marine deposits (HKMD). Figure 2.16a illustrates axial strain, ε_a, versus deviatoric stress, q; and Figure 2.16b illustrates effective stress paths normalized with respect to preconsolidation pressure, σ'_c, at various overconsolidation ratios (OCRs) for overconsolidated HKMD samples (Yin et al. 2002).

Kelln's EVP model:

Kelln (2007) comments that Yin's model is intriguing but is difficult to assess due to the mathematics and terminology with which it is expressed. Kelln (2007) argues that many of terms introduced by Yin and his colleagues such as the 'instant time line', 'equivalent time', 'reference time line' and 'viscoplastic limit line' can all be linked "with well-established elements of time-independent elastic-plastic models to produce a simpler, more accessible, and equally effective representation of time-dependent behaviour".

The formulation of Kelln's model (Kelln 2007; Kelln et al. 2008*b*) is more logical than Yin's models. Kelln uses the specific volume, *V*, to describe the volumetric state as opposed to a strain variable. He reduces the material constants to simply κ and λ in *V*-ln(*p'*) space, and ψ in *V*-ln(*t*) space, (C_r and C_c in *V*-log(*p'*) space and C_α in *V*-log(*t*) space, respectively). In addition, Kelln uses a specific volume variable, V_m, to indicate the specific volume during 'secondary compression' (e.g. along the ψ-line). He allows the bulk modulus, *K*, and shear modulus, *G*, to vary with changes in specific volume. The big improvement in Kelln's model is incorporation of a viscoplastic limit line that overcomes an inadmissibility in Yin's model when dealing with stress increments in the normally consolidated range. Kelln's model also focuses more on strain rates. Figures 2.17 and 2.18 show inadmissible and admissible development of volumetric viscoplastic strains in Kelln's model (Kelln 2007).

Kelln's model has been used to analyze settlements of a highway embankment near Limavady in Northern Ireland (Kelln 2007; Kelln et al. 2008*a*; Kelln et al. 2009). A comparison between measured data and predicted results using Kelln's EVP model and MCC shows the strength of the new EVP model. Figure 2.19 shows a comparison of vertical displacements (settlement gauge) and Figure 2.20 shows a comparison of lateral displacements (inclinometer profile) at the Limavady site. The new model provides considerably better simulations of the displacements. A known limitation of the MCC model is its inability to successfully model lateral displacements.

2.7 Expansion to an elastic thermo-viscoplastic model

2.7.1 Similarities between time and temperature

The behaviour of clay displays many similarities when comparing the effects of time and the effects of temperature. These similarities indicate that it may be possible to combine earlier formulations that describe each behaviour separately. The similarities include the compression index, recompression index, and the coefficient of secondary compression.

Compression index, C_c and Recompression index, C_r:

The compression index describes the rate of plastic deformation with respect to log(stress) and is referred to as λ in V-ln(p') space. Bjerrum (1967) proposed a system of parallel time lines, as shown in Figure 2.15). These time lines describe delayed compression in e-log(σ'_z) space and the relationship between vertical load, void ratio and loading durations. Because the time lines are parallel in log(p') plots, they also essentially define constant strain rates. Graham et al. (1983) and Leroueil et al. (1985) show experimental, parallel lines corresponding to varying strain rates. The conclusion is that C_c, or λ, is independent of time. This has been modeled by Yin (1990), Yin et al. (2002), and Kelln (2007). Campanella and Mitchell (1968) and Eriksson (1989), among others, show similar behaviour with respect to temperature (Figures 2.3 and 2.21). This behaviour was included in the model presented by Tanaka (1995) (Figure 2.13).

It is widely accepted that neither time or temperature has a significant impact on the recompression index, C_r, or κ in V-ln(p') space. Tanaka (1995) assumed $\kappa = \kappa(T)$; however this theory was disproven by Crilly (1996). In the literature, more evidence supports Crilly's conclusions; however, some authors mention a noticeable change in

behaviour of clay for different overconsolidation ratios (OCRs). For example, Hueckel and Baldi (1990) showed that a clay with a low OCR would compress with drained heating, while the same clay at high OCR would expand. This type of behaviour was one of the important observations that led to Tanaka's (1995) model. For drained heating from temperature T_1 to T_2, Figure 2.13 shows specific volumes increasing from P_1 to P_2 and decreasing from N_1 to N_2. The model represents the observations correctly but is based on the incorrect assumption that $\kappa = \kappa(T)$.

Coefficient of secondary compression, C_α:

The coefficient of secondary compression describes the rate at which a soil, particularly clay, will deform with time under a constant effective stress after the dissipation of excess pore water pressure. The parameter C_α is obtained from the constant slope found in V-log(t) space. This behaviour is shown in Figure 2.22, where it is termed ψ in V-ln(t) space. Mesri and his colleagues have studied extensively, the effect of C_α and the relationship to the compression index, C_c and the ratio, C_α/C_c (e.g. Mesri 1973; Mesri and Godlewski 1977; Mesri and Choi 1979; Mesri and Choi 1985; Mesri and Vardhanabhuti 2005). Mesri and his colleagues found little variation in the ratio, C_α/C_c, for several types of clay. This may indicate that C_α, or ψ, is independent of stress state and more a function of mineralogy, DDLs and temperature. Kelln (2007), following Yin, assumes ψ as a material constant in the formulation of his EVP model.

Research at the University of Manitoba on a relatively low-plastic clay with a clay fraction around 50% indicates little variation on C_α with temperatures between 3°C and 21°C (Batenipour et al. 2009*a*, Batenipour 2012). This evidence alone does not disprove

the postulation that creep may be a function of temperature. High silt contents in specimens have been shown to greatly impact the performance of the specimen, especially for creep (e.g. Demars and Charles 1982). In addition, it may be plausible to assume that this particular clay is not as thermally active as another type of clay, the temperature range was insufficient to produce a noticeable change in C_α, or experimental error may be present (accuracy of the equipment and/or user). Mesri (1973) states that effects of temperature on C_α have garnered more attention than they deserve, but Leroueil and Marques (1996) state that compressibility of the soil should be described as a 'stress-strain-strain rate-temperature' relationship. Houston et al. (1985) show compelling evidence of temperature-dependent creep for undisturbed Pacific illite. They define the creep parameter as $\Gamma_{\varepsilon\alpha} = \Delta\varepsilon_v/\log(t)$ (in %/1 log cycle) and give values of 0.4%/log cycle at 40°C and 2.1%/log cycle at 200°C. A linear relationship of $\Gamma_{\varepsilon\alpha} = 0.0105T$ is fitted to their data (Houston et al. 1985). Burghinoli et al. (2000) identify a relationship between creep and temperature in their experiments and conclude that it requires more scrutiny.

Conceptually, the idea that secondary compression is a function of temperature makes sense. Evidence is not widely available, but the dependence on temperature is apparent in several publications. This thesis proceeds under this assumption.

2.7.2 Existing Mechanics-based Models

Perzyna's Research:

Perzyna discussed the theory and mechanics of the behaviour of EVP material during thermodynamical processes and published many papers with his colleagues. His work is largely mechanics-based and directed toward metals, but is still partially applicable to

soils. Perzyna (2005) presents recent modeling and mathematical advances in the development a model that describes thermo-elasto-viscoplasticity. Perzyna's formulations are very complex, at least for the author. Olszak and Perzyna (1969), for instance, introduce nine parameters to describe the thermodynamic response of a material. These parameters describe variations in physical and thermal properties with time and relate to force equilibrium, and mass and energy conservation.

Semi-empirical Mechanics Models:

The semi-empirical Cam-clay model and Perzyna's (1963) viscoplasticity framework have served, either in combination or separately, as a foundation for the models outlined in Section 2.6. Several of these models have since been used as a foundation for expanding the model to include the effects of temperature.

Modaressi and Laloui (1994) discuss a thermodynamical approach for both OCC and MCC. They focus on the formulation of a 'free energy' and a 'dissipation' function but do not define separately the impact of temperature on plastic straining. Modaressi and Laloui (1997) introduce a cyclic thermoviscoplastic constitutive model building on Modaressi and Laloui (1994), among others. This model includes formulation of a friction angle that depends on temperature and the resulting cyclic yield surface from this friction angle. Although still based in mechanics, this model requires fewer parameters and is less robust than other thermoplastic and viscoplastic models. Laloui and François (2009) develop a generalized thermoplasticity model using some of the formulations from Modaressi and Laloui (1997) and conclude that this model is easier to implement in finite element software and to reintroduce time effects.

Yashima et al. (1998) present a model that builds on Adachi and Oka's (1982) model to reproduce the behaviour of clays at different strain rates and temperatures. Results of their modeling indicate a temperature dependence on preconsolidation pressure. Oka et al. (2004) improves on that model further with a coupled finite element method with energy balance equations. They conclude that the initial temperature affects the strain localization of clay. Laloui et al. (2008) developed a new vertical yield stress function to describe the dependence of the yield stress on strain rate and temperature. In all of these models, calibration is again a concern.

2.7.3 A new semi-empirical approach

Current semi-empirical models describe separately time- and temperature- dependent behaviour of clays (e.g. Yin 1990, Tanaka 1995, Yin et al. 2002, Kelln 2007). These models, built on the MCC framework, require only easily understood parameters that have a physical meaning. Calibration of the models has been shown to be straightforward and produce results that correlate well with observed behaviour at field scale.

Several of the models listed in the previous section are based on mechanics and successfully combine the effects of viscoplasticity and thermoplasticity together. Mechanics-based models, however, are mathematically more complex than semi-empirical models and can be more difficult to calibrate and use. As mentioned earlier, a concern with many of these models is the ability to reliably determine these parameters in laboratory testing and to understand what these parameters mean (Graham et al. 1997). It is unclear whether resulting solutions are unique.

Evidence described earlier indicates there is a distinct similarity between time and

temperature behaviour. The approach presented in this thesis will remain purely semi-empirical in nature. The goal of the elastic thermo-viscoplastic (ETVP) model described in Chapter 5 is to provide a simple, effective, and easily accessible representation of the effects of the combined effects of time (as expressed, for example, by strain rate) and temperature on the load-deformation behaviour in clays.

2.8 Justification for Research

Considerable attention has been given in the last 50 years to developing an understanding of the effects of time (viscoplasticity), and temperature (thermoplasticity) on the stress-strain behaviour of clay soils. Further research indicates there are mathematical similarities describing viscoplasticity and thermoplasticity. In more recent years, numerical models have been developed to help explain deformations of geotechnical structures that are not described well by traditional soil mechanics approaches (e.g. Yin et al. 2002 and Kelln 2007). Research also shows that mechanical, physical, and thermal properties may all be altered due to changes in temperature, and that these changes may or may not be reversible (Campanella and Mitchell 1968).

Thermal numerical models are important, powerful tools that can be used to examine the impact of changes in temperature, such as those caused by climate change, on geotechnical structures. They are used to predict isotherms in the ground. These thermal models, however, do not address the relationship between temperature and deformation under applied loading.

The purpose of this research is to investigate and understand how numerical modeling can provide insight into the relationships over time between temperature and

load-deformation distributions in clay soils subject to heating and mechanical loading. Several of the currently available mechanics-based models do indeed describe viscoplasticity and thermoplasticity; however the models are complex and difficult to calibrate. To the author's knowledge, no easily accessible and easily calibrated semi-empirical model currently exists that describes both viscoplasticity and thermoplasticity in an encompassing elastic thermo-viscoplastic (ETVP) model. One of the goals of this research program is to explore this opportunity.

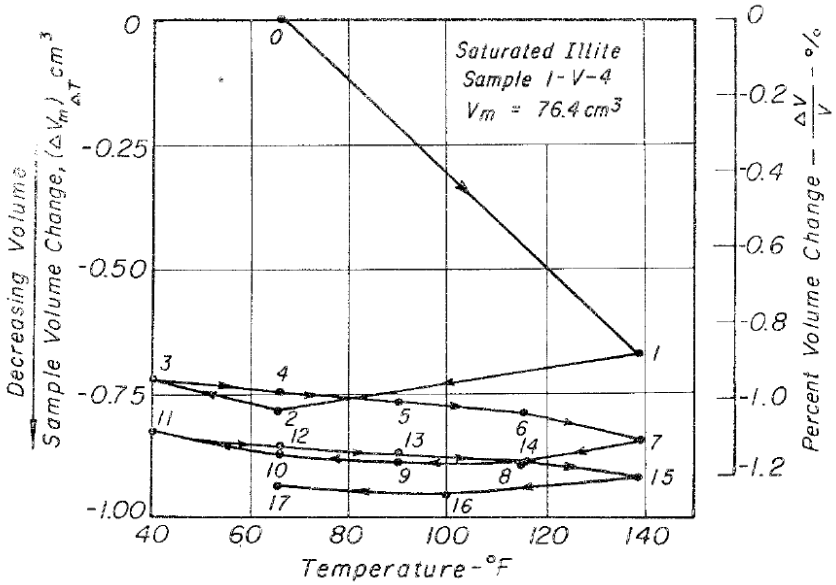

Figure 2.1: Effect of temperature variation on volume change (Campanella and Mitchell 1968) (Used with permission)

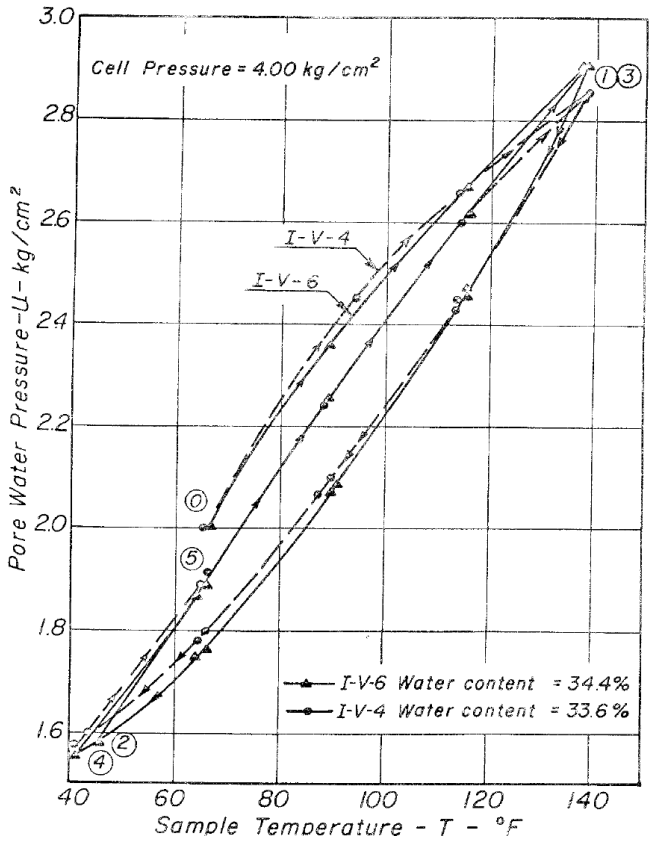

Figure 2.2: Effect of temperature on pore water pressure in saturated illite specimens under undrained conditions (Campanella and Mitchell 1968) (Used with permission)

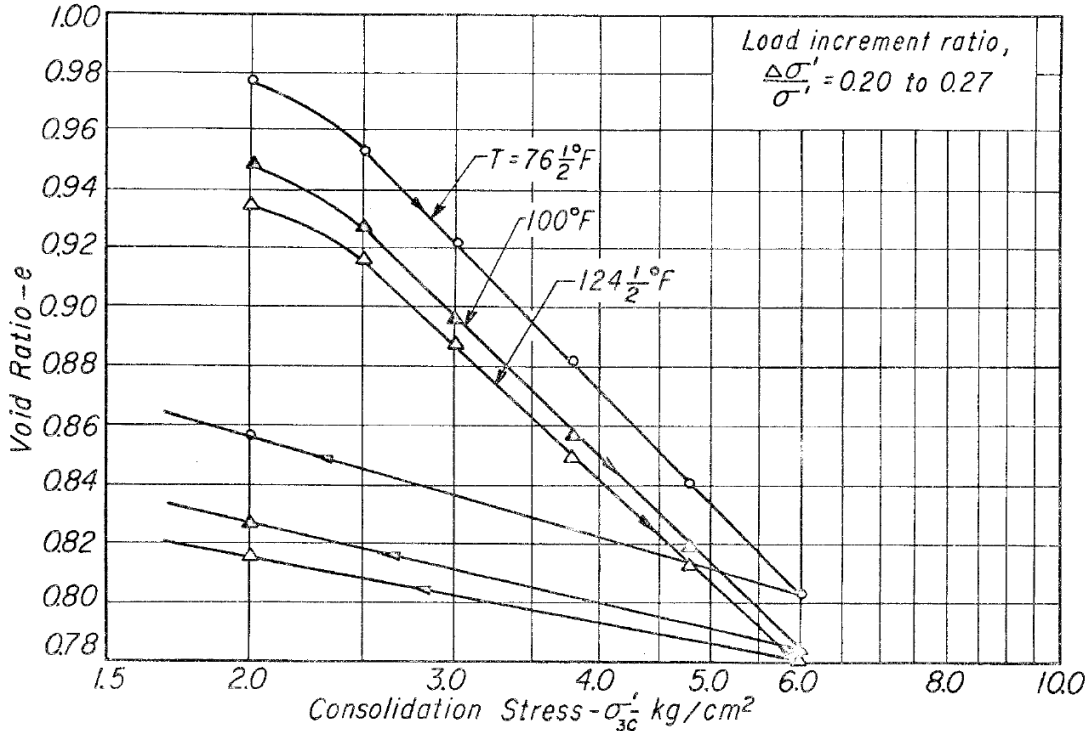

Figure 2.3: Effect of temperature on isotropic consolidation behaviour of saturated illite (Campanella and Mitchell 1968) (Used with permission)

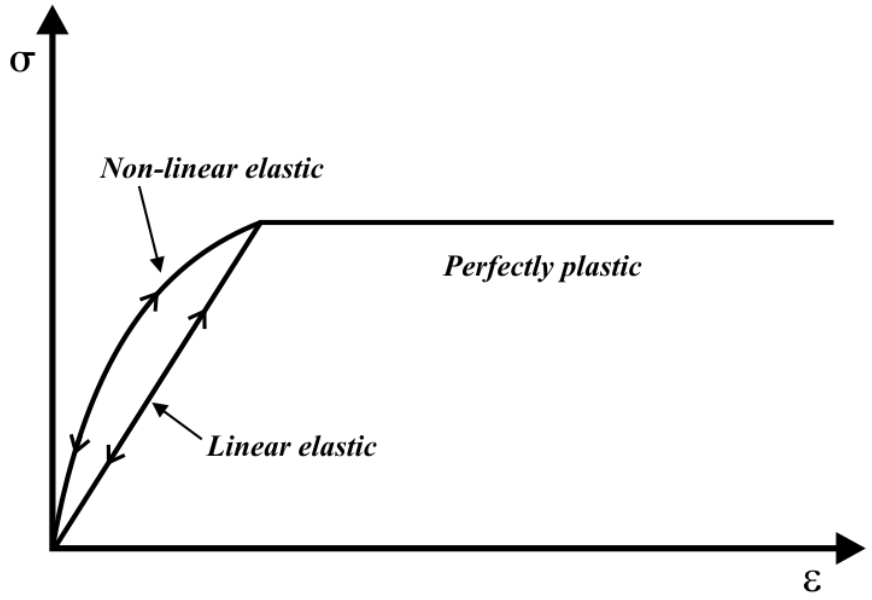

Figure 2.4: An elastic perfectly plastic model

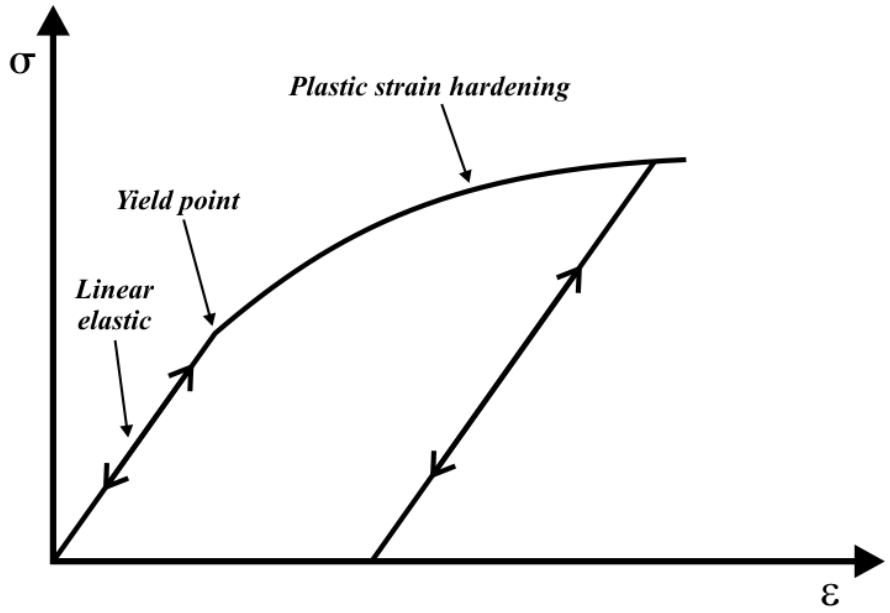

Figure 2.5: An elastic-plastic model with strain hardening

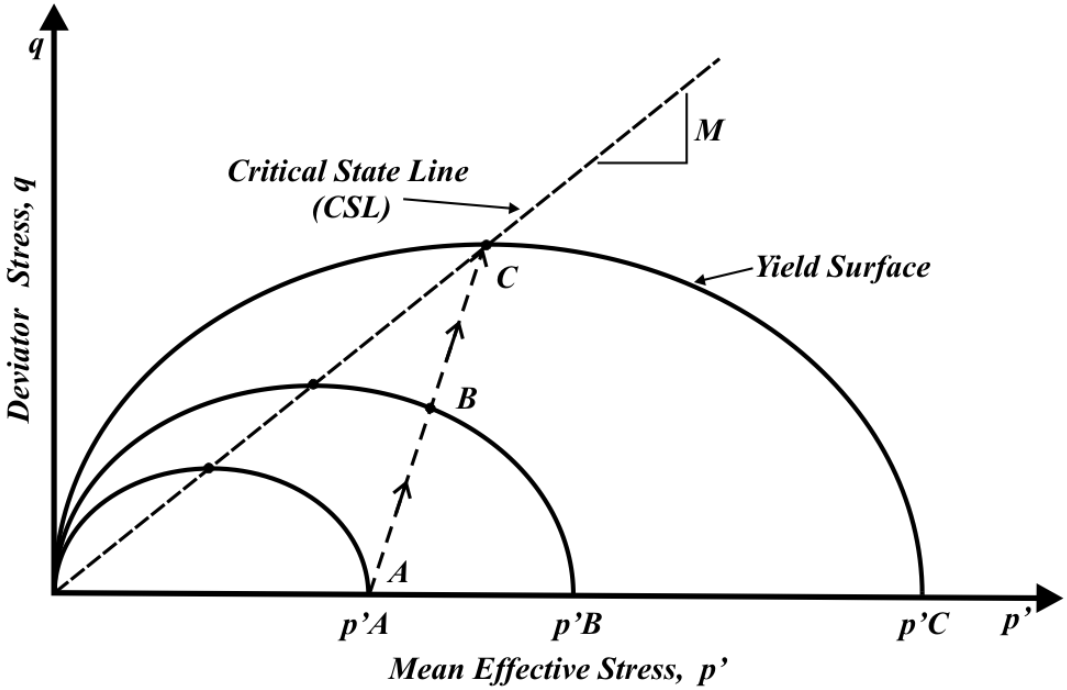

Figure 2.6: Volumetric hardening of the yield surface for a state of stress, A, moving to C in q-p' stress space

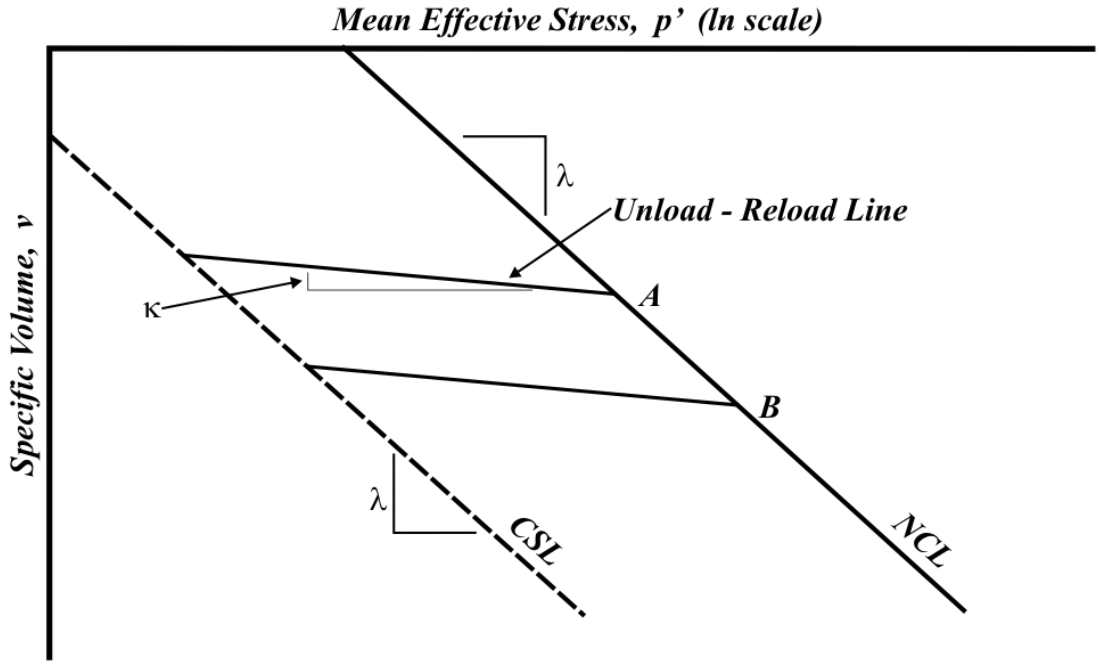

Figure 2.7: Compression space V-ln(p') in the Cam-clay model

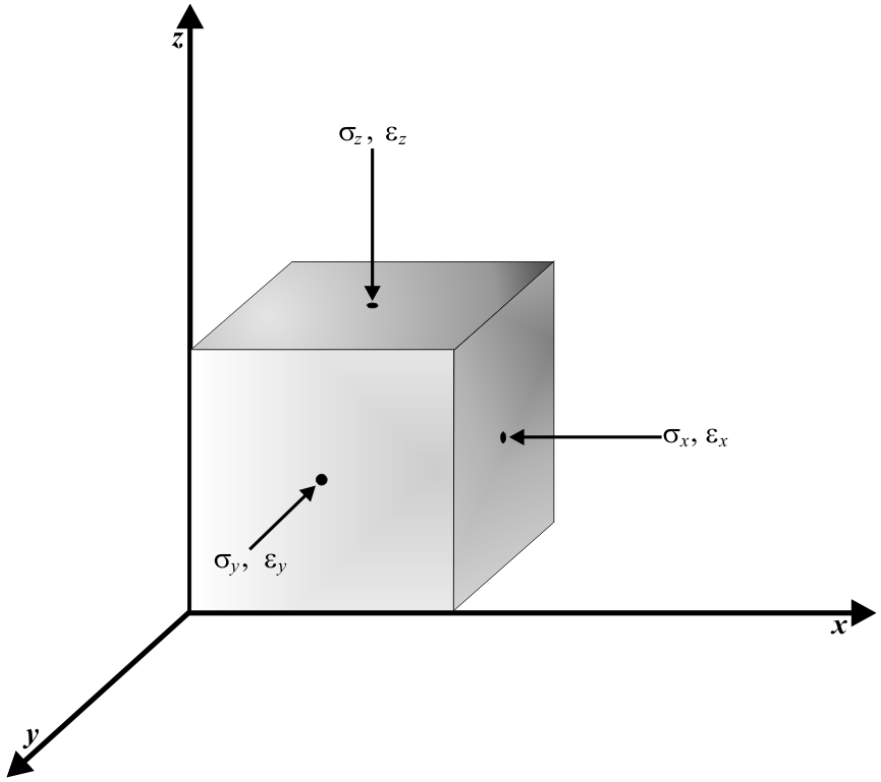

Figure 2.8: A general state of stress

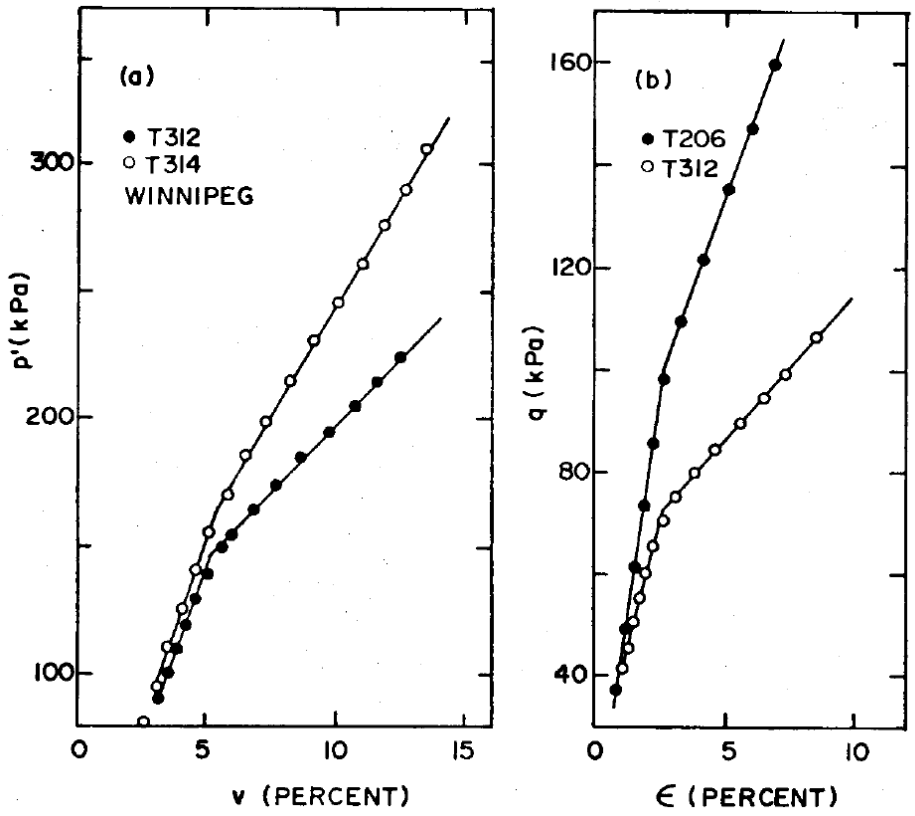

Figure 2.9: Observed yielding behaviour in (a) p' vs. volume strain and (b) q vs. shear strain (Graham, Noonan, and Lew 1983) (Used with permission)

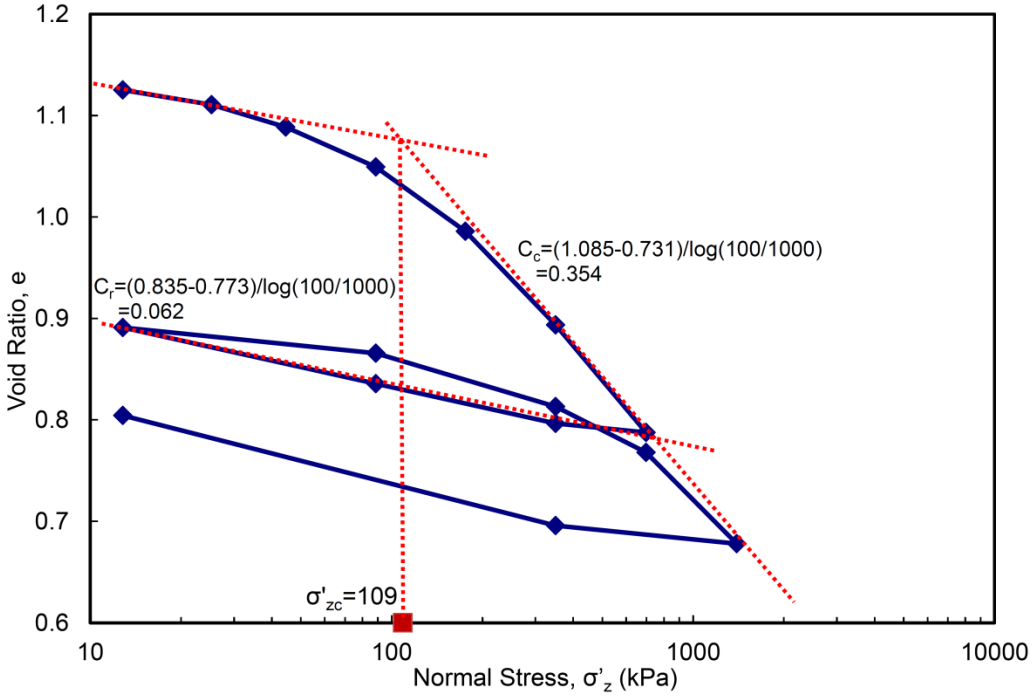

Figure 2.10: Typical Oedometer results (Batenipour 2012) (Used with permission)

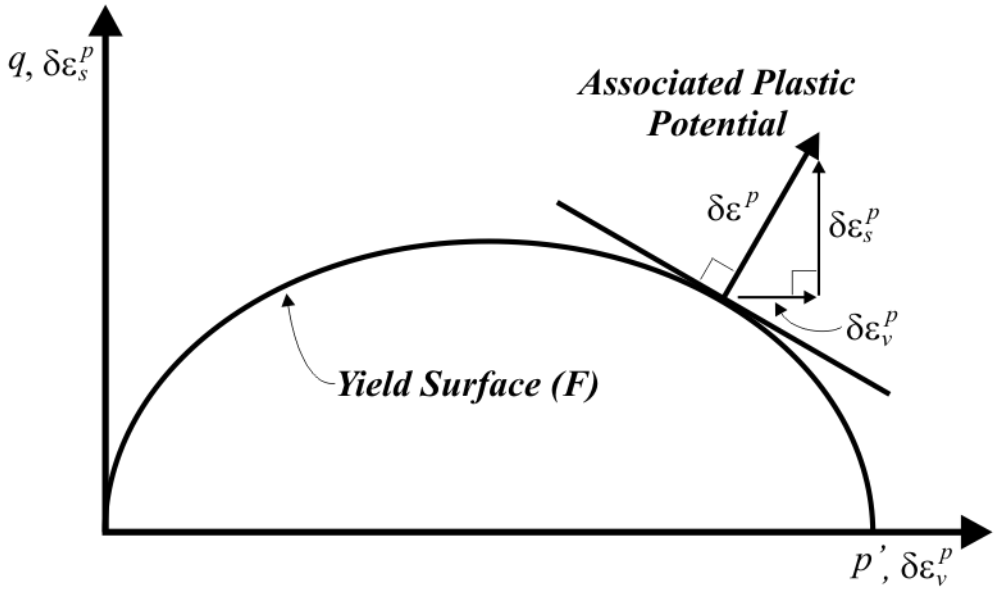

Figure 2.11: The associated flow rule concept

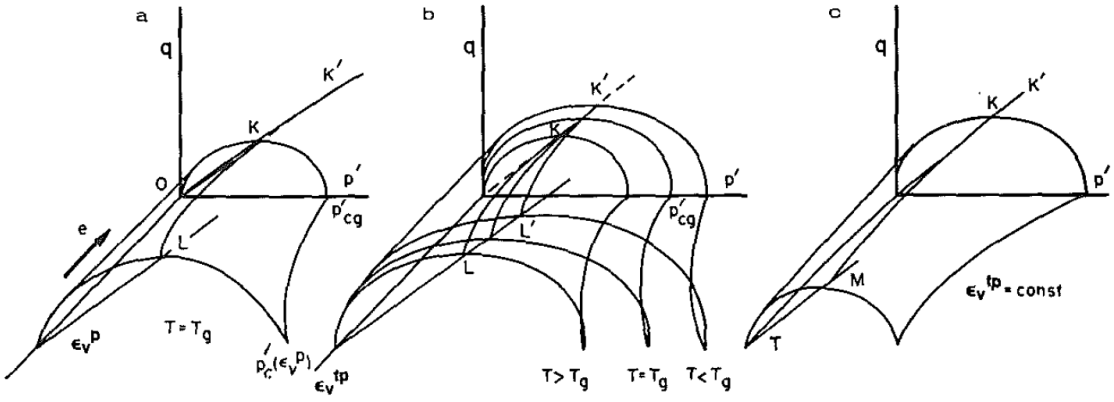

Figure 2.12: Representation of the yield surface (a) at constant temperature, T, (b) at variable thermoplastic volumetric strain, ε_v^{tp}, and variable temperature, ΔT, and (c) at constant ε_v^{tp} and variable ΔT (Hueckel and Baldi 1990) (Used with permission)

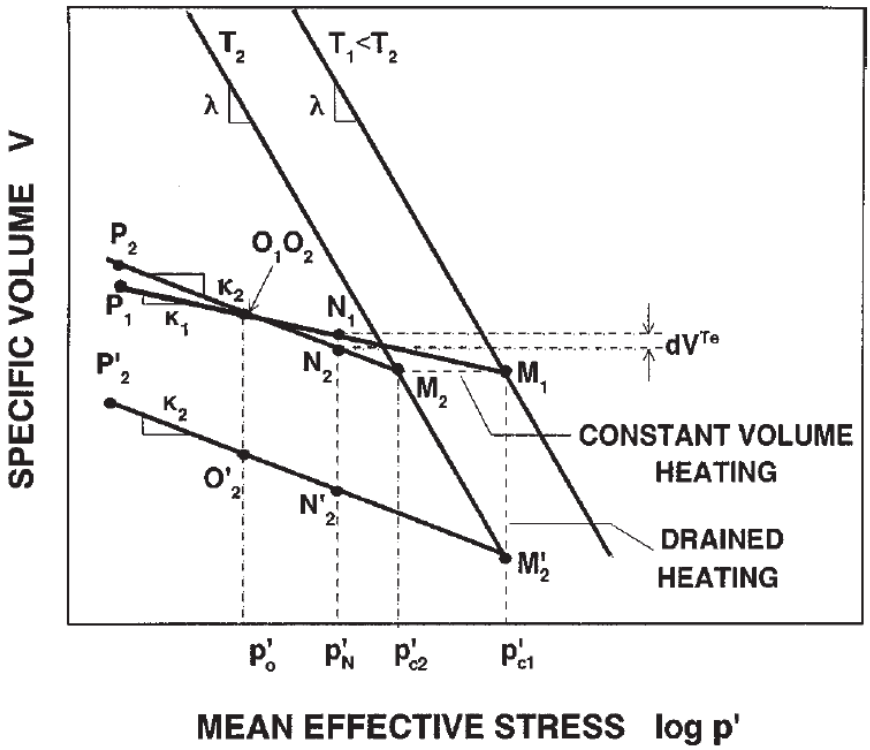

Figure 2.13: Representation of Tanaka's TEP model showing the relationship between thermally induced volumetric strains and mean effective stress (Graham et al. 2001) (Used with permission)

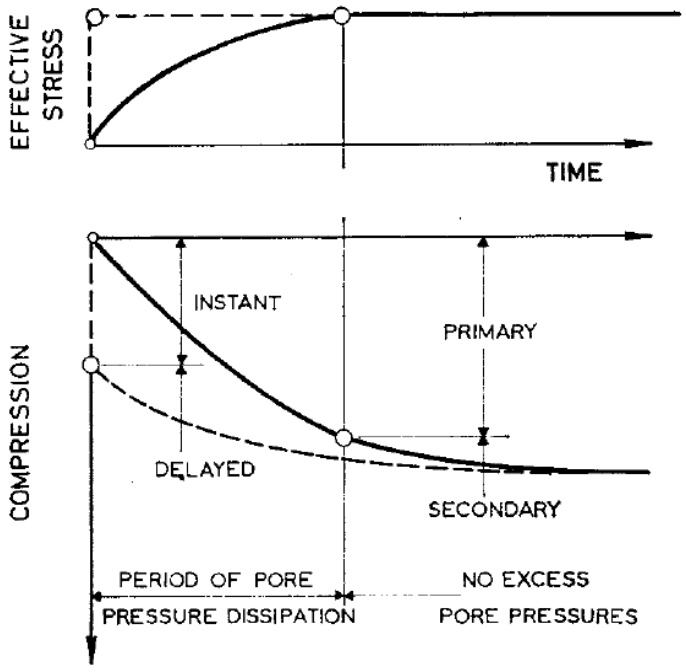

Figure 2.14: Definition of 'instant' and 'delayed' compression compared with 'primary' and 'secondary' compression (Bjerrum 1967) (Used with permission)

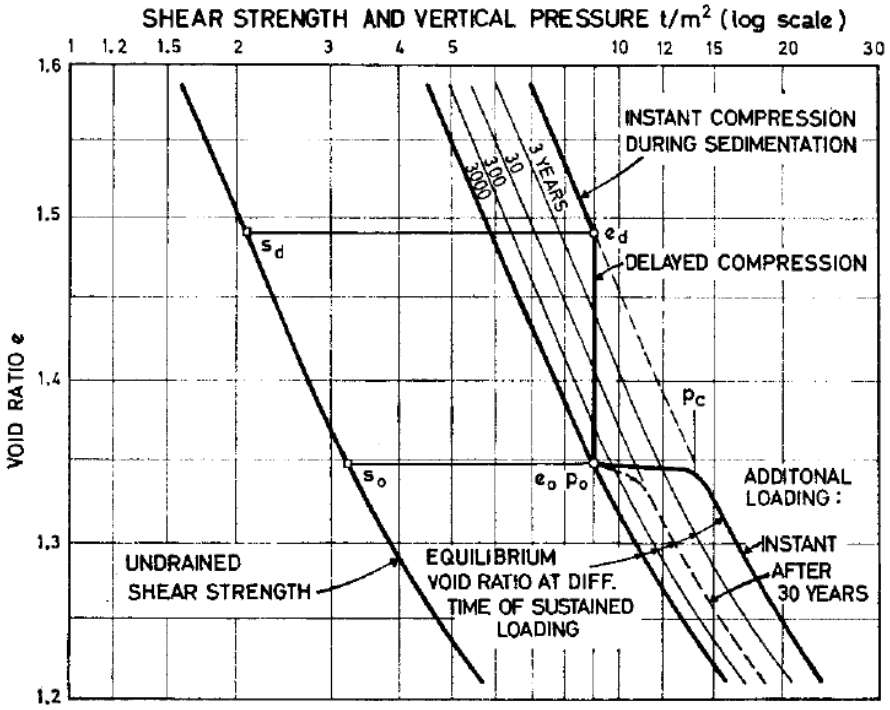

Figure 2.15: The time-line model (Bjerrum 1967) (Used with permission)

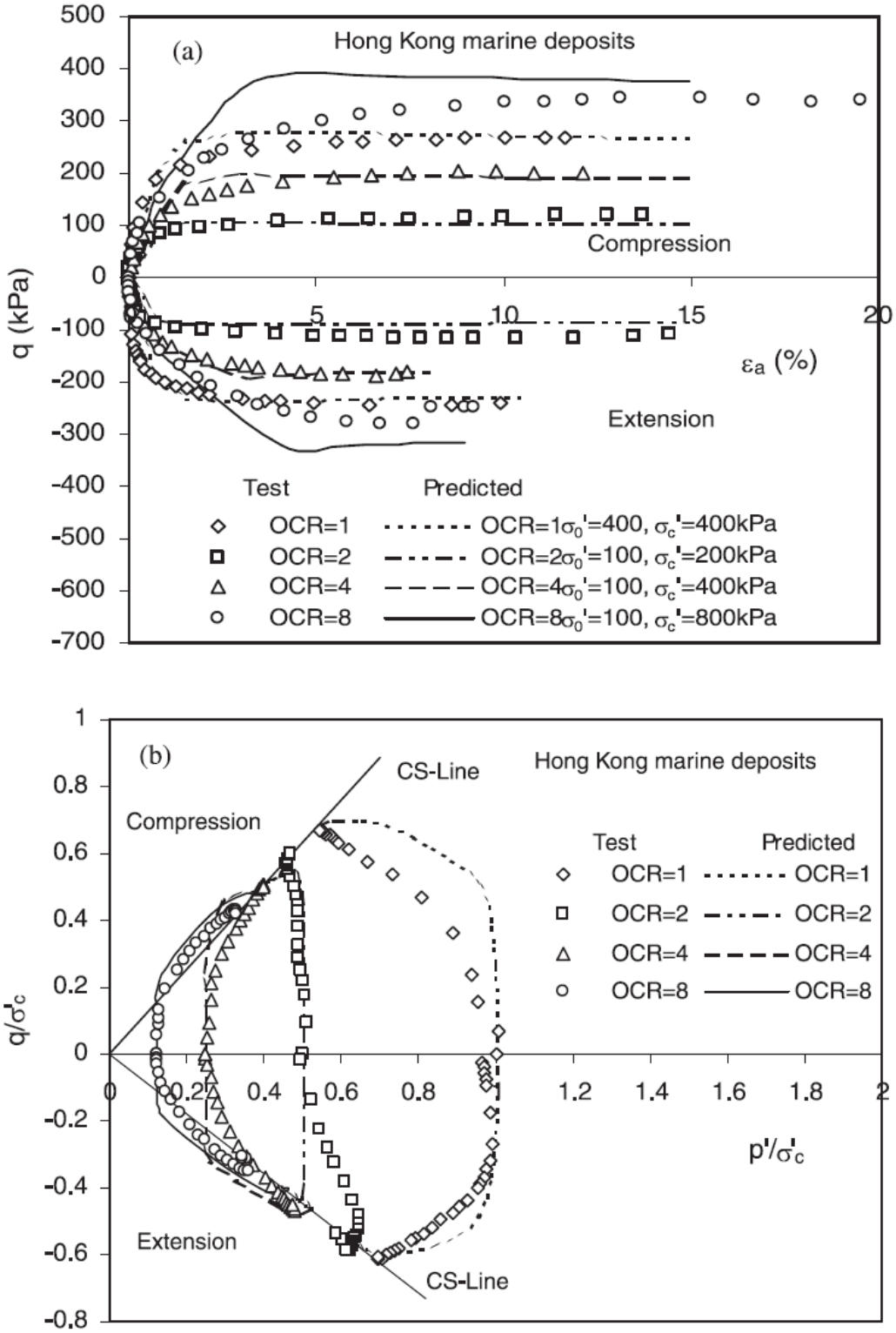

Figure 2.16: Measured and predicted results from consolidated-undrained tests on Hong Kong marine deposits (a) axial strain εa vs. q and (b) effective stress paths normalized with preconsolidation pressure, σ'c (Yin et al. 2002) (Used with permission)

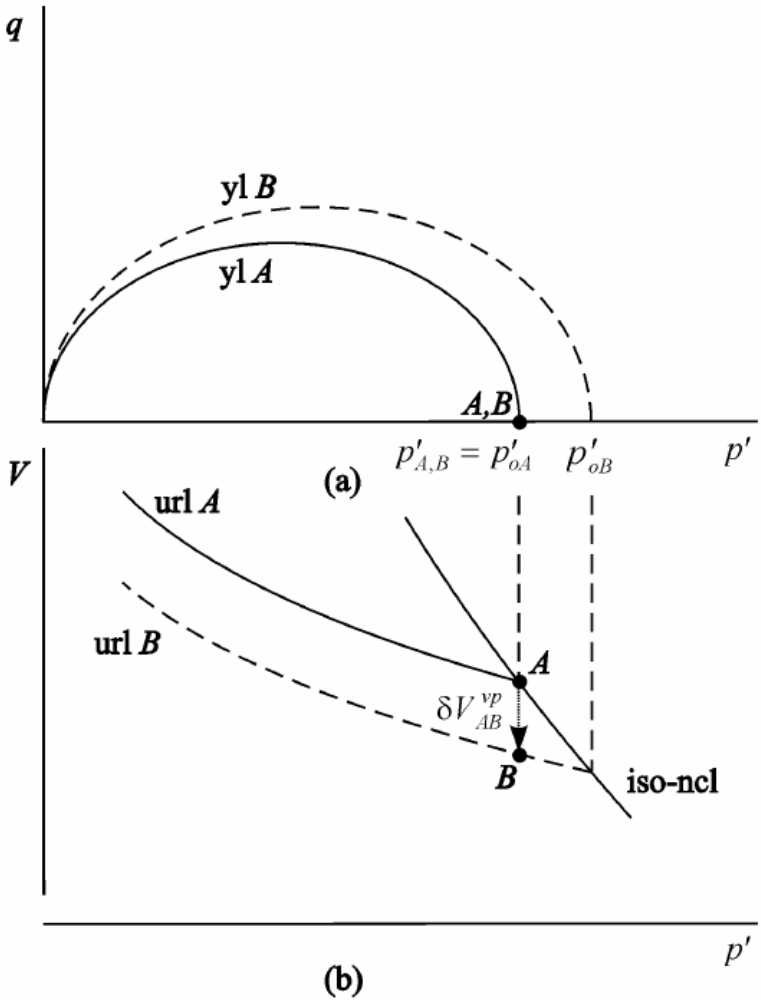

Figure 2.17: Inadmissible development of viscoplastic volumetric strains with constant stress for a stress state that resides inside a current yield locus which has its size defined by p'_o on the isotropic normal compression line (iso-ncl) (Kelln 2007) (Used with permission)

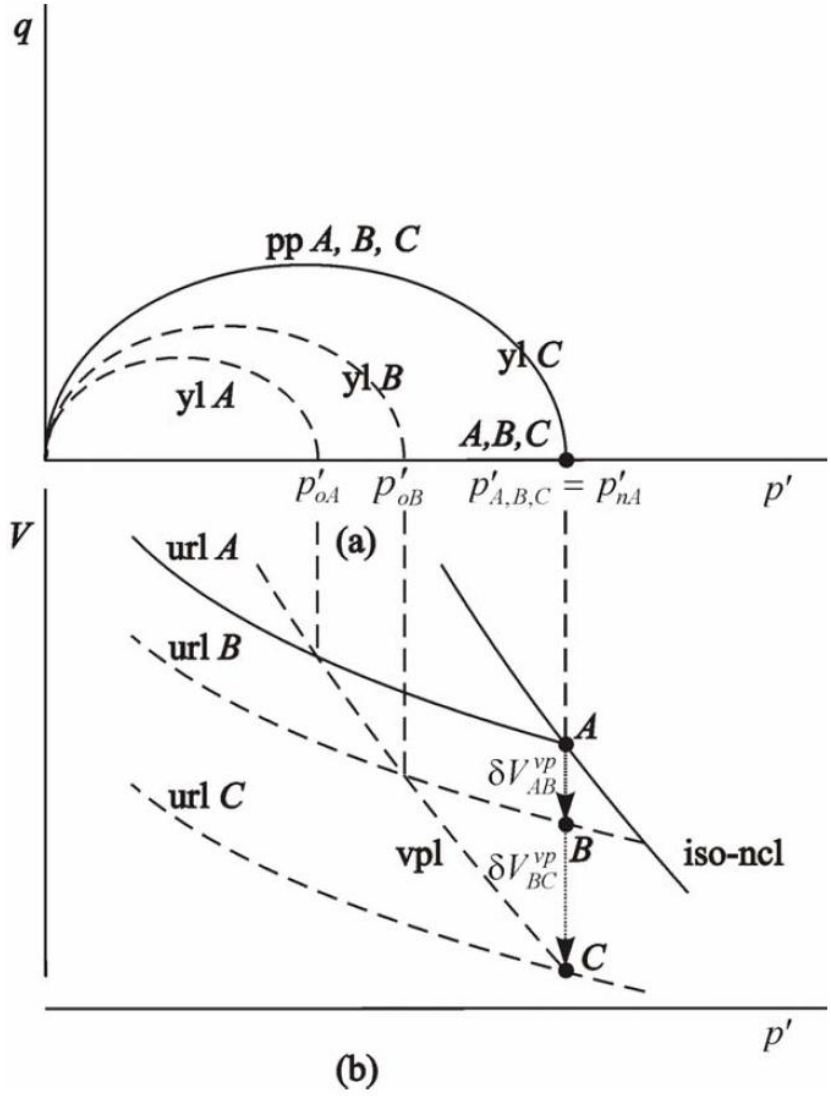

Figure 2.18: Admissible development of viscoplastic volumetric strains with constant stress for a stress state that resides outside a current yield locus which has its size defined by p'_o that does not fall on the isotropic normal compression line p'_n. The locus of p'_o in the V-p' compression plane forms the viscoplastic limit line (vpl) parallel with the isotropic normal compression line (Kelln 2007) (Used with permission)

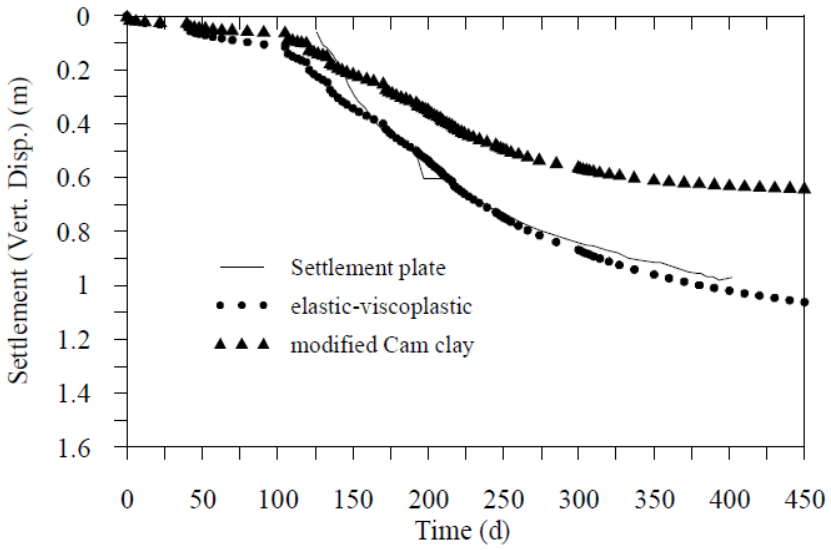

Figure 2.19: Computed and measured surface settlement beneath the south shoulder of the embankment near Limavady (Kelln 2007) (Used with permission)

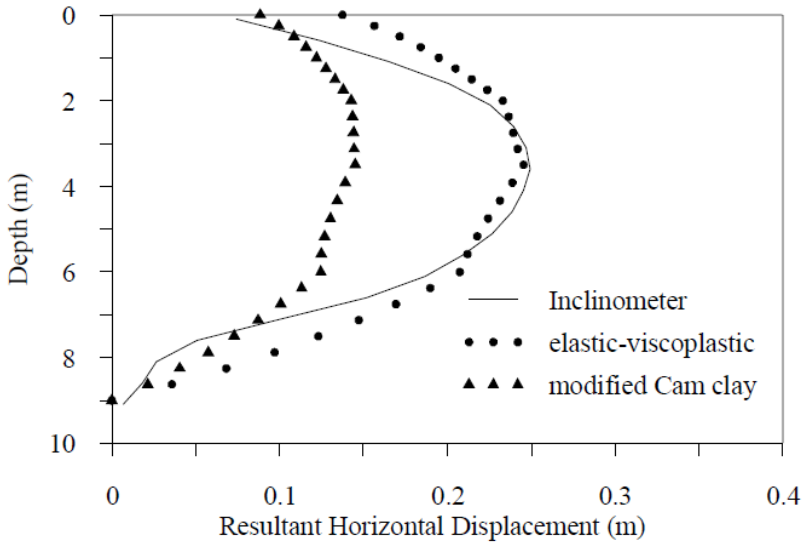

Figure 2.20: Computed and measured inclinometer profile (Kelln 2007) (Used with permission)

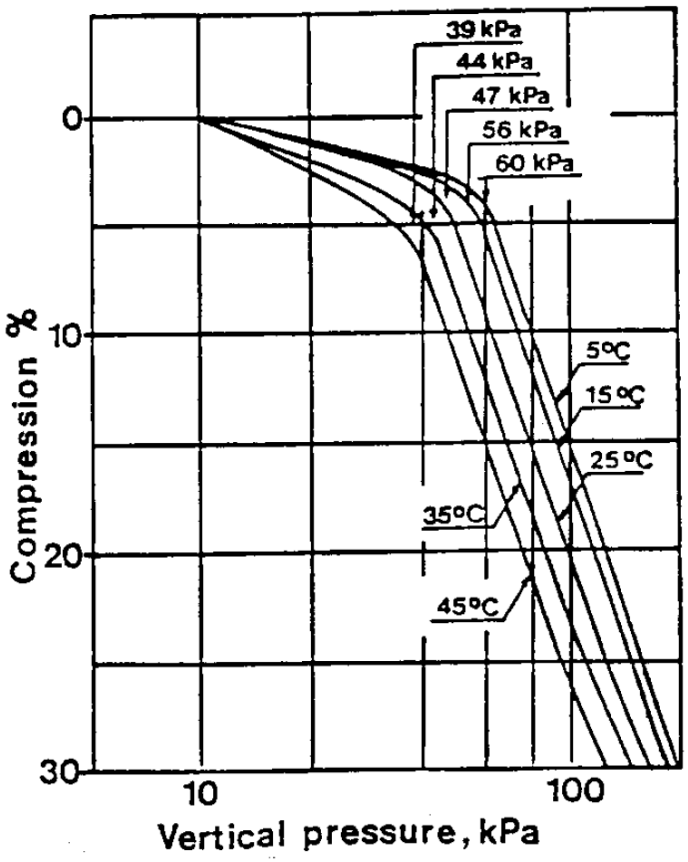

Figure 2.21: Stress-strain behaviour in oedometer tests at different temperatures (Eriksson 1989) (Used with permission)

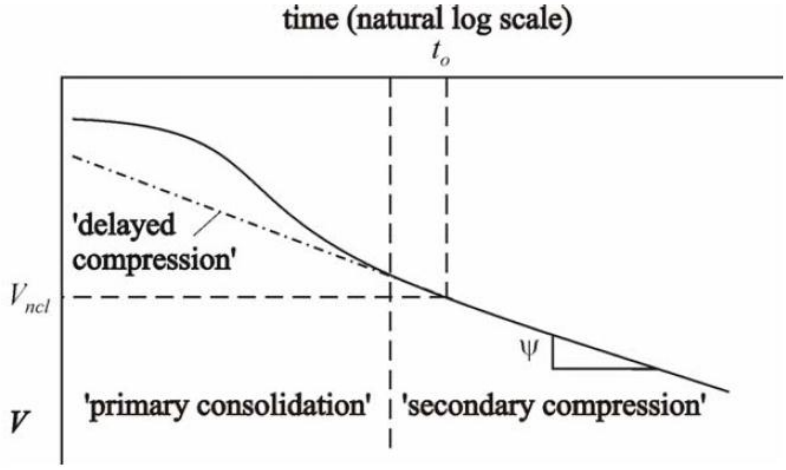

Figure 2.22: Description of 'primary consolidation', 'secondary compression', 'delayed compression' and the material constant, ψ, in V-ln(t) space (Kelln 2007) (Used with permission)

Chapter 3: Laboratory Testing: Thermal Conductivity

3.1 Introduction

Thermal properties of a soil are required before thermal behaviour can be modeled numerically. Software such as TEMP/W[1] allows the user to input basic thermal parameters like thermal conductivity and volumetric heat capacities when analyzing frozen and unfrozen states as will be done in the next chapter. Sites described later in this chapter and in Chapter 4 may be modeled to examine the impact of changes in the thermal regime induced, for example, by construction and climate change.

Thermal conductivity is a measure of the quantity of heat flowing through a unit area of a substance in unit time under a unit temperature gradient (Farouki 1986). This means that thermal conductivity can be measured by applying known heat energy to a specimen and measuring the change in temperature with elapsed time. Devices such as the thermal needle described in Section 3.2 can be used to determine thermal conductivity. Thermal conductivity depends primarily on soil type, soil density, water content, degree of saturation, and temperature (Farouki 1986). The thermal conductivity of a frozen soil is greater than that of the same soil when not frozen. This is in part due to the thermal properties of water, which is approximately four times more thermally conductive as ice than as a liquid. Soil behaves in similar fashion: denser material has more particle contacts and can therefore conduct heat more effectively.

---

[1] GeoStudio 2007, GeoSlope International, Calgary, Alberta.

This chapter focuses on measuring thermal conductivity in laboratory tests. It will be the only parameter discussed. The results will be used in Chapter 4, which describes the thermal modeling done by the author in his research program.

3.2 Apparatus and Procedure

Steady-state thermal conductivity tests require well-engineered systems to ensure heat flow is controlled and that equilibrium is achieved. This setup typically involves heat exchangers and heat diffusers on either side of the specimen, several thermistors to monitor heat flow, and insulation to minimize heat loss in the system. These systems, however, generally take a long time (roughly 12 - 24 hours, depending on the specimen) to reach equilibrium (steady-state). An example of a steady-state thermal conductivity cell can be found in Côté and Konrad (2005a).

In contrast with this steady-state system, the author's tests used a transient heating system that used a heating source (thermal needle) and measured the resulting changes in temperature with time.

Thermal conductivities presented in this thesis are in accordance with ASTM D 5334-05, Standard Test Method for Determination of Thermal Conductivity of Soil and Soft Rock by Thermal Needle Probe Procedure. Hukseflux Thermal sensors state in the manual for the TP08 that the probe is compliant with ASTM D 5334-05.

Thermal Needle Probe:

The stainless steel probe (TP08, Figure 3.1) was manufactured by Hukseflux Thermal Sensors. The TP08 needle has a diameter of 1.2 mm and a length of 70.0 mm. Inside the

needle is a heating wire and a single thermocouple located approximately 15.0 mm from the tip. An additional temperature sensor is located in the base of the probe near the needle. This is used to establish the base temperature for measuring changes in temperature during the tests. The TP08 is entirely enclosed and the internal circuitry cannot be accessed without causing damage to the probe. A schematic of the internal circuitry and the connection of the probe to a data acquisition unit is provided in the manual for the TP08 probe (Hukseflux Thermal Sensors 2001). Connection of the TP08 probe to a CR23X data acquisition unit is discussed later in this chapter.

The TP08 probe operates on a non-steady-state principle based on the transient line source method (Hukseflux Thermal Sensors 2001). An infinite line source with a constant power per unit length produces a temperature profile that depends on thermal conductivity and thermal diffusivity. The solution assumes an infinite full space, isotropy and homogeneity. The temperature profile for a given radius and time is described as:

[Eq. 3.1] $$T(r,t) = \left(\frac{Q}{4\pi\lambda}\right) \times Ei\left(\frac{r^2}{4\alpha t}\right)$$

where T = temperature (K), Q = heater power per unit length (W/m), λ = thermal conductivity (W/mK), $Ei(x)$ = an exponential integral, r = radius (m), α = thermal diffusivity (m^2/s), and t = time (s).

This equation is typically used to determine the change in temperature with time at a specific radius and may be simplified (Hukseflux Thermal Sensors 2001):

[Eq. 3.2] $$\Delta T(t) = \left(\frac{Q}{4\pi\lambda}\right)[\ln(t) + B]$$

where B (constant) = $[\ln(4\alpha t/r^2) - \gamma]$ and γ (Euler's constant) = 0.5772. The manufacturer, Hukseflux Thermal Sensors, uses this equation to approximate the thermal conductivity

of a material in the immediate vicinity of the needle. The company recommends a minimum sample radius of 20.0 mm to provide a reading within acceptable error.

The probe applies a specific heat flux (power) for a preselected time duration and records changes in temperature of the specimen. A test typically requires only a few minutes. After a short transient period, the probe begins to read a relatively linear increase in temperature versus the natural logarithm of time, ln(*t*). Equation 3.2 may be rearranged to solve for the thermal conductivity, λ:

[Eq. 3.3] $$\lambda = \left(\frac{Q}{4\pi \cdot \Delta T}\right) \ln\left(\frac{t_2}{t_1}\right)$$

where t_1 = initial time, t_2 = final time, and ΔT = temperature rise between t_1 and t_2. This relationship is used to determine the thermal conductivity of the specimen.

Probe circuitry and Data Acquisition Unit:

The TP08 is designed for use with a data acquisition system. Hukseflux Thermal Sensors recommended the use of a Campbell Scientific data logger and provided a program that controls the excitation values (heating) applied to the probe and the appropriate circuit schematic. The CR23X micrologger, shown in Figure 3.2 was used in the testing. Data were exported to a laptop in a delimited text file for further analysis. The program and wiring diagram are available on the accompanying DVD (see Appendix I).

The TP08 probe can be used with three (recommended) power levels; low, medium, and high. The supply voltage to the CR23X data acquisition (DA) unit was kept constant at 12.0 V through the use of a power supply. These power levels are controlled by directing the applied voltage through different precision resistors, thereby changing

the current applied to the heating wire, and consequently the amount of heat to the sample. Resistors with resistances of 50.0 Ω and 100.0 Ω are used either individually or together in parallel. The parallel arrangement gives a resistance of 33.3 Ω.

Modification to the circuitry and/or program would allow for different power levels by using combinations of different resistors in series or parallel. Care must be taken to ensure that the voltage across the heating wire does not exceed 3.0 V or the probe may become damaged. The authors' program did not modify the standard circuitry.

The program for the CR23X DA unit records voltage drop across (resistance, R) and the current (I) through the probe. These records allow the power P (wattage, $P = I^2R$) radiated by the needle to be calculated. The program also allows the user to select the power level and duration of the test. Calculation of thermal conductivity is discussed further in Section 3.5.

Guiding Tubes:

Stainless steel guiding tubes (GT01) and their plastic caps, manufactured by Hukseflux and shown in Figure 3.3, are used for specimens that might damage (bend) the needle when inserting the probe. These types of specimens may be coarse grained, stiff, or frozen. For the testing presented in this chapter, GT01 tubes were used with frozen specimens. The tubes had an outer diameter of 2.0 mm, were 90.0 mm in length, and sleeved the needle of the TP08 probe.

The GT01 tubes were carefully inserted into unfrozen specimens contained in a stainless steel test cell (Figure 3.4). After the specimen was frozen, the guiding tube provided the ability to insert the probe without damaging the needle. The guiding tubes

may be recovered after the specimen thaws. Caps are applied to the tubes when the specimen is not being tested.

Following the manufacturer's recommendation, a thin coating of glycerin (glycerol) was applied to the TP08 probe before it was inserted into GT01 tubes in the specimens. Care was taken to minimize pollution of the specimen by ensuring the majority of the glycerin stayed inside the guiding tube. Although not mandatory, the application of glycerin improved the repeatability of tests by providing an improved thermal contact between needle and the inner diameter of the guiding tube.

The glycerin, as determined by Hukseflux, has negligible impact on the measured thermal conductivity of the sample. However, due to the overall increased effective diameter of the "needle" in the specimen (e.g. increased overall thermal mass), the combined use of glycerin and the guiding tube increases the transient time required for the thermal probe to reach a linear increase in temperature with respect to the natural logarithm of time.

Stainless Steel Cells:

Four stainless steel cells and one top cap were machined for holding the specimens. Figure 3.4 shows a base plate, cylinder, and top cap. The cells are a modified design based on a container outlined in the TP08 manual. The cell can contain a specimen 71.2 mm (2.8") in diameter, and a maximum 88.9 mm (3.5") in height. The height of the specimen can be adjusted to account for thermal expansion upon freezing. The cell can be removed from the base plate to allow specimens to be inserted or removed easily. This allows the use of natural undisturbed samples from a Shelby Tube, for example, instead

of strictly reconstituted samples. The cell and base plate are fitted tightly with an O-ring to ensure that loss of water does not occur from specimens such as peats that have high water contents.

The top cap has a machined hole that allows the probe to be inserted vertically into the top surface of the specimen (Figure 3.5). The top cap fits into the top of the cell and ensures that the probe does not move within the specimen after it has been inserted. It reduces the potential for bending the needle should the cell be moved with the needle inserted. The top cap also fully encompasses the probe. This means that before a test is performed, the temperature of the cell and specimen can be verified as stable (neither increasing nor decreasing with time), consistent with each other (within a reasonable temperature margin), and (relatively) free of external influences.

Temperature Control - Environmental Storage Chamber and Chest Freezer:

An environmental (cool) storage chamber designed for sample storage was used for testing specimens at 3°C and 10°C. The storage chamber was not designed for sub-zero temperatures, so a commercial chest freezer was used for tests on frozen specimens at -16°C and -10°C. Variations of temperature in the cool storage chamber and chest freezer were not more than ±1°C. This was deemed acceptable since each test lasted only a few minutes. Section 3.4 provides more details regarding testing procedures in the environmental chamber and chest freezer.

Probe Calibration:

The TP08 thermal probe was originally calibrated by the manufacturer. To gain a better

understanding of the thermal probe and circuitry, a series of calibration tests was performed using distilled water as the recommended medium. The thermal conductivity of water at 20.0°C is widely reported as 0.60 W/mK (Watts per metre-Kelvin). Normally, liquids cannot be tested by the TP08 because heat is quickly dispersed by convection and no change in temperature is recorded within the short duration of a non-steady-state test.

A thin solution of Agar in water in the form of a gel was used for calibration. Agar is a phycocolloid extracted from marine algae and is used mainly in microbiological applications. Powdered Agar was mixed with boiling water in 500 mL graduated cylinders and then allowed to cool overnight to room temperature to form a gel. The semi-transparent gel, shown in Figure 3.6, is dense enough to allow the TP08 to obtain a measurement. Hukseflux Thermal Sensors, among others, state that Agar does not affect the thermal properties of water.

Several Agar solutions with concentrations varying from 3.0% to 5.0% were prepared and placed in an anti-freeze temperature bath set at 20.0°C. The TP08 was carefully inserted to ensure the gel was in complete contact with the needle. Tests were performed on each solution. Thermal conductivity, λ, ranged from 0.58 to 0.63 W/mK. These values fall within the inherent error in the probe of ±(3.0% + 0.02 W/mK) at 20.0°C. Hukseflux Thermal Sensors states that at temperatures other than 20.0°C, temperature dependence of the sensor in the TP08 must be accounted for with an additional ±(0.02%/°C). This would give errors of approximately 3.20%, 3.34% and 3.60% at the test temperatures of 10.0°C, 3.0°C, and -10.0°C, respectively.

3.3 Description of Soil Samples

Provincial Road 391:

The research site is located on Provincial Road PR391 approximately 18 km northwest of Thompson (Figure 3.7). This was the primary research site used by Dr. Batenipour (2012), a colleague of the author. The principal purpose of Dr. Batenipour's research was to investigate and evaluate the performance of a road embankment on thawed ground using data from field instruments. Chapter 4 provides additional details of the research at the site and includes research done by the author for this project. This current section describes the soil material that was tested by the author. The research programs for Dr. Batenipour and the author were complementary but had different emphases.

The soil samples from the PR391 site were obtained between the depths of 1.0 m and 4.0 m from the mid-slope of the road embankment at a 'stable' section which was not showing major signs of vertical or horizontal deformations. This soil profile consisted of soft clayey silt with peat intrusions near the surface and progressed to a firm silty clay with increasing depth. The clay was found to decrease in plasticity with increasing depth, ranging from a highly plastic clay near the surface and a low plastic clay at depth. Results of thermal conductivity testing on these specimens are presented in Table 3.1 and discussed in Section 3.5.

Provincial Road 373:

Provincial Road PR373 is approximately 200 km south of Thompson (Figure 3.7) and is the only road connecting the community of Norway House to the rest of the province. This site is part of ongoing research by Manitoba Infrastructure and Transportation into

construction methods on peat embankments using geotextiles and corduroy for strengthening. The research includes field instrumentation, laboratory testing, and numerical modeling. The author's contribution to the PR373 project is restricted to thermal conductivity testing.

The soil at the PR373 project site consists of approximately 4.0 m of organic peat, followed by 8.0 m of highly plastic silty clay underlain by bedrock. Only two peat samples from this site were tested for thermal conductivity. The remaining seven samples were from the clay. The peat samples were examined using a Scanning Electron Microscope (SEM) and classified using the von Post peat classification system. The examination and classification of these peat samples were performed by Mr. Cory-Jay Pyziak and are independent of the author's program. At the time of writing this thesis, the data provided by Mr. Cory-Jay Pyziak are unpublished.

Figure 3.8 illustrates a peat specimen classified as H3. This peat had a distinct, mostly identifiable plant structure, and was weakly decomposed. Liquid in the specimen was brownish and only slightly turbid. Specimen S7 in Table 3.2 is a sample of this peat. Organic content was not measured for this specimen.

Figure 3.9 illustrates a peat specimen classified as H5. This means the specimen had some visible plant structure but was indistinct, difficult to identify, and was moderately decomposed. Liquid in the specimen was strongly turbid and contained some peat in suspension. This peat contained approximately 90% organic material. It corresponds to specimen S3 in Table 3.2. Results of thermal conductivity testing on these specimens are presented in Table 3.2 and discussed in Section 3.5.

Manitoba Hydro:

The 138 kV Radisson-Churchill transmission line is the most northern line constructed by Manitoba Hydro, extending from Gillam to Churchill (Figure 3.7). The purpose of the research was to evaluate the performance of the transmission tower foundations. Chapter 4 presents additional details regarding the nature of the research for the tower foundations. This section describes the soil material under a typical tower foundation.

The general terrain along the length of the transmission line is heavily vegetated with poor drainage in the south and becoming more barren further north. The ground is typically a muskeg (peat) material ranging in thickness from a few centimetres to upwards of 3.0 metres. Underlying the muskeg are primarily marine silts and sands.

The soil samples tested in the laboratory part of the project were all 'grab' samples collected by Manitoba Hydro technicians and kept in storage for several years before the author began working on them. To the author's knowledge, all soil material used in each tower foundation was available locally. The samples consisted of peat, clayey silt, and gravelly sand. The dark brown-black peat had a marginally identifiable plant structure and was slightly decomposed (more fibrous). An SEM analysis and a von Post classification were not performed on this material. The clayey silt was light brown and was considered to be similar to till material. The gravelly sand was visually assessed as well-graded. Some gravel was removed to ensure the TP08 could be fully inserted without causing damage or bending the needle. Results of thermal conductivity testing on these specimens are presented in Table 3.3 and discussed in Section 3.5.

3.4 Testing Procedures

Sample Preparation:

The silty clay and clayey silt samples from PR391 and PR373 were collected using Shelby tubes and both were unfrozen. Samples were stored at 3.0°C until they were prepared for testing in a 20.0°C laboratory. To prepare specimens from the samples, soil was extracted from the tubes and inserted into the test cells using a hydraulic press. Care was taken to avoid compression of the specimen. This was more easily accomplished if the base plate was removed from the cells. This meant that specimens could be pushed through the cell cylinder and trimmed at each end to the appropriate specimen height. The test cells have a maximum calculable volume. It was decided that this volume should coincide with that of a frozen specimen, assuming that upon freezing the specimen could only expand vertically. Simple calculations, using an estimate of 9.0% volumetric expansion of water after freezing, determined the height to which unfrozen specimens should be trimmed.

Material properties such as gravimetric water content, bulk density and dry density were obtained from the laboratory programs of Dr. Hamid Batenipour and Mr. Cory-Jay Pyziak for the samples from PR391 and PR373, respectively. Visual observations upon freezing confirmed this was adequate for these specimens. After the specimens were prepared and sealed using plastic wrap, they were stored in the cool storage chamber at 3.0°C until needed for testing.

The peat samples from PR373 were also received at the University of Manitoba in Shelby tubes and unfrozen. These samples, however, could not be extracted from the tube without some disturbance. Care was taken to minimize the disturbance and maintain most

of the sample's inherent structure and density. To do this, the samples were compressed as little as possible and loose peat was used to carefully patch any cavities in the specimens. Inevitably, water escaped from the peat during insertion into the test cells. The author believes the loss of water is minor and did not significantly affect the results of thermal conductivity tests. Table 3.2 reports measured gravimetric water contents of 618.0% and 756.0% for the peat specimens S3 and S7, respectively.

As mentioned in Section 3.3, grab samples from Manitoba Hydro's foundations for transmission towers had been collected several years prior to the author's laboratory program. The samples were kept in relatively poorly sealed bags in a sealed ten-gallon pail. Information about the conditions under which the samples were stored is not available. Since the natural water content of the samples at the time of collection is also not available, the author relied on the initial water content of the samples at the beginning of the tests as a base line estimate. Only reconstituted samples with approximate estimations of gravimetric water content could be formed.

Given that the soil was used in tower foundations, and that both dry density and water content affect the thermal conductivity, compaction tests were performed on the silt and sand samples to determine the approximate optimal water contents. The compaction tests revealed an optimal water content of approximately 10-11.0% for the sand and approximately 12-13.0% for the silt. Both samples had dry unit weights around 18.5 kN/m^3 at those respective water contents. The water contents closely matched the initial water content from the sample bags. This was not a viable option for the peat material. It was tested at approximately 250.0% water content as determined from the initial grab sample. Because of the spongy nature of the material, the corresponding density was

difficult to maintain during preparation of specimens.

Tables 3.1 to 3.3 specify dry density as γ_d to be consistent with an empirical method. The author acknowledges that γ_d is more commonly used for dry unit weights.

Test Setup:

With four test cells, specimens were prepared in groups. New specimens were only prepared after all cells became available. Since specimens were prepared at room temperature (around 21.0°C), it was decided that testing would begin at the highest temperature and proceed in descending order. Each specimen was tested at two above-zero temperatures of 10.0°C and 3.0°C, and a sub-zero temperature of either -10.0°C or -16.0°C. This minimized the movement of both the specimens and the test apparatus from the cool storage chamber to the chest freezer. The cool storage chamber took several hours to change and stabilize the temperature from 10.0°C to 3.0°C. When required, the temperature was set to change overnight. Several hours were also required to freeze specimens and this too was done overnight.

The cool storage chamber was able to house the specimens, the data acquisition unit, and the probe. The chest freezer, however, was too small to house the data acquisition unit, therefore only the probe and specimens remained in the freezer during testing. Care was taken to ensure that the freezer remained relatively free of outside influence; insulation was placed in the gap between the seal on the freezer lid and the probe's cable and the freezer lid remained closed unless specimens were being switched.

Probe Operation:

As mentioned in Section 3.1, the TP08 was programmed to operate at three different power levels (low (L), medium (M), and high (H)) and two test durations (200 and 400 seconds). The first half of the test is reserved for the program to determine if initial temperatures are stable: heat is only applied in the second half of the test; The different power levels are needed depending on the type of material being tested and the temperature at which it is tested. The thermal conductivity measured from a test may not be accurate for a number of reasons. These may include:

(1) the quantity of heat, whether too low or too high;

(2) inconsistent heat, the specimen has convective properties such as a liquid;

(3) unstable or inconsistent temperatures at the probe and the needle;

(4) measured thermal conductivity falls outside the capable range of the probe;

(5) test duration is too long or too short, and;

(6) power instability, meaning the voltage supplied to the probe is not stable.

Thermal conductivity was determined by performing several tests on each specimen at each controlled temperature. The manufacturer recommends that all power levels and both test durations be run on each specimen to help determine the thermal conductivity more reliably through repeatability of the test, and to troubleshoot any potential errors should the measured results be dissimilar. This recommendation was followed. At least five tests were performed on each specimen and at each temperature. Tests were repeated on some specimens to improve confidence in the results.

Given the number of tests performed on each specimen, no more than one or two

specimens were tested each day. Although the test durations were quite short, time was needed between each test for the temperature in the specimen to re-equilibrate before testing at a different power level or duration. The time for equilibration could vary from several minutes to several hours depending on the specimen, temperature, and amount of heat to be dissipated. During this time for equilibrium, the specimens remained undisturbed to ensure that additional heat was not introduced.

Data Analysis:

Data collected from each test were analyzed using a Microsoft Excel spreadsheet provided by Hukseflux Thermal Sensors, as well as spreadsheets developed by the author. The spreadsheet formulations were verified prior to use to ensure proper formulations and to improve an understanding of the analysis process. Figure 3.10 illustrates part of the analysis where thermal resistivity is plotted against the natural log of time. With several tests performed on the same specimen, outliers are removed and an average of the regression line for each test is plotted along the linear sections of the test results. The inverse of the slope of the linear line is the thermal conductivity of the specimen (Equation 3.3). This procedure is performed on all specimens for each temperature stage.

3.5 Results

As mentioned earlier, thermal conductivity testing was performed on a select series of samples from the PR391 and PR373 road embankments, and from the foundation of a Manitoba Hydro transmission tower. Water contents, Atterberg limits, and dry densities

of the specimens were also determined. Data discussed in following paragraphs can be found in Tables 3.1, 3.2, and 3.3. Raw data is available on the accompanying DVD (see Appendix I)

Soil from PR391:

The specimens from PR391 consisted of one silt specimen, S10, and four clay specimens, S11 – S14. Specimen names correspond to the naming convention used by Dr. Hamid Batenipour. As expected, Table 3.1 and Figure 3.11 show that the frozen thermal conductivity is greater than the unfrozen thermal conductivities for the same specimens. With the exception of specimen S14, the results also indicate consistency between the tests performed at 10.0°C and 3.0°C.

Despite the reported difference of 0.09 W/mK (Watts per metre per Kelvin) between the unfrozen results for specimen S13, the values fall within the expected error of the thermal probe (Section 3.2) and give an average value of 1.36 W/mK. The values of 1.51 and 1.18 W/mK listed for specimen S14 do not fall within acceptable error limits. Given the trend of the data, the author concludes that the value of 1.51 W/mK at 10.0^{o}C is closer to the actual thermal conductivity. The unacceptable reading of 1.18 W/mK at 3.0^{o}C may be due to a loss of contact between the thermal needle and the soil.

Overall, the data reasonably indicate increasing thermal conductivity with increasing dry density and also correlates with decreasing plasticity and water content. Figure 3.11 shows a plot of thermal conductivities versus temperature for all the specimens from PR391. The data broadly support the assumption that thermal conductivity is constant in the range 3.0^{o}C to 10.0^{o}C. The constant relationships with

changes in temperature for frozen specimens have been assumed by the author but are based on published information (Farouki 1986). Additional tests at sub-zero temperatures just below 0.0°C are needed to clarify the assumed relationships implied in the figure.

Soil from PR373:

Specimens from PR373 included two peat specimens, S3 and S7, with the remaining seven specimens, S24 to S30, being highly plastic silty clay. Specimen names correspond to the naming convention used by Mr. Cory-Jay Pyziak. Results are presented in Table 3.2 and Figure 3.12.

Despite the physical differences in the peat specimens discussed in Section 3.3, the thermal conductivities are similar. The unfrozen thermal conductivities are slightly below the thermal conductivity of water at the respective temperatures. Given the high water content and low dry density of the peat, the results of these tests are quite similar to the calibration tests using Agar gel. Even though the frozen thermal conductivities were obtained at different temperatures, they are within the expected error for a value of 1.61 W/mK. This value is lower than the thermal conductivity of ice (approximately 2.39 W/mK at -15.0°C). The difference indicates the effect of organic material on thermal conductivity (e.g. organic material affects density, water content, and saturation).

All unfrozen thermal conductivities of the clay specimens are within expected error except specimen S24 which falls just outside the error margin by 0.02 W/mK. Specific trends are harder to identify in this dataset, unlike the data from PR391, but do indicate the amount of variability in natural samples. Figure 3.12 shows a plot of thermal conductivities (with error limits) versus temperature for selected specimens with assumed

constant relationships for unfrozen specimens with changes in temperature. There appears to be a trend for thermal conductivities at 10.0^{o}C to be a little higher than those at 3.0^{o}C but this will probably not have a significant effect in thermal modeling of ground temperatures. Additional tests at sub-zero temperatures just below 0.0°C are needed to clarify the assumed relationships implied in the figure.

Soil from Manitoba Hydro:

The specimens from the foundation of a transmission tower consisted of one peat specimen, HO1, two silt specimens, HM1 and HM2, and two sand specimens, HS1 and HS2. Specimen names were assigned with an 'H' for Hydro followed by the Unified Soil Classification System (USCS) naming convention for the soil type. Depths of the specimens are approximate and based on the depth range provided on the sample labels. Results are summarized in Table 3.3 and Figure 3.13.

Similar to the results of natural soil specimens from PR391 and PR373, these reconstituted specimens show the frozen thermal conductivity is greater than the unfrozen thermal conductivities for the same specimens. However, the increase is small and nearly negligible in its expected effect on thermal analysis. All specimens indicate good consistency between the tests performed at 10.0°C and 3.0°C. The two sand specimens display overlapping results, even with the slightly different densities. Figure 3.13 shows a plot of thermal conductivities (with error limits) versus temperature for all specimens with assumed constant relationships for frozen specimens with changes in temperature. Measured thermal conductivities of the unfrozen specimens are approximately constant. Additional tests at sub-zero temperatures just below 0°C are needed to clarify the

assumed relationships implied in the figure. The data (and Figure 3.13) indicate the two silt samples (HM1 and HM2) may be averaged to unfrozen and frozen thermal conductivities of 1.67 and 1.75 W/mK, respectively.

3.6 Comparison with Empirical Relationships

Other research has studied the effects specific parameters on thermal conductivity. Resulting empirical relationships are available in the literature, see for example Andersland and Ladanyi (2004), Farouki (1986), Harlan and Nixon (1978) and Johansen (1975). Many of these empirical methods allow calculation of thermal conductivity using parameters easily obtained from routine laboratory tests such as dry density and water content. This section compares the thermal conductivities measured in the author's laboratory program with published empirical relationships.

Some of the empirical methods include parameters that make them unnecessarily complicated while providing no substantial gain in accuracy of the thermal conductivity compared with simpler methods. These more complicated methods require information about mineralogy; percentages of solids, water, and ice; and sample dimensions. They also involve more intermediate steps to get to the final value. Another important factor to consider is the system of units under which an empirical method was developed. Some of the empirical relationships are not dimensionally neutral.

For example, the method developed by Johansen (1975) is a commonly used approach for calculating thermal conductivities and is often considered reliable. It is an interpolation technique between dry and saturated thermal conductivities and does not

take into consideration possible moisture migration at intermediate degrees of saturation (Andersland & Ladanyi 2004). It does, however, require knowledge of the quartz fraction of the total solids content and involves stipulations on whether the material is crushed or natural. Quartz has a relatively high thermal conductivity (8.4 W/mK) and will impact the overall thermal conductivity of the soil. Quartz contents were not available for the samples that were tested in this laboratory program; therefore, Johansen's method could not be used.

The simpler relationships can be resolved using available chart solutions or equations that relate simple soil parameters to the thermal conductivities of frozen and unfrozen soils. For example, Harlan and Nixon (1978) published a series of plots summarizing the work of Kersten (1949) and graphically relate thermal conductivity to water content, dry density, and degree of saturation. Plots are available for silt/clay, sand/gravel, and peat. These plots are discussed in following paragraphs to compare the author's measured values with empirical values.

Data for each specimen listed in Tables 3.1, 3.2 and 3.3 were plotted on Figures 3.14 and 3.15 using water content, dry density, and degree of saturation (for the Manitoba Hydro specimens). Estimates of thermal conductivity were then read off the charts and listed in Table 3.4 for direct comparison to the measured results. Figures 3.14 and 3.15 show the silt and clay specimens plotted on the unfrozen and frozen thermal conductivity plots summarized by Harlan and Nixon (1978). Plots for sand and peat are not shown in this thesis. The PR373 peat values cannot be plotted because the water contents of the measured peats exceed the limits of the plot.

3.7 Commentary

Overall, there is generally good agreement between the measured thermal conductivities and values obtained from routine classification tests. Some results compare better than others, and some do not compare well at all. There can be many reasons why the measured and estimated thermal conductivities do not match perfectly. Possible explanations include:

(1) Values have only been compared to one empirical method. Other methods may provide different values (or ranges of values);

(2) Tested specimens have an unknown mineralogy and unfrozen water content. The mineralogy (especially quartz content) and unfrozen water content are known to have an impact on thermal conductivity. With knowledge of these parameters, a more appropriate empirical method could be chosen for comparison;

(3) Experimental error may have given improper results. It is possible that the insertion of the needle into the specimen may have created gaps compromising the contact between the needle and the specimen. Also, freezing the sample may have caused a heave in the specimen that would cause the guiding tube (and needle) to lose contact with the soil. This may explain how some of the PR373 specimens have lower frozen conductivities than estimated values. It may also explain the large difference in unfrozen thermal conductivities for Specimen S14;

(4) Probe or equipment malfunction. It is possible that the probe has faulty internal wiring from the manufacturing process or the data acquisition unit and circuitry malfunctioned. Sometimes the probe would return an anomalous (outlier) reading that was inconsistent with the previous or subsequent readings. The possibility of a

malfunction was checked with the manufacturer. No obvious signs of malfunction were identified.

In Figures 3.14 and 3.15, the natural specimens all lie above 80.0% saturation with several specimens above 100%. Technically, this is not possible. It indicates some minor errors in measuring densities, water content, and average specific weight of the soil particles. These errors can accumulate and produce calculated degrees of saturation above 100%. Soil logs from these sites indicate groundwater near the surface and ponding in some areas. The scatter in the data also illustrates the high variability in natural soils.

The reconstituted silt (HM1 and HM2) and sand (HS1 and HS2) specimens showed less difference between frozen and unfrozen thermal conductivities. Given the similar results from the empirical method (more so for the silt), it can be inferred that silt and sand are not as susceptible to freezing as specimens with higher clay content.

3.8 Summary

Values of thermal conductivity reported in this chapter were measured using a thermal needle probe for soils recovered from two road embankment sites in northern Manitoba (PR391 and PR373) and for a foundation of a transmission tower operated by Manitoba Hydro. Results from the laboratory testing are generally in good agreement with values of empirical methods available from the research literature. These values can be used for thermal numerical modeling of each site. Modeling of the PR391 site and the foundations of the transmission towers is presented in Chapter 4. Modeling of the PR373 site was not part of the author's program.

Table 3.1: Thermal Conductivity for PR391

Specimen	Depth [m]	λ [W/mK] 10°C	3°C	-10°C[1]	w_n [%]	γ_d [Mg/m^3]	I_p [%]
S10[2]	1.0	1.41	1.43	2.42[3]	25	1.62	13.5
S11	1.7	0.90	0.91	1.21	36	1.30	24.2
S12	2.5	1.35	1.32	1.88	26	1.52	15.8
S13	3.3	1.41	1.32	2.06	28	1.49	14.1
S14	4.0	1.51	1.18	2.31	25	1.65	8.3

[1]Frozen specimens used guiding tubes; [2]Silt specimen; [3]Obtained at -16°C

Table 3.2: Thermal Conductivity for PR373

Specimen	Depth [m]	λ [W/mK] 10°C	3°C	-16°C[1]	w_n [%]	γ_d [Mg/m^3]	I_p [%]
S3[2]	2.6	0.50	0.52	1.56[3]	618	0.13	--
S7[2]	2.7	0.52	0.54	1.67	756	0.12	--
S24	4.9	1.48	1.32	1.96	27	1.51	24.3
S25	6.4	1.61	1.59	2.50	29	1.53	21.7
S26	7.9	1.15	1.15	1.65	46	1.13	33.5
S27	9.5	1.11	1.12	1.56	45	1.07	36.9
S28	11.0	1.09	0.99	1.71	49	1.02	33.0
S29	12.5	1.02	1.02	1.79	46	1.10	30.2
S30	14.0	1.27	1.17	2.29	41	1.33	16.1

[1]Frozen specimens used guiding tubes; [2]Peat specimen; [3]Obtained at -10°C

Table 3.3: Thermal Conductivity for Manitoba Hydro Samples

Specimen[1]	Depth[2] [m]	λ [W/mK] 10°C	3°C	-10°C[3]	w_n [%]	γ_d [Mg/m^3]	Sat. [%]
HO1	0.5	0.39	0.35	0.68	257	0.22	61
HM1	1.3	1.56	1.60	1.67	12	1.74	59
HM2	2.0	1.77	1.75	1.81	12	1.76	61
HS1	1.5	2.00	1.96	2.25	11	1.73	56
HS2	1.5	2.10	1.97	2.24	10	1.80	54

[1]Naming based on USCS (O = Organic, M = Silt, S = Sand)
[2]Depths are approximate; [3]Frozen specimens used guiding tubes

Table 3.4: Measured vs. Estimated Thermal Conductivity

Specimen	Measured[1]		Estimated[1]		Comments
	λ_u	λ_f	λ_u	λ_f	
S10	1.42	2.42	1.55	2.20	- Compares reasonably
S11	0.90	1.21	1.10	2.06	- Compares poorly
S12	1.34	1.88	1.35	2.00	- Compares well
S13	1.36	2.06	1.35	2.07	- Compares well
S14	1.51[2]	2.31	1.63	2.30	- Compares reasonably
S3	0.51	1.56	--	--	- Off the chart
S7	0.52	1.67	--	--	- Off the chart
S24	1.40	1.96	1.35	2.06	- Compares well
S25	1.60	2.50	1.45	2.25	- Compares reasonably
S26	1.15	1.65	0.95	2.12	- Compares poorly
S27	1.12	1.56	0.84	1.90	- Compares poorly
S28	1.04	1.71	0.81	1.90	- Compares poorly
S29	1.02	1.79	0.90	2.04	- Compares reasonably
S30	1.22	2.29	1.25	2.35	- Compares well
HP1	0.37	0.68	0.35	0.75	- Compares well
HM1	1.58	1.67	1.37	1.38	- Compares reasonably
HM2	1.76	1.81	1.33	1.35	- Compares reasonably
HS1	1.98	2.25	2.00	2.30	- Compares well
HS2	2.04	2.24	2.10	2.35	- Compares well

[1]All values reported in [W/mK]; [2]Higher value chosen

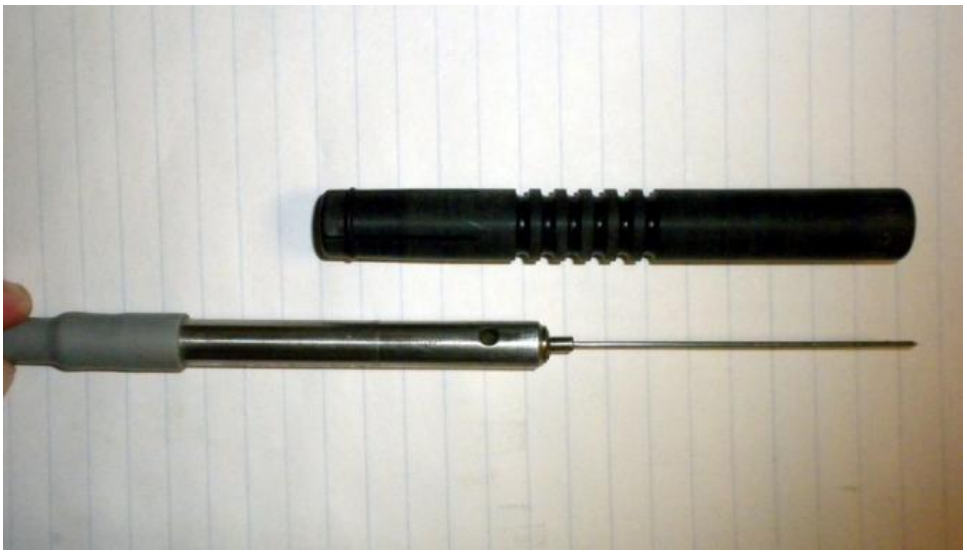

Figure 3.1: TP08 Thermal Probe and Storage Cap

Figure 3.2: Campbell Scientific CR23X micrologger

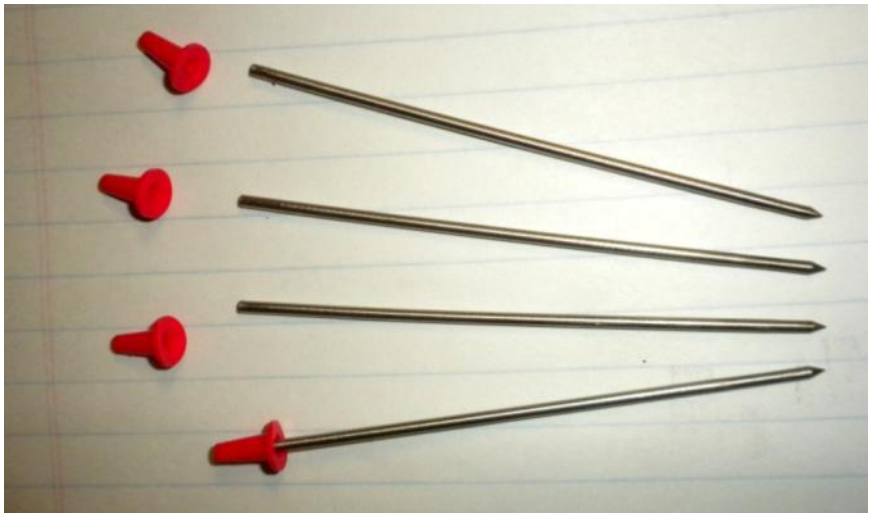

Figure 3.3: GT01 Guiding Tubes

Figure 3.4: Stainless Steel Cell (base plate, cylinder, top cap)

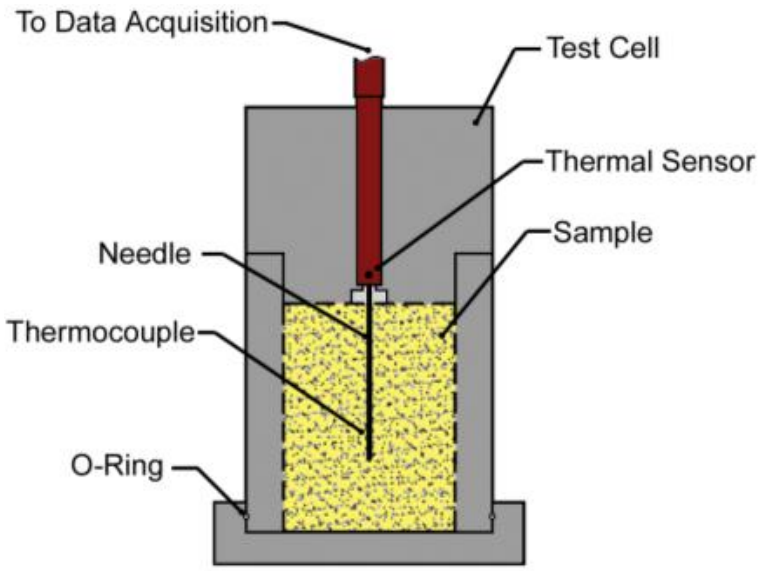

Figure 3.5: Schematic of test cell with specimen and thermal probe inserted

Figure 3.6: A 4.0% Concentration Agar-Water Gel

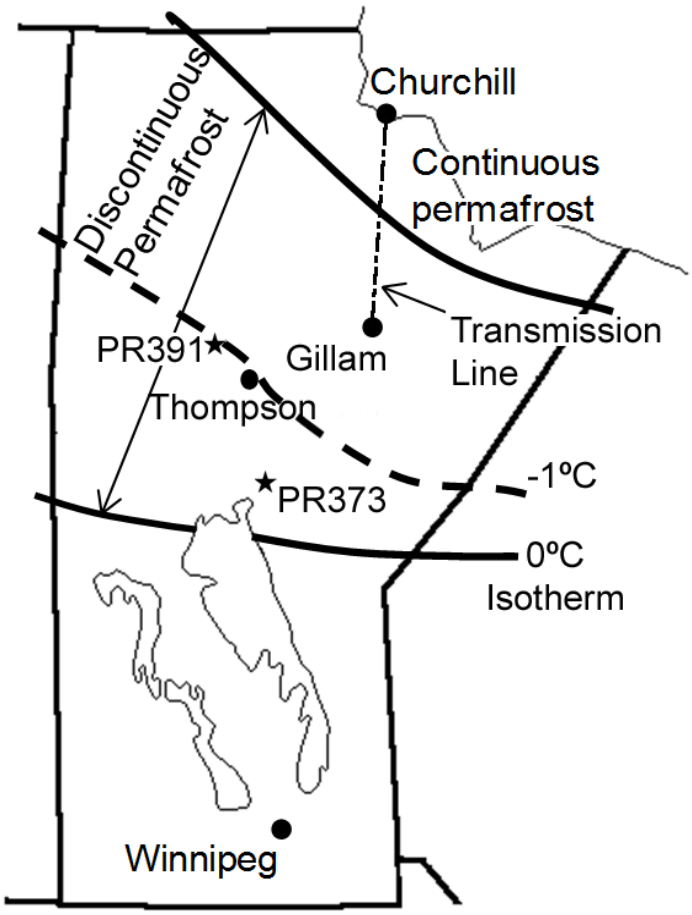

Figure 3.7: Location of project sites and permafrost in Manitoba

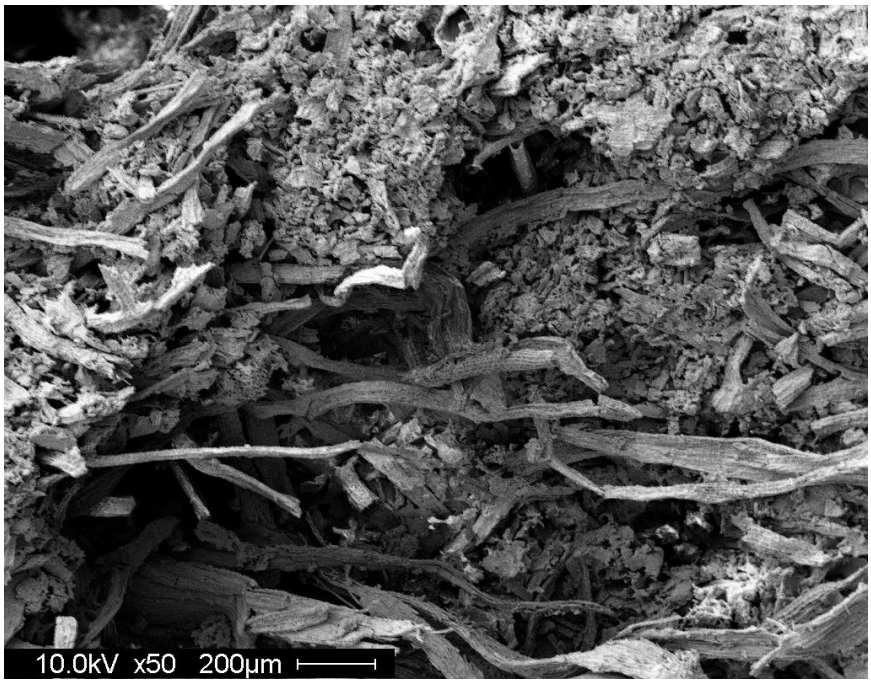

Figure 3.8: SEM micrograph for weakly decomposed peat sample at x50 magnification . (Image provided courtesy of Mr. Cory Jay Pyziak, unpublished)

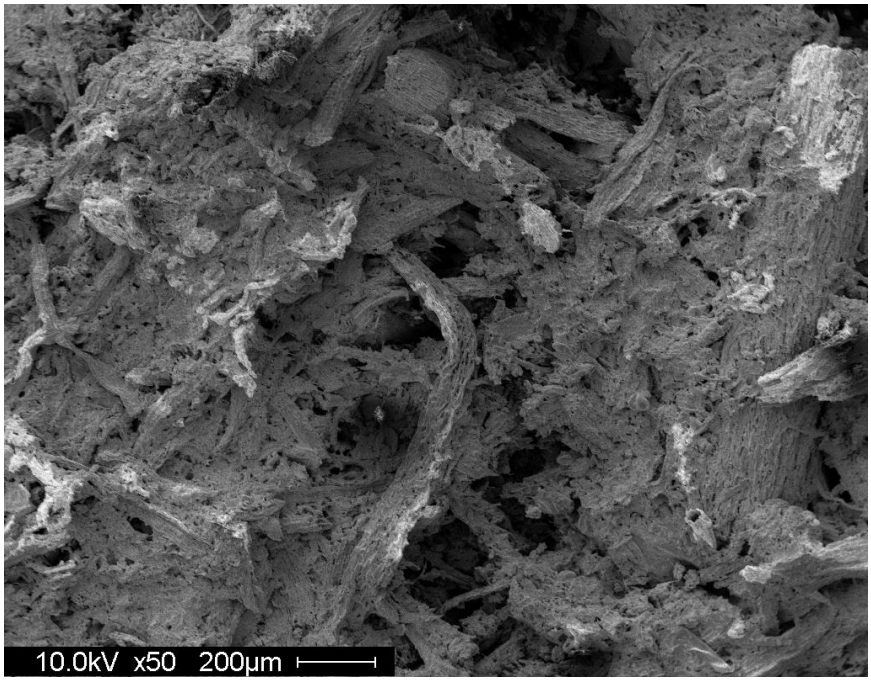

Figure 3.9: SEM micrograph for moderately decomposed peat sample at x50 magnification (Image provided courtesy of Mr. Cory-Jay Pyziak, unpublished)

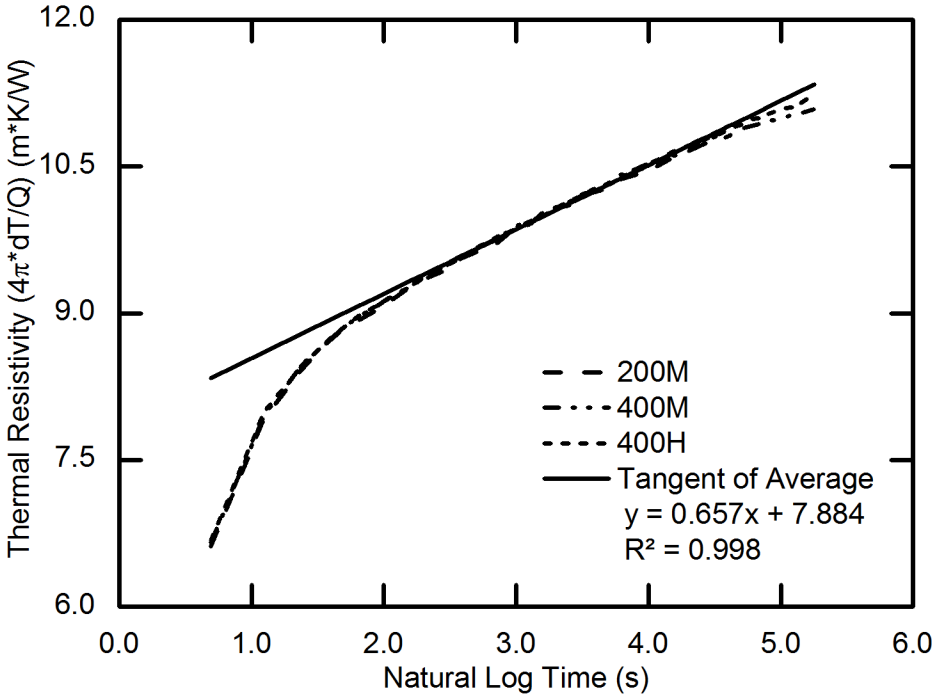

Figure 3.10: Example analysis of the tests performed on each sample

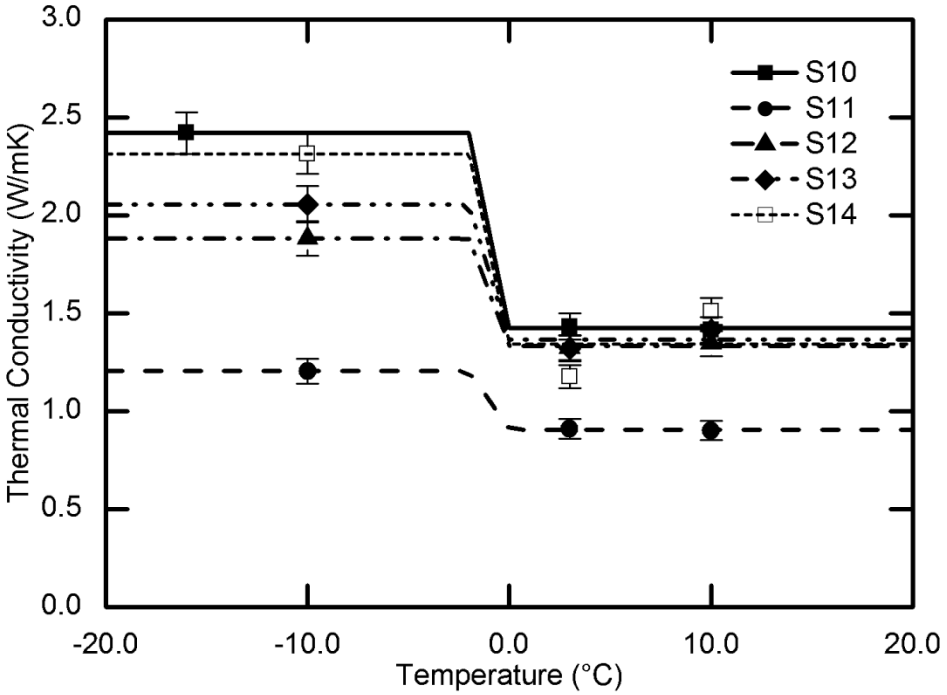

Figure 3.11: Thermal conductivity vs. temperature; PR391 specimens with assumed relationships

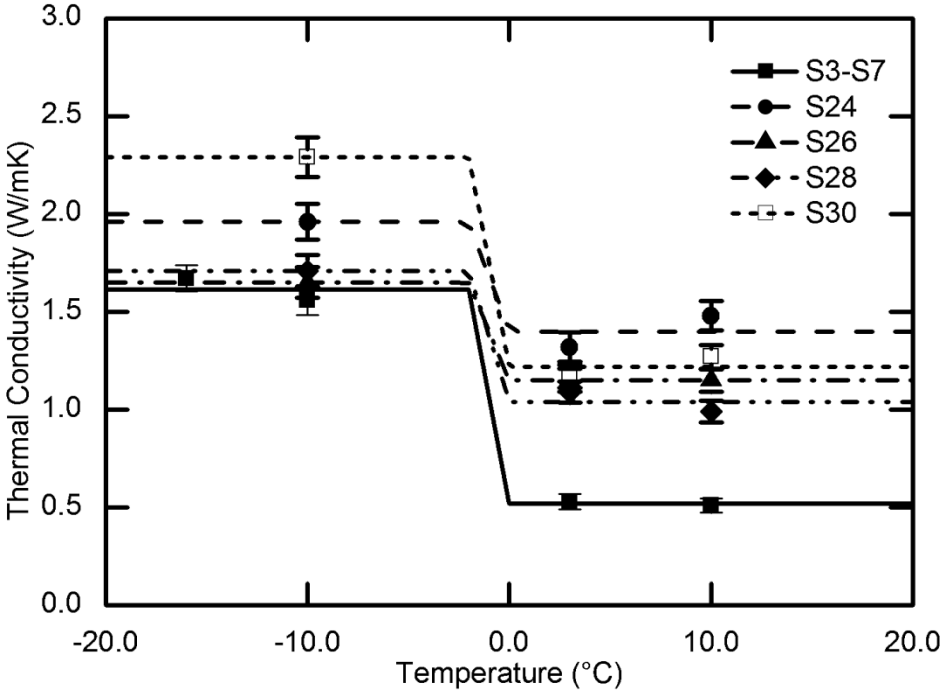

Figure 3.12: Thermal conductivity vs. temperature; selected PR373 specimens with assumed relationships

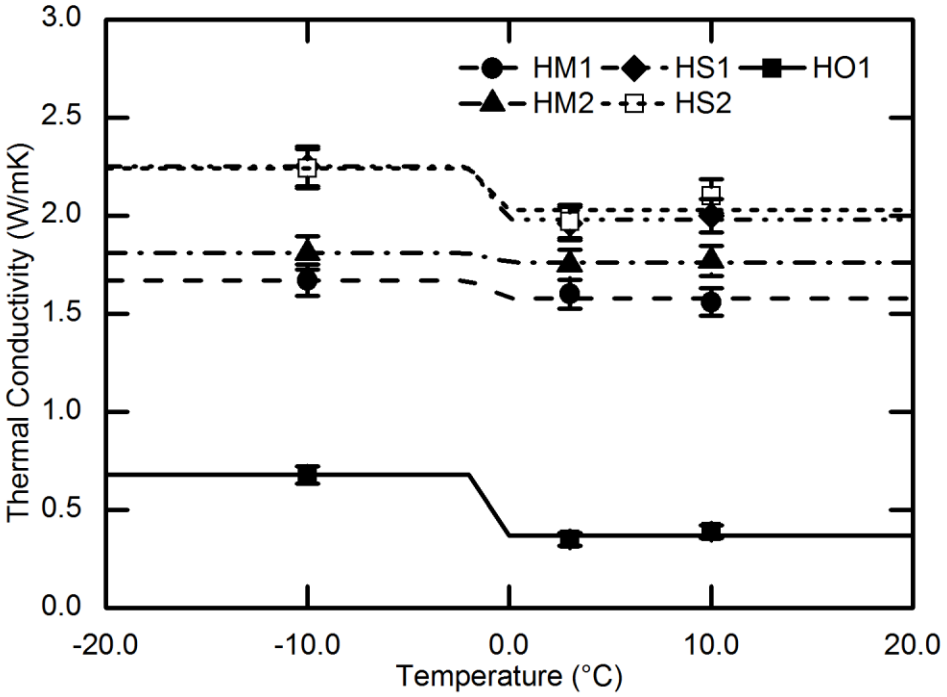

Figure 3.13: Thermal conductivity vs. temperature; Manitoba Hydro specimens with assumed relationships

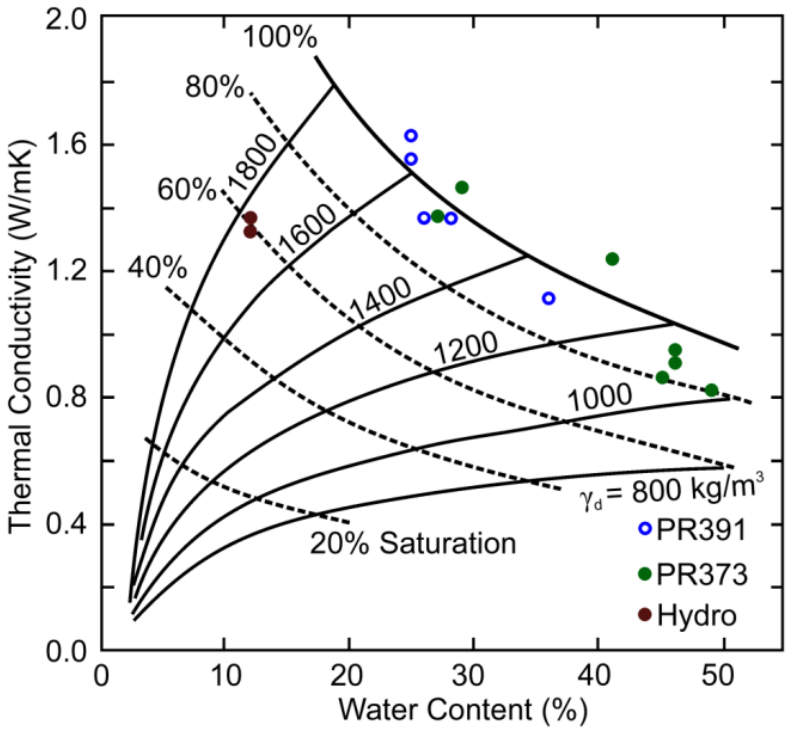

Figure 3.14: Unfrozen Silt and Clay; re-plotted after Harlan and Nixon (1978) (Used with permission)

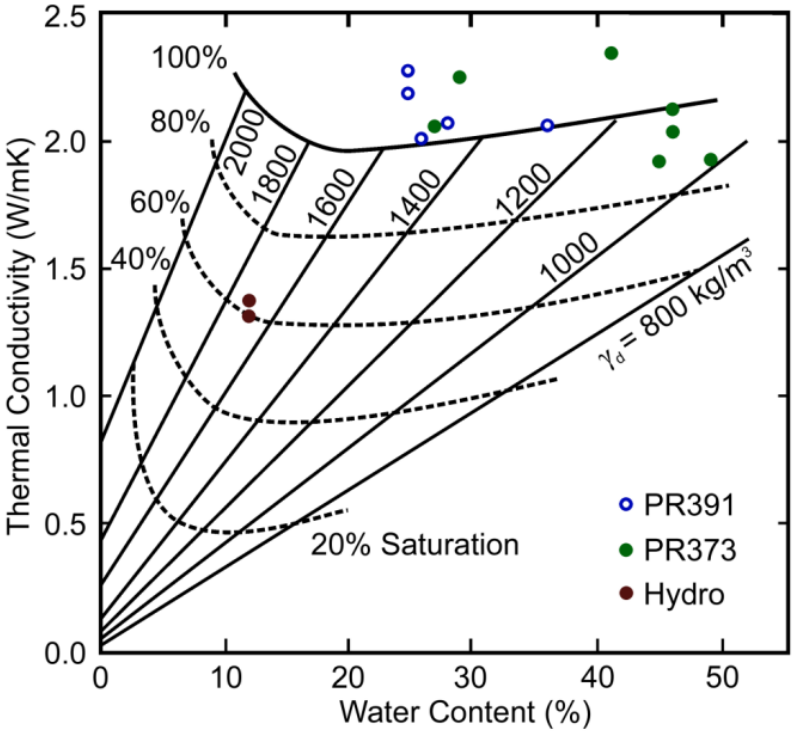

Figure 3.15: Frozen Silt and Clay; re-plotted after Harlan and Nixon (1978) (Used with permission)

Chapter 4: Case Histories: Thermal Numerical Modeling

4.1 Introduction

Thermal numerical modeling permits simulation of changes in temperature in the ground. These simulated temperatures provide an understanding of the thermal behaviour of the modeled soil profile with its selected material properties. The purpose of the modeling in this chapter is to simulate and evaluate the field performance of two case histories: a section of road embankment; and, the foundations of electrical transmission towers. With climate changes over time providing added cause for concern, several options for assigning surface boundary conditions are explored. This allows evaluation of the performance of the thermal models.

4.2 PR391

4.2.1 Site Description

The test site on Provincial Road PR391 is located approximately 18 km northwest of Thompson (Figure 3.7). The site was initially constructed as a compacted earthen road in the mid-1960s and converted to a gravel road in the early 1970s. Since construction, changes in heat transfer under this embankment have thawed some of the previously discontinuous permafrost that was detected earlier. Thawing has led to large ongoing irregular deformations and dangerous trafficability issues. This site, pictured in Figure 4.1, was the primary research site of Dr. Hamid Batenipour (2012), a colleague of the

author. Dr. Batenipour's research investigated and evaluated the performance of a road embankment on thawed ground. Additional information regarding the history, site investigation, instrumentation, and laboratory testing for the project is published in Alfaro et al. (2009), Batenipour et al. (2009*a*,*b*, 2010, 2011), and Batenipour (2012).

Instrumentation at the site included thermistor strings with sensors at 1.0 m spacing, vibrating wire piezometers and standpipes, slope inclinometers, surface settlement plates, and lateral displacement extensometers. The instruments were grouped in clusters and installed at the mid-slope and toe of both a 'stable' and 'unstable' section. The labels 'stable' and 'unstable' are applied for serviceability limit state, not ultimate limit state and are discussed in Batenipour (2012). Figure 4.2 illustrates the soil stratigraphy for only the unstable section as it is the focus of the modeling and discussion in this thesis.

Readings were taken once every two weeks on a data acquisition system during spring and fall, and monthly during summer months. Measurements were taken between October 2008 and April 2011 as a part of Dr. Batenipour's research. A continuation of this research under Mr. David Flynn began in September 2012 with installation of additional instruments in the shoulder and midpoint of the road. Monitoring is planned for an additional two years to allow improved calibration of modeling over several freeze-thaw cycles and to determine the impact on the frozen soil.

The soil conditions, and graphs of the modeling results later in this chapter, are described with reference to the original ground level, here taken as an elevation of 0.0 m. Soil conditions beneath the toe of the unstable section consist of 1.0 m of clayey peat-silt, approximately 1.0 m of fine gravel, followed by a layer of highly plastic clay. The mid-

slope of this section consists of nearly 2.0 m of clayey peat-silt, over 2.0 m of loose fine gravel, followed by the same clay layer. The clay is firm, brown, and silty at upper levels. Below approximately 8.0 m the clay becomes soft and grey to a depth approaching 18.0 m. The site is underlain by gneissic bedrock. The surrounding area has relatively poor drainage – free-standing water is present within approximately 20.0m of the embankment toe for most of the year.

4.2.2 Geotechnical Material Properties

Thermal numerical modeling requires input of many soil parameters for both frozen and unfrozen states. These parameters include frozen and unfrozen volumetric heat capacities (C_f and C_u), thermal conductivities (λ_f and λ_u), in-situ volumetric water content (VWC), and unfrozen volumetric water content.

Volumetric heat capacities and in-situ volumetric water contents were calculated from measured water contents and dry densities using relationships from Andersland and Ladanyi (2004). Thermal conductivities for clayey silt and silty clay were measured in the University of Manitoba laboratory. They have been presented in Chapter 3 and a conference paper, Kurz et al. (2012*a*).

Heat capacity is the quantity of heat required per unit mass of material to raise its temperature by one degree. Volumetric heat capacity is the same formulation expressed in volume instead of mass. Heat capacity is described as follows:

[Eq. 4.1] $$C\ (kJ/kg/°C) = \frac{1}{m}(c_s m_s + c_w m_w + c_i m_i + c_a m_a)$$

where c_s, c_w, c_i, c_a = heat capacities and m_s, m_w, m_i, m_a = masses of solid, water, ice, and air, respectively for a total mass, m, in a particular volume, V (e.g. a unit volume)

(Andersland and Ladanyi 2004). The mass of air is negligible. The heat capacity ratios (compared to water) for solids, water, and ice may be typically assumed as 0.17, 1.0, and 0.5, respectively. Therefore, by taking Equation 4.1 and dividing it by the volume, incorporating the relationships between mass fractions, water contents, density of dry soil and water, and specific heat of water, one can arrive at the following equations as presented in Andersland and Ladanyi (2004):

[Eq. 4.2] $$c_{vu} = \left(\frac{\rho_d}{\rho_w}\right)\left[0.17 + 1.0\left(\frac{w_n}{100}\right)\right] c_{vw}$$

[Eq. 4.3] $$c_{vf} = \left(\frac{\rho_d}{\rho_w}\right)\left[0.17 + 1.0\left(\frac{w_u}{100}\right) + 0.5\left(\frac{w_n - w_u}{100}\right)\right] c_{vw}$$

where c_{vu}, c_{vf} = unfrozen and frozen volumetric heat capacities, c_{vw} = volumetric heat capacity of water (4.187 MJ/m^3/°C), ρ_d and ρ_w = density of dry soil and water, w_n and w_u = gravimetric water content and unfrozen gravimetric water content (as percentages).

Water content greatly affects the thermal properties of a material. The gravimetric water content, w_n, is easily measured in the laboratory whereas the unfrozen gravimetric water content, w_u, is more difficult. The volumetric water content, θ, represents the volume of water within a total unit volume of soil. It can be calculated using the gravimetric water content and the density of dry soil and water as follows:

[Eq. 4.4] $$\theta = w_n\left(\frac{\rho_d}{\rho_w}\right)$$

It should be noted that many sources refer to the dry density (wt. of solids/total volume) as simply "(*dry*) bulk density, ρ_d" however, this can be confused with "(*wet*) bulk density, ρ_b" which is typically defined as total weight/total volume.

The unfrozen volumetric water content is the percentage of water that remains

unfrozen at sub-zero temperatures. This portion of water is related to the water adsorbed on the surface of particles and is calculated as a function of surface area of particles. This was not measured as part of the laboratory program in Chapter 3. Typical relationships found in the literature were used to gain an understanding of the relationship of unfrozen volumetric water content to sub-zero temperatures for various soil types (such as Andersland and Ladanyi 2004). The modeling software, TEMP/W, allows the user to input this function or to make use of the built-in functions. The relationships of clay, silty clay, and gravel (Figure 4.3) were chosen using built-in functions to represent soil used in this modeling. Measurement of these relationships were not part of this thesis program.

The unfrozen volumetric water content function assumes 5.0% of the volumetric water content remains unfrozen. This reflects similar values found in the research literature, for example, Andersland and Ladanyi (2004) and Farouki (1986). The relationship implies that more water remains unfrozen at sub-zero temperatures in finer grained material than in coarser grained material. This function is a reverse trend ("mirror image") of the relationship between thermal conductivity and temperature shown in Figure 4.4 for the materials modeled. These functions describe the gradual change in thermal conductivity as a soil freezes or thaws, and the corresponding volume of unfrozen water as a percentage of the volumetric water content. The soil type determines the rate of change (faster for coarse-grained, slower for fine-grained). A similar less-defined step function was assumed for the author's data presented in Chapter 3 (see figures 3.11, 3.12 and 3.13). Values of thermal conductivity are given in kJ/d/m/°C as required by the software as opposed to W/mK given in Chapter 3. The conversion factor for Watts into kilojoules per day is 1 W = 86.4 kJ/day.

The gravel from PR391 was not tested in the laboratory; therefore, its thermal properties were assumed. Based on the site conditions, the 'dense' compacted gravel was assumed to be near full saturation, especially at depth. A first attempt at thermal modeling was published by Batenipour et al. (2010). For the latest revision of the modeling shown here, approximate values of 12.0% water content and 2000.0 kg/m^3 were used. Values for c_{vu}, c_{vf}, and θ were calculated using Equations 4.2, 4.3, and 4.4. Thermal conductivities, λ_u and λ_f, were estimated from the literature (Andersland and Ladanyi 2004, Farouki 1986, Harlan and Nixon 1978, Johansen 1975).

For comparison, modeling parameters used in Batenipour (2012) and Kurz et al. (2012*b*) are presented in Table 4.1. The latest revisions of these parameters employ a better understanding of thermal properties by the author and are presented in Table 4.2.

4.2.3 Thermal Numerical Modeling

Cross-Section and Model Design:

The cross section of the research site on PR391 (Figure 4.2) was developed using TEMP/W into a thermal numerical model, as shown in Figure 4.5. The vertical lines at distances of approximately 8.7 m and 12.0 m illustrate the locations of the thermistor strings for the mid-slope and toe of the embankment. As mentioned earlier, the model was designed such that the original ground level is set as 0.0 m; the road surface is 2.0 m higher. The model was developed as a two-dimensional (2D) plane-strain model with symmetry around the centreline of the road embankment.

The principal mechanism for heat flow in soils (that is, the passage of heat energy between particles) is conduction. The TEMP/W software (GEO-SLOPE International

Ltd. 2010) assumes heat flow (flux) due to conduction follows the general equation:

[Eq. 4.5] $$q = -k\frac{\partial T}{\partial x}$$

where q = heat flux, k = thermal conductivity (previously defined as λ), T = temperature, and x = distance. This equation shows that positive heat flux is a result of decreasing temperatures over an increasing distance. From this equation, the governing 2D differential equation in TEMP/W can be defined as:

[Eq. 4.6] $$\frac{\partial}{\partial x}\left(k_x\frac{\partial T}{\partial x}\right) + \frac{\partial}{\partial y}\left(k_y\frac{\partial T}{\partial y}\right) + Q = \left(c + L\theta\frac{\partial \theta_u}{\partial T}\right)\frac{\partial T}{\partial t}$$

where k_x, k_y = thermal conductivities in the x- and y-directions, respectively, Q = applied boundary flux, c = volumetric heat capacity, L = (volumetric) latent heat of freezing water, θ = volumetric water content, θ_u = unfrozen volumetric water content, T = temperature, and t = time. This equation is applied to each node in the finite element analysis to account for changes in temperature in transient analyses.

The mesh of finite elements in the model extended outwards 30.0 m from the centreline of the embankment and to a depth of 18.0 m from the original ground surface. Small 4-node elements (0.25 m x 0.25 m) were used near the embankment and ground surface for added precision and improved calculation of the isotherms in regions where high variations in temperature were expected. Larger 4-node elements (0.50 m x 0.50 m) were used away from areas of principal interest. The software used a meshing algorithm that transitioned the size of the elements by using the least amount of triangular elements. A sensitivity analysis on the finite element mesh was performed. Figure 4.6 illustrates that the design of this 2D model was not sensitive to selected mesh sizes (Fine: 0.15-0.30 m, 2351 elements; Original: 0.25-0.50 m, 4452 elements; Coarse: 0.50 m, 11966

elements). It is possible that a larger mesh might have had a detrimental effect. Insolation (the effect of the direction of the sun versus a north- or south-facing slope) was not considered in this model.

Calibration of the model used historic climate data from Environment Canada's monitoring station at the nearby Thompson Airport and thermistor data measured at the site at both the mid-slope and toe of the embankment. More details regarding climate data and surface boundary conditions is provided later in this chapter.

Boundary Conditions:

Modeling was completed in two phases – first a steady-state phase, second a transient phase. The steady-state phase was used to obtain initial isotherms for the second phase, which used time-dependent boundaries, such as climate data.

The steady-state analysis assumed zero heat flux (q = 0) across the leftmost (centreline) boundary (Figure 4.5). The temperature from the assumed initial day of the Environment Canada climate data (25 months before the first measured data) was applied along the ground surface as a constant. Batenipour et al. (2010) discussed varying the start dates for the transient analysis. It was found that starting the analysis about two years (25-months) before beginning the field measurements reduced potential negative influence of the assumed initial steady-state analysis. Including the 25-month stabilization period, the transient analysis had a starting date of 01 October 2006 and an end date of 30 September 2011, six months after the last data were collected.

A constant temperature of 1.8°C was assumed along the bottom boundary (Elevation -18.0 m). This was based on a typical geothermal gradient and the distance

from the Depth of Mean Zero Annual Amplitude (DMZAA) to bedrock (Batenipour et al. 2010). This is the maximum depth that the effect of the climate can be observed. The DMZAA reported for the thermistor string at the toe of the embankment (~1.65°C) was input to the model at approximately 12.0 m from the centre of the embankment at a depth of approximately 9.0 m. The DMZAA reported for the thermistor string at the mid-slope (~0.2°C) was input in separate calculations as both a 'point' and as a 'line', as shown in Figure 4.5. The difference between these boundary conditions is explained further in Section 4.2.4.

Zero heat flux was applied on the right boundary. This corresponds to setting no boundary condition in TEMP/W. Figure 4.7 shows that model results are unaffected by this boundary when set at reasonable distances from the centreline of the embankment. Calculated isotherms were essentially horizontal at the right boundary. This indicated that the design of the model provided adequate distance from the embankment toe to the right boundary. The transient analysis used the same boundary conditions for the left, bottom and right boundaries as the steady-state analysis. The influence of the top (surface) boundary was explored using three different sets of boundary conditions.

Climate Boundary:

The transient models were analyzed with three sets of surface boundary conditions, *'Kurz'*, *'Sine'*, and *'CCCma'*. These boundary conditions represent, respectively, the measured climate data (*Kurz*); a simplification of those data using a sine function (*Sine*); and predicted temperature data using the same sine function simplification (*CCCma*).

For the *'Kurz'* set, input data were taken from Environment Canada's (2012)

website for the weather monitoring station at nearby Thompson Airport. The data are for five years between 01 October 2006 and 30 September 2011. Entering the data into TEMP/W required re-formatting the dataset. The data included maximum and minimum daily temperatures, maximum and minimum daily relative humidities, average daily wind speeds, and total daily precipitation (as a total water equivalent). The latitude of the monitoring station, 55.8° N, was set to a fixed value as well. The distribution pattern of the climate over the day was chosen as a Constant Averaged distribution. GEO-SLOPE International Ltd., the vendors for TEMP/W, recommend this pattern as being well suited for analysis of multiple design options based on a 1-day time interval.

Data for the second boundary condition – the *'Sine'* set - used a 'smoothed' sine function fitted to the same mean daily temperatures as in the *'Kurz'* set. Climate data are normally highly variable, with dramatic short-term changes in measured daily temperatures as well as wind and precipitation. Quick changes in the entered data can produce anomalies inside the modeling that may lead to numerical instabilities. An alternative to using measured climate data is to use 'smoothed' data, usually expressed as a manually fitted sine function and so-called n-Factors. As explained later, n-Factors are empirical parameters values that relate air (climate) temperatures to ground surface temperatures. The selected sine function had the form:

[Eq. 4.7] $$T\,(°C) = A + Bt + C\sin\left(2\pi\left[\frac{t+D}{365}\right]\right)$$

where A = Mean Annual Air Temperature (MAAT) (a vertical shift calculated as -2.47 °C), B = a temperature increase with time (gradient set as 0), C = constant (amplitude set as 23), t = day number, D = constant (a horizontal shift set as 160 days). Figure 4.8 shows

the fit for nearly two years of data (700 days shown).

The third boundary condition that was examined used data predicted by the Canadian Centre for Climate Modelling and Analysis (CCCma) (2007). The *'CCCma'* data set, also used a 'smoothed' sine function fitted to the mean daily temperatures extracted from 'generated' climate model data.

The CCCma developed several models that permit climate prediction and variability. The author's research program employed the CCCma Third Generation Coupled Global Climate Model (CGCM3.1/T47) which uses the Third Generation Atmospheric Climate Model (AGCM3). Mean daily temperature data from this model indicated an increase of 1.4°C over 25 years. Figure 4.9 shows a sine function, with a linear trendline, fitted to the 25 year data and accommodating 1.4°C increase over that period. These data were used in forward prediction modeling discussed in Section 4.2.4. Parameters for this sine function follow Equation 4.7, with A = 0.47°C, B = 0.00015°C/day, C = 22, D = 160 days. It is of note that the predicted temperature data, *'CCCma'*, have an MAAT nearly 3.0°C higher than the measured climate data, *'Sine'*, but a slightly smaller amplitude.

Due to the use of climate data, the model time steps were fixed at 1-day increments. No sensitivity analysis was performed on the time steps.

Surface Layer and n-Factors:

TEMP/W uses a surface layer at the free ground boundary to apply climate data to a model. The layer consists of thin layers of finite elements, accommodates all the variables in the climate data, and calculates appropriate values for the materials below the

surface layer in the underlying ground. These calculations are internal and account for the changes in temperature and precipitation in such a way that, for example, an estimated snow cover can be determined.

The calculations use modification factors known as n-Factors, which are defined as the ratio of thawing (or freezing) degree days at the surface of the soil to those in the air. The factors allow a simple conversion of air temperatures to ground temperatures based on the thermal properties of the ground material and whether it is frozen or unfrozen. Table 4.3 summarizes the n-Factors adopted for the modeling that used the sine function fitted to the data for air temperatures. The n-Factors were taken from Andersland and Ladanyi (2004).

Parametric Studies:

Four studies were used to better understand the influence of the modeling parameters, boundary conditions, and especially the surface boundary conditions, on estimates of temperature in the PR391 embankment.

The first parametric study involved comparing the effects of thermal conductivity measured in the laboratory (*'Measured'*) with thermal conductivity calculated using broad assumptions and empirical relationships from the literature. This study also compared the results presented in Batenipour (2012) (*'Batenipour'*) with results using the revised material parameters (*'Kurz'*) from Table 4.2.

The second parametric study explored the effects of different boundary conditions applied between the centreline of the model and the thermistor string at the mid-slope of the embankment. This study compared the impact of this constant temperature boundary

condition as a point or as a line. This study renamed the *'Kurz'* data set as *'Point'* and *'Line'* according to the applied boundary condition.

The third parametric study compared results from using locally-observed climate data (boundary condition *'Kurz'*) with results from a 'smoothed' sine function, *'Sine'*, fitted to the mean daily temperatures as described above. This study was performed because climate data are highly variable. The surface layer used by TEMP/W handles the conversion of climate data to applicable ground temperatures internally. To address potential instabilities and uncertainty with 'black box' calculations for the surface layer, the third parametric study also used the n-Factors shown in Table 4.3.

The fourth parametric study compared results from using *'Kurz'* and *'Sine'* boundary conditions with those from *'CCCma'* data that had a sine function applied to the generated mean daily temperatures in the CCCma CGCM3.1/T47 climate prediction model. This comparison explored whether the CCCma data provide reasonable results that could be used for forward prediction.

4.2.4 Modeling Results and Forward Prediction

Measured versus Assumed Parameters:

Figure 4.10 illustrates a comparison obtained from field measurements (*'Measured'*) at the toe and mid-slope of the embankment with the numerical modeling for mid-2009 and early-2010. In the figures, *'Assumed'* refers to preliminary work reported by Batenipour et al. (2010) that used empirically estimated thermal conductivities; *'Batenipour'* refers to later modeling presented by Batenipour (2012) in his doctoral thesis, which used measured thermal conductivities (Table 4.1) and was reported in Kurz et al. (2012b);

'Kurz' refers to more recent modeling presented in this thesis using data from Table 4.2. Dates in the figures allow the best comparison of modeled and measured temperatures. There is typically a small difference in dates originating from the nearest corresponding 'saved' step in the models and the date that measurements were taken.

Comparing temperatures measured by the thermistors and temperatures calculated by TEMP/W showed that modeling using measured thermal conductivities (Tables 4.1 and 4.2) produced better simulations of ground temperatures than when *'Assumed'* thermal conductivities were used. The differences between *'Batenipour'* and *'Kurz'* are more subtle. There is no clear advantage of one set of parameters over the other; *'Batenipour'* appears to be a closer match to *'Measured'* at the toe of the embankment; *'Kurz'* appears to be a closer match at the mid-slope of the embankment.

'Line' versus 'Point' Boundary Condition:

This *'Line'* boundary condition (Figure 4.5) is located just below 8.0 m depth and extends from the centreline of the model out to approximately 10.0 m. It crosses the thermistor string at the mid-slope at a depth around 8.75 m. This corresponds, approximately, with the lowest average temperature (~0.2°C) measured by the thermistor string at the mid-slope over the first year of data. The 'Point' boundary condition applies the temperature of 0.2°C at 8.75 m instead of using the *'Line'* boundary condition.

Figure 4.11 illustrates a comparison between *'Measured'* field temperatures and temperatures from using the *'Line'* and *'Point'* boundary conditions at the toe and mid-slope of the embankment for mid-2009 and early-2010. The simulations used modeling parameters from Table 4.2. The impact of these boundary conditions on the simulations is

less evident at the toe of the embankment, but is greater at the mid-slope of the embankment. The *'Point'* boundary condition indicates warmer temperatures than what is recorded by the thermistors, primarily between depths of 4.0 m and 8.0 m.

Previous publications regarding the thermal numerical modeling of the PR391 embankment did not discuss the impact of this boundary condition and reported findings using only the *'Line'* boundary. The implication of this boundary condition is discussed in the commentary in Section 4.2.5.

'Kurz, 'Sine', and 'CCCma' Boundary Conditions:

Figures 4.12 and 4.13 illustrate a comparison obtained from field measurements (*'Measured'*) at the toe of the embankment and the numerical modeling for late-2008 to early-2011. Figures 4.14 and 4.15 illustrate this comparison at the mid-slope of the embankment over the same dates. Dates shown are spaced to provide a reasonable representation for all seasons during the collection of field measurements. A complete comparison is available on the accompanying DVD (see Appendix I). In the figures, *'Kurz'*, *'Sine'*, and *'CCCma'* represent the results from the three different surface boundary conditions previously discussed in Section 4.2.3.

Compared with using the *'Kurz'* data set, an overall improvement in the results of the modeling was observed when the 'Sine' data set and the n-Factors (Table 4.3) were used. This improvement is more noticeable at the mid-slope of the embankment (Figures 4.14 and 4.15) where the measured and simulated results are in excellent agreement. Compared with using the *'Sine'* data set, the *'CCCma'* data set provides an improvement in the results at the toe of the embankment (Figures 4.12 and 4.13), but does not compare

as well at the mid-slope. Overall, the use of *'CCCma'* data set and n-Factors do provide an improvement in the results of the modeling when compared to *'Kurz'* data set.

Figures 4.16 to 4.19 show the relationships between measured temperatures, simulated temperatures, and time for given locations below the ground surface at both the toe and mid-slope of the embankment. For the toe of the embankment, depths of 0.0 m and 1.0 m are shown in Figure 4.16; depths of 4.0 m and 8.0 m are shown in Figure 4.17. For the mid-slope of the embankment, depths of 2.0 m and 5.0 m are shown in Figure 4.18; a depth of 8.0 m is shown in Figure 4.19. The data in these figures coincide with the commencement (October 2008) and completion (April 2011) of field measurements. These figures illustrate the same reduced effect of the surface boundary condition with depth as Figures 4.10 to 4.15, however, the cyclic nature of the measured data and modeling results can be more closely analyzed. For example, the *'Kurz'* data set appears to show that the winter of 2009-2010 was relatively warmer than the other winter seasons, and that the summer-fall of 2010 peaked at higher temperatures as well.

In Figure 4.17b, a slightly downward trend can be observed in the 'Sine' and *'CCCma'* results whereas the *'Kurz'* results, using measured climate data, shows a slight upward trend for this relatively short period of time. It should be noted that while the sine function for 'Sine' had a neutral trend, an increase of 1.4°C over 25 years was applied to the sine function for the *'CCCma'* data. Figure 4.19, which has been drawn to an enlarged vertical scale, shows relatively neutral trends for the three modeling results, but the measured data show an increase from approximately 0.2°C to over 0.9°C in 2.5 years. Similar trends were also observed for the thermistors below 8.0 m.

Figures 4.12 to 4.19 show a good relationship between modeling results that used

the *'Sine'* and *'CCCma'* data sets for this site. This implies that the *'CCCma'* data set may be used in the model to provide forward prediction for some future time. For clarity, modeling results obtained using the *'CCCma'* data set have been presented here for only 10 of the 25 years for which the model was run. The trendline shown in Figure 4.20a indicates an increase in temperature of approximately 0.4°C over a 10 year period at 1.0 m below the toe of the embankment. The trendline in Figure 4.20b indicates nearly 0.3°C increase over the same period at 2.0 m below the mid-slope of the embankment.

4.2.5 Commentary

The thermal numerical models for the PR391 road embankment indicate there is an improvement in the results when measured and calculated values of material properties are used instead of parameters estimated empirically. Although the difference between the parameters used in Batenipour (2012) and this thesis is subtle, the evolution of the parameters reflect an improved understanding of thermal properties and their relationship to water content, dry density, and saturation. Additional laboratory testing (such as mineralogy) may help identify soil conditions that may alter modeling parameters.

The effect of the surface boundary condition has been explored by using three different sets of air temperature data. The models indicate that fitting sine functions to either simple temperature data or a more complete set of measured climate data provides better agreement with measured data than simply using ‘raw’ data that are often highly variable. An improvement in modeling were observed when sine functions were fitted to the *'Kurz'* data set from the nearby Thompson Airport monitoring station and also to the *'CCCma'* predicted temperature data set.

Additional improvements may be possible by adjusting the n-Factors given in Table 4.3. New n-Factors could be determined using a broader database directly related to soil materials at PR391. In addition, climate data from the Thompson Airport could be further analyzed to determine the actual freezing and thawing indices for the region.

Changes to the design of the numerical model may provide better agreement with the measured temperatures. Figure 4.2 shows an 'assumed' boundary between the gravel and the underlying clay. Additional site investigations may help to clarify this boundary. Transition zones with mixed thermal properties may provide better agreement than strict material boundaries. Measurements of temperature closer to the bedrock would clarify uncertainty about the actual rather than the assumed geothermal gradient.

The implications of the *'Point'* and *'Line'* boundary conditions require more attention. Currently, the *'Line'* boundary condition provides better agreement to measured results than the *'Point'* boundary condition. This implies that colder soil, such as a frost bulb, exists beneath the centreline of the road. This postulation was confirmed in September 2012 by Mr. David Flynn in the continuation of the Dr. Batenipour's and the author's research programs at PR391. Recent drilling in late 2012 revealed more than 1.0 m of frozen soil under the shoulder and more than 3.0 m under the centreline of the road. In addition, the increase in temperature with time (Figure 4.19) indicates that assuming a constant temperature boundary condition around the bottom of the thermistors at the mid-slope of the embankment may be incorrect. This suggests the quantity of frozen soil beneath the road embankment is reduced annually and implies a positive heat flux into the ground (such as the case with a changing climate).

4.2.6 Concluding Comments

Numerical modeling has simulated temperature distributions beneath a road embankment in northern Manitoba. Additional studies examined ways in which the surface boundary condition can be most effectively applied. These boundary conditions showed that 'smoothing' naturally variable climate data produced improved simulations of ground temperatures. The reasonably good agreement that has been obtained between modeled and measured temperatures over several winter and summer seasons is encouraging and contributes to improved ability to calibrate and validate the TEMP/W coding for this application.

Studying temperature distributions, as has been done in this modeling, is valuable but not sufficient. The relationship between temperature change and long-term stress-deformation behaviour also needs to be established. It is deformations that cause trafficability and maintenance issues, and not simply the changes in ground temperature. Chapter 5 investigates the development of a model that will include effects of viscosity (creep) with changes in temperature.

4.3 Radisson-Churchill Transmission line

4.3.1 Site Description

The most northern line constructed by Manitoba Hydro, the 138 kV Radisson-Churchill transmission line, extends from Gillam to Churchill (Figure 3.7). This transmission line traverses areas of both discontinuous and continuous permafrost. The ground is mostly muskeg whose thickness varies from a few centimetres to over 3.0 metres. The muskeg overlies a deposit comprised of primarily marine silts and sands. Surface drainage varies

from fair to poor; the region contains many scattered lakes. The surrounding terrain is heavily vegetated in the south and becomes more barren further north (Staudzs 1986).

Manitoba Hydro used a tower design supported by four guy wires for this transmission line. Both the towers and foundations were adapted as necessary for variable soil conditions along the route. The design consisted of a single 0.3 m diameter hollow structural steel (HSS) tower (Figure 4.21) founded on wide flange beams connected to a 0.075 m thick rectangular timber footing.

The timber footings were underlain by 0.2 m thick polystyrene insulation and granular fill. The insulation was used to reduce heat transfer in foundation soils in the warmer southern portions of the transmission line and to help prevent frost heaving in the colder northern portions. Empirical design methods were originally used to determine the thickness and lateral extent of the insulation in these foundations. Figure 4.22 shows a simplified diagram of a typical tower foundation used by Manitoba Hydro. In this thesis, 'footing,' refers to the combination of the gravel, insulation, and wood materials. 'Foundation' refers to the whole system, including the footing and surrounding soil.

4.3.2 Geotechnical Material Properties

Thermal modeling of the tower foundations requires input of the same material properties as those discussed in Section 4.2.2. These include the frozen and unfrozen volumetric heat capacities (c_{vf} and c_{vu}), thermal conductivities (λ_f and λ_u), and the in-situ volumetric water content. These modeling parameters, provided in Table 4.4, differ from those presented in Kurz et al. (2008) and Kurz et al. (2009). The differences reflect laboratory testing performed by the author and an improved understanding of thermal properties.

Chapter 3 presented results of thermal conductivity testing on the soils present in the foundations of the towers; peat (muskeg), a clayey silt (mineral soil) and a gravelly sand. Equations 4.2 to 4.4 were used to calculate values for volumetric water content and heat capacities. Figure 4.23 shows the built-in functions chosen to represent the unfrozen volumetric water content relationships for the material used in this modeling. Measurement of these relationships was not part of this thesis program.

The foundations also included a timber (wood) footing, polystyrene insulation, and the HSS tower. Values for the wood and steel were based on published literature such as Andersland and Ladanyi (2004), the Departments of the United States Army and Air Force (1988), Forest Products Laboratory (1999). The difference in thermal properties between hardwoods and softwoods was viewed as negligible for this application. Slightly higher-than-typical values were chosen to reflect uncertainty about the type of wood used in the footings. Thermal properties of standard high-density expanded polystyrene insulation were taken from Horvath (1995) and Andersland and Ladanyi (2004).

4.3.3 Thermal Numerical Modeling

Cross-Section and Model Design:

The foundations of the transmission towers were modeled using TEMP/W. The brief discussion on the theory in TEMP/W formulations presented in Section 4.2.3 applies to this model as well. Despite the footings being rectangular, the models were designed as axisymmetric. Equation 4.6 is modified appropriately for axisymmetric conditions using "r, θ" coordinates instead of "x, y" coordinates. This was done to simplify the modeling and eliminate potential complexities due to the geometry and the need for a 3D analysis.

Figure 4.22 indicates that footing depths varied from the ground surface (0.0 m) to 3.7 m. Placement of the footing depths reflected site variability between Gillam and Churchill. Manitoba Hydro did not make available a record of footing depths for each tower.

Two model configurations, Figures 4.24a and 4.24b were used to reflect the extremes in the design depths and were labeled 'deep' and 'shallow', respectively. Both models maintain a 0.3 m peat layer (mound) above the foundation. The 'deep' foundation model extends the peat mound 0.5 m past the outer edge of the footing (Figure 4.22).

Two sizes of the insulating sheet were modeled; a 2.5 m by 2.5 m sheet and a 4.0 m by 4.0 m sheet. This resulted in insulation lengths of 1.25 m and 2.0 m in the axisymmetric models for both deep and shallow foundations. Construction reports suggested that the area of the insulation varied with depth, though details were not given. In addition, the deep and shallow foundation models were primarily analyzed with and without the vertical hollow section of structural steel shown in Figure 4.22. Reasons for this decision are discussed in Section 4.3.4. The steel was introduced as a solid material to provide analysis on the 'worst case' effect of steel without introducing an unmeasured convective boundary within the hollow steel towers.

The mesh of finite elements in the models extended outwards 20.0 m from the centreline of the model and to a depth of 11.5 m from the ground surface. Shorter distances are shown in Figure 4.24 so that the section could be enlarged for publication. Small 4-node elements (0.1 m x 0.1 m) were used near the footing and the ground surface for added precision with the calculated isotherms. Larger 4-node elements (0.5 m x 0.5 m) were used away from areas of principal interest. The meshing algorithm in the software was used to minimize the number of triangular (3-node) elements. A similar

sensitivity analysis, as presented in Section 4.2.3, was performed on the finite element mesh. Similar results were obtained but are not presented in this thesis. The size of the small elements was chosen to maximize the use of 4-node elements within the footing and was limited by the geometry of the footing.

Boundary Conditions:

The boundary conditions used in this modeling were similar to the models described in Section 4.2 for PR391. Modeling was completed in two phases: a steady-state phase followed by a transient phase. The first phase was used to obtain initial isotherms required to begin the transient phase that used climate data.

For symmetry, the steady-state analysis assumed zero heat flux ($q = 0$) along the leftmost (centreline) boundary. The mean temperature from the first day of the climate data was applied along the ground surface. Two different constant temperature boundaries were applied along the bottom boundary. These boundaries were chosen from thermistor data from transmission towers near Gillam. There was considerable variation in the data, but a values of -1°C and +1°C were chosen. Zero heat flux was applied on the rightmost boundary of the model.

The transient analysis used the same boundary conditions for the left, bottom and right boundaries as the steady-state analysis. The influence of the top (surface) boundary was explored using climate data as discussed in following paragraphs.

Climate Boundary:

Climate data were obtained from the Gillam Airport weather monitoring station on Environment Canada's (2008) website. The data correspond to 21 years of data between 01 April 1987 and 31 March 2008. The data were compiled and re-formatted for input into TEMP/W in the same manner described in Section 4.2.3. The latitude of the monitoring station, 56.2° N, was set in the model. The distribution pattern of the climate over the day was also chosen as a Constant Averaged distribution. Due to the use of climate data, the model time steps were fixed at 1-day increments. A sensitivity analysis on the time steps was not performed. Given the duration of the climate data used, it was decided not to make use of predicted data from the CCCma data.

Parametric Studies:

Parametric studies were used to better understand the effects of the modeling parameters on the foundations of the towers. These studies focused on altering the design of the model to observe the effect of various changes in the design of the foundation. Construction details on a per tower basis were not available.

As mentioned earlier, two 'base' numerical models were designed based on the minimum (0.0 m) and maximum (3.7 m) depths at which footings were installed (Figures 4.24a and 4.24b). The 'base' models were then modified to examine two radii of insulation (1.25 and 2.0 m).

Models were also analyzed with and without the hollow structural steel sections (Figure 4.22) to investigate direct heat transfer along the length of the steel section and its impact of the steel tower on the foundation. The steel sections were not included in the

'base' models because data regarding the impact of direct sunlight, climatic effects, and heat dissipation on the steel have not been quantified.

The temperature boundary condition at the bottom of the models was set at two values, -1.0°C and 1.0°C. The choice of two different temperatures at this boundary reflected uncertainty in the measured temperatures at several transmission towers. Sporadic, inconsistent, and incomplete data were provided by Manitoba Hydro for only four towers believed to be closer to Gillam than Churchill. Selected dates of the measured data for Towers 3 and 45, the more complete data sets, are shown in Figures 4.25 and 4.26. These figures show temperatures for radial distances of 0.6 m (2.0 ft) and 6.0 m (20.0 ft) from the transmission towers. The data show inconsistent temperatures below about 3.0 m depth, suggesting that not all of the thermocouples were working properly.

4.3.4 Modeling Results

Shallow Foundation:

Modeling of the shallow foundation (depth 0.0 m) suggests annual thawing of frozen soil that may potentially have an impact on the performance of the superstructure. Figure 4.27 shows temperature versus depth results from a model for a shallow foundation with short insulation and a base temperature of -1.0°C. This figure shows the shallow foundation can experience several freeze-thaw cycles in soil beneath the footing within a year. This may affect performance of the superstructure by influencing the present water (influx and drainage), frost heave, and resulting settlement.

Lengthening the insulation provides a longer path for heat directly above the foundation to travel beneath the footing. Given the high thermal conductivities of the

sand base and surrounding clayey silt, there is a marginal difference between the isotherms for either model (not shown). The difference is more noticeable immediately below the insulation, but at greater depths, temperatures coincide with those shown in Figure 4.27.

The addition of steel was expected to affect lateral heat conduction. Given the shallow depth of the models, the effect of the steel was not observed outside of the immediate vicinity of the footing. Kurz et al. (2009) found the isotherms beneath the footings for each of the two lengths of insulation were nearly identical to those for the models with and without steel.

Use of either a -1.0°C or +1.0°C boundary condition at the base of the model also produced only a marginal difference in isotherms. Temperatures above a depth of approximately 5.0 m differ less than 1.0°C. Below 5.0 m there is greater influence from the base boundary and temperatures approach either respective boundary temperature. The major difference between the models is an ability examine the maximum depth of thawing versus the maximum depth of freezing. The maximum observed depth of thawing (active zone) is around 9.0 - 9.5 m, whereas the maximum observed depth of freezing is around 4.5 - 5.0 m.

Deep Foundation:

The models of the deep foundation (depth 3.7 m) suggest thawing of annual frost may potentially have no adverse effects on the performance of the superstructure. Figure 4.28a shows temperature versus depth for a deep foundation model with short insulation and a base boundary temperature of -1.0°C. Lengthening the insulation gave no

discernible difference between the isotherms for either model (not shown). This is, in part, due to the footing remaining frozen during the initial period of study.

The addition of steel allows transfer of heat directly to and from the foundation of the tower. Figure 4.28b illustrates the effect of steel on the foundation at a radial distance of 0.6 m. The results show that the insulation length of 1.25 m was sufficient to resist the applied heat flow and prevents thawing beneath the footing. With the onset of winter, the steel acts as a heat sink, allowing the heat in the ground to dissipate faster. This permits the ground adjacent to the tower to freeze more quickly. An increase in the insulation length for this model helps maintain the frozen ground beneath the footing during the initial period of study (not shown, but discussed in Kurz et al. 2009). Length of insulation was found to have a negligible effect on the deep foundations in models that did not include steel.

The effect of steel was further explored by analyzing the temperatures directly above the footing and below the base of the footing. Figure 4.29a shows the variations of temperature over 15 years for a model with short insulation and no steel at a radial distance of 0.6 m. Figure 4.29b shows the same points in a model with steel. The climate data do not indicate a warming trend, but even without steel in the model (Figure 4.29a), temperatures exceed 0.0°C above the footing and begin to exceed 0.0°C below the footing. This trend is more noticeable for the model with steel (Figure 4.29b).

Use of either a -1.0°C or +1.0°C boundary condition at the base of the model had a greater impact on the isotherms than with the shallow foundation. For the model using a -1.0°C boundary and no steel, the active zone reached a depth of approximately 2.5 m across the model. With steel, the active zone reached a depth of 3.4 m near the footing

and 2.5 m at a radial distance of approximately 4.0 m. For the model using a +1.0°C boundary, frost penetration was approximately 1.5 m.

4.3.5 Commentary

The purpose of this numerical modeling was to gain insight into the performance of the foundations for the transmission towers. Records from Manitoba Hydro indicate that many of these towers are tilting (leaning) in non-specific directions. The tilts range from 0.0° to upwards of 9.0° in the records provided. When the towers start to lean there is disproportionate strain on some guy wires. Depending on wind direction and velocity the lines begin to sway. This action results in a rhythmic tug in the support structure. Dampers on the lines help to keep this under control but nonetheless it still can occur. If the foundation either settles or heaves, the guy wires may become over-stressed and fail, causing the towers to collapse. Temperature data were collected at select towers. There is no record, however, of deformation data or pore water pressures within the soil. This meant that a thermal model could be developed but the model can only provide a qualitative assessment of the stability of the towers.

This program of numerical modeling adequately reproduced measured seasonal ground temperatures of tower foundations for the Radisson-Churchill transmission line. High variability and inconsistencies in the measured data meant that a direct comparison of temperatures at specific dates was not possible. The thermal properties in all models were also assumed to be identical despite the varying terrain along the length of the transmission line.

As might be expected, the length of the insulation (in plan) had less impact for the

deep foundation (3.7 m) as compared to the shallow foundation (0.0 m). However, the shallow foundation will inevitably thaw even with reasonable dimensions for the insulation layer. Given warming climate trends and the results shown in Figure 4.29, it appears that longer insulation would help attenuate increasing ground temperatures at depth. This means that future foundation designs may need to be altered to account not only for the areal dimensions of the insulation as a function of the foundation depth, but also the warming climate.

The introduction of steel into the model had a marginal effect on the isotherms for the shallow foundation. For the deep foundation, however, the introduction of steel had a noticeable effect on isotherms above the footing (Figure 4.29). The impact of the steel on isotherms below the footing was only noticeable after approximately 10 years. This means a warming climate will amplify this effect and subsequently have an even greater impact beneath the footing. In addition, in the deep foundation, the steel causes radial thawing during warmer months and promotes ground freezing during colder months.

Overall, these parametric studies indicate key areas that relate to the stability of the transmission towers. The measured tilts cannot be quantified in these thermal models without additional field data. Qualitatively, the cycle of radial thawing and freezing caused by the steel may lead to instability of the tower that could lead to tilting. Further instability, in more recent years, may be caused by the 0.0°C-isotherm attaining a depth below the footing (that is, thawing below the footing). The shallow foundations are likely more susceptible to frost heave given that they experience annual freezing and thawing.

4.3.6 Concluding Comments

The thermal numerical modeling of foundations for transmission towers can provide qualitative information about long-term serviceability and maintenance schedules for northern structures in areas of continuous or discontinuous permafrost. As stated for Section 4.2.6, studying temperature distributions is valuable but not sufficient by itself. Even without the use of predicted climate (or temperature) data with a warming trend, it can be seen that previously-stable northern structures will begin to experience deformations that may lead to problems. This places more emphasis on the need to establish a relationship between temperature change and long-term stress-deformation behaviour. This is examined further in Chapter 5.

Table 4.1: Thermal Material Properties (PR391) (after Batenipour 2012)

Material	Vol. Heat Capacity ($kJ/m^3/°C$)		Thermal Conductivity ($kJ/d/m/°C$)		In-situ VWC (m^3/m^3)
	c_{vu}	c_{vf}	λ_u	λ_f	θ
Gravel[1]	2400	2300	216	346	0.40
Clayey Silt w/ Organics	3270	2510	126	205	0.45
Silty Clay	3220	2230	78	104	0.55

[1]Values based on empirical relationships

Table 4.2: Revised Thermal Material Properties (PR391)

Material	Vol. Heat Capacity ($kJ/m^3/°C$)		Thermal Conductivity ($kJ/d/m/°C$)		In-situ VWC (m^3/m^3)	Water Content (%)	Dry Density (Mg/m^3)
	c_{vu}	c_{vf}	λ_u	λ_f	Θ	w_n	γ_d
Gravel[1]	2430	1950	250	346	0.24	12	2.00
Clayey Silt w/ Organics	2850	2050	123	207	0.41	25	1.62
Silty Clay	2760	1960	117	173	0.41	27	1.50

[1]Values based on empirical relationships

Table 4.3: n-Factors

Material	Thawing, n_t	Freezing, n_f
Gravel	2.00	0.90
Trees cleared, peat soil	0.73	0.25

Table 4.4: Revised Thermal Material Properties (MB Hydro)

Material	Vol. Heat Capacity ($kJ/m^3/°C$)		Thermal Conductivity ($kJ/d/m/°C$)		In-situ VWC (m^3/m^3)	Water Content (%)	Dry Density (Mg/m^3)
	c_{vu}	c_{vf}	λ_u	λ_f	Θ	w_n	γ_d
Peat	2760	1630	32	59	0.570	257	0.22
Clayey Silt	2125	1710	144	151	0.210	12	1.75
Sand	1980	1630	173	194	0.180	10	1.75
Insulation	38	38	3	3	0.004	--	--
Timber/Wood	1300	1300	13	13	0.020	--	--
Steel	3750	3750	3720	3720	0.000	--	--

Figure 4.1: Photograph of PR391 site (provided courtesy of Dr. H. Batenipour)

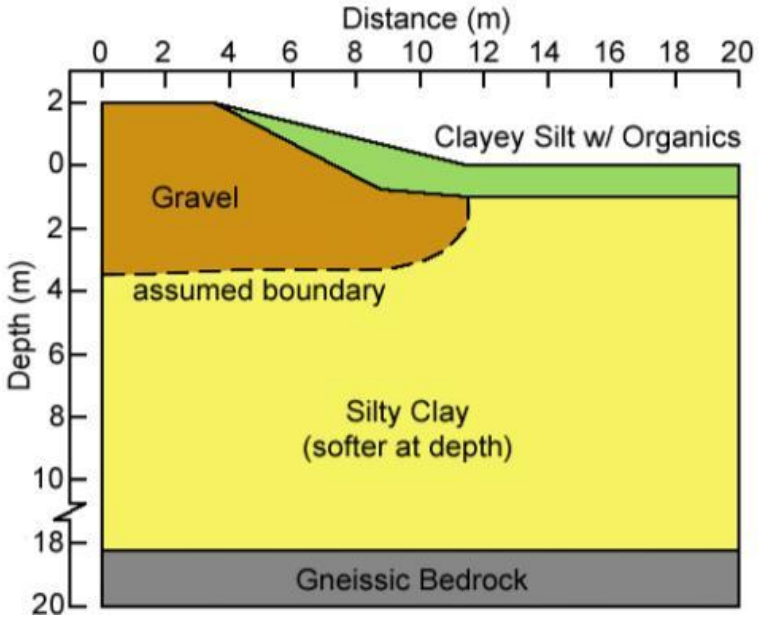

Figure 4.2: Soil stratigraphy of PR391, 'unstable' section

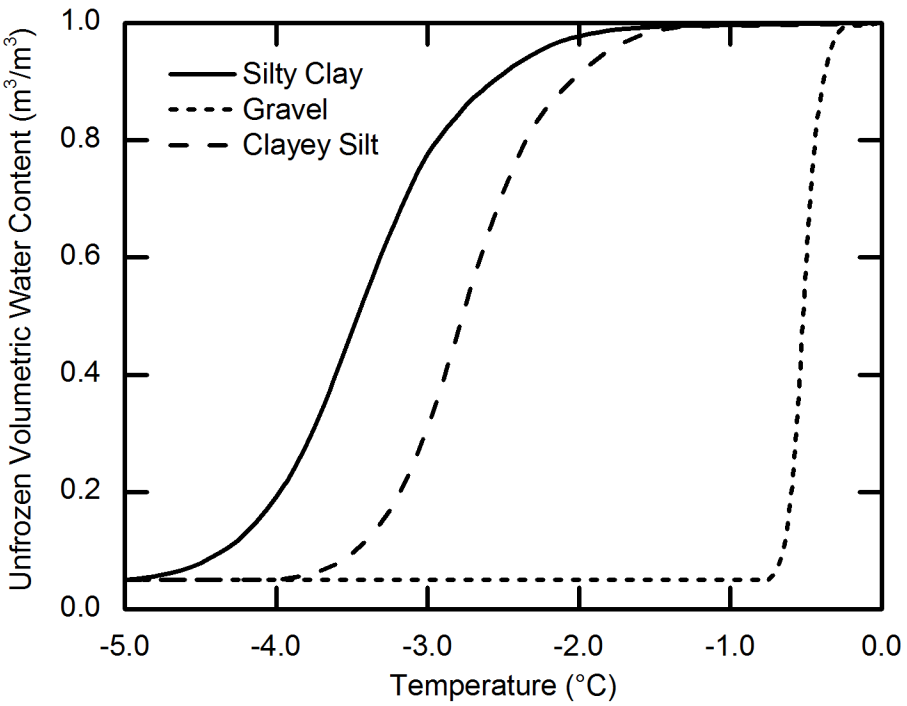

Figure 4.3: Unfrozen Water Content vs. Temperature (PR391)

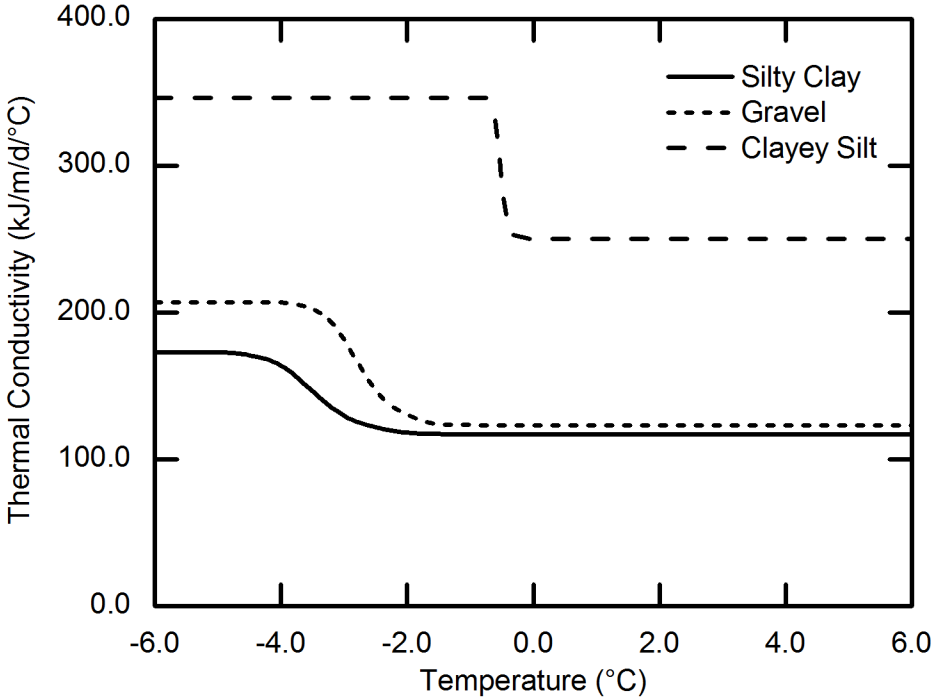

Figure 4.4: Thermal Conductivity vs. Temperature (PR391)

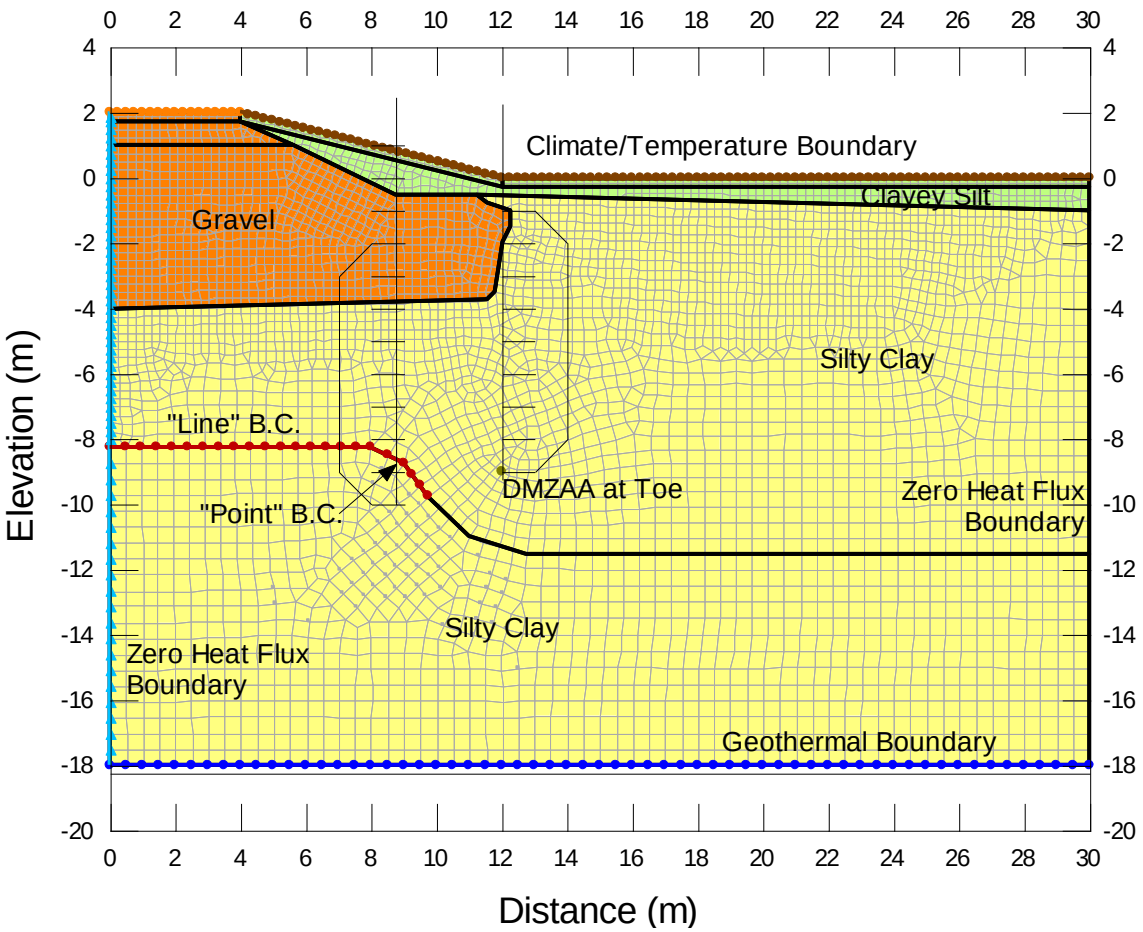

Figure 4.5: Model Cross Section for PR391 Unstable Section with materials, finite element mesh, boundary conditions, and thermistor string locations

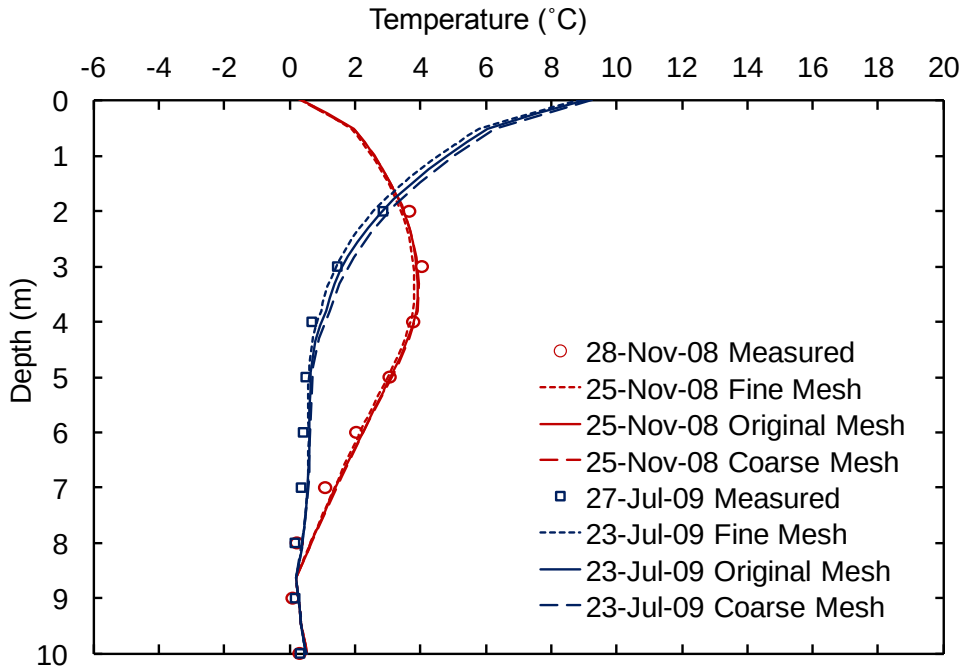

Figure 4.6: Sensitivity of PR391 2D model to selected mesh sizes (Fine: 0.15-0.30 m; Original: 0.25-0.50 m; Coarse: 0.50 m) at the mid-slope of the embankment

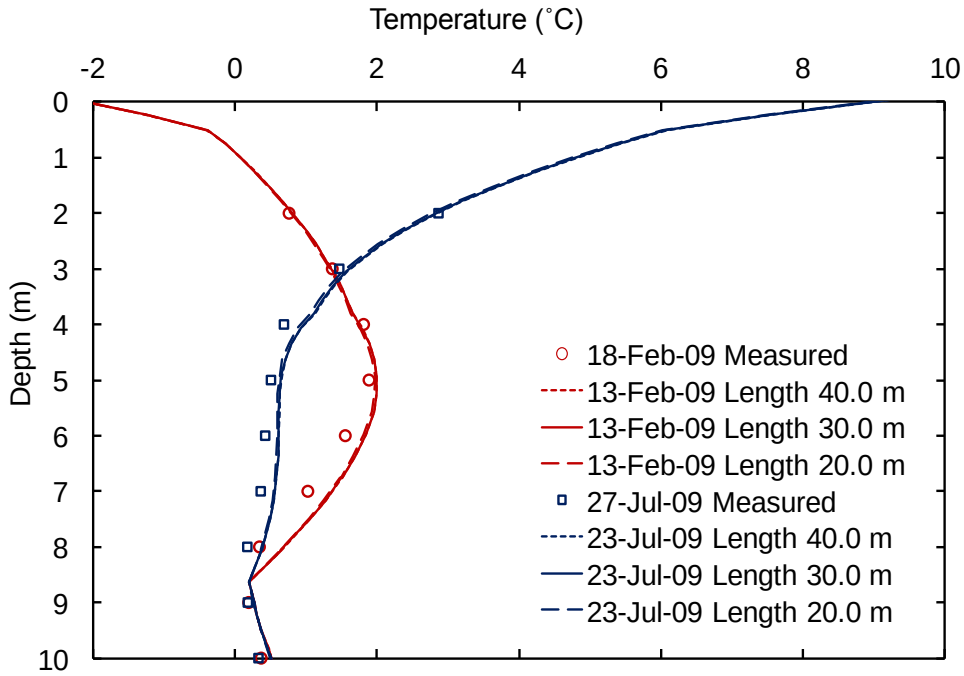

Figure 4.7: Sensitivity of PR391 2D model to location of the far (right hand) no heat flux boundary at the mid-slope of the embankment

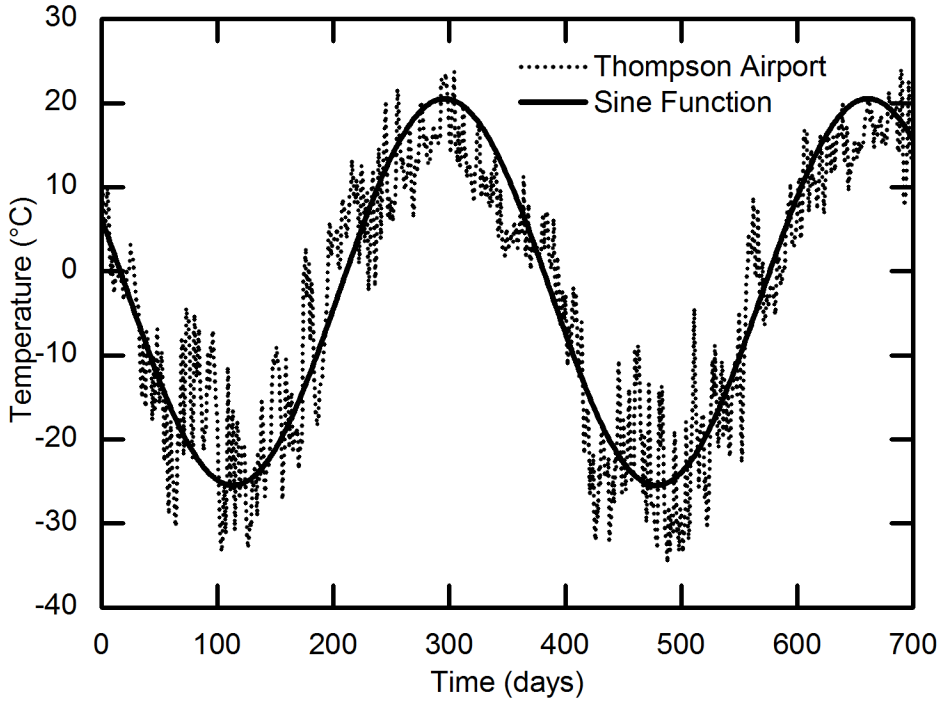

Figure 4.8: Approximately 2-year Mean Daily Temperature; Climate data and fitted sine function

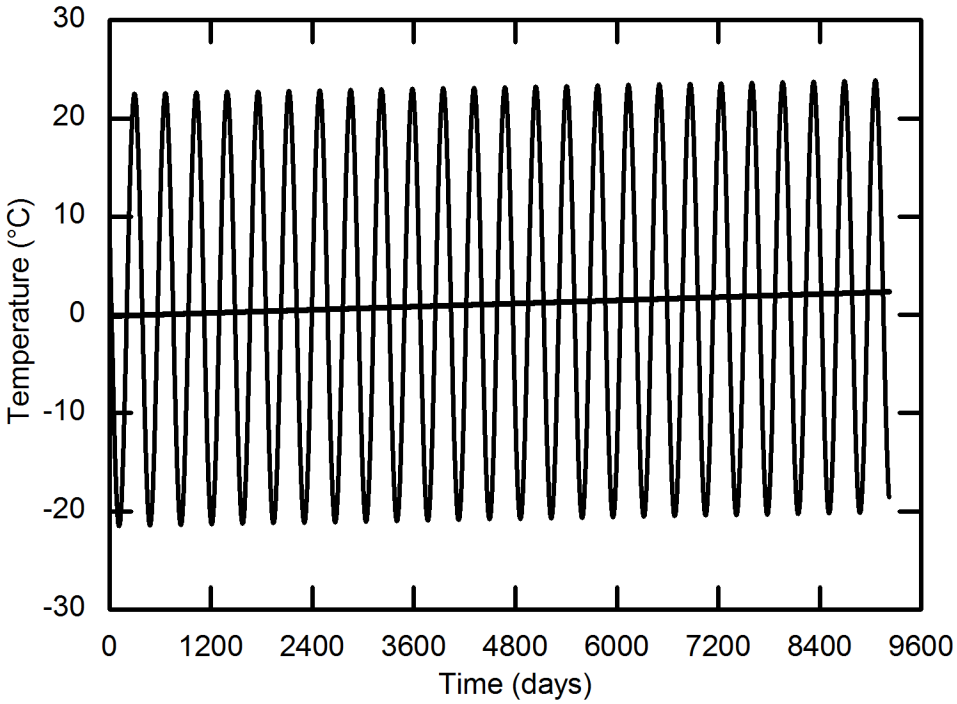

Figure 4.9: 25-year Mean Daily Temperature; sine function fitted to CCCma data and linear trendline

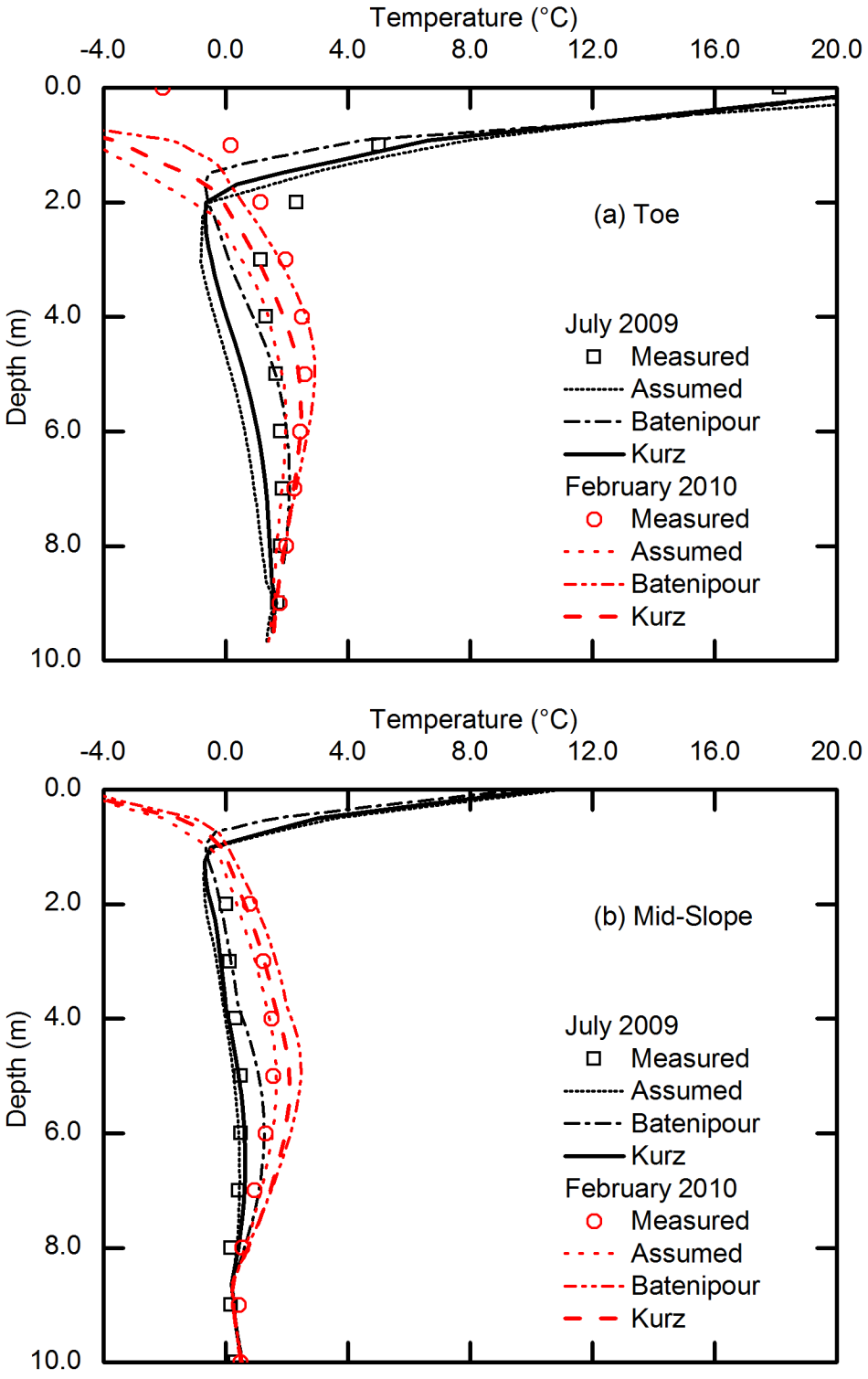

Figure 4.10: Comparison of thermistor, *'Assumed'*, *'Batenipour'* and *'Kurz'* below the (a) toe and (b) mid-slope of the embankment

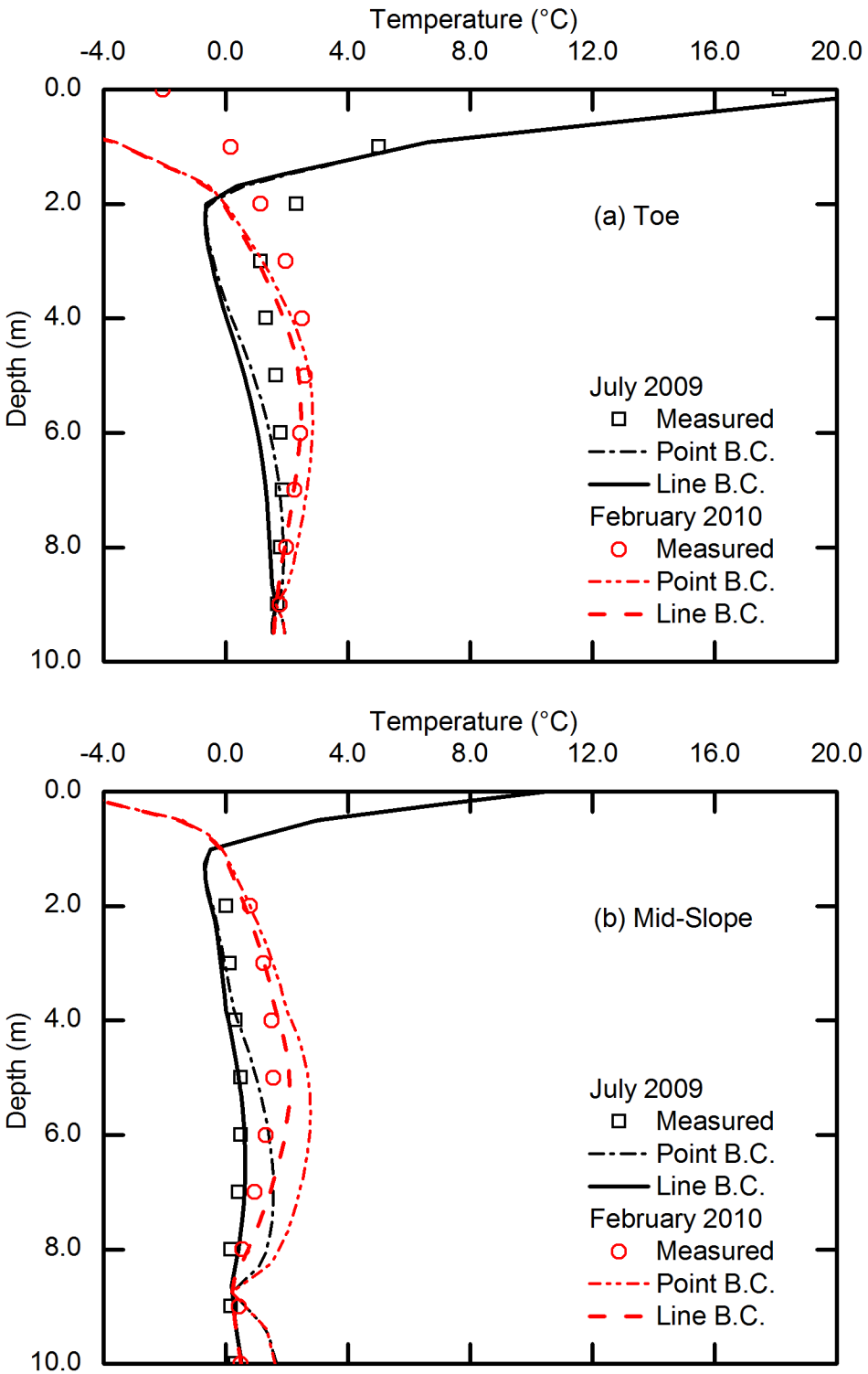

Figure 4.11: Comparison of thermistors to a mid-slope boundary condition of *'Point'* and *'Line'*. Temperatures below the (a) toe and (b) mid-slope of the embankment

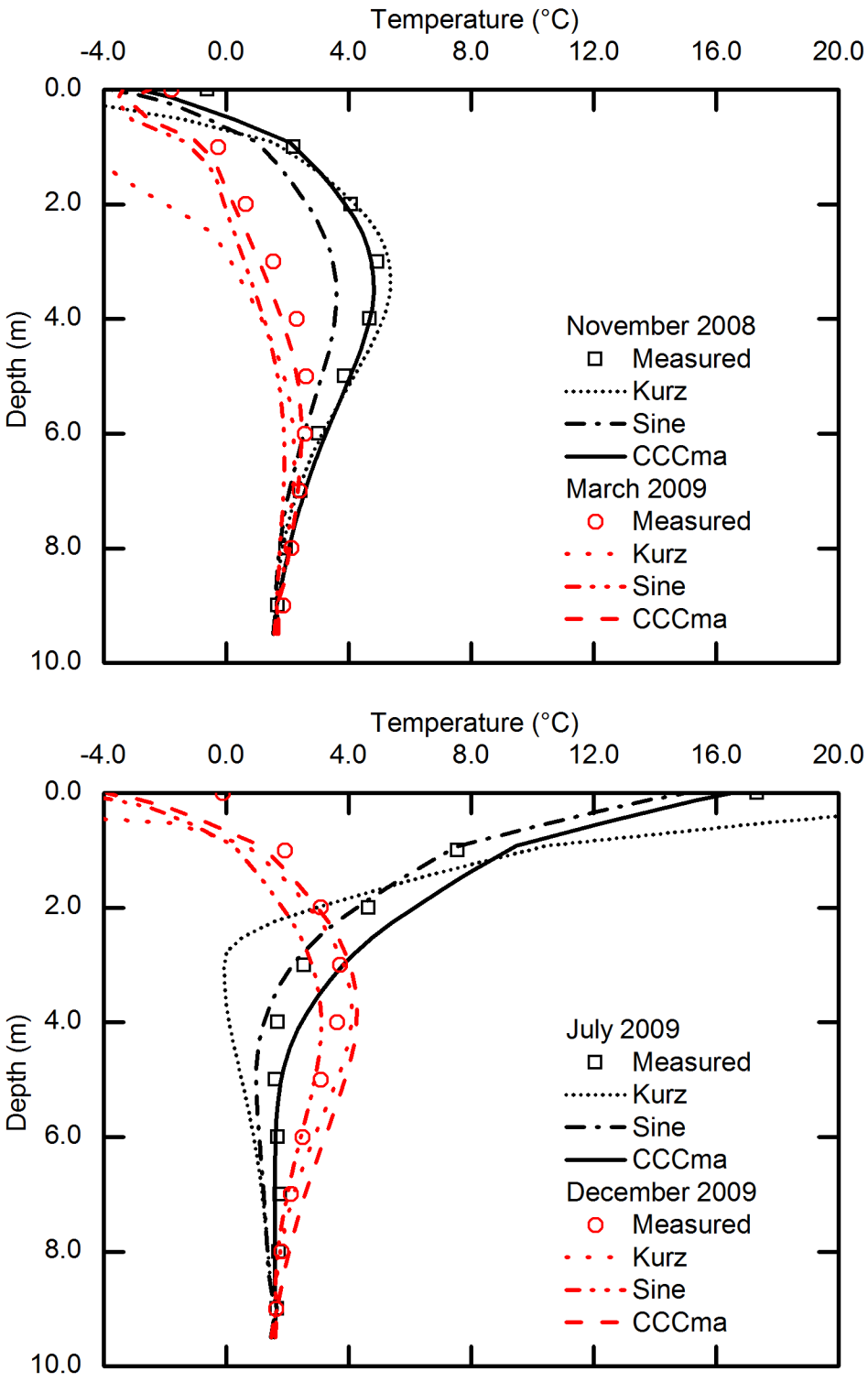

Figure 4.12: Comparison of thermistors to *'Kurz'*, *'Sine'*, and *'CCCma'* below the toe of the embankment (see also related data in Figure 4.13)

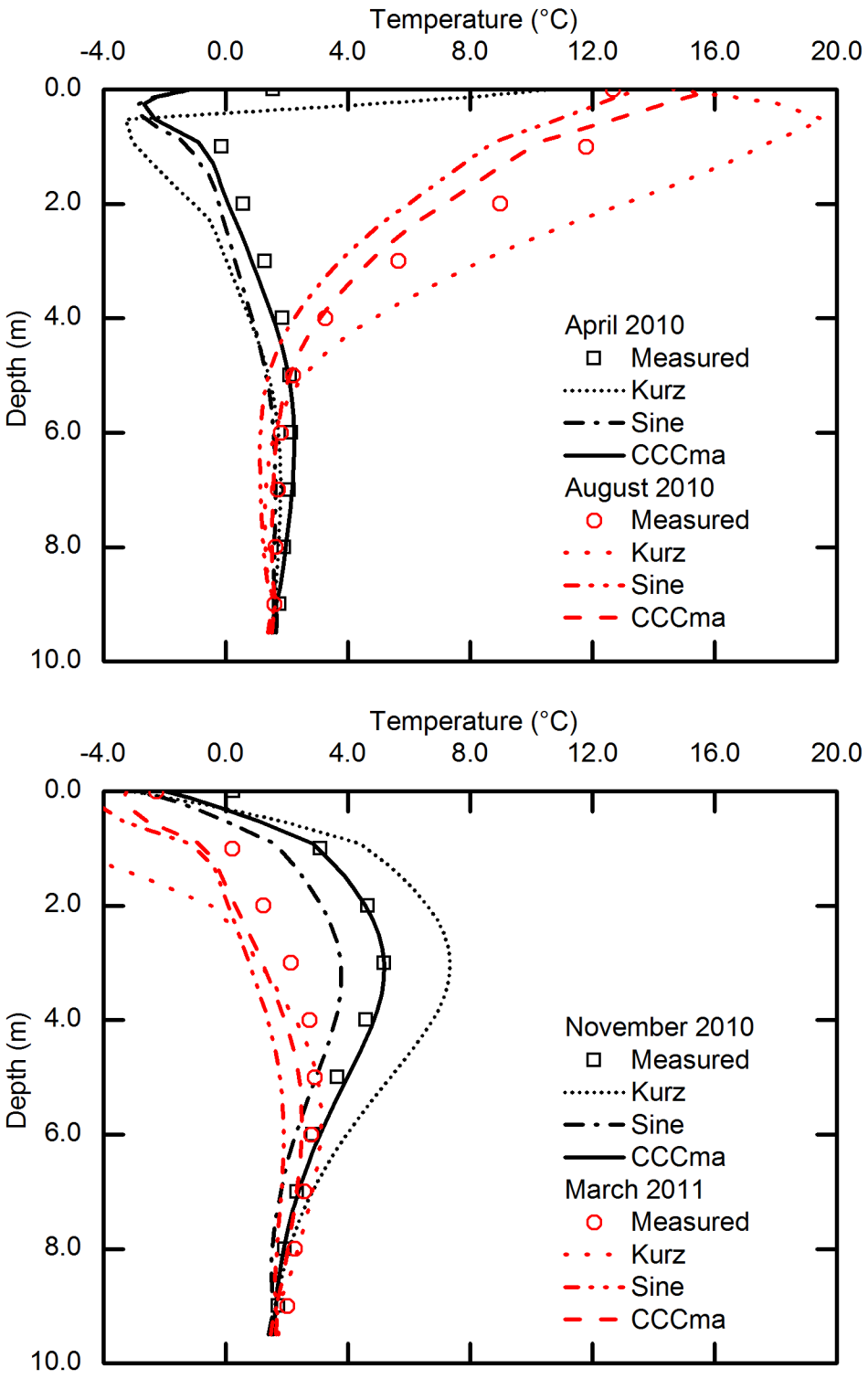

Figure 4.13: Comparison of thermistors to *'Kurz'*, *'Sine'*, and *'CCCma'* below the toe of the embankment (see also related data in Figure 4.12)

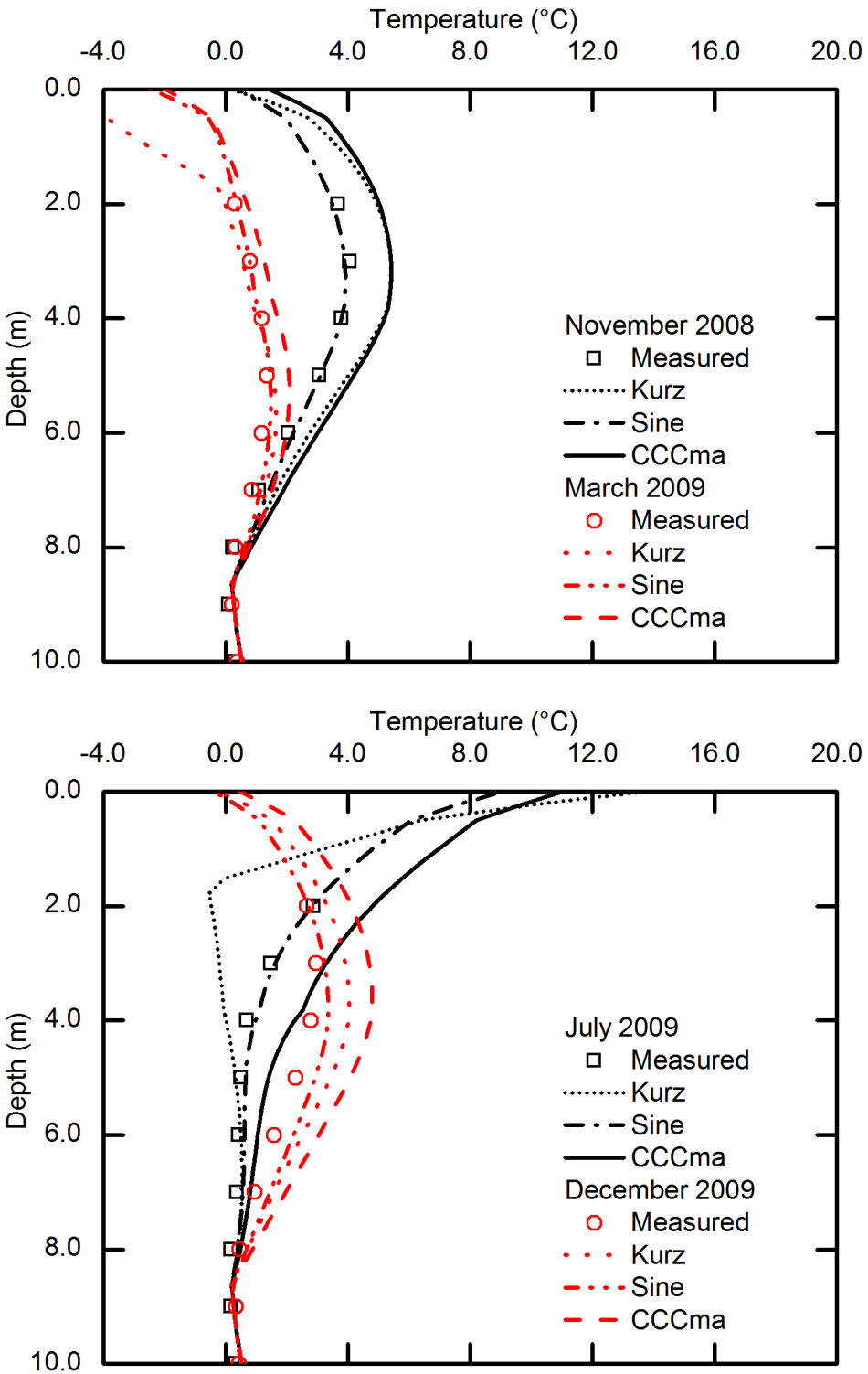

Figure 4.14: Comparison of thermistors to *'Kurz'*, *'Sine'*, and *'CCCma'* below the mid-slope of the embankment (see also related data in Figure 4.15)

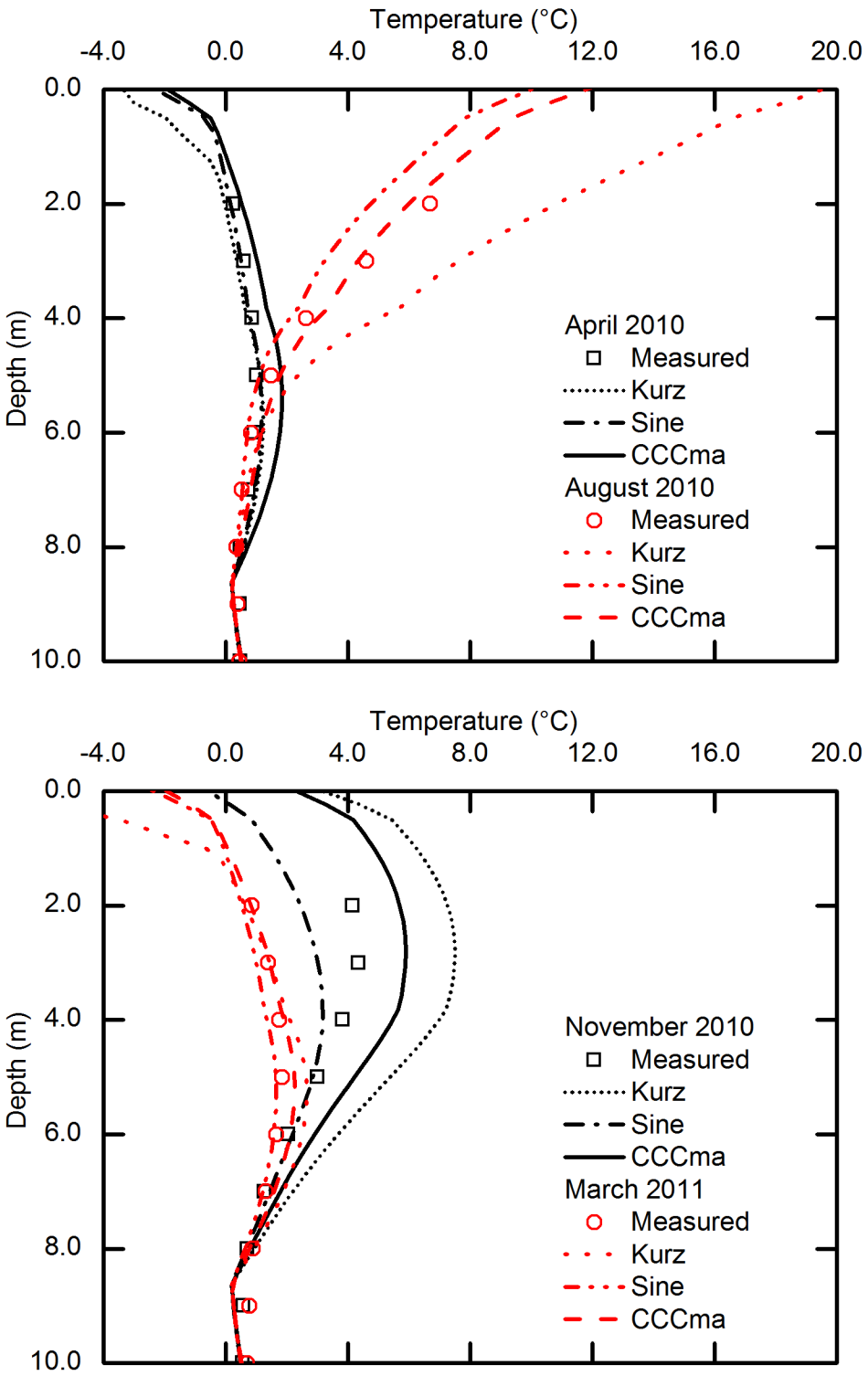

Figure 4.15: Comparison of thermistors to *'Kurz'*, *'Sine'*, and *'CCCma'* below the mid-slope of the embankment (see also related data in Figure 4.14)

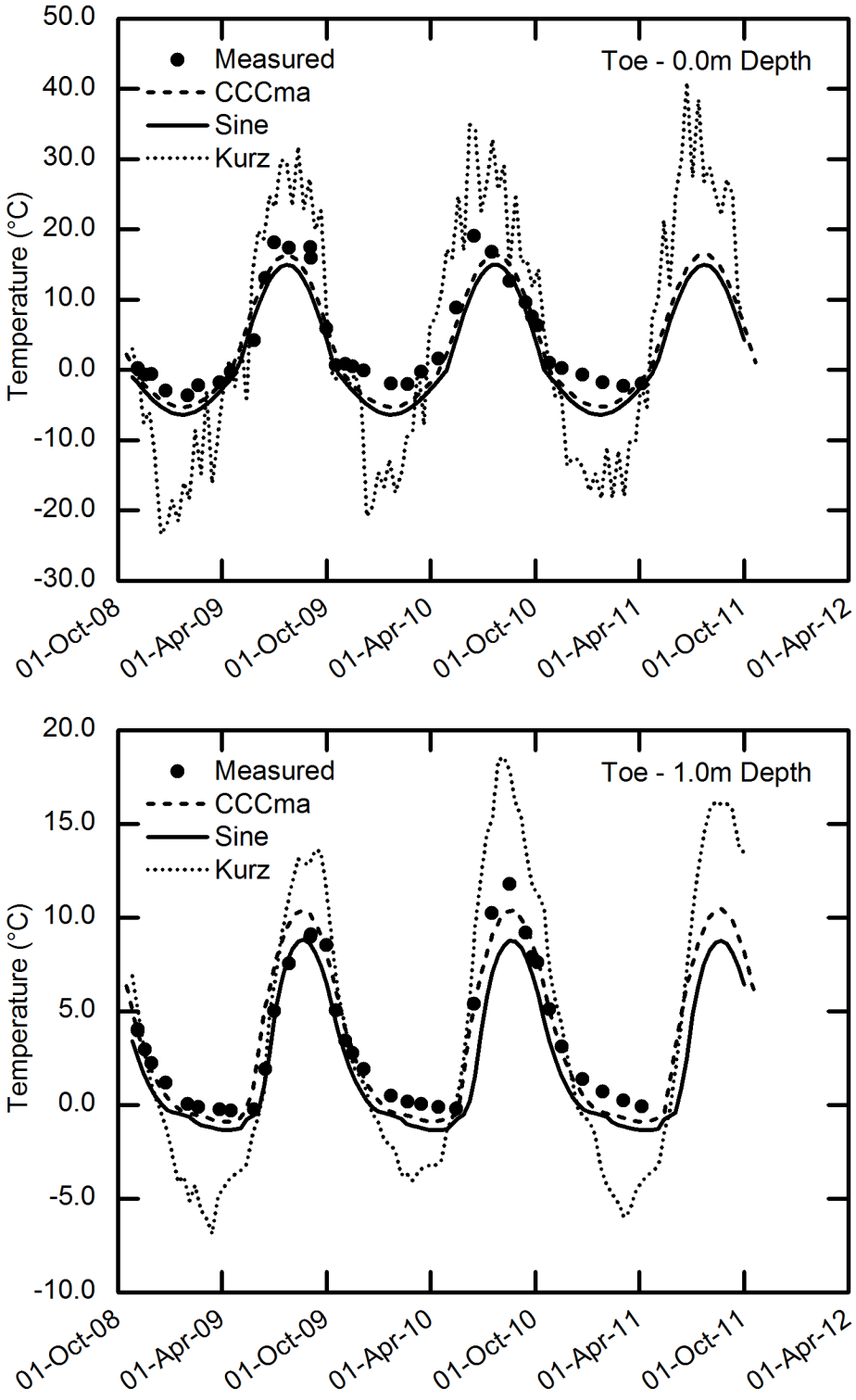

Figure 4.16: Temperature versus Time for (a) 0.0 m and (b) 1.0 m at the toe of the embankment (see also related data in Figure 4.17)

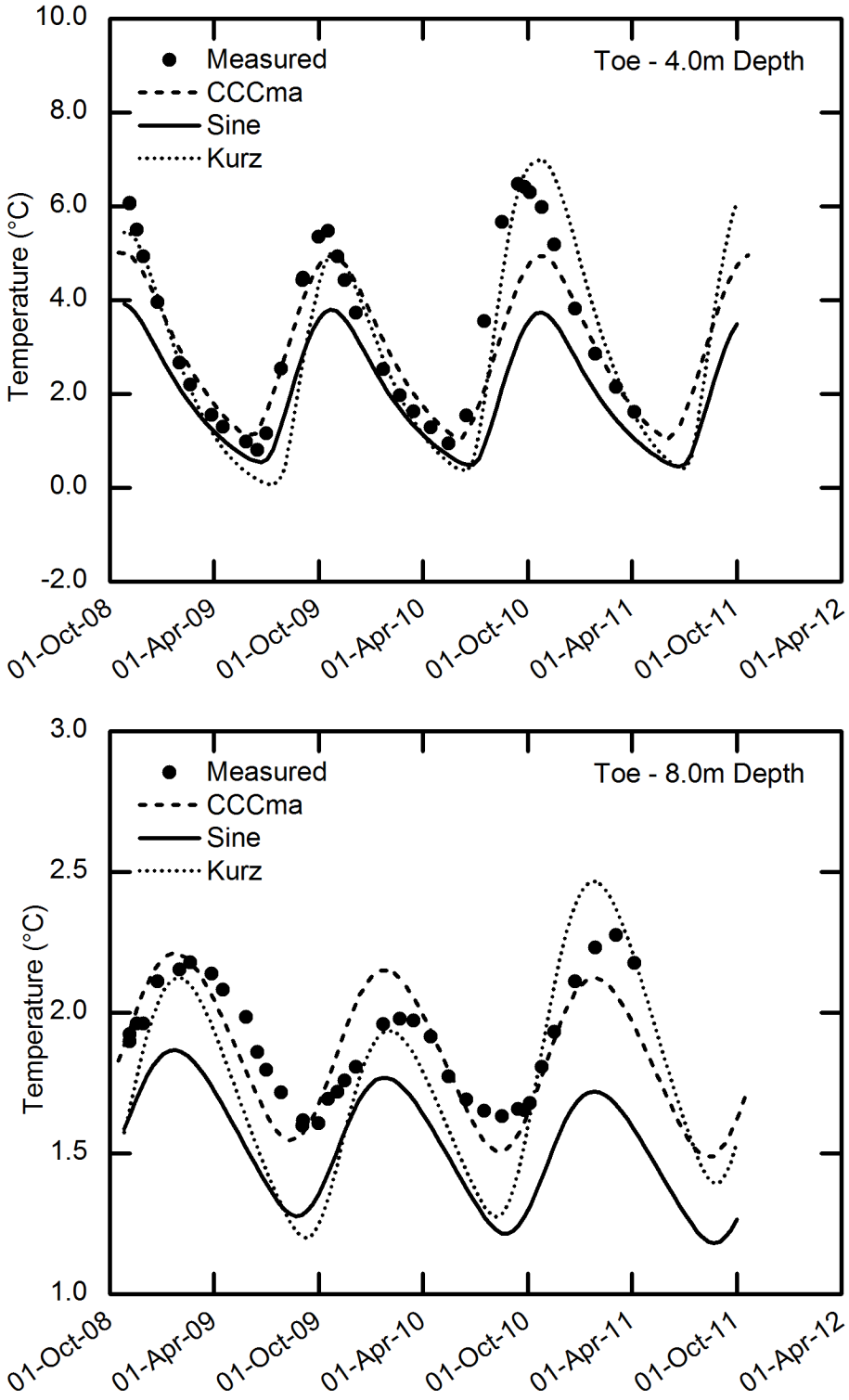

Figure 4.17: Temperature versus Time for (a) 4.0 m, and (b) 8.0 m at the toe of the embankment (see also related data in Figure 4.16)

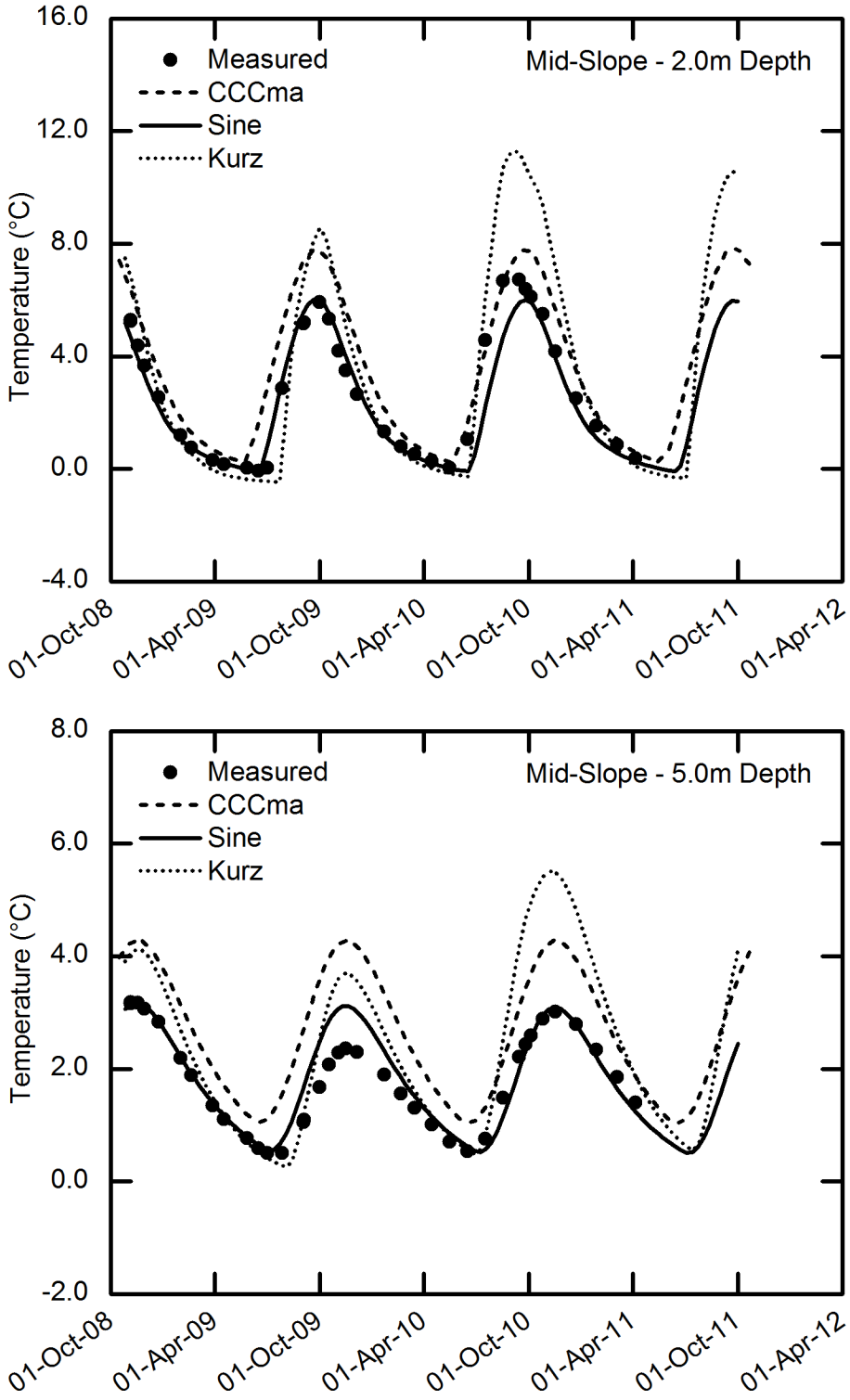

Figure 4.18: Temperature versus Time for (a) 2.0 m and (b) 5.0 m at the mid-slope of the embankment (see also related data in Figure 4.19)

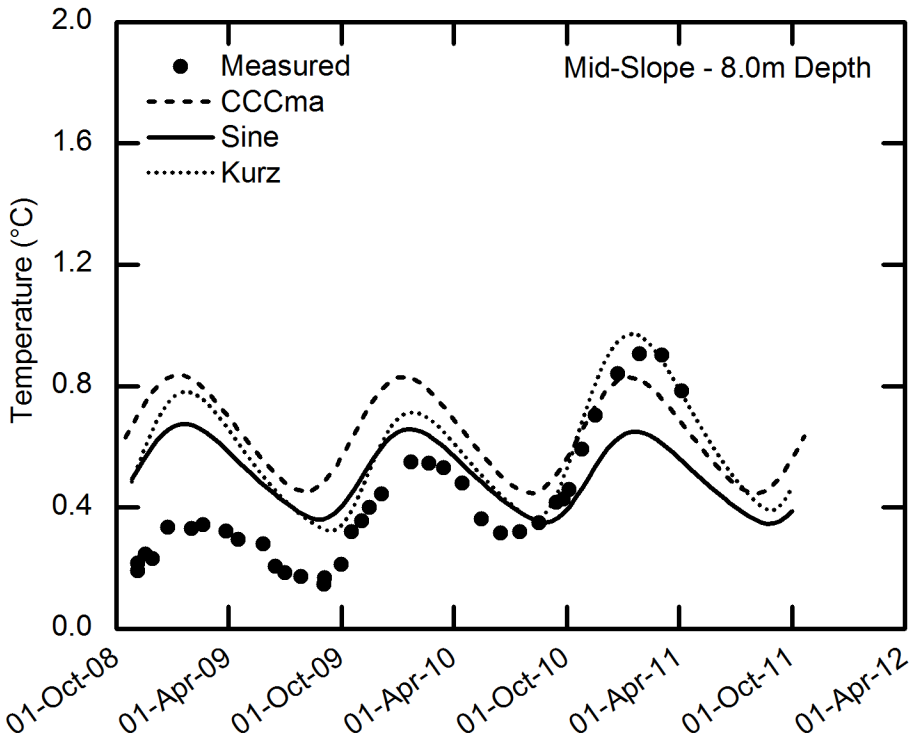

Figure 4.19: Temperature versus Time for (a) 8.0 m at the mid-slope of the embankment (see also related data in Figure 4.18)

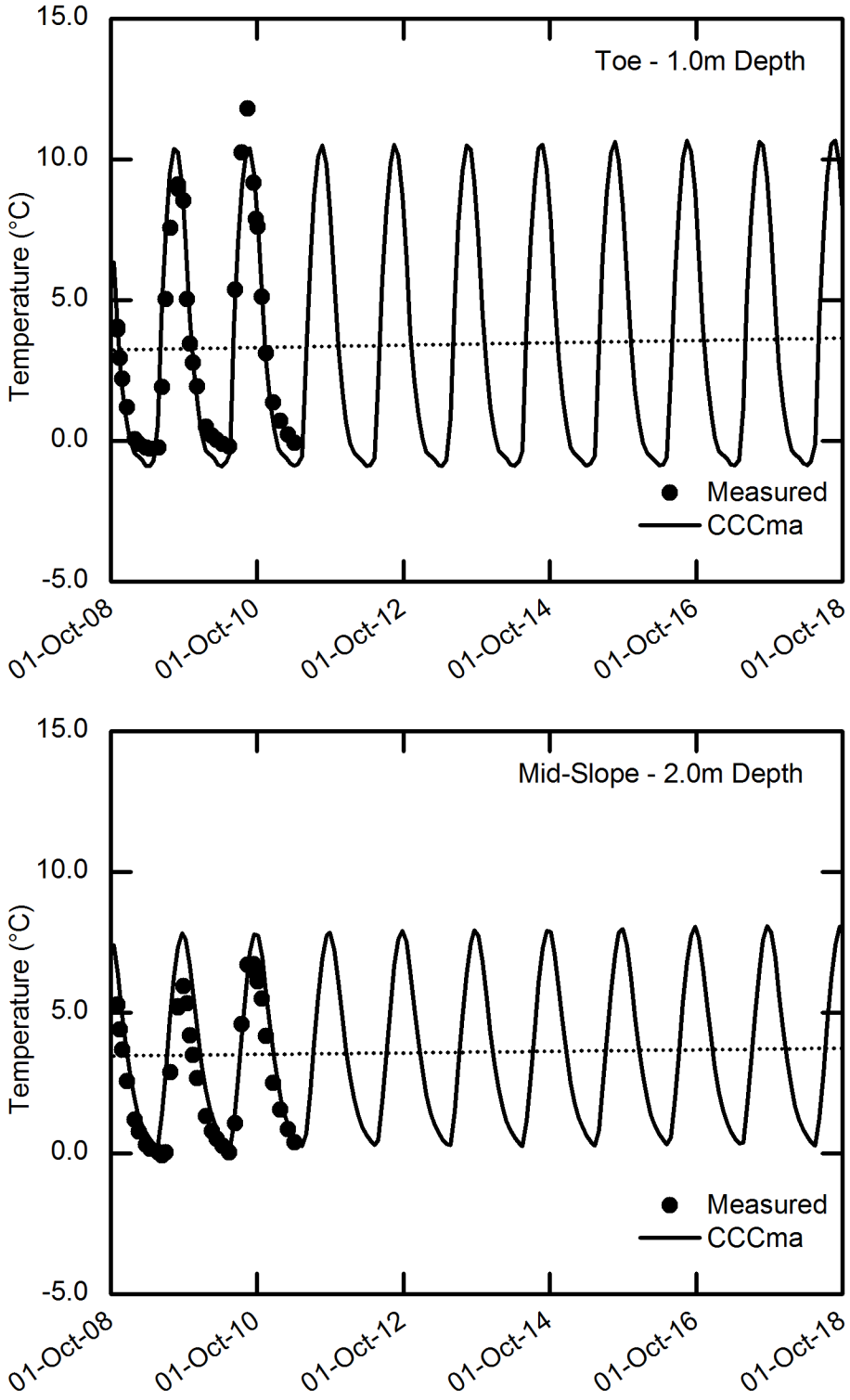

Figure 4.20. Temperature versus Time for 10 years; (a) 1.0 m below the toe of the embankment and (b) 2.0 m below the mid-slope of the embankment.

Figure 4.21: Photograph of a transmission tower in the 138 kV Radisson-Churchill transmission line (provided courtesy of Dr. Marolo Alfaro)

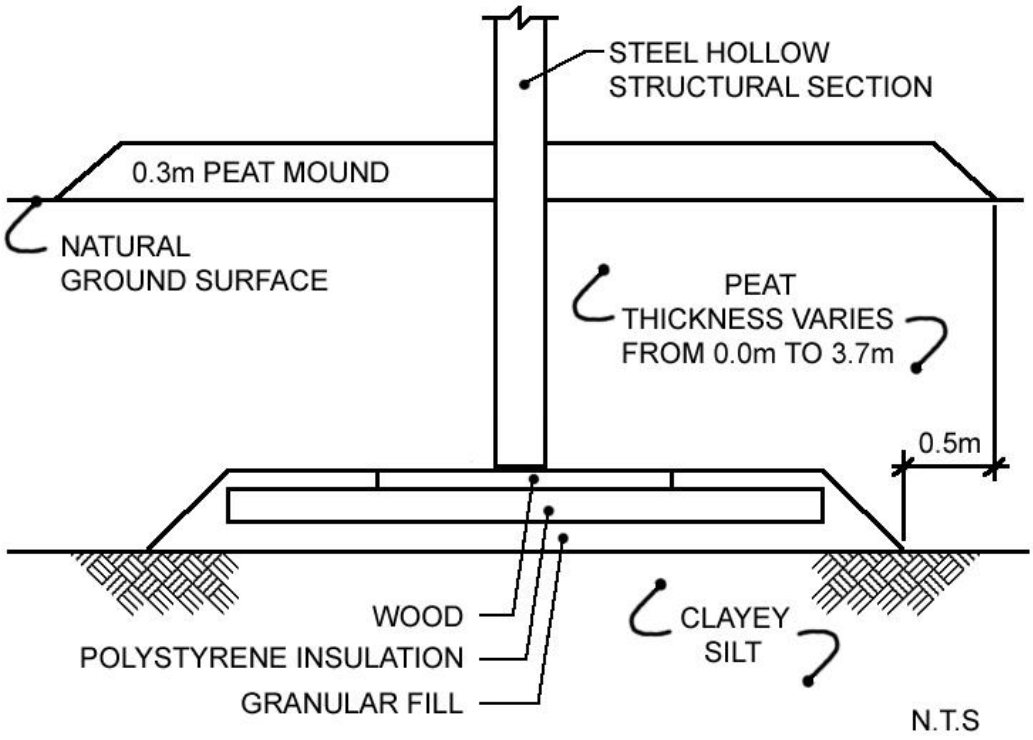

Figure 4.22: Typical foundation design

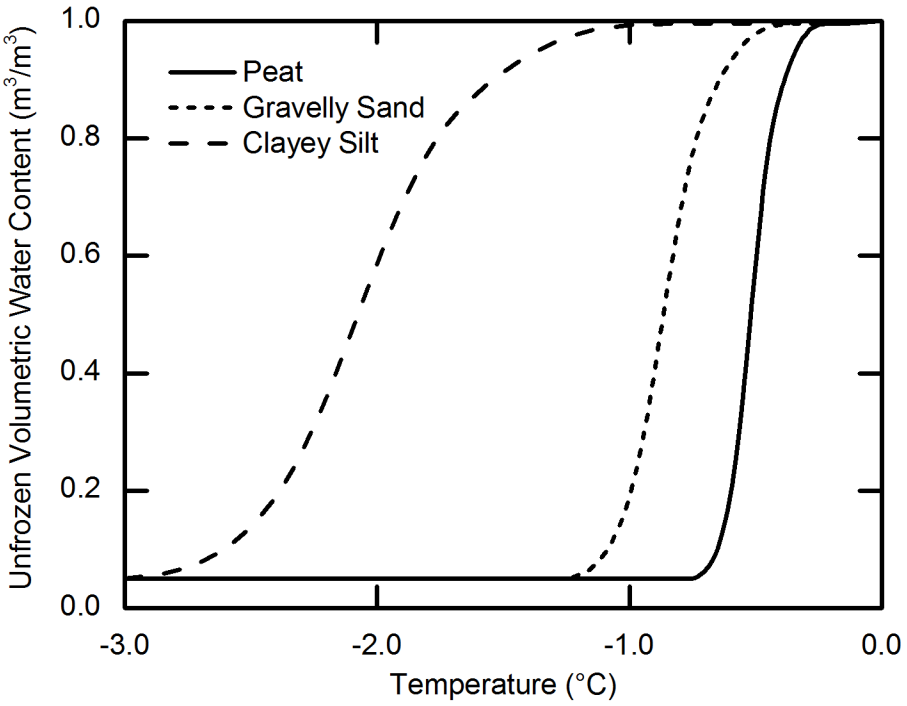

Figure 4.23: Unfrozen Water Content vs. Temperature (Hydro)

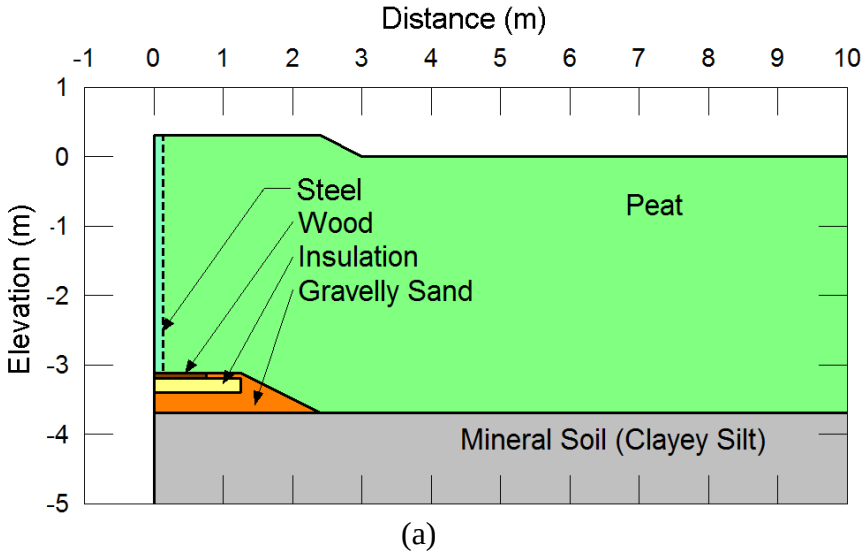

(a)

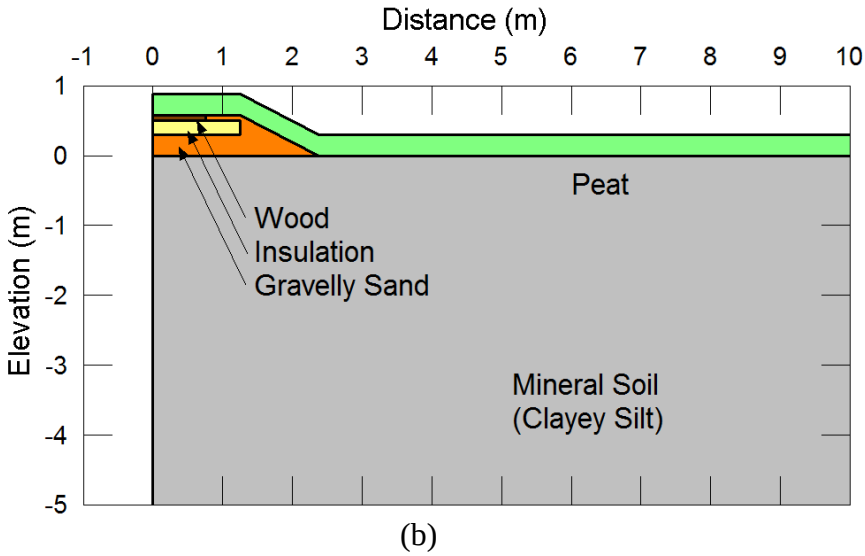

(b)

Figure 4.24: Model Cross Sections (truncated at 5 m depth, 10 m radius) for transmission tower (a) deep foundation (showing steel) and (b) shallow foundation (no steel)

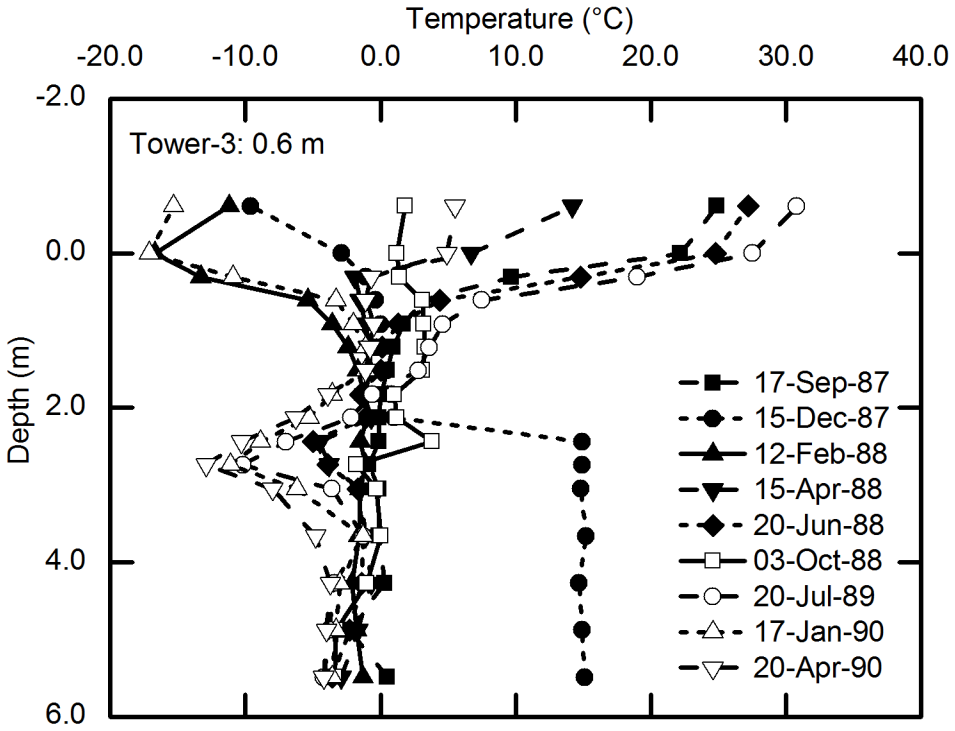

(a)

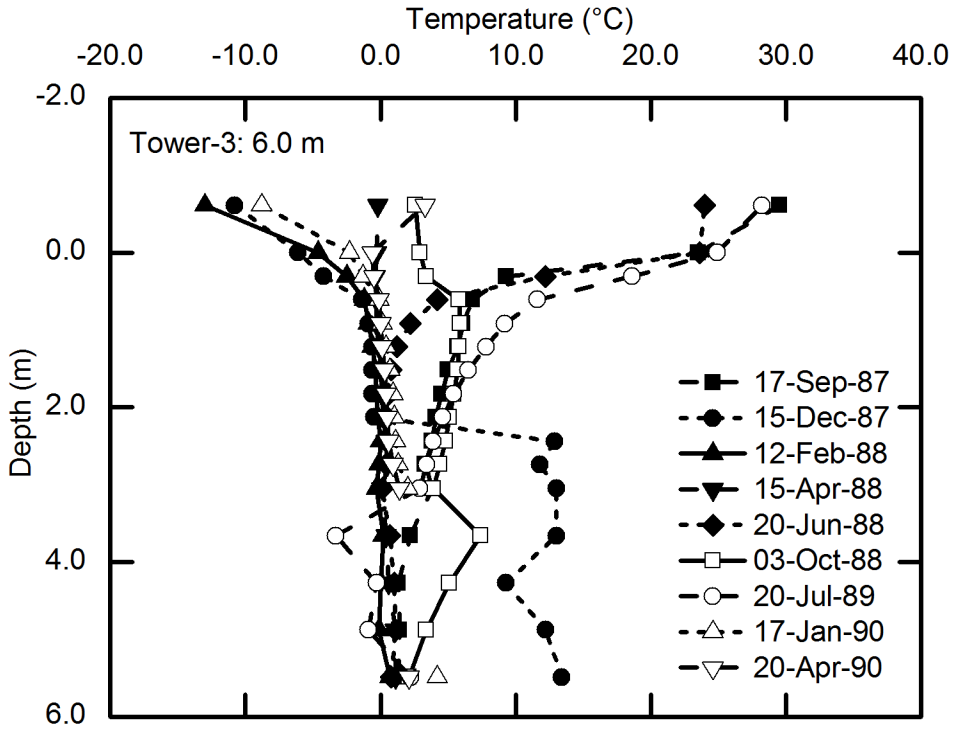

(b)

Figure 4.25: Measured Thermocouple data from Tower 3 at (a) 0.6 m (2.0 ft) and (b) 6.0 m (20.0 ft) from the tower

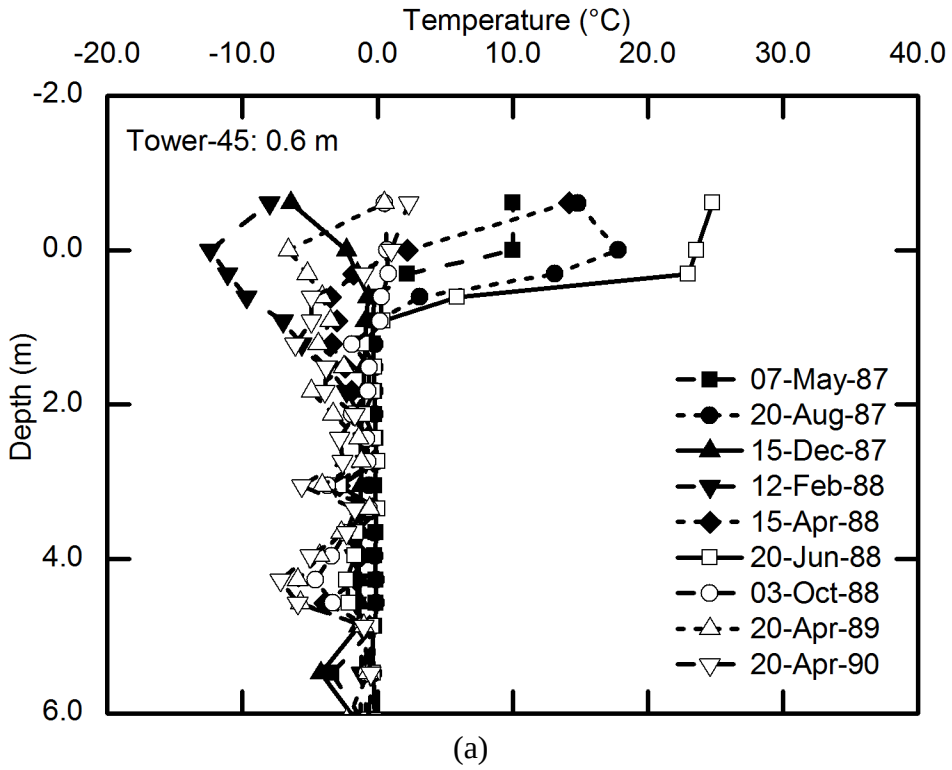

(a)

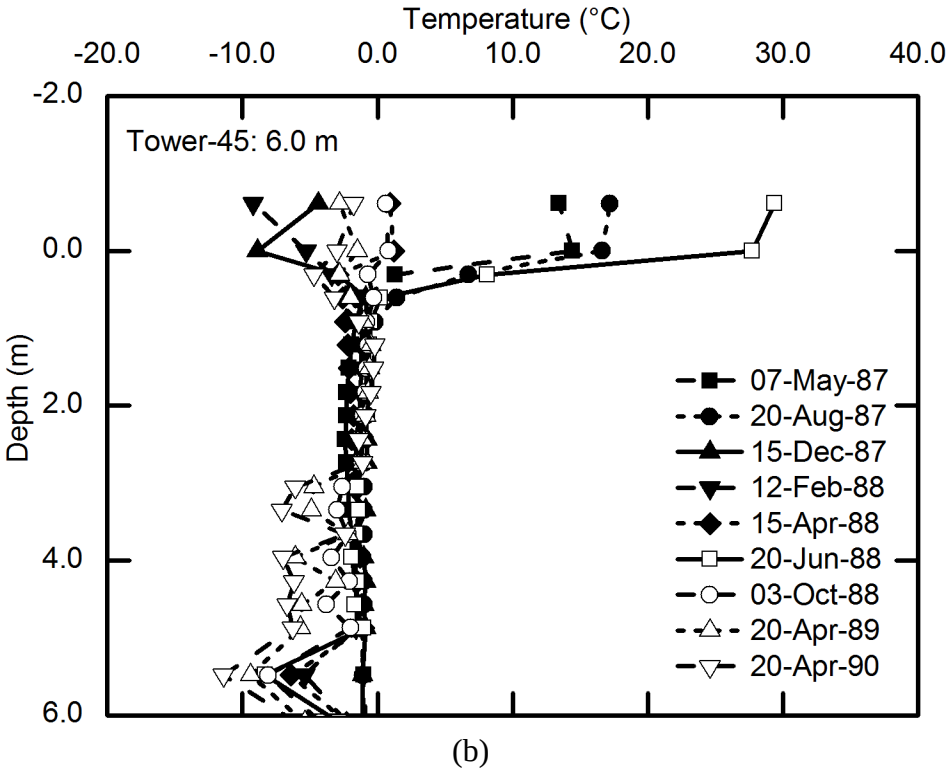

(b)

Figure 4.26. Measured Thermocouple data from Tower 45 at (a) 0.6 m (2.0 ft) and (b) 6.0 m (20.0 ft) from the tower

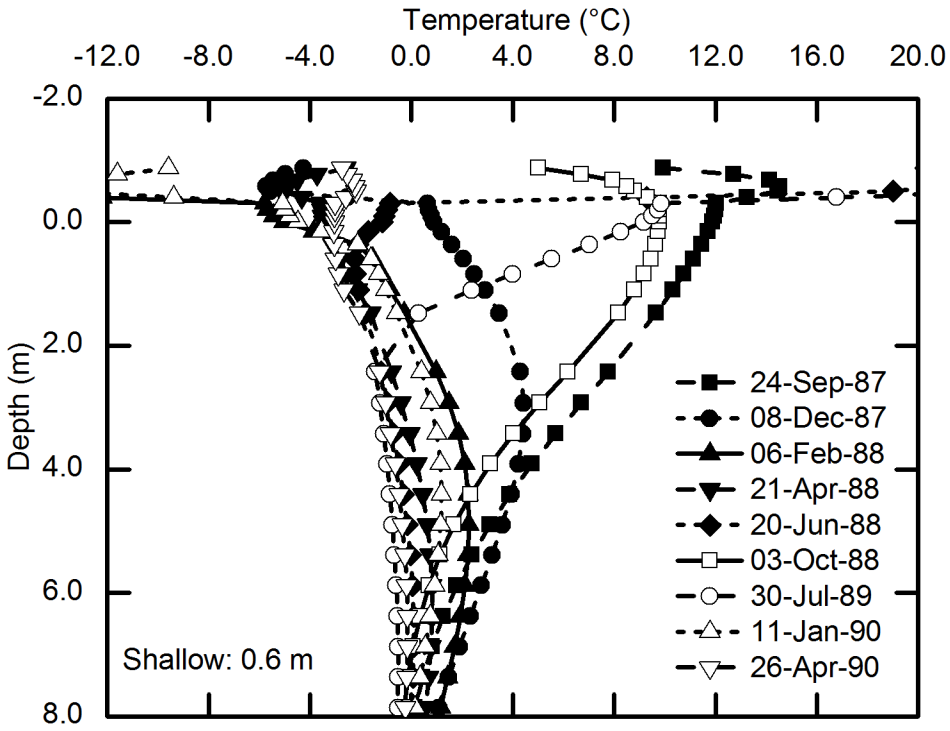

(a)

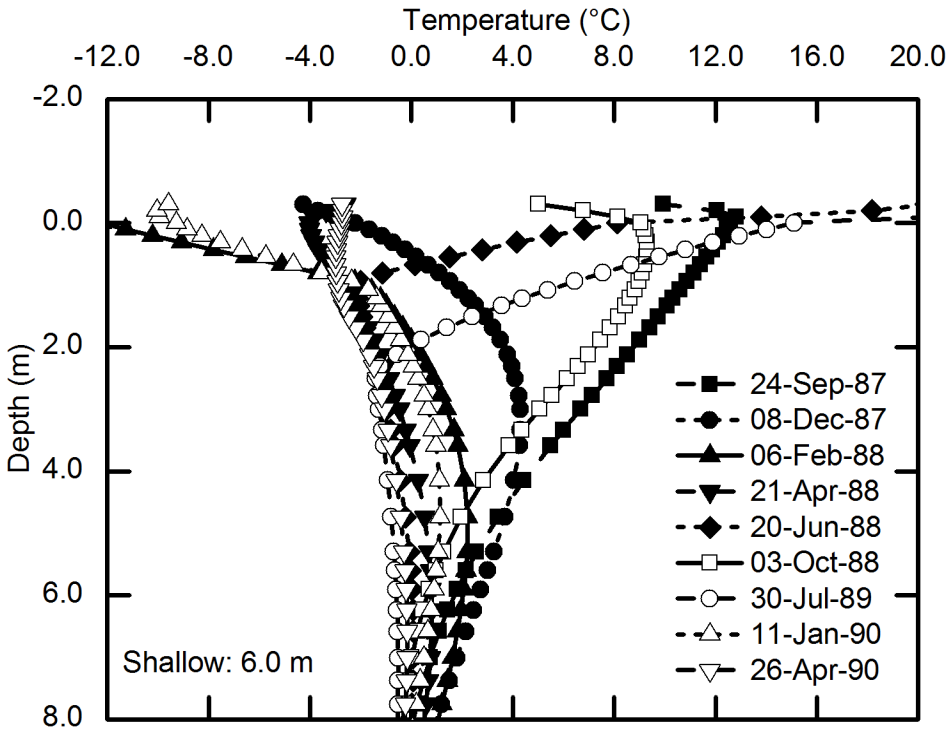

(b)

Figure 4.27: Modeled Temperature profile for the Shallow Foundation and short insulation at (a) 0.6 m (2.0 ft) and (b) 6.0 m (20.0 ft) from the tower

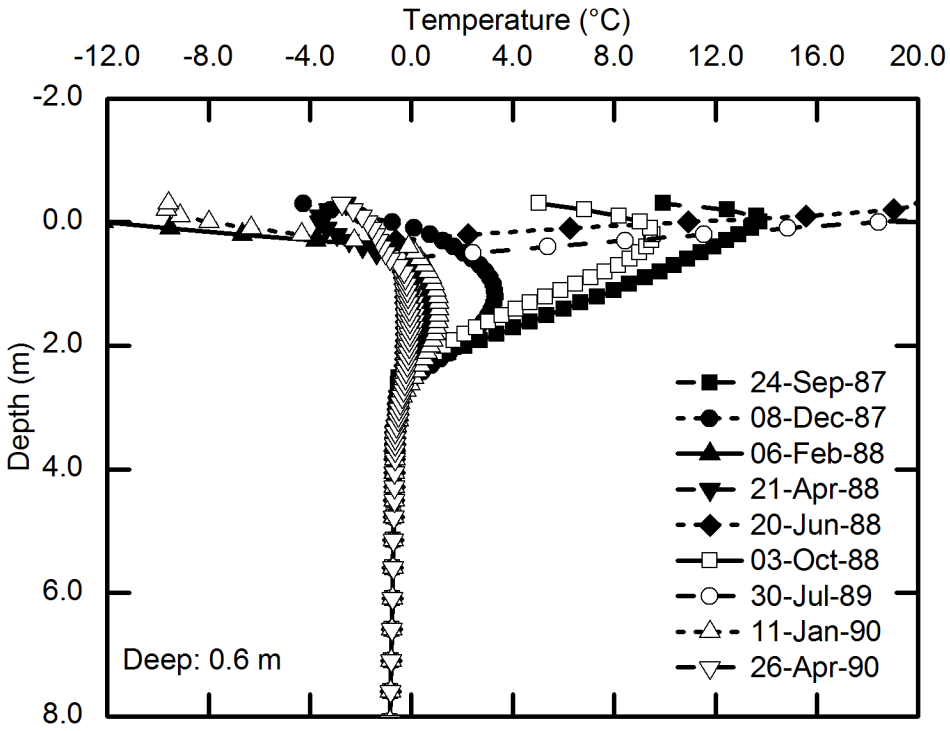

(a)

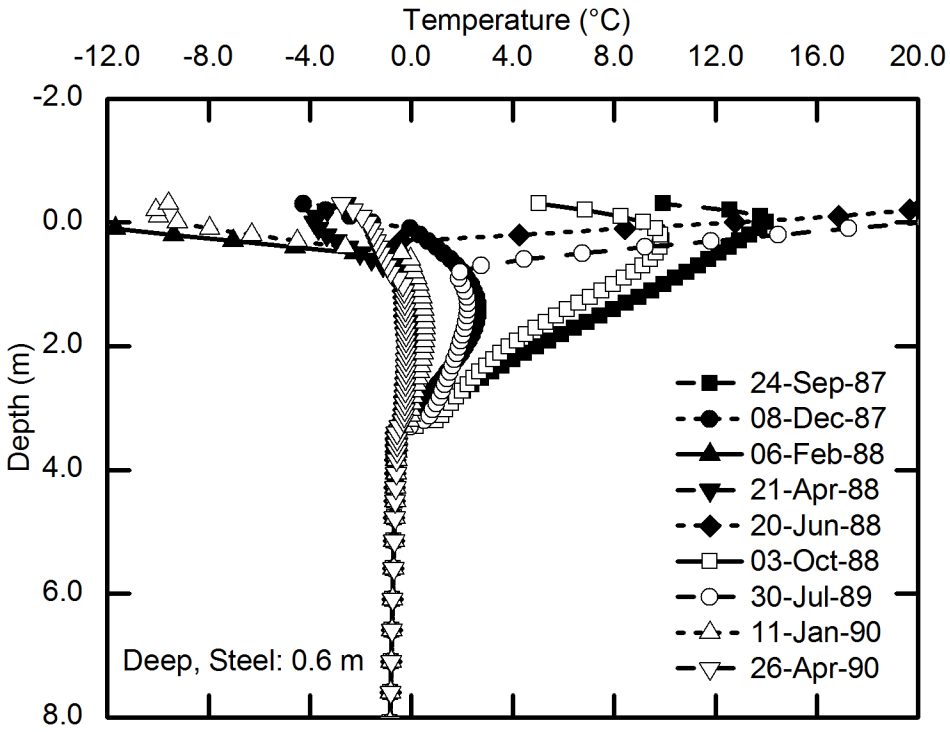

(b)

Figure 4.28: Modeled Temperature profile for the Deep Foundation at 0.6 m (2.0 ft) from the tower (a) without steel and (b) with steel

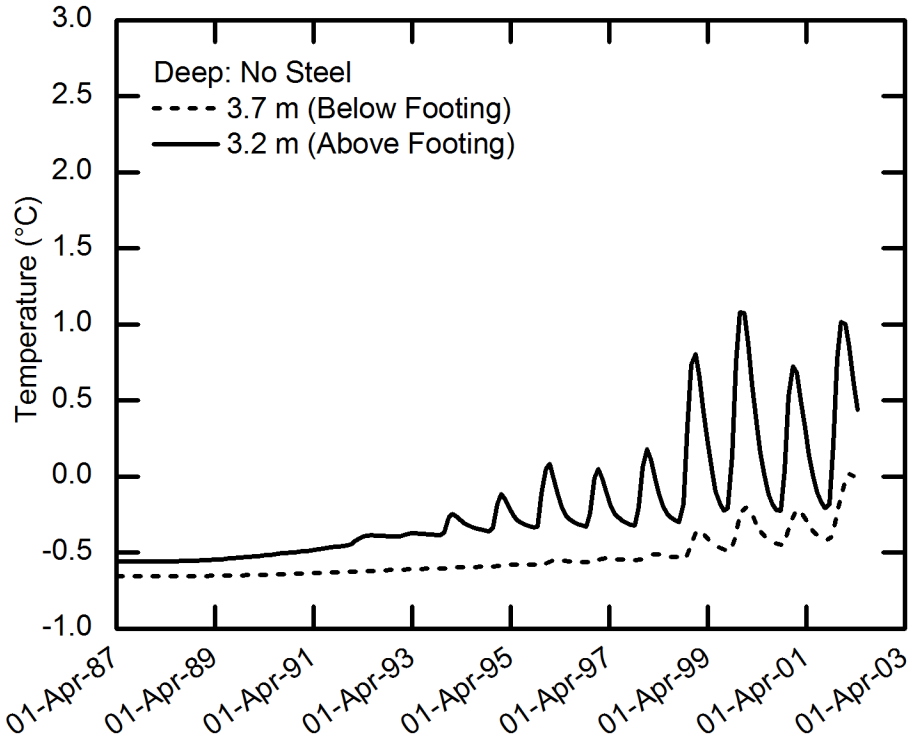

(a)

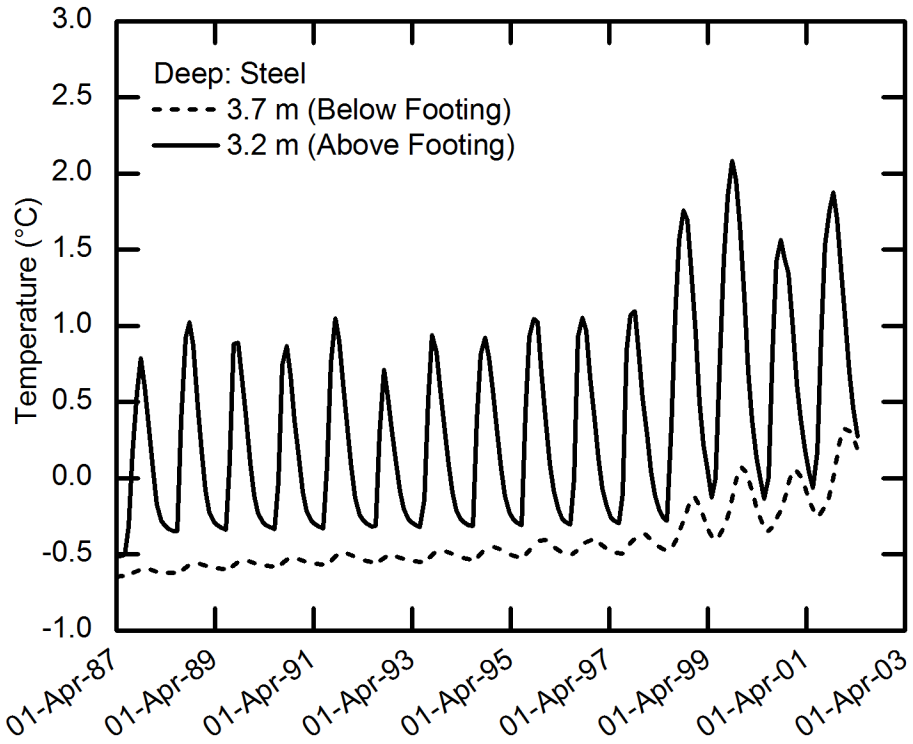

(b)

Figure 4.29: Temperature versus Time above and below the footing for 15 years in the Deep Foundation; (a) without steel (b) with steel

Chapter 5: An ETVP Framework

5.1 Introduction

The concepts of viscoplasticity and thermoplasticity were outlined in Chapter 2. Viscoplasticity describes (strain) rate-dependent inelastic behaviour; thermoplasticity describes temperature-dependent inelastic behaviour. It was shown that the mathematics of the two concepts are broadly similar. Viscoplasticity and thermoplasticity have separately been defined in the form of semi-empirical models (e.g. Kelln 2007, Yin 1990, Yin et al. 2002, Tanaka 1995). To the author's knowledge no easily accessible semi-empirical model currently exists that combines an elastic viscoplastic (EVP) model with thermoplasticity concepts in the form of an elastic thermo-viscoplastic (ETVP) model. (Mechanics-based models do exist, but are difficult to calibrate.) One of the objectives of this research program is to develop an ETVP model capable of reproducing the effects of temperature and viscosity on the load-deformation behaviour of clay soils observed in the laboratory and the field.

5.2 Elastic thermo-viscoplastic modeling

Current semi-empirical models describe separately time- and temperature-dependent behaviour of clays (see Chapter 2). These models are consistent with the critical state soil mechanics framework (Schofield and Wroth 1968, Wood 1990) but provide important additions to the basic Modified Cam-clay (MCC) model.

The constitutive equations in the MCC framework are mathematical descriptions of the relationships observed between generalized stress increments of a soil and its specific volume. For calibration, the equations require easily understood parameters that have a physical meaning and are obtained from commonly available oedometer and triaxial tests in laboratory testing. The models can be calibrated relatively easily and produce results that correlate well with observed behaviour.

The MCC model is widely used as a constitutive model for load-deformation problems (for example settlement analysis) and can be combined with hydrodynamic effects for coupled consolidation problems. These problems can be conveniently modeled using, for example, SIGMA/W for the former and a coupling of SIGMA/W and SEEP/W for the latter in the GeoStudio software suite produced by GEO-SLOPE International Ltd.

The MCC model does not include viscoplasticity or thermoplasticity. Kelln (2007) improved the earlier EVP model suggested by Yin et al. (2002). His EVP model originates from an improved understanding of loading rates and strain rates and the coefficient of secondary compression (creep parameter), $\psi = \partial V/\partial t$ in 1D compression. The EVP model has produced significant improvements in simulating the performance of embankments on soft clay (Kelln 2007). The purpose of this part of the author's research is to incorporate an understanding of temperature effects into Kelln's EVP model and in doing so, produce a new elastic thermo-viscoplastic (ETVP) model.

The new ETVP model will build upon the established framework of MCC and EVP modeling and will remain semi-empirical in nature. The goal of the new model is to provide a simple, effective, and easily accessible representation of the effects of both time- (as expressed, for example, by strain rate) and temperature-dependent behaviour in

clays. The model was developed as a spreadsheet model using Microsoft Excel 2007. Integrating the model into finite element software was not part of the author's program.

5.2.1 Terminology

Terminology used in this thesis is consistent with Wood (1990) and the EVP model developed by Kelln (2007). That is, shear stresses and shear strains are denoted with the subscript *q* and volumetric (mean effective) stresses and volumetric strains are denoted by the subscript *p*. This is in contrast to the subscripts *s* and *v*, respectively, found in other publications, for example, Graham et al (2001). The latter assumes a decoupling of volumetric strains from *q*-stresses and shear strains from *p'*-stresses in isotropic soils. The author's model assumes isotropy and an associated flow rule, but could be expanded to include anisotropy and a non-associated flow. This research program focused on isotropically consolidated clay.

Other commonly used subscripts include *i*, *y*, *c*, *cs*, *m*, and *x* to describe the states of stress as initial, yield, preconsolidation pressure, critical state, isotropic compression, and current state, respectively. The subscripts *1*, *3* designate principal stresses and strains in the axial and radial directions. Superscripts *e*, *p*, *vp* indicate elastic (recoverable), plastic (irrecoverable), and viscoplastic (time-dependent and irrecoverable) states. Time is denoted by *t* (and *dt*); temperature by *T* (and *dT*). Specific volume is denoted as *V*; pore water pressure as *u*. These terms are used in the spreadsheet model provided on the accompanying DVD (see Appendix I). Compression is defined using unload-reload (recompression) lines with slope κ and normal consolidation (hardening) lines with slope λ. The creep function, ψ denotes the rate of secondary compression.

5.2.2 Kelln's EVP Framework

Kelln proposed an elastic-viscoplastic (EVP) soil model that has been successfully used to analyze settlements of a highway embankment near Limavady in Northern Ireland (Kelln 2007; Kelln et al. 2008*a*; Kelln et al. 2009). The model was discussed in Chapter 2, where advantages of the model were presented. A detailed description of the model and a more complete derivation of formulas are available in the references provided above. This section provides only a brief overview of the formulation of the model.

The specific volume of a specimen for a state of stress (p'_m:V_m) at a time t can be expressed as:

[Eq. 5.1] $$V_m = N - \lambda \ln p'_m - \psi \ln\left(\frac{t_0 + t}{t_0}\right)$$

where N is the intercept of the normal consolidation line, NCL, at the assumed mean stress of p' = 1 kPa (Figure 5.1). The specific volume on the NCL, V_{ncl}, for the mean stress p'_m is calculated using the first two terms. The secondary compression line, the third term, is plotted vertically in compression space. This assumes that under a constant load, viscoplastic strains develop with time (Figures 2.16 and 5.1). The creep parameter ψ is defined as a function of time (Figure 2.22). For t = 0, $V_{ncl} = V_m$ for a given stress state (p'_m:V_m) and thereby assumes no viscoplastic component of strain. Limitations on Equation 5.1 are more completely explained in Kelln (2007) and are not the focus of the author's work. Using the third term, which defines creep, an incremental form of the secondary (delayed) compression line can be obtained and expressed as viscoplastic strain (Equation 5.2). In addition, time t can be isolated in Equation 5.1 and substituted into this incremental form to obtain the viscoplastic volumetric strain rate (Equation 5.3):

[Eq. 5.2] $$\delta\varepsilon_p^{vp} = \left(\frac{\delta V_m}{V_m}\right) = \left(\frac{\psi}{V_m(t_0 + t)}\right)\delta t$$

[Eq. 5.3] $$\dot{\varepsilon}_p^{vp} = \frac{\delta\varepsilon_p^{vp}}{\delta t} = \left(\frac{\psi}{V_m t_0}\right) exp\left(\frac{V_m - N}{\psi}\right)(p'_m)^{\frac{\lambda}{\psi}}$$

This equation, as implied by the subscript *p* is applicable to an isotropically consolidated state (p'_m:V_m). Parameters in this formulation such as λ and ψ are obtained from straightforward laboratory testing and *N* can be calculated knowing λ.

The mathematics of the formulation is not yet complete. The MCC framework assumes an associated flow rule and this criterion must be satisfied. Similar to Equations 2.4 and 2.7 and the work of Perzyna (1963), Kelln defines the flow rule using a scalar function *S* (Yin et al. 2002) and a plastic potential *g* as follows:

[Eq. 5.4] $$\dot{\varepsilon}_p^{vp} = S\frac{\partial g}{\partial p'}$$

which leads to the scalar function defined as:

[Eq. 5.5] $$S = \left(\frac{\psi}{V_m t_0}\right) exp\left(\frac{V_m - N}{\psi}\right)(p'_m)^{\frac{\lambda}{\psi}} \frac{1}{|\partial q/\partial p'|}$$

A general expression of the viscoplastic strain rate can then be expressed as:

[Eq. 5.6] $$\dot{\varepsilon}_{ij}^{vp} = \left(\frac{\psi}{V_m t_0}\right) exp\left(\frac{V_m - N}{\psi}\right)(p'_m)^{\frac{\lambda}{\psi}} \frac{1}{|\partial q/\partial p'|}\left(\frac{\partial g}{\partial \sigma'_{ij}}\right)$$

In this model, the scalar function is limited to positive values (via the absolute bars). Negative viscoplastic strain rates may be developed by the partial derivative of the plastic potential, $\partial g/\partial \sigma'_{ij}$ (Kelln 2007).

Kelln (2007) examines and adopts the concept of a viscoplastic limit line from Yin et al. (2002) who described this line as the limit at which viscoplastic straining ceases such that the void space within a unit of soil has collapsed. Kelln (2007) states that this

limit should be introduced to assist with computational efficiency, but for practical purposes, calculated viscoplastic strain rates become negligible past a practical timeframe. He recognized that an isotropic state lying on or below the viscoplastic limit line (point C in Figure 2.18), for example by unloading, Equation 5.6 would not experience viscoplastic strains, and the response would be purely elastic (Kelln 2007). This implies that the secondary compression line needs to be redefined (third term in Equation 5.1) Yin et al. (2002) recognized (for different reasons) that the secondary compression line needed to be redefined and proposed a hyperbolic creep function. Kelln slightly reworked this hyperbolic function such that Equation 5.1 is replaced with:

[Eq. 5.7] $$V_m = N - \lambda \ln p'_m - \frac{\psi \ln\left(\frac{t_0 + t}{t_0}\right)}{1 + \frac{\psi}{N - Z} \ln\left(\frac{t_0 + t}{t_0}\right)}$$

where Z is the intercept of the viscoplastic limit line at the assumed mean stress of p' = 1 kPa (Figure 5.1). The viscoplastic limit line (vpl) takes the form:

[Eq. 5.8] $$V_{vpl} = Z - \lambda \ln p'_o$$

and can be related to N via the NCL and a given unload-reload line:

[Eq. 5.9] $$Z = N - (\lambda - \kappa) \ln \frac{p'_m}{p'_o}$$

This leads to the viscoplastic volumetric strain rate and scalar functions defined as:

[Eq. 5.10]

$$\dot{\varepsilon}_{ij}^{vp} = \left(\frac{\psi}{V_m t_0}\right)\left(1 - \frac{N - \lambda \ln p'_m - V_m}{N - Z}\right)^2 exp\left[\frac{N - \lambda \ln p'_m - V_m}{\left(\frac{N - \lambda \ln p'_m - V_m}{N - Z} - 1\right)\psi}\right] \frac{1}{\left|\frac{\partial g}{\partial p'}\right|}\left(\frac{\partial g}{\partial \sigma'_{ij}}\right)$$

[Eq. 5.11]

$$S = \left(\frac{\psi}{V_m t_0}\right)\left(1 - \frac{N - \lambda \ln p'_m - V_m}{N - Z}\right)^2 exp\left[\frac{N - \lambda \ln p'_m - V_m}{\left(\frac{N - \lambda \ln p'_m - V_m}{N - Z} - 1\right)\psi}\right]\frac{1}{\left|\frac{\partial g}{\partial p'}\right|}$$

where $N - \lambda ln(p'_m) = V_{ncl}$.

Kelln explains that Equations 5.10 and 5.11 do not operate if $V_{ncl} - V_m > N - Z$. He further explains that the location of the viscoplastic limit line, *Z*, has a small effect on the calculated viscoplastic strain rates, but rather controls the overconsolidation ratio at which the behaviour becomes purely elastic (Kelln 2007). Kelln compared the differences between Equations 5.6 and 5.10 noting that although they are different in form, they produce similar predictions of stress-strain behaviour. He explained that larger differences become apparent if creep is simulated over extraordinary lengths of time and higher overconsolidation ratios (Kelln 2007).

5.2.3 Incorporation of T in ETVP

Attempts have been made with varying degrees of success to model the effects of temperature on the stress-strain behaviour of clay soils. An introduction to the concept of thermoplasticity was provided in Chapter 2. Two models in particular were discussed. They present broadly similar yet also rather different approaches.

Hueckel and his colleagues (Hueckel and Baldi 1990, Hueckel and Borsetto 1990) developed a model that reasonably predicts thermoplastic consolidation and cyclic undrained heating and cooling, among others. The model introduces thermal coefficients to explain the physical effects of expansion and contraction with changes in temperature. As pointed out by Tanaka (1995), however, the model focuses on *q:p'* stress space, and fails to expand the understanding of compression space (*V*:ln(*p'*)). The model is further

complicated by incorporating the temperature-dependency of elastic parameters, namely the bulk modulus K and other auxiliary parameters, and using compliance formulas to bridge the gap between known physics and the semi-empirical MCC framework.

Tanaka (1995) took a step forward by performing an extensive triaxial testing program on drained and undrained specimens. In defining his model, Tanaka focused on explaining the effects of temperature on his experimental data, particularly in relation to compression space. Tanaka also included thermal expansion coefficients in his model, but leaned towards explaining thermally induced pore water pressures and their effect on effective stresses. Tanaka (1995), and later with slight modification Graham et al. (2001), tried to explain the differences between constant volume heating and drained heating (Figure 2.13) with emphasis on compression space and determining thermally induced elastic and plastic volumetric strains. As described in Chapter 2, Tanaka's model hinged upon his hypothesis that the unload-reload lines vary with temperature, that is, $\kappa = \kappa(T)$. This was later proven incorrect by Crilly (1996).

Descriptions of other mechanics-based models are provided in Chapter 2. These models include several formulations and modifications that, although they reproduce observed behaviour well, are overly complicated. Un-typical parameters are used to bridge the mathematics between an established model framework based on our understanding of physics, and specific observations in 'specialized' laboratory tests. It is the author's opinion that it is difficult for new users to fully appreciate all the mathematics involved in these models. These difficulties provide an opportunity for examining temperature effects as an addition to the viscosity (creep) function used by Kelln (2007) in his isothermal EVP model.

A temperature-dependent viscosity function:

Kelln (2007) postulated that his elastic viscoplastic model could be modified to accommodate changes in temperature. Although the idea was not developed in his thesis, he felt this would be possible by simply modifying the secondary compression line to be a function of temperature, that is, $\psi = \psi(T)$. The introduction of the viscoplastic volumetric strain rate function produced similar effects to those described by Bjerrum (Figures 2.15 and 5.1), such that lower strain rates produce successively lower 'time-lines' in compression space, and vice versa. It also explains in principle the differences seen in the experimental work of Crilly (1996) and the model developed by Tanaka (1995).

The introduction of a secondary compression coefficient that depends on temperature implies that viscoplastic volumetric strains would now become thermo-viscoplastic strains. This model will then require a defined function outlining the relationship between secondary compression and temperature. The author reviewed available literature for previous work that would define this relationship. Mesri (1973) argued against the effect of temperature on creep stating that "more importance has been attached to the influence of temperature on the rate of secondary compression than it really deserves." Towhata et al. (1993) concluded that secondary compression is accelerated upon heating (meaning a faster decrease in void ratio or specific volume) but is followed by a similar rate of deformation as observed at a lower temperature. Batenipour (2012) and Batenipour et al (2009*a*) show a small difference in C_α for oedometer tests performed between 3.0°C and 21.0°C. These specimens contained high silt contents, which has been documented to greatly impact the performance of the specimen, especially by decreasing observed creep rates (Demars and Charles 1982).

Leroueil and Marques (1996) conclude that the compressibility of the soil should be described as a 'stress-strain-strain rate-temperature' relationship and cite evidence of an increase in both strain and strain rate with an increase in temperature. A potential relationship between creep and temperature is acknowledged in Burghinoli et al. (2000) and a linear relationship is presented in Houston et al (1985). Andersland and Ladanyi (2004) and Wijeweera and Joshi (1991), among others, discuss creep behaviour in frozen specimens. Although creep in frozen soils is not the focus in the author's model it is important in establishing a relationship with temperature. Fox and Edil (1996) show strong evidence of a C_α-temperature relationship for peat materials. Based on their results, Fox and Edil (1996) proposed an exponential relationship between C_α and temperature:

[Eq. 5.12] $$C_{\alpha 2} = C_{\alpha 1}\exp[C_T(T_2 - T_1)]$$

where $C_{\alpha 1}$ is the coefficient of secondary compression at temperature T_1 and $C_{\alpha 2}$ is the coefficient of secondary compression at temperature T_2. The constant, C_T, is described to be independent of void ratio, stress level, magnitude of temperature change.

Overall there are conflicting views in the literature regarding the effect of temperature on secondary compression. Based on an understanding of the diffuse double layers (DDLs) of viscous water that are present around many clay mineral particles, it seems reasonable that a material at a higher temperature would experience higher creep rates and therefore more creep strains. The thickness of the DDL depends on many parameters (such as mineralogy, pore fluid chemistry and temperature) but the DDL typically expands with an increase in temperature as expressed in the Gouy-Chapman theory (Mitchell and Soga 2005). For soils, which are multiphase materials, the picture

becomes further complicated depending on whether the pore water can drain or is prevented from draining (Campanella and Mitchell 1968).

For this project, two relationships were examined for the assumed relationship $\psi = \psi(T)$. The simpler assumption is a linear increase in ψ with an increase in T. The linear relationship presented in Houston et al. (1985) is defined for positive temperatures starting from 0.0°C; however, given evidence of creep in frozen soils, the author feels this relationship should still consider frozen soils. This linear relationship requires two 'anchor' points to be properly defined. Knowing that all atomic motion ceases at this temperature, it can safely be assumed that there is no creep behaviour and therefore that $\psi = 0.0$ at 0.0K. Therefore the first anchor point is defined at a chosen laboratory temperature; the second anchor point is defined at 0.0K, that is, -273.15°C. This relationship assumes a continuous linear relationship across the phase-change boundary for water. The author acknowledges that frozen and unfrozen creep has different mechanisms: frozen creep is a combination of ice and interparticle contacts; unfrozen creep involves only interparticle contact. It is more likely that creep rates for frozen and unfrozen soil differ; however, for the purpose of this project, a simple linear relationship was explored. Values of ψ associated with the first anchor point are discussed in following section.

The second relationship adopts the form of the basic exponential relationship proposed by Fox and Edil (1996) with the creep parameter defined as ψ instead of C_α:

[Eq. 5.13] $$\psi_2 = \psi_1 \exp[\Omega(T_2 - T_1)]$$

where ψ_1 is the coefficient of secondary compression at temperature T_1 and ψ_2 is the coefficient of secondary compression at temperature T_2. The 'material' constant was

redefined as Ω to further reflect the use of ψ instead of C_α. The only anchor point for this relationship is consistent with the first anchor point in the linear relationship. That is, the relationship is anchored to a measured ψ at an appropriate laboratory temperature. Values associated with this anchor point are discussed in the following section.

Implementing the $\psi = \psi(T)$ function:

To test the temperature-dependent viscosity functions, a spreadsheet 'triaxial' model was developed in Microsoft Excel 2007 based on the MCC framework (Schofield and Wroth 1968) and the viscoplastic formulations of Kelln (2007) summarized earlier in this Chapter. The spreadsheet allows a user to analyze various triaxial stress paths (drained, undrained, lateral expansion, or user defined) from an initial isotropic stress to failure (critical state). Stresses and strains are calculated incrementally and both stress space (q:p') and compression space (V:ln(p')) can be analyzed. Functionality of the spreadsheet is not described in this thesis. Discussion is restricted to the response of the ETVP model.

Both temperature functions were implemented in the same way. An initial known point from laboratory data was inputted (ψ_1:T_1) and then either a new temperature, T_2, or a change in temperature, dT, could be specified. For the linear relationship, the model requires the input of the origin of the line (ψ_0:T_0) (This was specified as a constant 0.0:0.0K). For the exponential relationship, the model requires the input of the Ω constant. The creep parameter, ψ_2 is then calculated using either the linear or exponential relationship and is used in subsequent calculations of viscoplastic strains under specified triaxial test conditions.

The manner in which temperature effects have been implemented indicates that

the model is considered to be an isothermal model. That is, temperature is constant during simulation of the triaxial shearing, although the effects of different temperatures can be examined. The model calculates the incremental values for all stresses and strains for both (ψ_1:T_1) and (ψ_2:T_2). The EVP model (Kelln 2007) is considered to be the results obtained at (ψ_1:T_1) while the ETVP model is considered to be the results obtained from (ψ_2:T_2) as a result of $dT = T_2$-T_1. The spreadsheet model also calculates corresponding values from the base MCC framework for comparison of MCC, EVP, and ETVP values.

A second ETVP model was also developed by implementing the effect of temperature changes during triaxial shearing. This non-isothermal model allows the input of initial temperature, T_1, a change in temperature, dT, and a final temperature, T_2. The spreadsheet updates the value of ψ_2 at each increment. This model was developed simply for comparative purposes and it was not used for detailed analysis. The first (isothermal) model was the primary tool for implementing temperature effects into an EVP model.

Procedures for calculating the values in the spreadsheets are not provided in this thesis document, but details can be found in the spreadsheet on the accompanying DVD (see Appendix I). Formulations in the spreadsheet follow a similar procedure as outlined in Kelln (2007) with slight modification to the order that certain values are calculated. The change to the procedure did not alter the results but improved the author's understanding of the model and makes it easier to implement further modifications.

Assumptions and Limitations of the ETVP model:

Numerical modeling always requires a number of constraints and assumptions. As a result, the author’s ETVP model contains specific assumptions and limitations. Because

of the way it has been developed, the model contains all the constraints described briefly in Chapter 2 for the MCC framework (Schofield and Wroth 1968). It thereby maintains the predictive capabilities of the basic generalized elastic-plastic model. In addition, the model can capture effects of clay viscosity as seen in variable rates of straining and the development of plastic strains with constant stress (Kelln 2007). Specific to the author's new work on adding temperature capabilities, the model contains the following constraints and assumptions:

(1) The model focuses only on $\psi = \psi(T)$. That is, the purpose of the model is to gain an understanding on the functionality of creep parameter, ψ, within the viscoplastic strain formulation established by Kelln (2007). No other parameter has been directly altered.

(2) Physics related to thermal expansion and contraction is not implemented in the model. The purpose for leaving coefficients of thermal expansion and contraction out of the model was to isolate and identify only the impact of temperature on the creep parameter. This is to examine whether the model can reproduce similar behaviour (as in published data) for soil subjected to changes in temperature without incorporating thermodynamics. In this way, it represents the type of modeling that was identified earlier as 'semi-empirical'.

(3) The model does not implement phase changes. The creep functions have been defined on a Kelvin-scale such that sub-zero Celsius temperatures are achievable. In this sense, crossing the phase-change boundary is possible, but since point (2) states that physics related to thermal expansion and contraction is not implemented, it follows that the volumetric expansion of water and the strength of ice is not

considered in this model.

(4) Elasticity is assumed to be independent of temperature. That is, the creep parameter does not directly influence the elastic stiffnesses bulk modulus (K), shear modulus (G), and Young's modulus (E). In the model, these parameters change as a result of changes in specific volume and mean stress but are not a direct function of temperature. This is also addressed in the naming of the model as an elastic thermo-viscoplastic (ETVP) model, thus implying that temperature effects are accounted for only in the viscoplastic formulation of strains.

(5) The origin of the isotropic normal consolidation line, N, (defined at a mean stress, p' = 1.0 kPa in Figure 5.1) is independent of temperature. At first sight, this appears to contradict what is shown in Figures 2.3, 2.13, and 2.21 by Campanella and Mitchell (1968), Tanaka (1995), and Eriksson (1989), respectively. It is similar in principle, to what is done in the EVP modeling developed by Yin et al. (2002) and Kelln (2007). In the author's ETVP model, the apparent change to N is a direct result of a change in ψ and not an absolute change as implied in Tanaka's TEP model. It is similar in effect to the changes in NCL and critical state line, CSL, that arise naturally from viscoplastic straining in Kelln's EVP model.

(6) The material constant, Ω, is assumed to be constant for this study. This constant can be expected to be different for various types of clays and would thereby affect the rate at which the creep parameter changes with temperature. To the author's knowledge, specific literature pertaining to this value is not available. This project used a constant value of Ω = 0.015/°C (or 0.015/K). This provides a near zero value for ψ at 0.0K.

5.3 Sensitivity Analysis

Several parameters in the ETVP model impact the modeling results considerably. There is a broad range of conditions that affect the initial state of the soil. These need to be addressed in addition to the parameters that are actually included in the name of the model, namely viscosity (time) and temperature. The author decided that a sensitivity analysis was the most efficient way to compare the effects of each parameter on the overall behaviour of the model. Following paragraphs outline the ranges that have been examined for each of these parameters.

Analyzed Parameters:

The type of triaxial test (isotropic consolidated drained, CID or undrained, CI$\bar{U}$) was the first parameter that was varied. That is, the model was run considering only drained or undrained stress paths. The model is capable of other stress paths, but the sensitivity analysis has been limited to only the most common triaxial tests.

The isotropic overconsolidation ratio (OCR) was the second parameter that was varied. Isotropic preconsolidation pressures, p'_c of 25.0 kPa and 50.0 kPa were chosen. The author acknowledges that these pressures are low but were chosen as typical pressures experienced in many geotechnical applications in the field. The model was run using three OCRs; 1.00 for normally consolidated (NC), 1.67 for lightly overconsolidated (LOC), and 5.00 for heavily overconsolidated (HOC).

The next varied parameter was the axial strain rate, $\delta\varepsilon_{11}/\delta t$, expressed as a percentage. The sensitivity analysis was kept consistent with the results presented in Kelln (2007) for strain rates. Three values for axial strain rate were chosen with an order

of magnitude differences between values: 15.0%/day, 1.50%/day, and 0.15%/day. The author notes that while an axial strain rate of 15.0%/day can be incorporated into an ETVP analysis of a drained test, drainage will probably not be complete in an actual test at this shearing rate – excess pore water pressures will likely develop.

The final variables in the sensitivity analysis pertain to the focus of the analysis, namely temperature. Earlier in this chapter, two relationships for $\psi = \psi(T)$ were discussed; a linear relationship and an exponential relationship. These were implemented in the sensitivity analysis. The linear relationship was anchored at absolute zero (0.0K) and a typical laboratory value. The exponential relationship was anchored to a material constant, Ω, and a typical laboratory value. The constant, Ω, was held constant at an assumed value of 0.015/K. The known laboratory value (ψ_1:T_1) indicates a value that is measured by means of a standard creep test at a given laboratory temperature. Mesri and Choi (1985) list a range of C_α/C_c for all natural soils between 0.02 - 0.10 and clays as 0.04 ± 0.01. Naturally, C_c can greatly vary in soil. (The variation is commonly expressed in terms of the plasticity index I_P.) Three values of ψ_1 were chosen that the author feels is a representative range of creep values for soil; 0.002, 0.006, 0.010 at a temperature, T_1, of 28.0°C (301.15K). Figure 5.2 illustrates these relationships.

The chosen temperature, T_1, is a little higher than typical laboratory temperatures. It was chosen based on the set of temperatures used in Tanaka (1995). The author feels that this small difference between typical and modeling temperatures do not provide a quantitatively significant difference in the results and that they should be qualitatively similar. The complete sets of temperature used in the sensitivity analysis were 3.0, 28.0, 65.0, and 100.0°C. The temperature of 3.0°C is presented and discussed in Chapter 6.

Stress-Deformation Parameters:

The simulation of the conventional triaxial isotropic compression tests (CID and CI$\bar{U}$) in the ETVP model used the same parameters used in Kelln (2007) to simulate triaxial tests in the EVP model. These parameters are listed in Table 5.1. By setting up the model such that the anchor point (ψ_1:T_1) is considered an initial parameter, results for the ETVP model at temperature T_1 can be considered equivalent to Kelln's EVP model, which does not consider the effects of changes in temperature.

Response of the ETVP model:

The sensitivity analysis resulted in fifty-four separate cases for a single triaxial test, which could be either a CID or CI$\bar{U}$ test (that is, 3 OCRs, 3 strain rates, 3 ψ-values and 2 triaxial tests). Each CI$\bar{U}$ (or CID) case is analyzed in a five-graph format similar to Kelln (2007) that includes stress space (q:p'), compression space (V:ln(p')), deviatoric stress versus shear strain (q:ε_q), pore water pressure versus shear strain (u:ε_q), and the viscoplastic volumetric strain rate versus isotropic mean stress ($\dot{\varepsilon}_p^{vp}$:p'_m). In the CID cases, pore water pressure is replaced with specific volume, V. Each plot contained data for a minimum of three temperatures, typically 28.0, 65.0, and 100.0°C, as well as for both the linear and exponential relationships presented in Section 5.2.

Presentation of the model's response in this manner produced a total of over 540 graphs. Figure 5.3 shows an example of the response of the ETVP model for a CI$\bar{U}$ NC test at three elevated temperatures and both linear and exponential relationships anchored at (ψ_1:T_1) = (0.006:28.0°C). This figure shows, as expected, a larger impact of temperature for the exponential relationship as opposed to the linear relationship. For this

reason, further plots focus on the exponential relationship.

As expected, when compared to the response for the (ψ_1:T_1) = (0.006:28.0°C), plots using the anchor point (0.002:28.0°C) are attenuated while plots using the anchor point (0.010:28.0°C) are amplified. (Here, 'attenuated' means that differences between the responses of the model at various temperatures are less apparent. In each case, 'amplified' means the reverse.) A similar effect is present with the strain rates as is shown in Kelln (2007).

For comparative purposes only, the relationship between temperature and preconsolidation pressure can be observed in a CI$\bar{U}$ NC test (Figure 5.4). This plot has been normalized for each preconsolidation pressure to allow comparison. At the scale used in the plot, the difference between preconsolidation pressures is noticeable albeit small. Therefore, plots anchored to (0.006:28.0°C) and for axial strain rates of 15.0%/day and 0.15%/day are shown for each OCR and a preconsolidation pressure of 50.0 kPa.

Selected responses of the ETVP model are presented in Figures 5.5 to 5.10 for CI$\bar{U}$ tests and Figures 5.11 to 5.16 for CID tests. Remaining graphs and raw data are available on the accompanying DVD (see Appendix I). Results of the sensitivity analysis are presented in this chapter to differentiate between the responses of the model to various parameters and the author's interpretation of those responses. Chapter 6 presents a detailed analysis on the response of the ETVP model. Additional discussion regarding validation and application of the model is also presented.

It is important to note some anomalies in the responses of the model. At higher OCRs for both CI$\bar{U}$ (Figure 5.9) and CID (Figures 5.14 and 5.15) tests, the model produces unreliable responses. These responses are a function of the viscoplastic

formulations and a combination of strain rates, the updated creep parameter at the elevated temperature (ψ_2:T_2) and the high OCR. These responses are undesirable but allude to limitations of the values that can be used in the model such as an applicable range of strain rates for a given change in temperature, or vice versa. Due to these responses in the model, the results for CI$\bar{U}$ and CID tests from the different analyses sometimes have different ending points (for stress and strain) at different OCRs. As a result, many responses of the model end before critical state has been fully achieved. This is also observed in basic MCC modeling and in Kelln's EVP modeling, particularly for highly overconsolidated specimens.

5.4 Commentary

The purpose of this modeling was to incorporate temperature effects into an established elastic viscoplastic framework. Earlier in this thesis, Chapter 2 showed that the influence of temperature on secondary compression has been a debated area of research. Laboratory testing reported in the research literature confirms that creep behaviour changes with different temperature but there is still an ongoing debate about how they change. Without considering the actual physics of thermal expansion and contraction, the concept of temperature affecting the soil structure and creep behaviour seems plausible. Higher temperatures decrease the viscosity of a material, in our case the viscosity of both 'free' water in the void spaces and 'adsorbed' water in diffuse double layers surrounding particles. Lower viscosity increases the amount of creep the material will experience will be reduced. This was the inherent assumption upon which the modeling proceeded. The purpose of the modeling was to examine this assumption and if possible, to quantify the

effects of temperature on creep behaviour of clays.

Temperature was therefore implemented into the EVP model developed by Kelln (2007). This was achieved by employing two different temperature-dependent functions for the creep parameter, ψ, such that $\psi = \psi(T)$. The functions were: (1) a linear relationship tentatively anchored at absolute zero (0.0K) and at a known laboratory point (ψ_1:T_1); and (2) an exponential relationship anchored to a known laboratory point (ψ_1:T_1) and a material constant, Ω, controlling the shape of the exponential function.

Several key parameters were evaluated to assess the impact on the response of the model, namely the OCR, strain rate, and temperature. A sensitivity analysis was developed to assess this impact. An initial examination indicates that the response of the model is promising. Further analysis is provided in Chapter 6.

5.5 Summary

The concepts of viscoplasticity and thermoplasticity have now been combined in a semi-empirical framework. This framework is based upon an existing EVP model using a viscoplastic volumetric strain rate formulation developed by Kelln (2007). The effect of temperature has been accommodated by the introduction of two possible relationships between secondary compression (creep) and temperature. The response of the model is promising, but further analysis is required.

Table 5.1: Soil parameters used to simulate $CI\bar{U}$ and CID triaxial tests

Soil Parameter	Symbol	Value
Slope of the critical state line	M	1.00
Slope of the normal consolidation line	λ	0.25
Slope of the unload-reload line	κ	0.05
Slope of the secondary compression line[1]	ψ_1	0.006
Initial temperature[1]	T_1	28.0°C
Material constant	Ω	0.015/°C
Origin of the normal consolidation line	N	3.00
Origin of the viscoplastic limit line	Z	1.00
Curve fitting parameter	t_0	1.00 day
Poisson's ratio	ν'	0.30

[1]These values correspond to the anchor point for the $\psi = \psi(T)$.
Values of $\psi_1 = 0.002$ and 0.010 are also used.

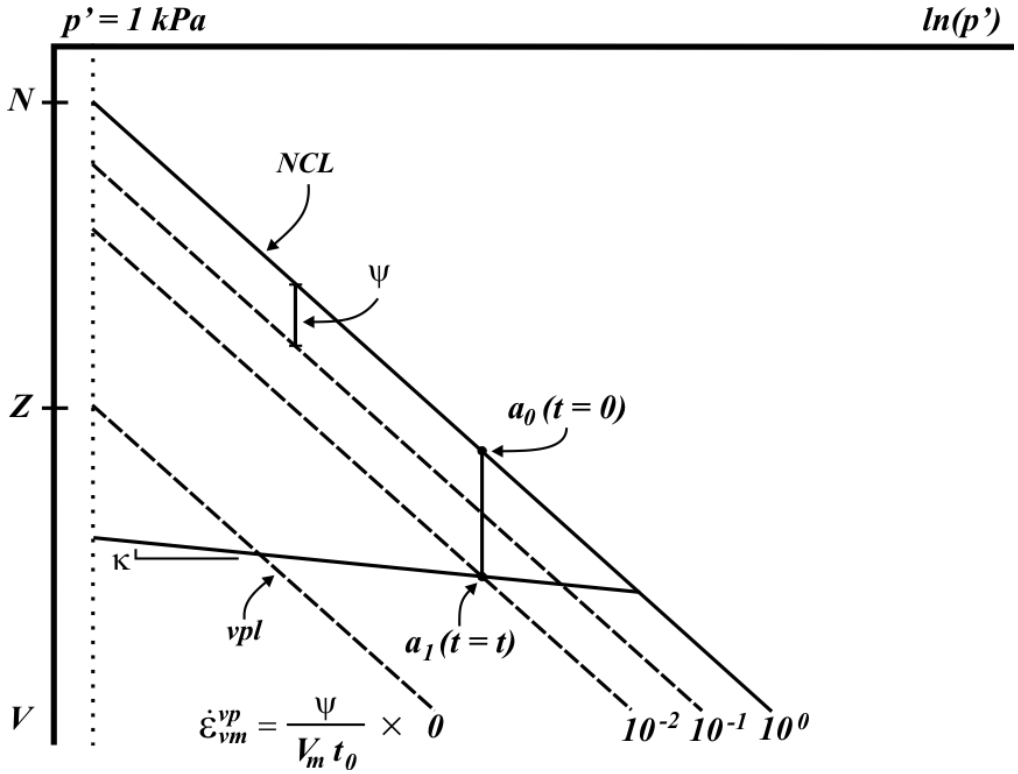

Figure 5.1: Compression space (V:ln(p')) showing a point a_0 proceeding to a_1 after time t (after Kelln 2007) (Used with permission)

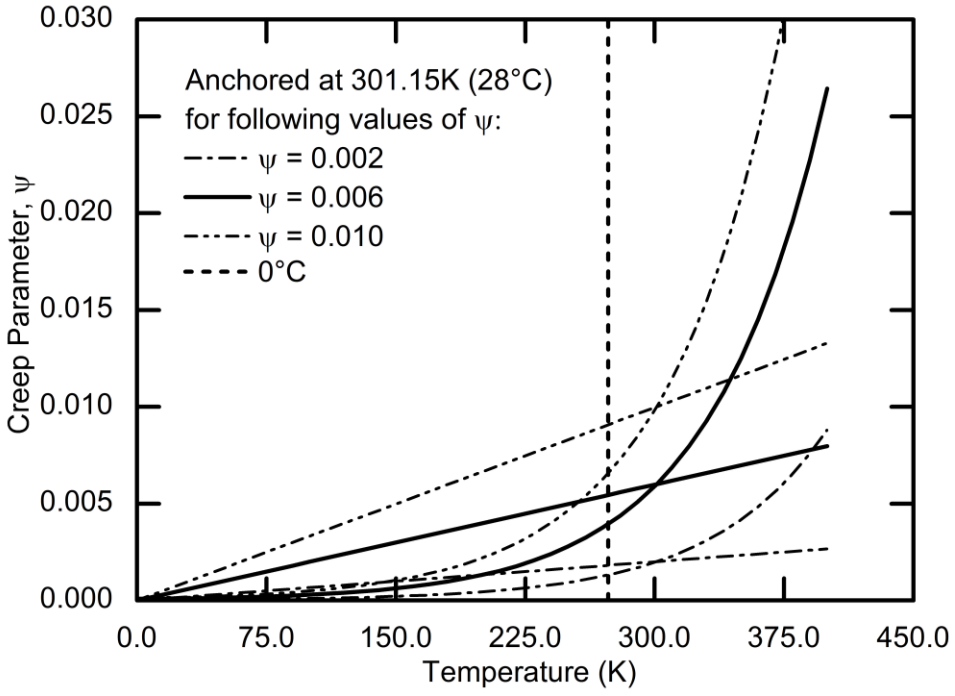

Figure 5.2: Linear and exponential relationships for the creep parameter versus temperature anchored at a temperature of 28°C (301.15K) for given values of ψ

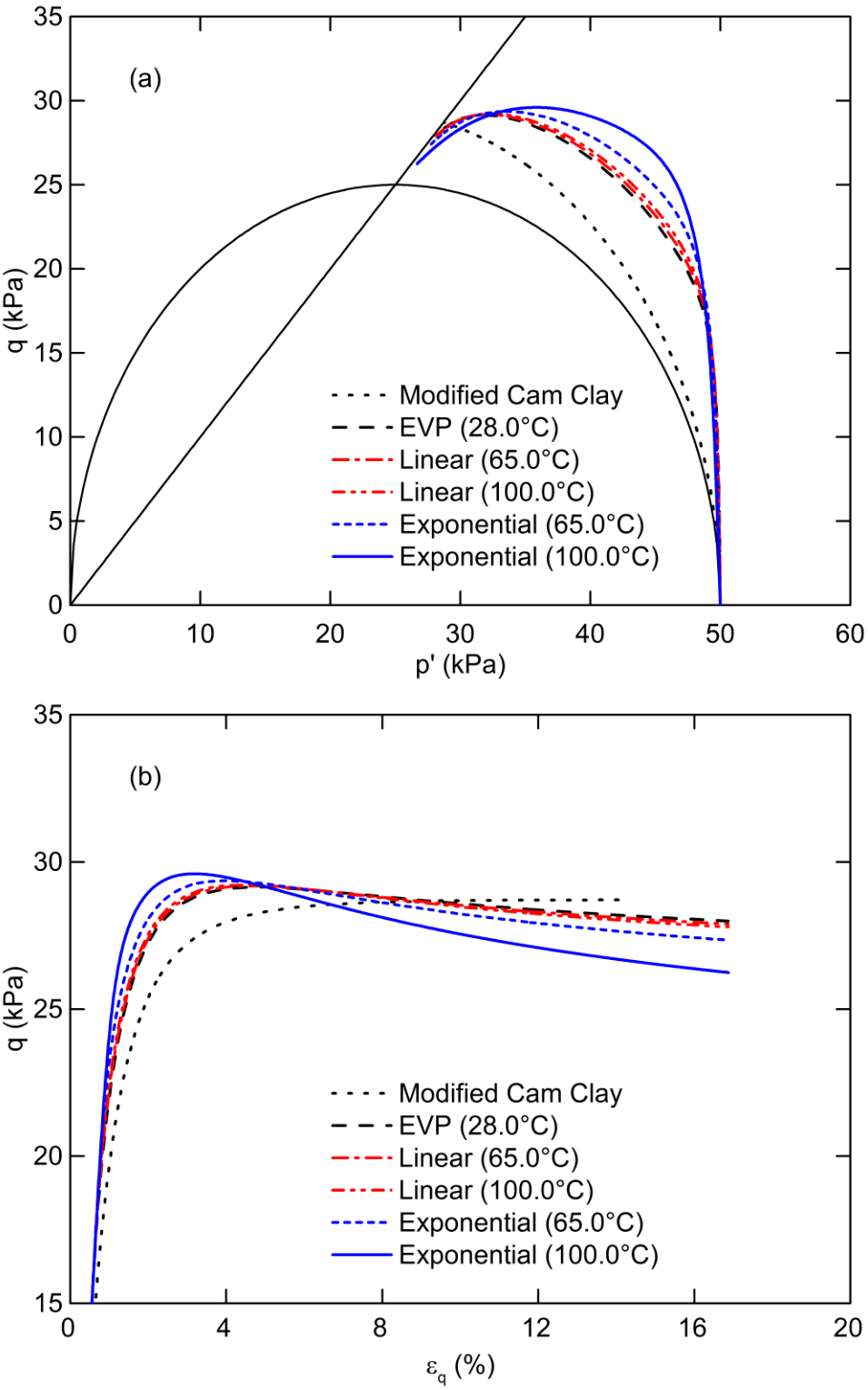

Figure 5.3: Response of the ETVP model on a CIŪ test for NC soil at a strain rate of 15.0%/day and (ψ_1:T_1) = (0.006:28.0°C): (a) stress space (q:p'); (b) deviatoric stress versus shear strain (q:ε_q)

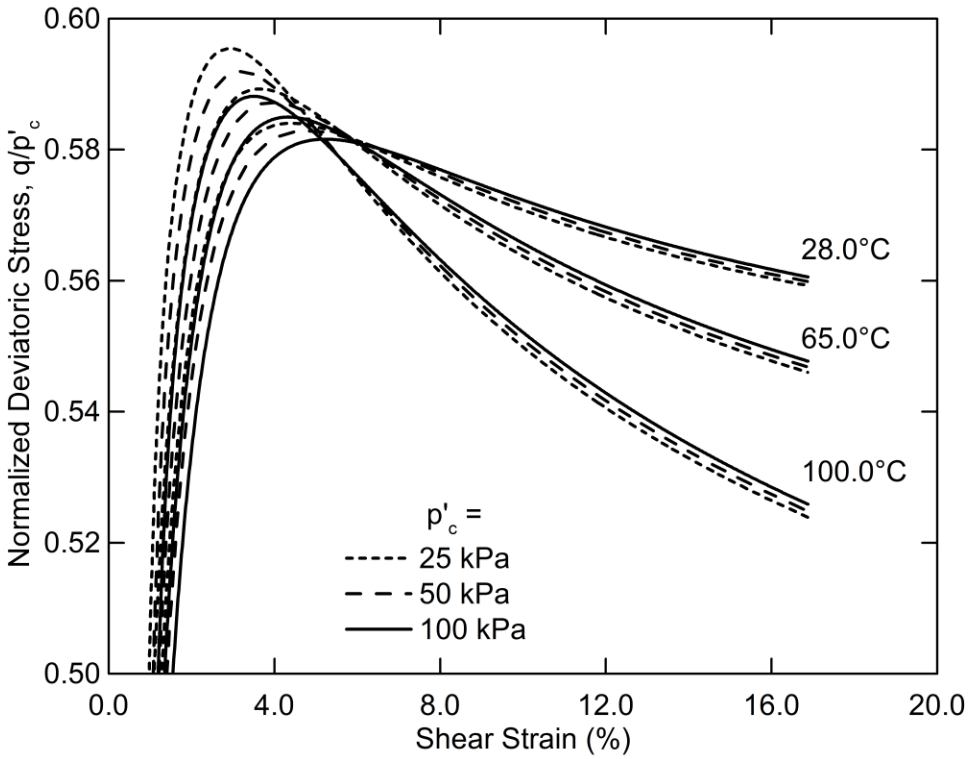

Figure 5.4: Comparison of temperature and preconsolidation pressure for CIŪ NC test at a strain rate of 15.0%/day for a stress-strain plot normalized to preconsolidation pressure

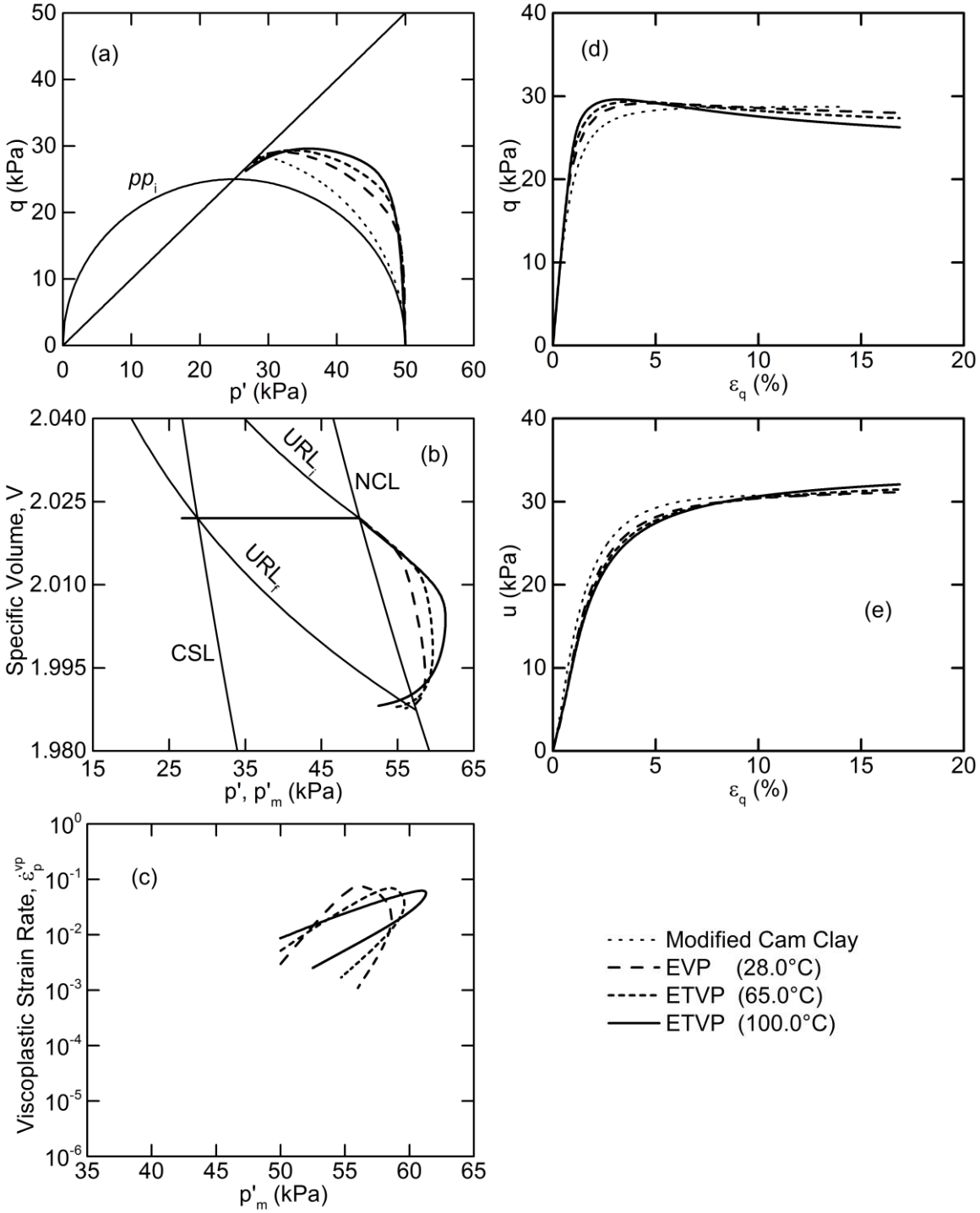

Figure 5.5: Response of the ETVP model on a CI$\bar{U}$ test for NC soil at a strain rate of 15.0%/day and (ψ_1:T_1) = (0.006:28.0°C): (a) stress space (q:p'); (b) compression space (V:p'); (c) viscoplastic volumetric strain rate versus isotropic mean effective stress ($\dot{\varepsilon}_p^{vp}$:p'_m); (d) deviatoric stress versus shear strain (q:ε_q); (e) pore water pressure versus shear strain (u:ε_q)

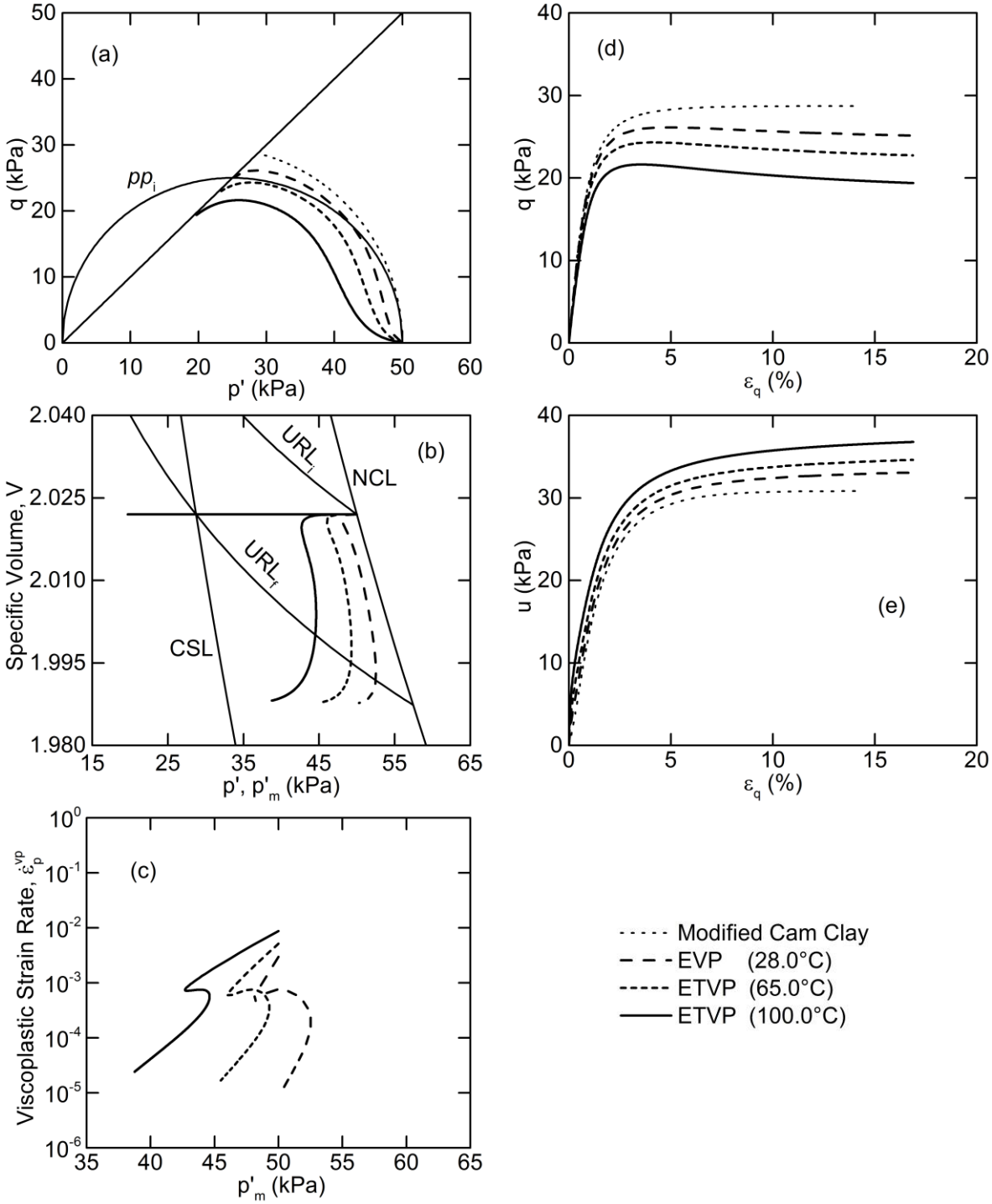

Figure 5.6: Response of the ETVP model on a CIŪ test for NC soil at a strain rate of 0.15%/day and (ψ_1:T_1) = (0.006:28.0°C): (a) stress space (q:p'); (b) compression space (V:p'); (c) viscoplastic volumetric strain rate versus isotropic mean effective stress ($\dot{\varepsilon}_p^{vp}$:p'_m); (d) deviatoric stress versus shear strain (q:ε_q); (e) pore water pressure versus shear strain (u:ε_q)

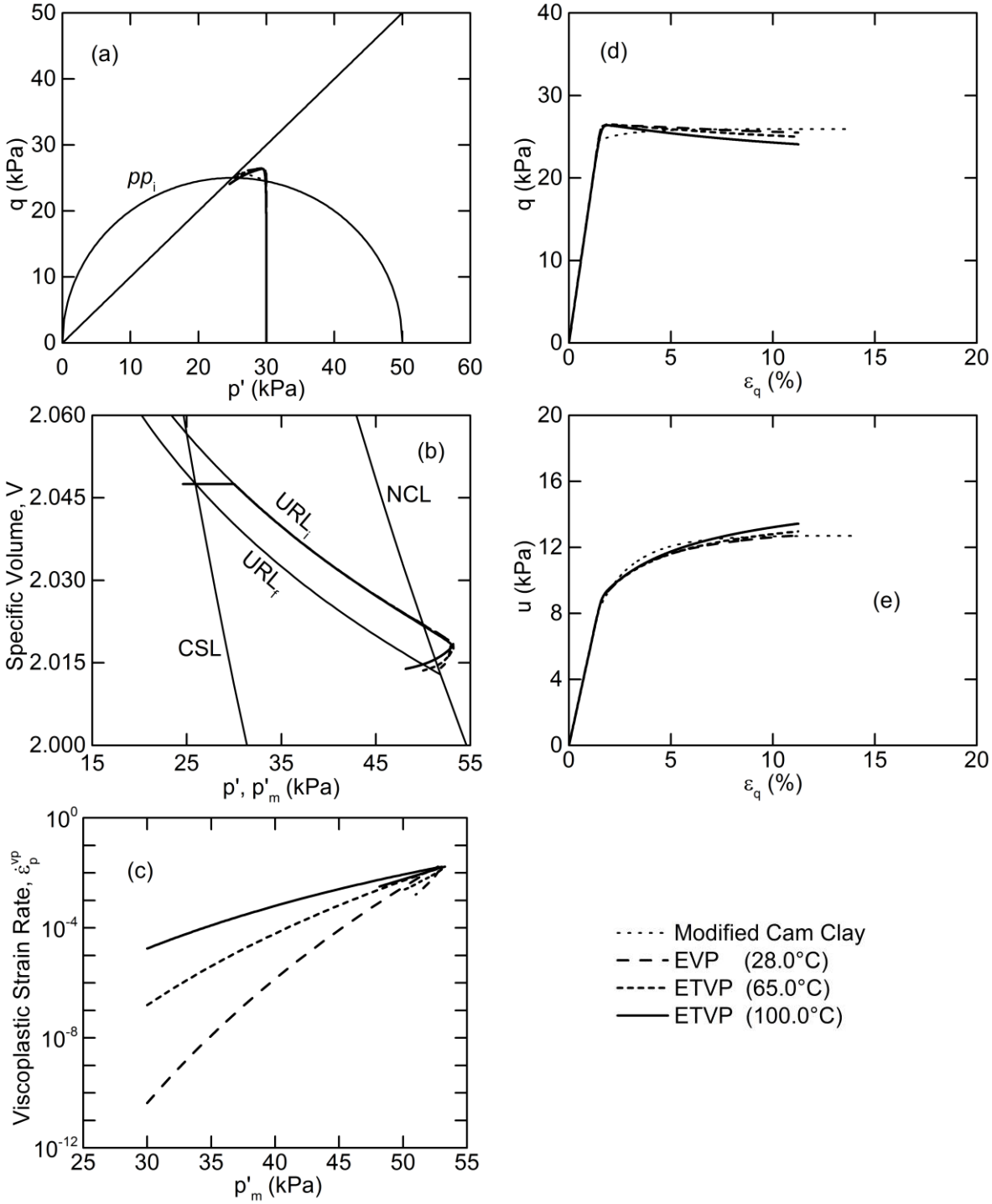

Figure 5.7: Response of the ETVP model on a CIŪ test for LOC soil at a strain rate of 15.0%/day and (ψ_1:T_1) = (0.006:28.0°C): (a) stress space (q:p'); (b) compression space (V:p'); (c) viscoplastic volumetric strain rate versus isotropic mean effective stress ($\dot{\varepsilon}_p^{vp}$:p'_m); (d) deviatoric stress versus shear strain (q:ε_q); (e) pore water pressure versus shear strain (u:ε_q)

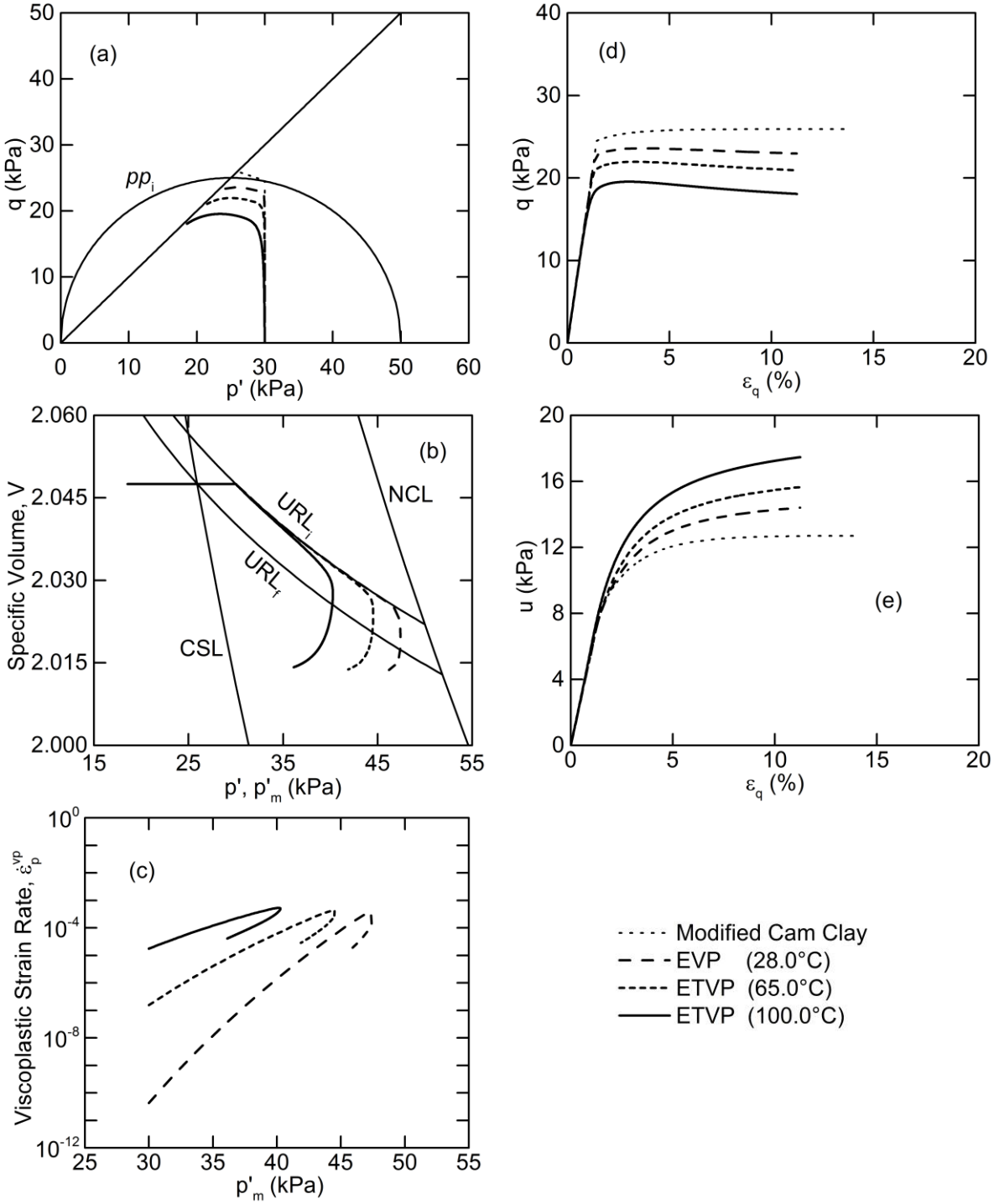

Figure 5.8: Response of the ETVP model on a CIŪ test for LOC soil at a strain rate of 0.15%/day and (ψ_1:T_1) = (0.006:28.0°C): (a) stress space (q:p'); (b) compression space (V:p'); (c) viscoplastic volumetric strain rate versus isotropic mean effective stress ($\dot{\varepsilon}_p^{vp}$:p'_m); (d) deviatoric stress versus shear strain (q:ε_q); (e) pore water pressure versus shear strain (u:ε_q)

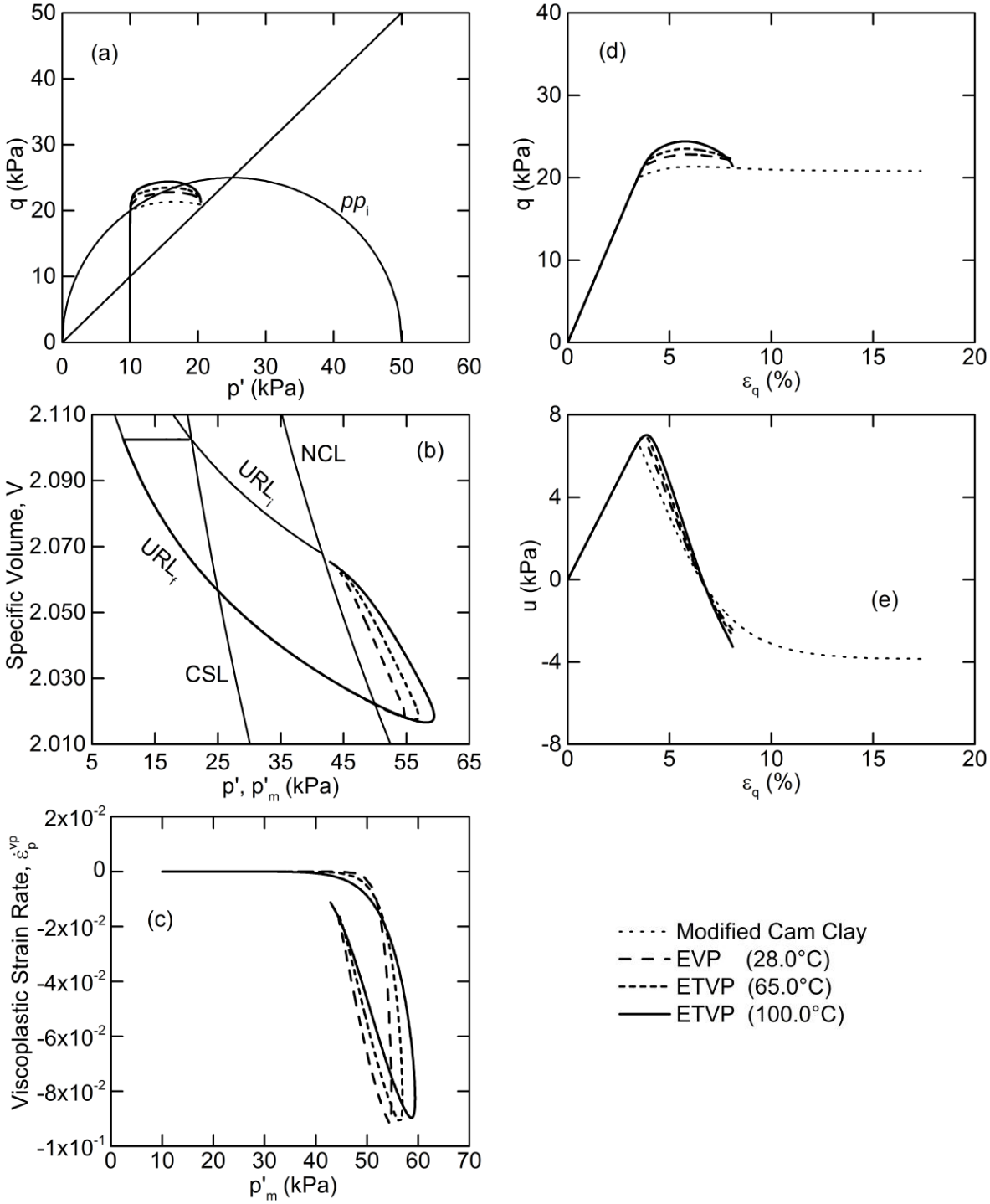

Figure 5.9: Response of the ETVP model on a CIŪ test for HOC soil at a strain rate of 15.0%/day and (ψ_1:T_1) = (0.006:28.0°C): (a) stress space (q:p'); (b) compression space (V:p'); (c) viscoplastic volumetric strain rate versus isotropic mean effective stress ($\dot{\varepsilon}_p^{vp}$:p'_m); (d) deviatoric stress versus shear strain (q:ε_q); (e) pore water pressure versus shear strain (u:ε_q)

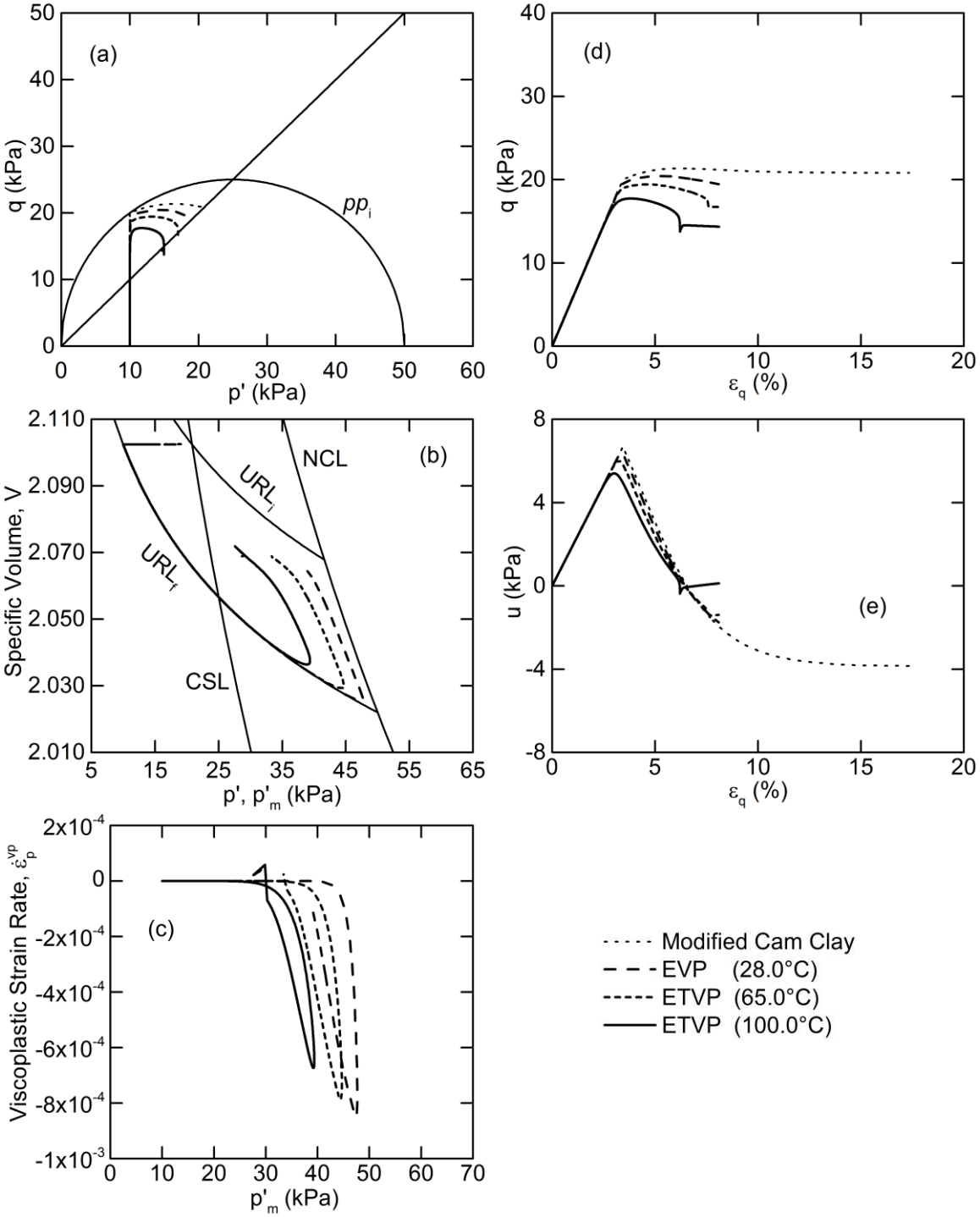

Figure 5.10: Response of the ETVP model on a CIŪ test for HOC soil at a strain rate of 0.15%/day and (ψ_1:T_1) = (0.006:28.0°C): (a) stress space (q:p'); (b) compression space (V:p'); (c) viscoplastic volumetric strain rate versus isotropic mean effective stress ($\dot{\varepsilon}_p^{vp}$:p'_m); (d) deviatoric stress versus shear strain (q:ε_q); (e) pore water pressure versus shear strain (u:ε_q)

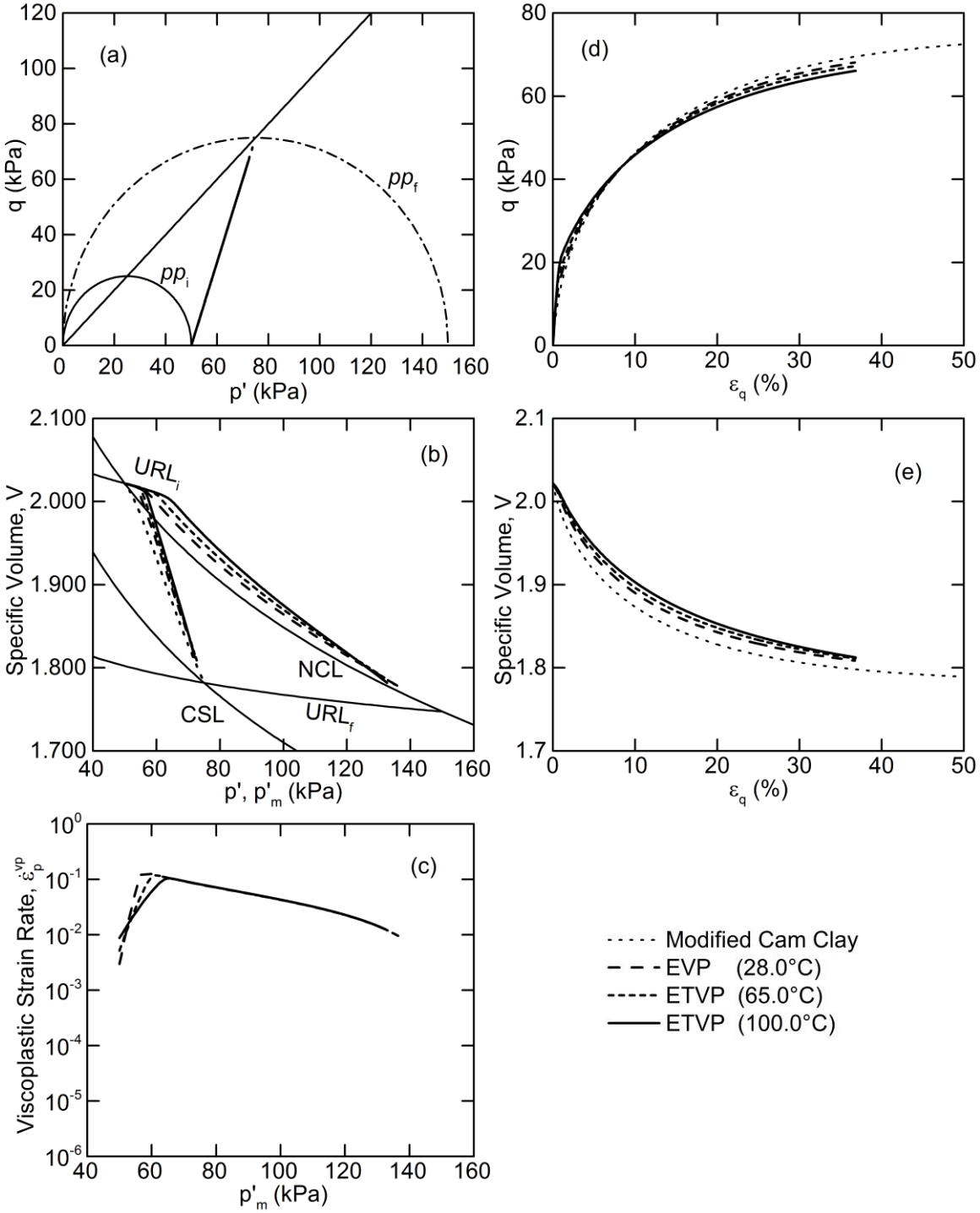

Figure 5.11: Response of the ETVP model on a CID test for NC soil at a strain rate of 15.0%/day and (ψ_1:T_1) = (0.006:28.0°C): (a) stress space (q:p'); (b) compression space (V:p'); (c) viscoplastic volumetric strain rate versus isotropic mean effective stress ($\dot{\varepsilon}_p^{vp}$:p'_m); (d) deviatoric stress versus shear strain (q:ε_q); (e) specific volume versus shear strain (V:ε_q)

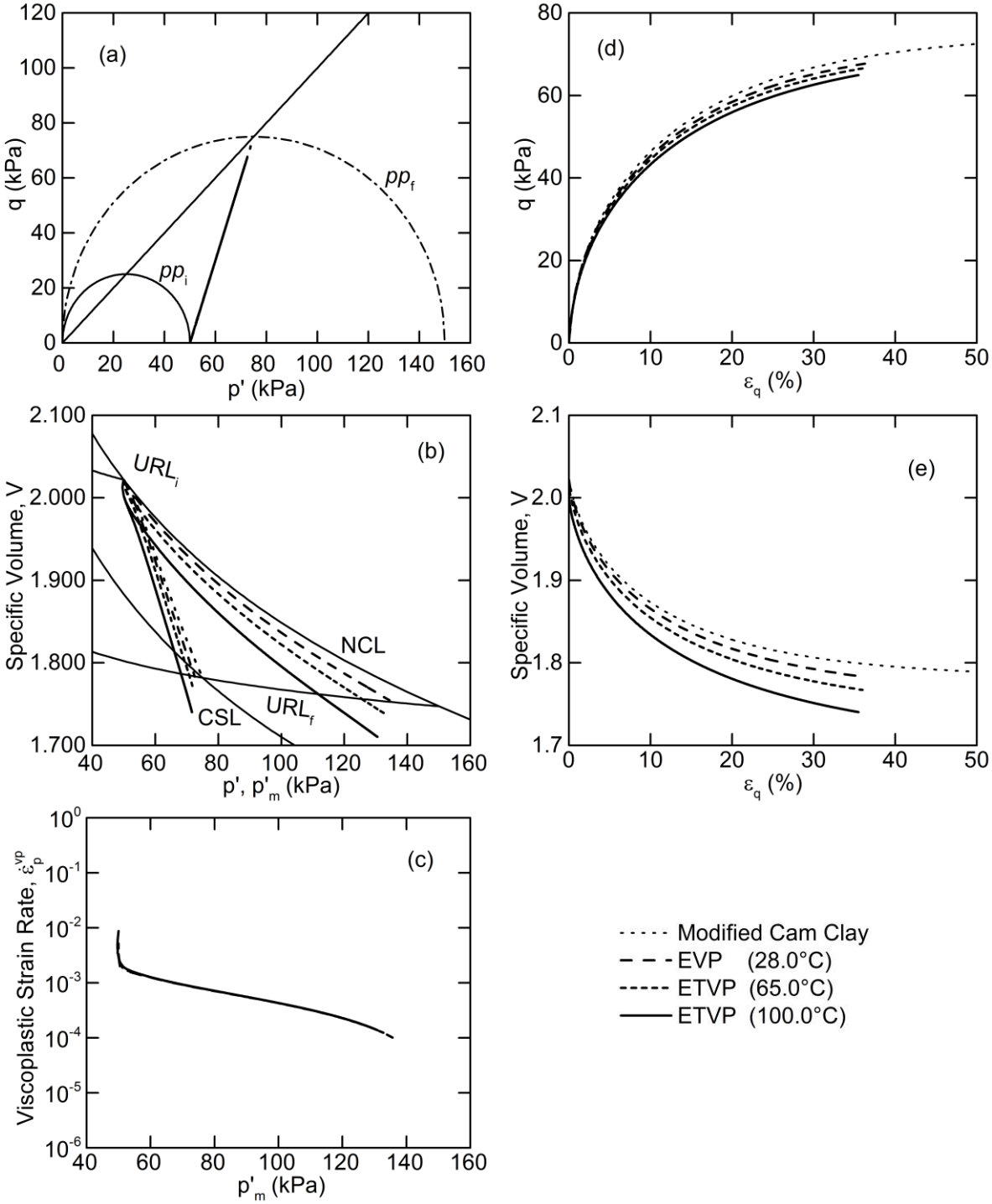

Figure 5.12: Response of the ETVP model on a CID test for NC soil at a strain rate of 0.15%/day and (ψ_1:T_1) = (0.006:28.0°C): (a) stress space (q:p'); (b) compression space (V:p'); (c) viscoplastic volumetric strain rate versus isotropic mean effective stress ($\dot{\varepsilon}_p^{vp}$:p'_m); (d) deviatoric stress versus shear strain (q:ε_q); (e) specific volume versus shear strain (V:ε_q)

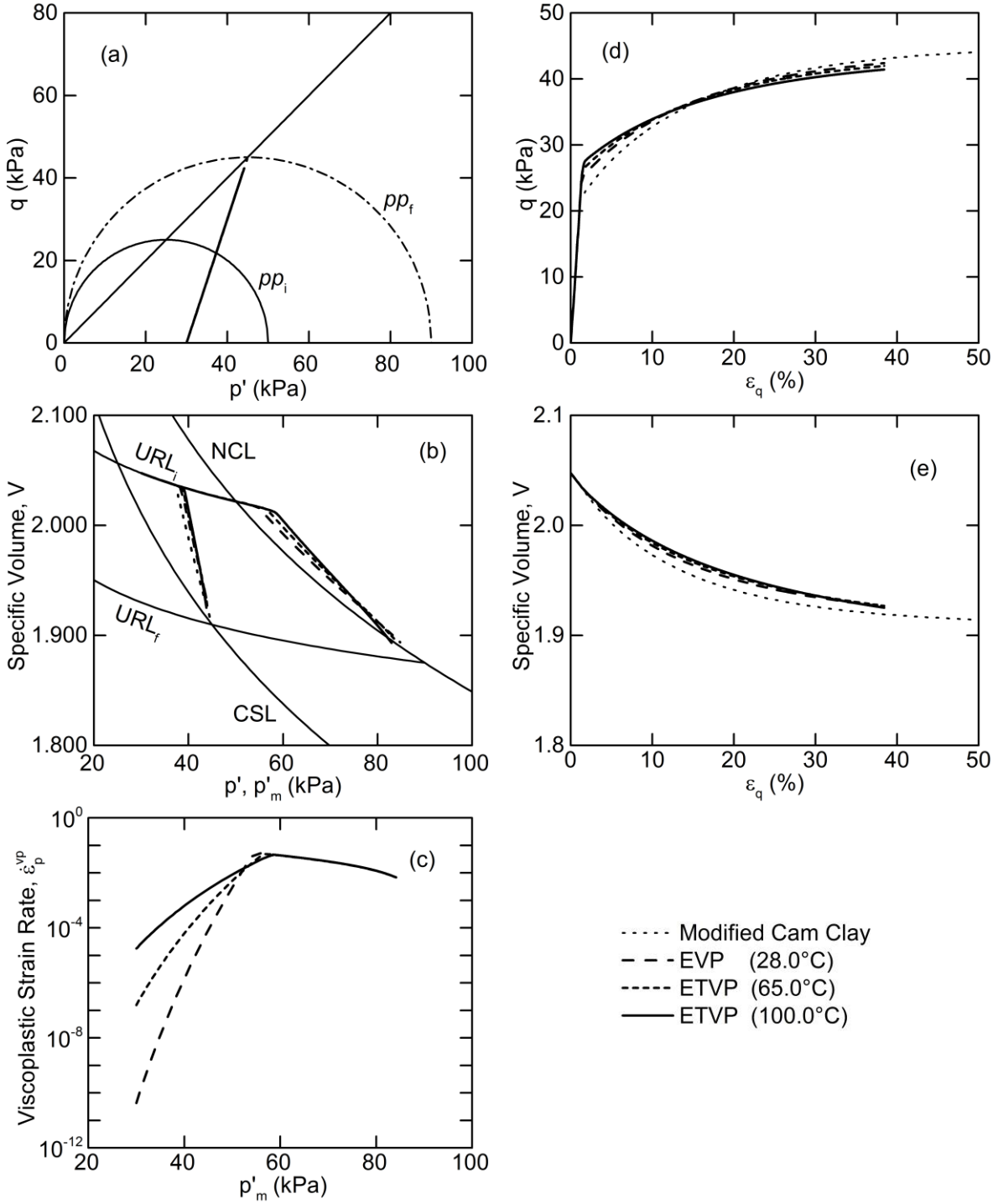

Figure 5.13: Response of the ETVP model on a CID test for LOC soil at a strain rate of 15.0%/day and (ψ_1:T_1) = (0.006:28.0°C): (a) stress space (q:p'); (b) compression space (V:p'); (c) viscoplastic volumetric strain rate versus isotropic mean effective stress ($\dot{\varepsilon}_p^{vp}$:p'_m); (d) deviatoric stress versus shear strain (q:ε_q); (e) specific volume versus shear strain (V:ε_q)

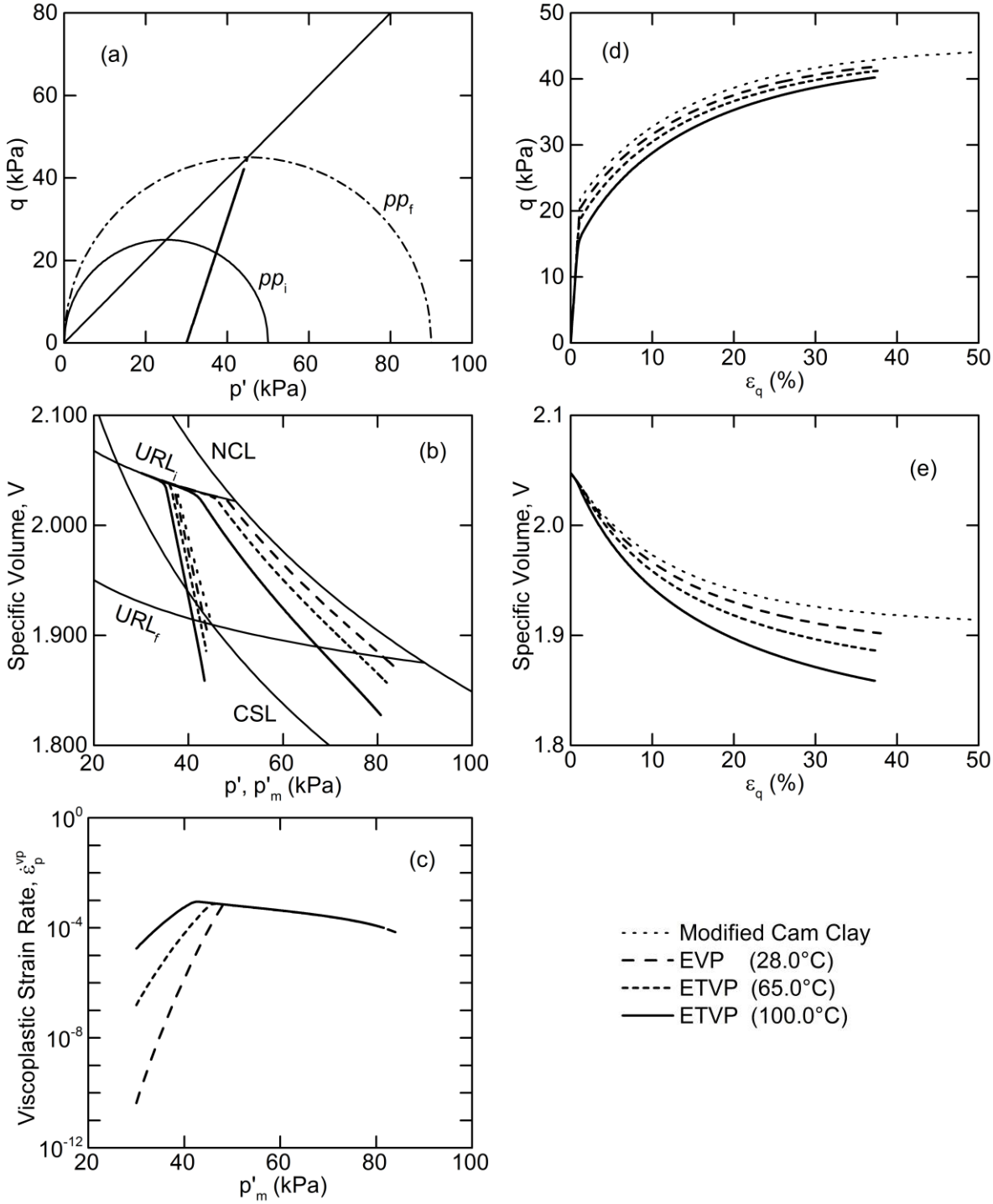

Figure 5.14: Response of the ETVP model on a CID test for LOC soil at a strain rate of 0.15%/day and (ψ_1:T_1) = (0.006:28.0°C): (a) stress space (q:p'); (b) compression space (V:p'); (c) viscoplastic volumetric strain rate versus isotropic mean effective stress ($\dot{\varepsilon}_p^{vp}$:p'_m); (d) deviatoric stress versus shear strain (q:ε_q); (e) specific volume versus shear strain (V:ε_q)

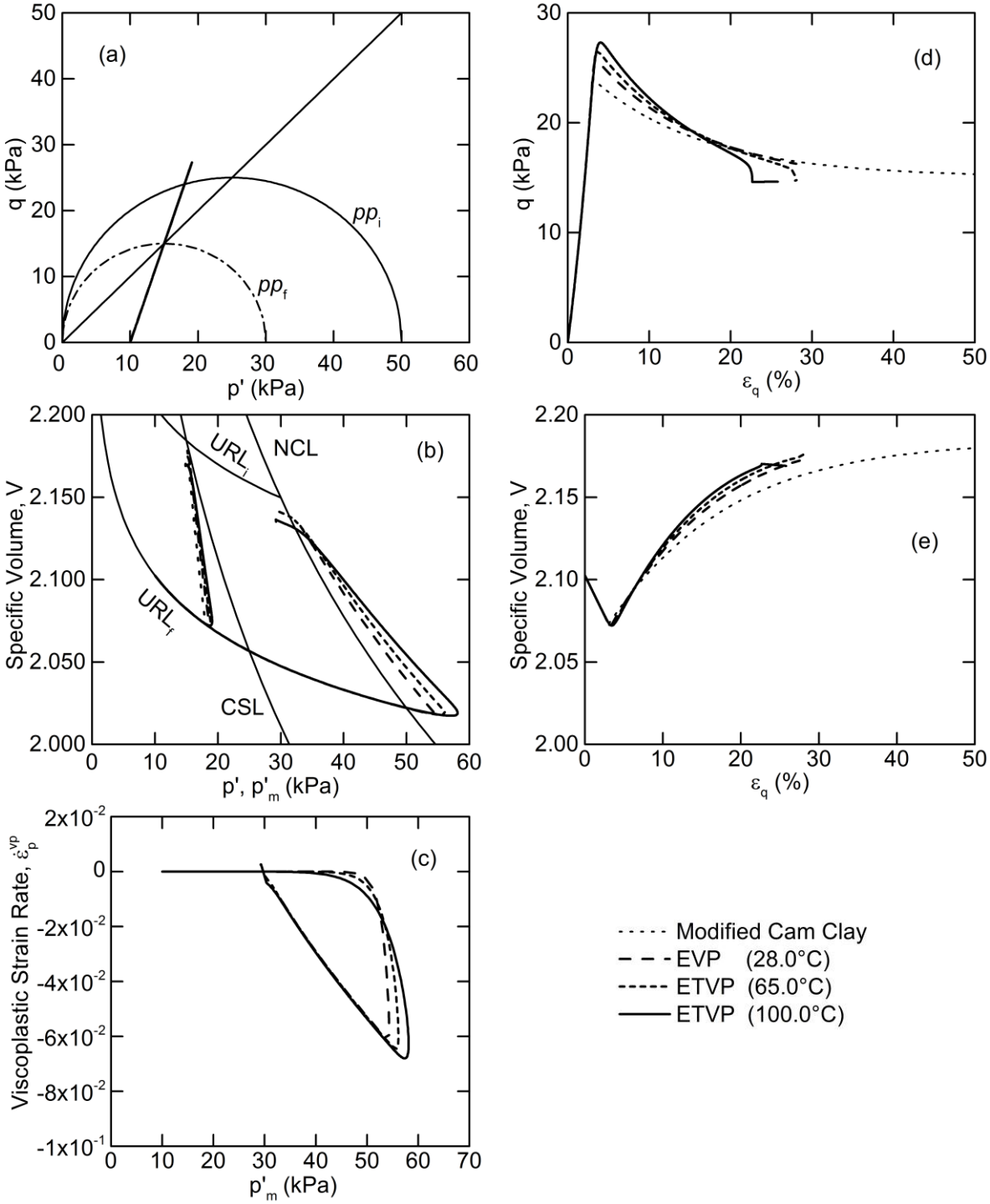

Figure 5.15: Response of the ETVP model on a CID test for HOC soil at a strain rate of 15.0%/day and (ψ_1:T_1) = (0.006:28.0°C): (a) stress space (q:p'); (b) compression space (V:p'); (c) viscoplastic volumetric strain rate versus isotropic mean effective stress ($\dot{\varepsilon}_p^{vp}$:p'_m); (d) deviatoric stress versus shear strain (q:ε_q); (e) specific volume versus shear strain (V:ε_q)

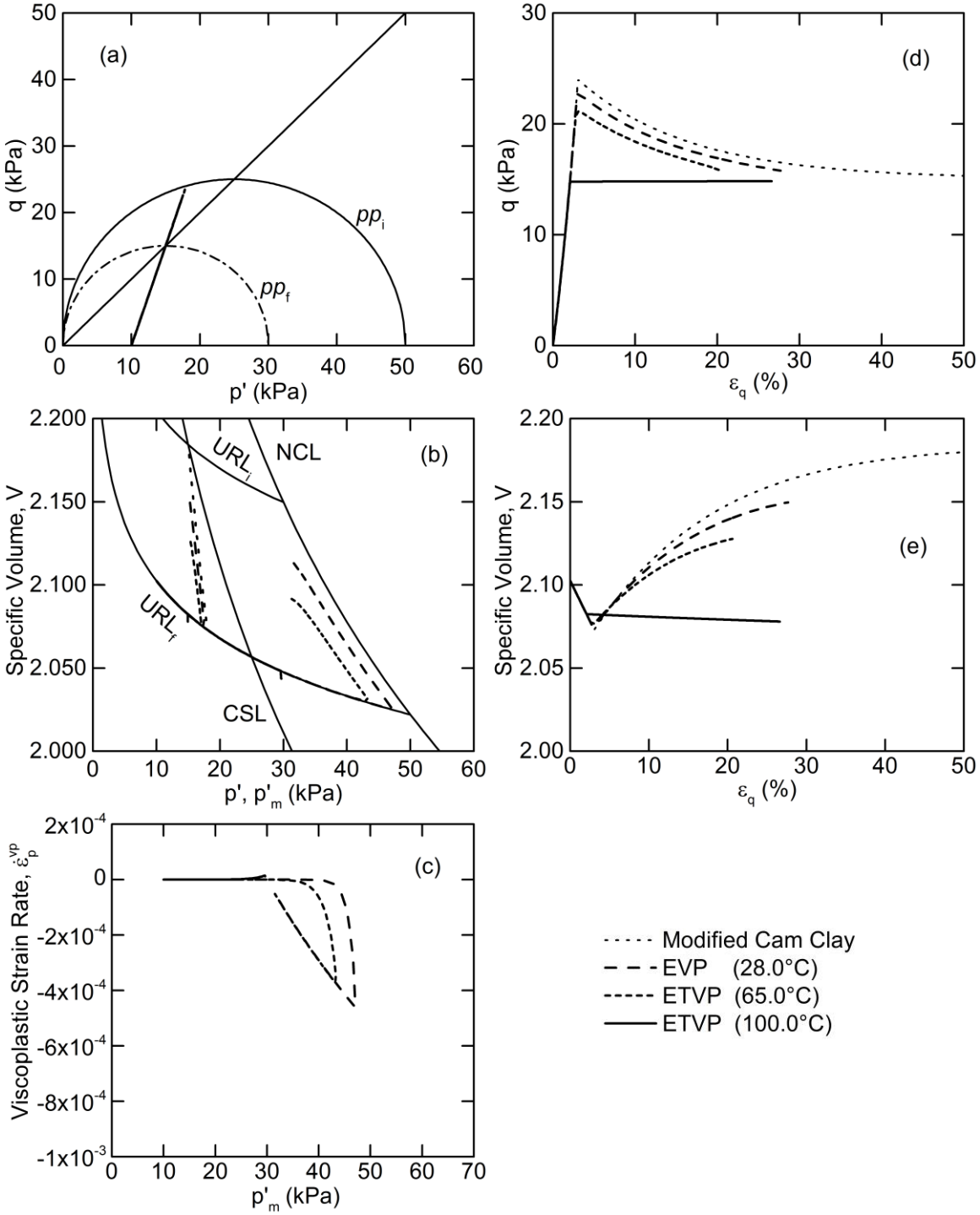

Figure 5.16: Response of the ETVP model on a CID test for HOC soil at a strain rate of 0.15%/day and (ψ_1:T_1) = (0.006:28.0°C): (a) stress space (q:p'); (b) compression space (V:p'); (c) viscoplastic volumetric strain rate versus isotropic mean effective stress ($\dot{\varepsilon}_p^{vp}$:p'_m); (d) deviatoric stress versus shear strain (q:ε_q); (e) specific volume versus shear strain (V:ε_q)

Chapter 6: Analysis and Discussion

6.1 Introduction

An elastic thermo-viscoplastic (ETVP) model was proposed in Chapter 5. This model was built upon the EVP model framework developed by Kelln (2007). Both linear and exponential relationships describing the effect of temperature on secondary compression (creep) were incorporated into the model. A sensitivity analysis was performed to gain an understanding of the performance of the model and the response of the model is presented. This chapter examines the response of the model and compares the performance to published data. The intended goal is to determine if the incorporation of temperature into the semi-empirical framework has been successfully achieved and if the result produced significant changes in the stress-strain behaviour of clay.

6.2 An Analysis of the ETVP Model

This section presents a detailed analysis of the response of the ETVP model. The effect of temperature modeled by means of the exponential relationship for $\psi = \psi(T)$ is examined more closely. The response of the model is referenced to the effect of temperature on different types of triaxial tests, strain rates, overconsolidation ratios and other parameters including peak strength, large strain strength, pore water pressures, specific volume, among others.

As mentioned in Chapter 5, this analysis focuses on the response of the model

using the exponential relationship for ψ = 0.006 at 28.0°C (Figure 5.2) and a preconsolidation pressure of 50.0 kPa. The impact of the exponential relationship was, as expected, greater than that of the linear relationship and provides a better analysis on the effect of temperature on the model.

6.2.1 Terminology

Abbreviated terminology has been used to simplify references to certain parameters used in this analysis. Chapter 5 discussed that the two types of triaxial (isotropic consolidation) tests used in this modeling have been abbreviated as CID for drained and CI$\bar{U}$ for undrained tests. Three overconsolidation ratios (OCRs) were used in the sensitivity analysis; 1.00 for normally consolidated, 1.67 for lightly overconsolidated, and 5.00 for heavily overconsolidated. These OCRs are abbreviated as NC, LOC, and HOC, respectively. The abbreviation "EOT" will be used to refer to the "end of test". This EOT point changes depending on the aforementioned parameters but generally refers to a point near the maximum percentage of shear strain obtained from the particular set of parameters and prior to any anomalies in the model's response. The percentage shear strain for this EOT point will be referred to on a per case basis. The term "peak" refers to the maximum deviatoric stress (strength) obtained in a respective test. Lastly, for strain rates, the unit of time "day" is abbreviated simply as "d" and the strain rates of 15.0%/d and 0.15%/d are referred to as "fast" and "slow", respectively.

6.2.2 Critical State

Chapter 5 mentions that the responses of the ETVP model end before critical state is fully achieved. Critical state is defined such that:

[Eq. 6.1] $$\frac{\partial q}{\partial \varepsilon_q} = \frac{\partial p'}{\partial \varepsilon_q} = \frac{\partial u}{\partial \varepsilon_q} = \frac{\partial V}{\partial \varepsilon_q} = 0$$

Upon visual inspection, the author determined that the modeled tests that ended closest to critical state were the CI$\bar{U}$ NC and LOC tests. The ratios in Equation 6.1 were calculated for these tests for each temperature and strain rate within the last 1.0% shear strain. The values presented in Tables 6.1 and 6.2 clearly indicate that critical state was not achieved, although three trends can be seen: (1) a decrease in strain rate usually corresponds to a decrease in the ratios; (2) an increase in temperature corresponds to a increase in the ratios; and (3) an increase in OCR corresponds to a increase in the ratios.

6.2.3 Interpretation of CI$\bar{U}$ tests

The response of the model to CI$\bar{U}$ tests was presented in Figures 5.5 to 5.10 for NC, LOC, and HOC tests. For all OCRs, the effects of combining viscosity and temperature are noticeable. Generally speaking, the slow strain rate allows more (larger) plastic strains to develop than the fast strain rate. The effect of increasing temperature amplifies this effect, thereby providing stress-strain relationships that better reflect the complexity of clay behaviour (e.g. strain softening).

For NC, the fast strain rate produces higher peak deviator stresses for increasing temperature but, due to strain softening, produces correspondingly lower stresses at larger shear strains (EOT) (Figure 5.5d). Conversely, the slow strain rate produces successively lower peak deviator stresses for increasing temperature, as well as lower stresses toward EOT as a result of strain softening (Figure 5.6d). These strengths are reflected in the pore water pressures (Figures 5.5e and 5.6e) such that higher pore water pressures result in lower effective stresses and vice versa. Strain softening is seen in testing real clays but

the reasons are not commonly known. It is not seen in MCC modeling. The ETVP (and EVP) models generate strain softening in NC tests due to the (thermo-) viscoplastic formulation and the rate at which (thermo-) viscoplastic strains develop.

The slow strain rate, as mentioned, allows the development of larger plastic strains and results in a greater tendency to cause plastic volumetric compression than the fast strain rate. Since the test is confined to a CI$\bar{U}$ test that cannot experience a volume change, the pore water pressures must increase as a response to counter the plastic volumetric compression. By definition, this results in an accelerated decrease in mean effective stress, p' (Figure 5.6a versus Figure 5.5a).

The viscoplastic strain rates (Figures 5.5c and 5.6c) for both fast and slow CI$\bar{U}$ tests correspond to changes in the plastic potential. As the tests approach the peak deviator stress, there is an increase in the rate of viscoplastic straining and the plastic potential (p'_m) increases (Figures 5.5b and 5.6b). As the tests pass the peak deviator stress and approach large strain 'failure' along the critical state line (M-Line) there is a decrease in the rate of viscoplastic straining and the plastic potential. (It should be noted that the peak deviator stress corresponds to neither the calculated increment for the maximum viscoplastic strain rate nor the maximum plastic potential.) The initial decrease observed in the viscoplastic strain rate for the slow NC CI$\bar{U}$ test (Figure 5.6c) is suspected to be due to the initial development of viscoplastic strains (and pore water pressures) at the start of the test. The shallower lines at higher temperatures (Figure 5.5c and 5.6c) imply that the change in the rate of viscoplastic straining decreases as temperature increases.

With a few exceptions, the CI$\bar{U}$ LOC tests (Figures 5.7 and 5.8) present similar responses of the model as observed for NC tests. The fast strain rate produces a similar

elastic response for all temperatures within the yield surface. Conversely, the slow strain rate begins to deviate from a purely elastic response once the viscoplastic strain rate (Figure 5.8c) becomes large enough to produce a plastic volumetric compression. This plastic volumetric compression is countered with an increase in pore water pressure (Figure 5.8e) and a decrease in mean effective stress (Figure 5.8a).

A similar response is observed for the CI$\bar{U}$ HOC tests: the fast strain rate produces higher peak deviator stresses at higher temperatures (Figure 5.9d); and slow strain rate produces lower peak deviator stresses at higher temperatures (Figure 5.10d). The difference lies with the response of the pore water pressure (Figures 5.9e and 5.10e). For stress ratios ($\eta = \delta q/\delta p'$) below the critical state line ($\eta < M$), the behaviour is primarily plastic volumetric compression (hence an increase in pore water pressure). Above the critical state line ($\eta > M$), behaviour transitions to plastic volumetric expansion and leads eventually to a decrease in pore water pressure. The peak of the pore water pressure (Figures 5.9e and 5.10e) does not coincide with a stress ratio of $\eta = M$, but rather a gradual (incremental) transition from compressive to expansive behaviour. Again, this is what is seen in laboratory tests but is missing from MCC modeling.

As discussed in Chapter 5, anomalies sometimes presented themselves in the form of a breakdown in the model formulations. They are evidenced for example, as inexplicable drops in strength and pore water pressure. For the CI$\bar{U}$ tests, this is primarily visible in the slow HOC test (Figures 5.10d and 5.10e). The author believes that these anomalies are a combination of the size of the increments used in the modeling, the axial strain rate, and the value of $\psi(T)$ (where $\psi(T)$ is calculated from the exponential

relationship defined in Equation 5.15). As a result, EOT values are more difficult to compare since critical state was not being achieved.

Tables 6.3, 6.4 and 6.5 respectively summarize values of peak deviator stress and EOT deviator stress. The corresponding pore water pressures are summarized for each temperature (3.0, 28.0, 65.0, and 100.0°C) and strain rate (15.0%/d, 1.50%/d, and 0.15%/d) in for CI$\bar{U}$ tests under NC, LOC, and HOC conditions. Calculated values such as the pore water pressure parameter, $A = du/dq$ are provided for peak strength and EOT. In addition, the strength ratio of q_f/q_p is calculated. The value of shear strain at which EOT is taken is also provided for reference. These values are illustrated graphically versus temperature as follows: Figures 6.1, 6.2, and 6.3 for NC tests; Figures 6.4, 6.5, and 6.6 for LOC tests; and Figures 6.7, 6.8, and 6.9 for HOC tests. Also included in the tables and figures are MCC values.

The CI$\bar{U}$ NC tests illustrate that both peak and EOT strengths (Figures 6.1a,b) diverge as temperature increases for the tested strain rates. For the EOT values, the three strain rates show a decrease in strength as temperature increases, albeit at different rates. The peak values show a decrease in strength for the medium and slow strain rates, but show a slight increase for the fast strain rate. This slight increase in strength may be explained such that for this strain rate, viscoplastic strains develop at a slower rate as temperature increases. (The apparent slopes in Figure 5.5c are shallower than in Figure 5.6c indicating a slower rate of change for viscoplastic straining.) Furthermore, Figures 6.1a,b indicate that as temperature decreases, these peak and EOT strengths converge to (separate) strength values such that strain rate would have a negligible effect. This is also evident in Figure 6.1c where the ratio of q_f/q_p converges as well. Similar divergent

behaviour is observed in Figures 6.2 and 6.3 for pore water pressure and the pore water pressure parameter, *A* as temperature increases.

Nearly identical behaviour is observed for the CI$\bar{U}$ LOC tests in Figures 6.4, 6.5, and 6.6. The divergence is less prominent and there is less spread in the values. One exception can be seen in Figure 6.4c. The same general behaviour as in Figure 6.1c is indicated, but the difference between strain rates is more obvious. Another exception can be noted for pore water pressures at q_p for 100°C. Inexplicably pore water pressures increase for the fast and slow strain rates while the medium strain rate continues to show a decrease (Figure 6.5a).

Values for CI$\bar{U}$ HOC tests are more difficult to compare effectively. Peak strengths and pore water pressures are captured, but the EOT values were taken from 6.0% shear strain (a value just past the peak). As such, the author does not feel a relationship to temperature can be properly ascertained from the EOT values. Given the behaviour of the tests, this may indicate a limitation in the model for the combination of OCR, strain rates, and temperatures (values of ψ). For peak values shown in Figures 6.7a and 6.8a, similar divergent behaviour can be seen for an increase in temperature as was seen in the LOC and NC tests. The increase in peak strength with temperature is more noticeable at the fast strain rate for HOC tests.

6.2.4 Interpretation of CID tests

The response of the model to the effects of viscosity and temperature in CID tests is presented in Figures 5.11 to 5.16 for NC, LOC, and HOC tests. As with CI$\bar{U}$ tests, the

slow strain rate allows more (larger) plastic strains to develop than the fast strain rate. Similar to the CI$\bar{U}$ tests, the effect of increasing temperature amplifies this effect, thereby providing stress-strain relationships that better reflect the complexity of clay behaviour.

The primary difference between the CI$\bar{U}$ and CID tests is that pore water pressures are allowed to dissipate in the CID tests and so volumes are not confined to be constant. Therefore changes in the specific volume, V are examined. (The author's ETVP model has not been coupled with a pore water pressure dissipation model. It assumes that tests are run sufficiently slowly that no excess pore water pressures develop.) Peak and EOT values for deviator stress and specific volume are equivalent for NC and LOC tests, whereas HOC tests provide different values.

For NC, the fast and slow strain rates both produce successively lower peak deviator stresses the temperature increases (Figure 5.11d and 5.12d). Since the viscoplastic formulation allows for the development of viscoplastic strains right from the beginning of the test, a rapid change in the viscoplastic strain rate is initially observed and is followed by slowly decreasing viscoplastic strain rate (Figures 5.11c and 5.12c). This indicates that volumetric compression dominates the behaviour observed in this test.

The change in specific volume as a function of strain rate and temperature can be tracked in Figures 5.11b,e and 5.12b,e. The response of the model at the fast strain rate appears be converging toward the same value calculated in the MCC model. However, for a given value of shear strain, it appears that the specific volume is increasing with an increasing temperature thereby implying volumetric expansion. In contrast, the slow strain rate produces successively lower specific volumes for increasing temperature and does not indicate a possible convergence point.

The LOC tests yield very similar responses with one primary exception; a distinct transition point from the stiff elastic region to the plastic region (Figures 5.13d and 5.14d). It is incorrect to assume that the elastic region is purely elastic since viscoplastic strains are allowed to develop at the onset of the test. At the transition point, a marked increase volumetric compression (Figures 5.13b and 5.14b) is seen, followed by a now-decreasing viscoplastic strain rate (Figures 5.13c and 5.14c). Kelln (2007) explains "the transition to a predominantly plastic response results from the increase in viscoplastic strain rate and not simply because of a sudden transition to a yielded condition."

The CID HOC tests also produce distinct transition points from the stiff elastic region to the plastic region (Figures 5.15d and 5.16d) but then, strain softening behaviour is observed. This corresponds to a change in direction in stress-space (Figures 5.15a and 5.16a) where the test approaches the yield surface and then begins to decrease back to critical state with plastic volumetric softening. For stress ratios ($\eta = \delta q/\delta p'$) below the critical state line ($\eta < M$) behaviour is primarily volumetric compression (hence an decrease in specific volume). Above the critical state line ($\eta > M$), there is a transition to dilative behaviour (see negative viscoplastic strain rates in Figures 5.15c and 5.16c), leading to an increase in specific volume (Figures 5.15e and 5.16e).

In regards to temperature effects, an increase in temperature results in successively higher peak strengths for the fast strain rate, and successively lower peaks for the slow strain rate. However, noting a crossover of the stress-strain paths approaching the EOT in Figure 5.15d, it also appears that higher temperatures at the fast strain rate lead to more strain softening. For the EOT values of specific volume, it

appears that the higher strain rate yields more dilation with an increase in temperature, whereas less dilation is observed at the slow strain rate.

As mentioned in Chapter 5 and earlier in this chapter for CIŪ tests, anomalies presented themselves in the form of a breakdown in the model formulations. For the CID tests, this is primarily visible in the slow HOC test (Figures 5.16d and 5.16e). Again, the author believes that these anomalies are a combination of the size of the increment, the axial strain rate, and the value obtained for $\psi(T)$ (Equation 5.13). Despite larger strains than what was achieved in the CIŪ tests, critical state was not achieved.

Values of peak deviator stress, EOT deviator stress, and the corresponding specific volumes are summarized for each temperature (3.0, 28.0, 65.0, and 100.0°C) and strain rate (15.0%/d, 1.50%/d, and 0.15%/d) in Tables 6.6, 6.7 and 6.8 for CID tests under NC, LOC, and HOC conditions, respectively. Except for HOC tests, peak deviator stress is equivalent to the EOT deviator stress; the strength ratio of q_f/q_p is calculated only for HOC tests. The value of shear strain at which EOT is taken is also provided for reference. These values are illustrated graphically versus temperature: Figure 6.10 for NC tests; Figure 6.11 for LOC tests; and Figures 6.12 and 6.13 for HOC tests. Also included in the tables and figures are MCC values.

The CIŪ NC tests illustrate that peak (EOT) strengths (Figure 6.10a) diverge as temperature increases for the tested strain rates. The three strain rates show a decrease in strength as temperature increases, albeit at different rates. The EOT values show a decrease in specific volume for the medium and slow strain rates, but show a slight increase for the fast strain rate. Kelln (2007) explains that a faster strain rate requires a greater mean effective stress and deviator stress before the viscoplastic strain rate is large

enough to cause significant plastic strains for a particular calculated increment. With respect to temperature, this explanation may be extended such that viscoplastic strains develop at a slower rate as temperature increases. The apparent slopes in Figure 5.11c are shallower for increasing temperature, indicating a slower rate of change for viscoplastic straining. In addition, the sharp decrease in viscoplastic strain rate occurs at a higher isotropic mean effective stress.

Nearly identical behaviour is observed for the CID LOC tests in Figure 6.11. One exception can be seen in Figure 6.11b. While the same general behaviour as Figure 6.10b is indicated, the difference for the fast strain rate is noticeable. In the NC tests, the specific volumes continue to increase with temperature, whereas in LOC tests, the specific volumes follow the same trend but show decrease in the volume for 100.0°C. This is indicated numerically in Tables 6.6 and 6.7 for a strain rate of 15.0%/d.

Similar divergent behaviour is observed in the CID HOC tests as temperature increases even though higher peak deviator stresses are expected at higher temperatures for the fast strain rate (Figure 6.12a) and the EOT deviator stresses are expected to decrease with temperature. Figure 6.12b illustrates this as a (relatively) constant relationship but it is a function of where EOT is chosen. If the response of the model yielded larger shear strains, the author is confident the model would show a gradual decrease in EOT strength with an increase in temperature. Figure 6.13a illustrates an increase in specific volumes for all strain rates as temperature increases. This implies that for HOC tests, the transition between predominantly elastic behaviour and predominantly plastic behaviour occurs sooner. It can be seen in Figures 5.15c and 5.16c that a negative viscoplastic strain rate develops sooner for an increase in temperature. Figure 6.13a does

not imply that an increase in temperature produces less volumetric compression within the elastic region.

6.2.5 Model Validation

A comparison to laboratory testing or to published results from other researchers is needed to validate the model. Bearing in mind the author's other work on thermal conductivity and thermal modeling, it was decided that a triaxial testing program at elevated temperatures would not be undertaken. This meant that a comparison could only be made with previously published data. This task has proved to be difficult.

Chapter 2 presented a brief discussion on the findings from other researchers regarding the effects of temperature. Published information includes information pertinent to those researchers' arguments but do not typically include all information regarding their testing program. For example, Hueckel and Baldi (1990) present arguments revolving around deviator stress, axial strain, volumetric strain and the yield surface, but do not provide any information regarding compression space (other than a reduction in volume with heating) or strain rate (mentioned but values are not given).

Similar comments can be made regarding the laboratory data provided in Campanella and Mitchell (1968), Tanaka (1995), Crilly (1996), and Graham et al (2001), among others. That is, the provided experimental data is by no means faulty, but a quantitative comparison to the response of the new ETVP model is difficult and data must be carefully considered before comparing results. In addition, many publications focus on a specific clay, usually different from other publications. This, in part, is where

some of the inconsistencies arise - different clay minerals have different properties and have different behaviour (e.g. dielectric constant).

For this thesis, a comparison will be made to determine if the ETVP model can qualitatively reproduce the behaviour observed in a few published papers, without considering the input values in detail. That is, this comparison examines if applying only the exponential (or linear) relationship in Chapter 5 without other modification to the mathematics produces behaviour similar to laboratory observations. Comparative figures for published data have not been included. This was done to avoid confusion with respect to specific aspects of the laboratory tests that do qualitatively compare to the ETVP model and the aspects that do not compare well. The differences in published figures cannot be fully accounted for since several parameters (e.g. material properties, test conditions, drained or undrained heating, experimental error) are not disclosed for many published tests. In addition, as a part of the sensitivity analysis in this thesis, many parameters have been held constant and only the effect of temperature on the varied parameters is examined.

Hueckel and Baldi (1990) present data for CID tests at an OCR of 5.0 and 12.5 and temperatures of 23.0°C and 98.0°C. They show strain softening behaviour for both temperatures. The cooler specimen has higher peak and EOT strengths and experiences more dilation. Their stress-strain figure does not identify peak strengths as one would expect for a CID HOC test (Their specimens do not show a stiff elastic region, but a more gradual transition more indicative of a CI$\bar{U}$ test). Regardless, the behaviour of their specimens is similar to the response of the model shown in Figures 5.16d,e. If a low strain rate is assumed in their data, the new ETVP model could predict similar behaviour.

Tanaka (1995) presents deviator stress-shear strain and volume strain-shear strain data for a CID LOC test at temperatures of 28.0, 65.0, and 100.0°C. The measured data are irregular but indicate decreasing strength with increasing temperature; the trend in the volume strain data is less convincing. Tanaka overlays the prediction from his model and shows both decreasing strength and increasing volume strain (more compression) with increasing temperature. In Figures 5.14d,e, the ETVP model illustrate similar behaviour.

Tanaka (1995) and Graham et al (2001) present deviator stress-shear strain and pore water pressure-shear strain data for a CI$\bar{U}$ NC test at temperatures of 28.0, 65.0, and 100.0°C. The data show an increase in strength and a decrease in pore water pressure for increasing temperature. Their data do not show strain softening behaviour but indicate possibly stiffer behaviour at the start of the test for higher temperatures. The ETVP model shows similar behaviour (Figures 5.5d,e) for a high strain rate prior to strain softening occurring. The strain softening shown in the ETVP model is a result of the viscoplastic formulation.

Crilly (1996) shows results from several CI$\bar{U}$ NC tests at different pressures (0.6, 1.5, 3.0 MPa) and temperatures (27.0, 65.0, and 100.0°C); and provides data for deviator stress, mean effective stress, and pore water pressure. The following is a summary of his results: (1) the 3.0 MPa specimens show negligible change in pore water pressure and only a slight decrease in strength for increasing temperature; (2) the 1.5 MPa specimens show an almost negligible increase in strength and an increase in pore water pressure for increasing temperature; and (3) the 0.6 MPa specimens shows a small decrease in strength and pore water pressure with increasing temperature. Almost negligible strain softening is observed. The closest comparison of this data to the response of the ETVP

model is illustrated with the fast strain rate (15.0%/d) in Figures 5.5d,e. This is fitting since Crilly states that the applied strain rate during shearing of his specimens was 0.9%/hour (or 21.4%/day) (Crilly 1996).

The TEP model proposed by Tanaka (1995) was based, in part, on the assumption that the unload-reload lines, κ were a function of temperature such that $\kappa = \kappa(T)$. This assumption was later proven incorrect by Crilly (1996). Tanaka originally included this assumption in his TEP model to account for the compressive behaviour observed in NC and LOC samples and the dilative behaviour in HOC samples (see Chapter 2 and Figure 2.13). It is possible that Tanaka was correct to assume this behaviour needed to be modeled, but incorrectly associated this behaviour as a function of elasticity and the κ-lines. The author's understanding is that this behaviour should be associated with a combination of temperature and viscous effects as has been done in his ETVP model. Figure 6.14 shows CID tests at OCRs of 1.20, 1.67, and 2.00 for temperatures of 28.0, 65.0, and 100.0°C. By extending a line through the points of maximum curvature for each OCR for a given temperature, Tanaka's incorrect assumption of increasing κ-lines can be illustrated. The behaviour he and others observed is more correctly handled by the combined effects of temperature and viscoplasticity in the ETVP model.

A common comparison for models using CID tests is the relationship between volumetric strain and temperature for different OCRs. Figure 6.15 shows this relationship for the CID tests simulated in this thesis for both fast and slow strain rates. Note that the fast CID NC test shows slight volumetric expansion. This is consistent with the trend observed in Figure 6.10b. This figure is consistent with published figures such that as OCR increases, the response transitions from compressive to dilative behaviour. The

difference between Figure 6.15 and published figures is that the published figures begin at 0.0% volumetric strain and branch outward as temperature increases indicating no volumetric strain at a common temperature and increasing compressive or dilative strains with increasing temperature. This is not modeled in the primary isothermal ETVP model discussed in this thesis.

Chapter 5 mentioned a second ETVP model developed for comparative purposes. This second ETVP model accounts for temperature changes during triaxial shearing, such that regardless of OCR or final temperature, the initial volumetric strains are considered to be 0.0% at the initial temperature. Figure 6.16 illustrates this behaviour and captures the initial compressive behaviour for HOC tests. This figure is presented simply for comparative purposes and neither the figure nor the second ETVP model are discussed in greater detail. This second model was not the primary tool for understanding the effect of temperature-dependent behaviour in the EVP model framework.

It is also important to note that the model does include physics (thermodynamics) related to thermal expansion or contraction of water and clay particles and phase change. The author acknowledges the thermodynamics are present but by not including them in his model, the author was able to examine if the model can reproduce similar behaviour (as in published data) for soil subjected to changes in temperature. This section shows that similar behaviour can be reproduced qualitatively in the new ETVP model. This represents the type of modeling that was identified earlier as ‘semi-empirical’.

6.3 Application of the ETVP Model

Throughout this thesis, scenarios have been examined where an understanding of the effects of time and temperature may have a significant effect on engineering projects. Two hypotheses were proposed in Chapter 1:

(1) Thermistors installed in field projects provide useful data for calibrating thermal numerical models for simulating and predicting temperature changes in clay soils.

(2) Existing viscoplastic and thermoplastic models can be combined into an encompassing elastic thermo-viscoplastic model using a semi-empirical framework.

Chapter 1 briefly introduced problems faced in northern "cold" regions, and Chapter 4 presented results from thermal numerical modeling on the PR391 road embankment and the 138 kV Radisson-Churchill transmission line in northern Manitoba. Chapter 4 showed that the first of the two hypotheses was correct and that field thermistors provide useful information for predicting temperature changes in soil. However, the chapter concluded that an understanding for temperature (thermal modeling) alone while valuable, is not sufficient to provide information on how the stress-strain relationship is affected. This led to examining second hypothesis.

Up to this point, the discussion regarding the ETVP model has revolved around whether the concepts of thermoplasticity and viscoplasticity can be combined into a single model. This concept was presented in Chapter 1 and Chapter 5 presented the model and its limitations. Section 6.2 analyzed the ETVP model results and has now shown that the ETVP model does provide reasonable predictions regarding the stress-strain behaviour of soil subjected to changes in temperature.

Both successful and unsuccessful projects are often used as guidelines in engineering design. This approach can be summarized - "use what worked in the past" and "do not use what failed in the past". Unsuccessful projects are usually examined to determine the cause of the failure (catastrophic or not) and provide reasoning as how to avoid the failure in the future, should a similar project be attempted. This is how many mathematical models are developed and validated. If a project is unique, it may employ 'new knowledge' and 'new techniques' uncommon to general geotechnical engineering in the initial design. Uncertainty is higher and so must be the ‘built-in’ reserves.

The base EVP model developed by Kelln (2007) was validated against laboratory data and applied successfully to a case history for a highway embankment near Limavady in Northern Ireland. (Yin’s earlier model has been validated in several important projects in Asia and Europe where settlements were an issue.)

In its current form, the ETVP model has only been validated qualitatively against published laboratory data. A separate laboratory program focused on triaxial testing at various temperatures and axial strain rates was not part of the thesis program. Validation of the ETVP model in a field application was also not part of this thesis program. Since the EVP model has been used successfully and the behaviour of the ETVP model qualitatively matches laboratory data, it follows that the ETVP model can be applied with reasonable confidence in appropriate field applications. This shows that the second of the two hypotheses is also correct.

Practical Applications:

In general, Northern Canada is experiencing an increase in human activities through operations relating to mining, oil and gas, hydroelectric energy developments, and the extraction of other natural resources. These operations require the construction of additional infrastructure such as housing for employees and access roads to the sites. In addition, it is the home to many First Nations communities. Engineering and industrial activities disturb the natural thermal regime in these areas by altering vegetation cover, drainage patterns, and snow cover. Furthermore, the region is experiencing an overall warming climate and thawing of permafrost in previously untouched areas. The Intergovernmental Panel on Climate Change (IPCC) has suggested that over the next 100 years the mean annual surface temperatures in northern Manitoba may increase upward of 4.0°C (IPCC 2007).

Increasing activity and increasing temperatures inevitably lead to geotechnical problems (for example, differential settlements and deformations) that need to be understood and addressed. This may include exploring ways to mitigate potential damage to infrastructure and exploring methods to preserve permafrost or to adapt to thawing ground. The types of infrastructure may include pipelines, buried cables, geothermal energy wells, pavement structures, and culverts to name a few. Mathematical models have been shown to adequately explain deformations of embankments and foundations that were not described well by traditional soil mechanics (e.g. Yin 1990, Hinchberger and Rowe 2005, and Kelln 2007). They do not, however, include the effects of changing temperatures. It follows that the ETVP model presented in this thesis can now be further

developed and applied in a similar fashion to embankments and foundations to gain an understanding of how changes in temperature and viscosity affect the their performance.

The effects of temperature and viscosity are not limited to infrastructure impacted by climate. Another application of the ETVP model relates to nuclear waste. The disposal of nuclear waste has been a concern for several decades with considerable research being directed to deep underground disposal facilities (also known as deep geological repositories) around the world. Typically, the nuclear waste is placed in containers surrounded by a dense buffer material comprised of sodium bentonite and quartz sand (Graham et al. 1996). The waste continually generates heat with temperatures in excess of 100.0°C. These temperatures "lead to heating, shrinkage, pressure changes, and possibly strength and stiffness changes in the buffer" (Graham et al. 2001).

Other applications pertain to the foundation soil for facilities such as foundries, large refrigeration plants, or sewage treatment plants using anaerobic digestion. These facilities, especially foundries, induce temperature changes in foundation soils that may affect the design of the foundation. The ETVP model can be used to evaluate the performance and serviceability of these facilities. The model can also be used to evaluate landfill (and other bioreactor) sites. Typically thick layers of clay are used as bases and liners between layers in the landfill. These types of sites often use aerobic digestion, anaerobic digestion, or a combination for bacteria to decompose the waste. As a byproduct of the decomposition, anaerobic digestion produces elevated temperatures. In addition to the settlement as a result of decomposition, the ETVP model can be employed to assess the performance of the clay liners.

6.4 Commentary

Throughout the thesis, the argument was presented that there is a need for a better understanding of the relationship between the effects of temperature and viscosity on the stress-strain behaviour of clay soils. Chapter 5 presented an addition for accommodating temperature in an established EVP framework, thereby creating an ETVP framework. This model was developed without considering the actual physics of thermal expansion and contraction. Chapter 5 tested and discussed the response of the ETVP model using a sensitivity analysis and selected results are shown; additional results are available on the accompanying DVD (see Appendix I). This chapter provided additional analysis and discussion. The following comments can be made as a result of this analysis:

(1) Chapter 5 focused the analysis on the exponential relationship for $\psi(T)$ since it meant that the effects of temperature on material properties become more strongly defined. This decision was primarily based on evidence published in Fox and Edil (1996) for the exponential relationship on peat materials. It is thought that the defined linear relationship would be the minimum anticipated effect of temperature, with the actual effect of temperature being exponential in nature. The exponential relationship was arbitrarily defined using the material constant, $\Omega = 0.015/K$, such that $(\psi_0 : T_0) \approx (0.0 : 0.0K)$. This constant has not been confirmed experimentally and variation of this constant was not examined in this thesis. The introduction of this material constant has also introduced potential limits to the input values in the ETVP model. A small change in this parameter leads to considerable changes in ψ at higher temperatures. This implies a limit on the constant may be needed to keep values of ψ within an acceptable range.

(2) Within the boundaries of the ETVP model, it was found that particular tests (for example, CI$\bar{U}$ HOC and CID HOC) exhibit anomalies in the response of the model. These anomalies may indicate a breakdown in the formulation of the model. This does not mean the formulation is faulty, but rather a particular combination of input parameters may produce an unexpected and unusual result. That is, the specific combination of the specific increment size, OCR, strain rate, temperature (or rather, the value of $\psi = \psi(T)$) and other basic parameters such as λ, κ, N, M, and Poisson's ratio may produce anomalies. A rigorous sensitivity analysis on each parameter in the model may reveal upper and lower limits on certain parameters. This will be a significant undertaking and was considered to be outside the scope of this project.

(3) It was mentioned in Chapter 5 and earlier in the current chapter that the responses of the ETVP model end before critical state is fully achieved. As such, the shear strains used to determine end of test (EOT) values vary considerably. Possible trends toward critical state are discussed, but given that some of the model responses (for example, CI$\bar{U}$ HOC and CID HOC) end well before critical state, these trends are difficult to properly assess. That is, the trends shown in the summary plots (Figures 6.1 to 6.13) and the differences between the various strain rates may change at strains closer to critical state.

(4) Some inexplicable data are found in the responses of the ETVP model. In particular, Figure 6.5a shows a constantly decreasing pore water pressure for a strain rate of 1.50%/d as temperature increases. However, the strain rates of 15.0%/d and 0.15%/d show an increasing pore water pressure at higher temperatures thereby

producing upward curvature in the plot. The reason for the change in behaviour at the medium strain rate is unknown.

(5) The TEP model developed by Tanaka (1995) adequately explained the results of his laboratory program. His model assumed that the response of the soil to changes in temperature was both thermoelastic ($\kappa = \kappa(T)$) and thermoplastic ($N = N(T)$ such that λ-lines are parallel at lower specific volumes for increasing temperature) in nature. Although the thermoelastic assumption was proven incorrect by Crilly (1996), Tanaka was correct in assuming this behaviour needed to be accommodated in the model. The current understanding is that this behaviour is associated with viscosity and its variation with changes in temperature as illustrated in Figure 6.14.

(6) The ETVP model has been qualitatively validated against published data. That is, qualitatively, the ETVP model displays similar behaviour in several scenarios. These scenarios involve different OCRs, CI$\bar{U}$ or CID tests, and trends pertaining to changes in temperature and strain rate. However, the validation process requires further attention. The model has not yet been validated in field conditions.

(7) Based on the two defined functions for $\psi = \psi(T)$ that were examined and the relationships shown in Figures 6.1 to 6.13 there is only a small difference between typical laboratory temperatures (mid-20.0s °C) to typical field temperatures in colder areas (closer 0.0°C). This implies that laboratory tests at 'room temperature' would not be significantly different than the conditions experienced in the field. However, for heating environments, the relationships show considerable differences and may need to be considered in engineering design.

6.5 Summary

A quantitative analysis of the model has been completed and the ETVP model has been validated qualitatively against published data. This means that the concepts of viscoplasticity and thermoplasticity have been successfully combined in a semi-empirical framework. This model is not without limitations. For example, the physics regarding thermal expansion and contraction and phase change have not been implemented. In addition, the relationships between secondary compression (creep) and temperature have been assumed. Overall, this ETVP model has been shown to reasonably explain the effects of time and temperature.

Table 6.1: Critical State ratios for CIŪ NC tests

	15.0%/d								
	ε_q = 15.0%			ε_q = 16.0%			Ratios		
T (°C)	p'	q	u	p'	q	u	$\partial p'/\partial \varepsilon_q$	$\partial q/\partial \varepsilon_q$	$\partial u/\partial \varepsilon_q$
3.0	28.54	28.35	30.91	28.47	28.30	30.97	7.40	5.20	5.70
28.0	28.37	28.12	31.00	28.28	28.05	31.08	9.70	6.90	7.30
65.0	27.91	27.54	31.27	27.76	27.43	31.38	14.40	10.70	10.80
100.0	27.05	26.53	31.79	26.85	26.37	31.94	20.60	15.60	15.40
	1.50%/d								
	ε_q = 15.0%			ε_q = 16.0%			Ratios		
T (°C)	p'	q	u	p'	q	u	$\partial p'/\partial \varepsilon_q$	$\partial q/\partial \varepsilon_q$	$\partial u/\partial \varepsilon_q$
3.0	27.49	27.30	31.61	27.42	27.25	31.67	7.10	5.00	5.50
28.0	26.87	26.63	32.01	26.78	26.57	32.08	9.10	6.50	6.90
65.0	25.41	25.08	32.95	25.28	24.98	33.05	13.00	9.60	9.80
100.0	23.17	22.73	34.40	23.00	22.60	34.53	17.40	13.20	13.00
	0.15%/d								
	ε_q = 15.0%			ε_q = 16.0%			Ratios		
T (°C)	p'	q	u	p'	q	u	$\partial p'/\partial \varepsilon_q$	$\partial q/\partial \varepsilon_q$	$\partial u/\partial \varepsilon_q$
3.0	26.48	26.30	32.29	26.41	26.26	32.34	6.70	4.70	5.20
28.0	25.46	25.24	32.95	25.37	25.18	33.02	8.60	6.10	6.60
65.0	23.18	22.88	34.44	23.07	22.80	34.53	11.60	8.60	8.90
100.0	19.95	19.57	36.58	19.80	19.46	36.69	14.60	11.00	10.90

Values for p', q, and u are in kPa

Table 6.2: Critical State ratios for CIŪ LOC tests

	15.0%/d								
	ε_q = 10.0%			ε_q = 11.0%			Ratios		
T (°C)	p'	q	u	p'	q	u	$\partial p'/\partial \varepsilon_q$	$\partial q/\partial \varepsilon_q$	$\partial u/\partial \varepsilon_q$
3.0	26.02	25.76	12.56	25.92	25.70	12.64	10.20	6.10	8.10
28.0	25.92	25.59	12.61	25.79	25.51	12.71	12.60	8.00	9.90
65.0	25.57	25.13	12.81	25.40	25.01	12.94	17.30	11.90	13.40
100.0	24.88	24.29	13.22	24.64	24.12	13.40	23.30	16.90	17.80
	1.50%/d								
	ε_q = 10.0%			ε_q = 11.0%			Ratios		
T (°C)	p'	q	u	p'	q	u	$\partial p'/\partial \varepsilon_q$	$\partial q/\partial \varepsilon_q$	$\partial u/\partial \varepsilon_q$
3.0	25.11	24.83	13.17	25.01	24.77	13.25	10.50	6.10	8.60
28.0	24.64	24.29	13.46	24.50	24.21	13.57	13.20	8.00	10.50
65.0	23.49	23.02	14.18	23.31	22.90	14.33	18.50	11.90	14.50
100.0	21.70	21.07	15.32	21.46	20.91	15.51	24.80	16.50	19.40
	0.15%/d								
	ε_q = 10.0%			ε_q = 11.0%			Ratios		
T (°C)	p'	q	u	p'	q	u	$\partial p'/\partial \varepsilon_q$	$\partial q/\partial \varepsilon_q$	$\partial u/\partial \varepsilon_q$
3.0	24.23	23.95	13.75	24.12	23.89	13.84	10.90	6.00	8.90
28.0	23.41	23.05	14.28	23.27	22.98	14.39	13.50	7.80	10.90
65.0	21.54	21.07	15.48	21.36	20.95	15.63	18.40	11.30	14.60
100.0	18.84	18.24	17.24	18.60	18.09	17.43	23.40	14.90	18.40

Values for p', q, and u are in kPa

Table 6.3: Summary for CI$\bar{\bar{U}}$ NC values

MCC							
T (°C)	q_p (kPa)	u_p[1] (kPa)	A_p	q_f[2] (kPa)	u_f[2] (kPa)	A_f	q_f/q_p
3.0	28.7	30.8	1.07	28.7	30.8	1.07	1.00
28.0	28.7	30.8	1.07	28.7	30.8	1.07	1.00
65.0	28.7	30.8	1.07	28.7	30.8	1.07	1.00
100.0	28.7	30.8	1.07	28.7	30.8	1.07	1.00
15.0%/d							
T (°C)	q_p (kPa)	u_p[1] (kPa)	A_p	q_f[2] (kPa)	u_f[2] (kPa)	A_f	q_f/q_p
3.0	29.0	28.7	0.99	28.3	30.9	1.09	0.98
28.0	29.1	27.9	0.96	28.1	31.0	1.10	0.96
65.0	29.4	26.2	0.89	27.5	31.3	1.14	0.94
100.0	29.6	24.0	0.81	26.5	31.8	1.20	0.90
1.50%/d							
T (°C)	q_p (kPa)	u_p[1] (kPa)	A_p	q_f[2] (kPa)	u_f[2] (kPa)	A_f	q_f/q_p
3.0	28.0	29.5	1.06	27.3	31.6	1.16	0.98
28.0	27.6	29.1	1.06	26.6	32.0	1.20	0.97
65.0	26.7	28.5	1.07	25.1	32.9	1.31	0.94
100.0	25.2	28.0	1.11	22.7	34.4	1.51	0.90
0.15%/d							
T (°C)	q_p (kPa)	u_p[1] (kPa)	A_p	q_f[2] (kPa)	u_f[2] (kPa)	A_f	q_f/q_p
3.0	26.9	30.3	1.12	26.3	32.3	1.23	0.98
28.0	26.1	30.2	1.16	25.2	33.0	1.31	0.97
65.0	24.3	30.4	1.25	22.9	34.4	1.51	0.94
100.0	21.6	31.2	1.45	19.6	36.6	1.87	0.91

[1] u_p obtained at same shear strain as q_p

[2] q_f and u_f obtained at 15.0% shear strain (EOT)

Table 6.4: Summary for CIŪ LOC values

MCC							
T (°C)	q_p (kPa)	u_p[1] (kPa)	A_p	q_f[2] (kPa)	u_f[2] (kPa)	A_f	q_f/q_p
3.0	25.9	12.7	0.49	25.9	12.7	0.49	1.00
28.0	25.9	12.7	0.49	25.9	12.7	0.49	1.00
65.0	25.9	12.7	0.49	25.9	12.7	0.49	1.00
100.0	25.9	12.7	0.49	25.9	12.7	0.49	1.00
15.0%/d							
T (°C)	q_p (kPa)	u_p[1] (kPa)	A_p	q_f[2] (kPa)	u_f[2] (kPa)	A_f	q_f/q_p
3.0	26.2	10.8	0.41	25.8	12.6	0.49	0.98
28.0	26.3	10.0	0.38	25.6	12.6	0.49	0.97
65.0	26.5	9.3	0.35	25.1	12.8	0.51	0.95
100.0	26.4	9.4	0.36	24.3	13.2	0.54	0.92
1.50%/d							
T (°C)	q_p (kPa)	u_p[1] (kPa)	A_p	q_f[2] (kPa)	u_f[2] (kPa)	A_f	q_f/q_p
3.0	25.2	11.5	0.46	24.8	13.2	0.53	0.98
28.0	24.9	11.1	0.45	24.3	13.5	0.55	0.97
65.0	24.1	10.6	0.44	23.0	14.2	0.62	0.95
100.0	22.8	10.1	0.44	21.1	15.3	0.73	0.92
0.15%/d							
T (°C)	q_p (kPa)	u_p[1] (kPa)	A_p	q_f[2] (kPa)	u_f[2] (kPa)	A_f	q_f/q_p
3.0	24.3	12.2	0.50	23.9	13.7	0.57	0.98
28.0	23.6	12.2	0.52	23.1	14.3	0.62	0.98
65.0	22.0	12.3	0.56	21.1	15.5	0.73	0.96
100.0	19.5	13.1	0.67	18.2	17.2	0.95	0.93

[1] u_p obtained at same shear strain as q_p

[2] q_f and u_f obtained at 10.0% shear strain (EOT)

Table 6.5: Summary for CIŪ HOC values

MCC							
T (°C)	q_p (kPa)	u_p[1] (kPa)	A_p	q_f[2] (kPa)	u_f[2] (kPa)	A_f	q_f/q_p
3.0	21.3	0.6	0.03	21.3	1.0	0.04	1.00
28.0	21.3	0.6	0.03	21.3	1.0	0.04	1.00
65.0	21.3	0.6	0.03	21.3	1.0	0.04	1.00
100.0	21.3	0.6	0.03	21.3	1.0	0.04	1.00
15.0%/d							
T (°C)	q_p (kPa)	u_p[1] (kPa)	A_p	q_f[2] (kPa)	u_f[2] (kPa)	A_f	q_f/q_p
3.0	22.5	1.2	0.05	22.5	1.1	0.05	1.00
28.0	22.8	1.4	0.06	22.8	1.2	0.05	1.00
65.0	23.5	1.9	0.08	23.5	1.4	0.06	1.00
100.0	24.4	2.4	0.10	24.4	1.7	0.07	1.00
1.50%/d							
T (°C)	q_p (kPa)	u_p[1] (kPa)	A_p	q_f[2] (kPa)	u_f[2] (kPa)	A_f	q_f/q_p
3.0	21.6	1.5	0.07	21.6	1.0	0.04	1.00
28.0	21.6	1.9	0.09	21.5	0.9	0.04	1.00
65.0	21.3	2.6	0.12	21.2	0.8	0.04	0.99
100.0	20.7	3.5	0.17	20.1	0.6	0.03	0.97
0.15%/d							
T (°C)	q_p (kPa)	u_p[1] (kPa)	A_p	q_f[2] (kPa)	u_f[2] (kPa)	A_f	q_f/q_p
3.0	20.8	1.8	0.09	20.8	0.8	0.04	1.00
28.0	20.4	2.3	0.11	20.3	0.8	0.04	0.99
65.0	19.4	3.2	0.17	19.0	0.6	0.03	0.98
100.0	17.7	4.2	0.24	16.0	0.5	0.03	0.90

[1] u_p obtained at same shear strain as q_p

[2] q_f and u_f obtained at 6.0% shear strain (EOT)

Table 6.6: Summary for CID NC values

	MCC		15.0%/d	
T (°C)	q_f[2] (kPa)	V_f[2]	q_f[2] (kPa)	V_f[2]
3.0	68.9	1.79990	67.9	1.80890
28.0	68.9	1.79990	67.5	1.81090
65.0	68.9	1.79990	66.7	1.81380
100.0	68.9	1.79990	65.5	1.81540
	1.50%/d		0.15%/d	
T (°C)	q_f[2] (kPa)	V_f[2]	q_f[2] (kPa)	V_f[2]
3.0	67.8	1.79970	67.8	1.79060
28.0	67.4	1.79780	67.3	1.78460
65.0	66.4	1.79130	66.2	1.76870
100.0	65.0	1.77840	64.8	1.74110

[1] q_f is equivalent to q_p

[2] q_f and V_f obtained at 35.0% shear strain (EOT)

Table 6.7: Summary for CID LOC values

	MCC		15.0%/d	
T (°C)	q_f[2] (kPa)	V_f[2]	q_f[2] (kPa)	V_f[2]
3.0	42.6	1.92130	42.2	1.92820
28.0	42.6	1.92130	42.0	1.92930
65.0	42.6	1.92130	41.6	1.93030
100.0	42.6	1.92130	41.0	1.92920
	1.50%/d		0.15%/d	
T (°C)	q_f[2] (kPa)	V_f[2]	q_f[2] (kPa)	V_f[2]
3.0	42.0	1.91960	41.9	1.91120
28.0	41.7	1.91730	41.5	1.90490
65.0	41.2	1.90970	40.8	1.88910
100.0	40.3	1.89580	39.8	1.86210

[1] q_f is equivalent to q_p

[2] q_f and V_f obtained at 35.0% shear strain (EOT)

Table 6.8: Summary for CID HOC values

MCC					
T (°C)	q_p (kPa)	V_p[1]	q_f[2] (kPa)	V_f[2]	q_f/q_p
3.0	24.0	2.07308	15.1	2.13365	0.63
28.0	24.0	2.07308	15.1	2.13365	0.63
65.0	24.0	2.07308	15.1	2.13365	0.63
100.0	24.0	2.07308	15.1	2.13365	0.63
15.0%/d					
T (°C)	q_p (kPa)	V_p[1]	q_f[2] (kPa)	V_f[2]	q_f/q_p
3.0	25.4	2.07265	19.2	2.13923	0.75
28.0	25.8	2.07265	19.2	2.14081	0.75
65.0	26.5	2.07333	19.4	2.14370	0.73
100.0	27.3	2.07478	19.4	2.14683	0.71
1.50%/d					
T (°C)	q_p (kPa)	V_p[1]	q_f[2] (kPa)	V_f[2]	q_f/q_p
3.0	24.3	2.07353	18.7	2.13476	0.77
28.0	24.2	2.07398	18.6	2.13427	0.77
65.0	23.7	2.07539	18.2	2.13177	0.77
100.0	22.4	2.07774	17.1	2.12399	0.77
0.15%/d					
T (°C)	q_p (kPa)	V_p[1]	q_f[2] (kPa)	V_f[2]	q_f/q_p
3.0	23.3	2.07418	18.3	2.13027	0.78
28.0	22.7	2.07521	18.0	2.12747	0.79
65.0	21.1	2.07740	17.0	2.11902	0.81
100.0	--	--	--	--	--

[1] V_p obtained at same shear strain as q_p

[2] q_f and V_f obtained at 15.0% shear strain (EOT)

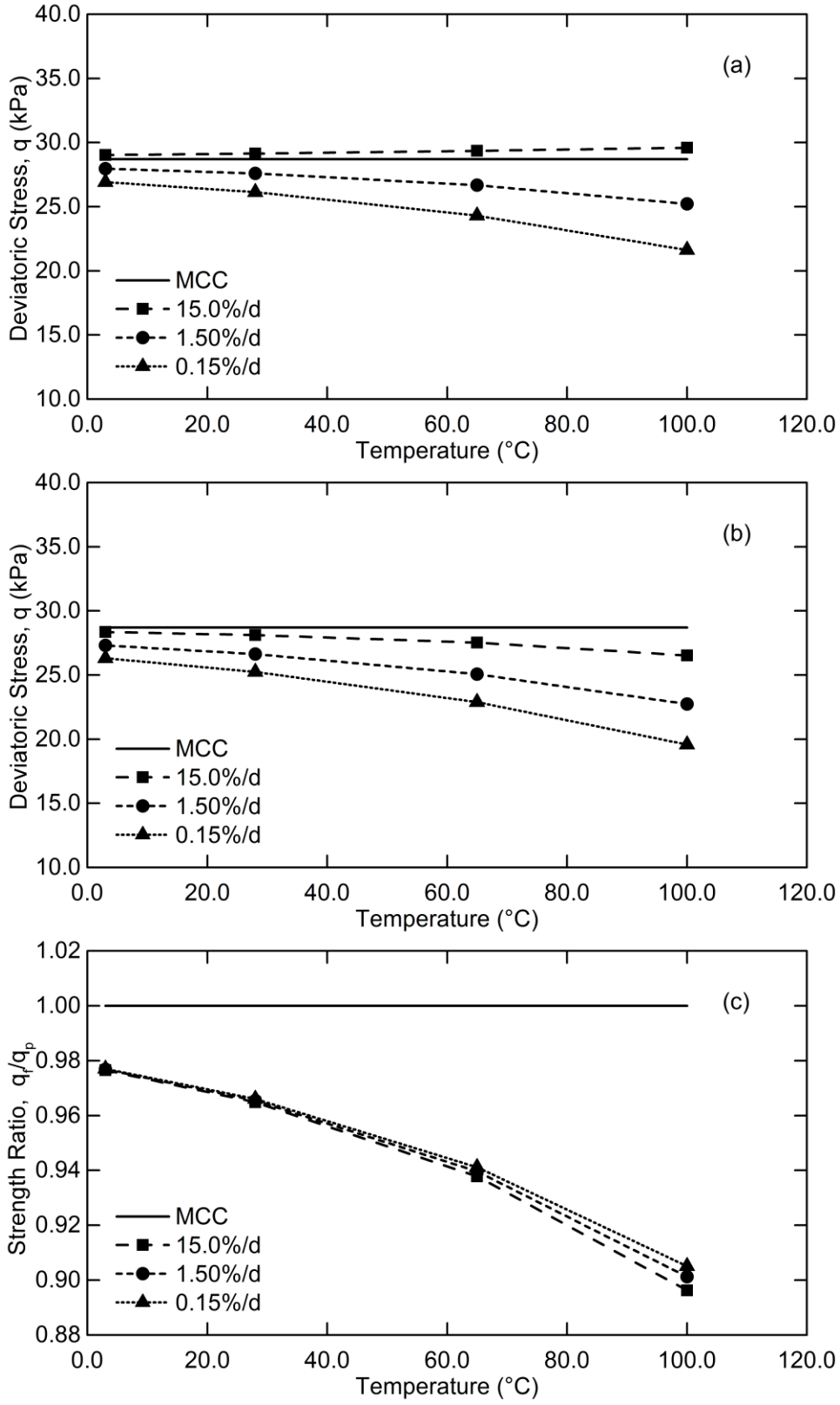

Figure 6.1: CIŪ NC deviator stress at (a) Peak, (b) EOT, (c) Ratio of EOT/Peak

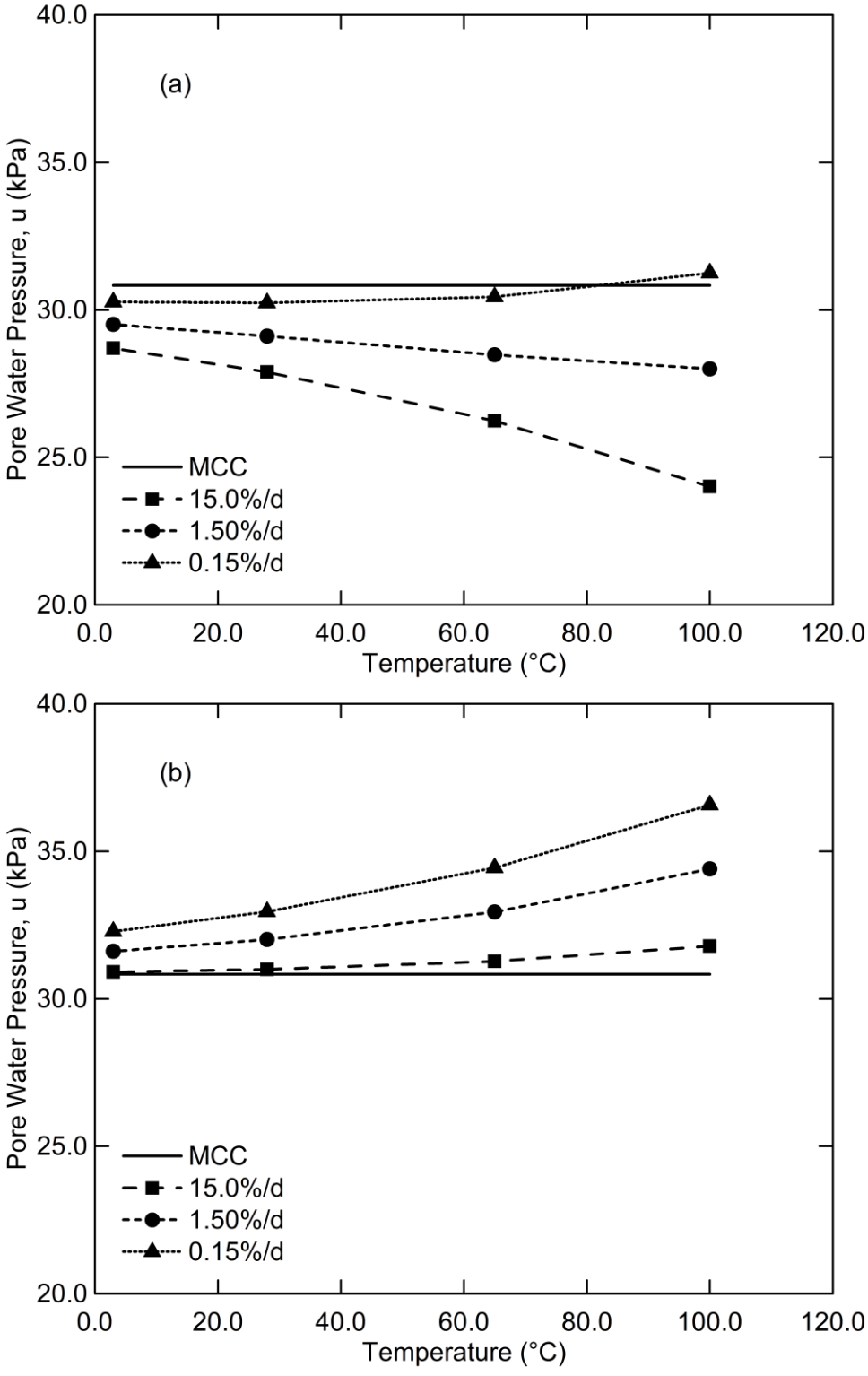

Figure 6.2: CIŪ NC pore water pressures at (a) Peak, (b) EOT

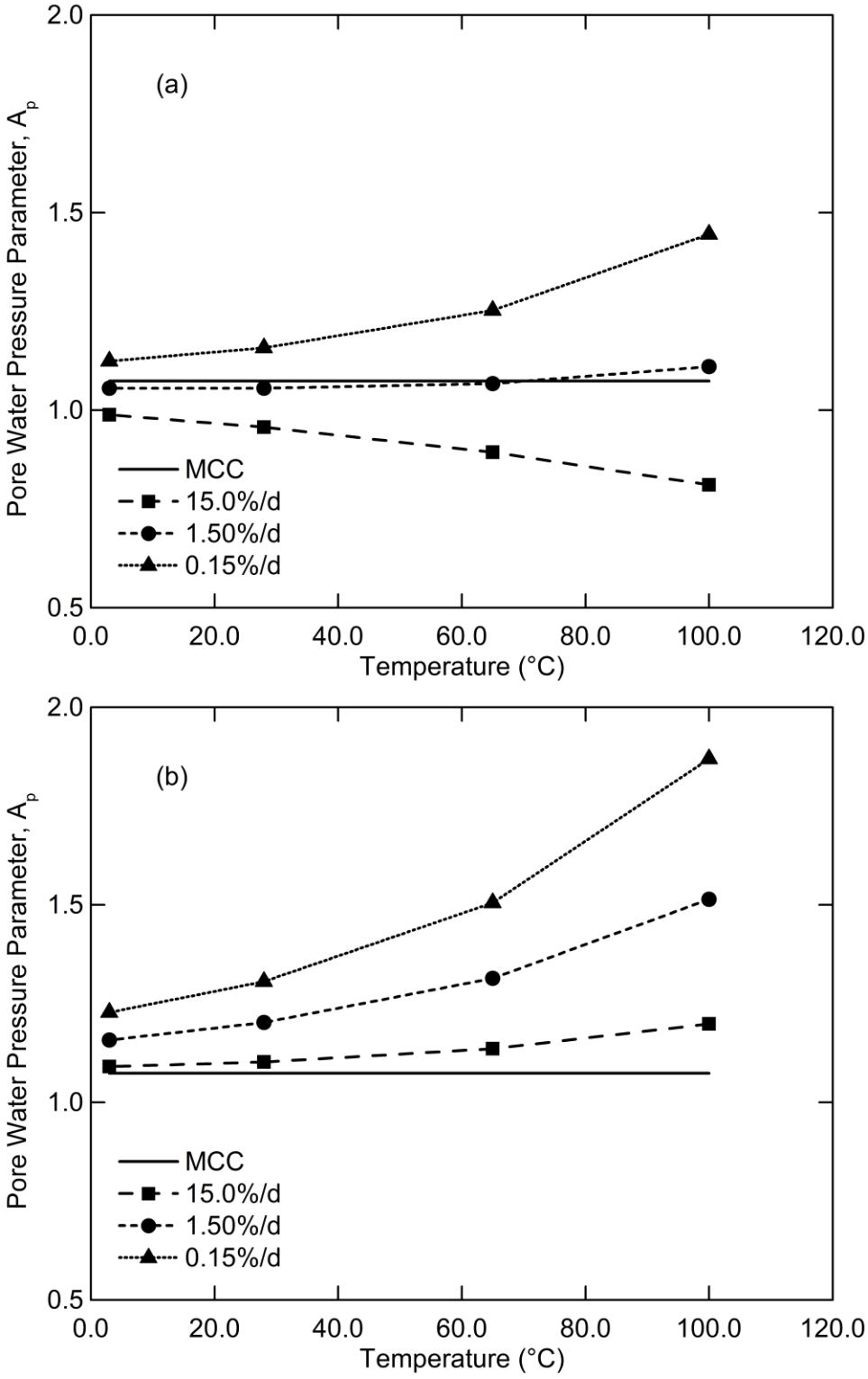

Figure 6.3: CIŪ NC pore water pressure parameter, A at (a) Peak, (b) EOT

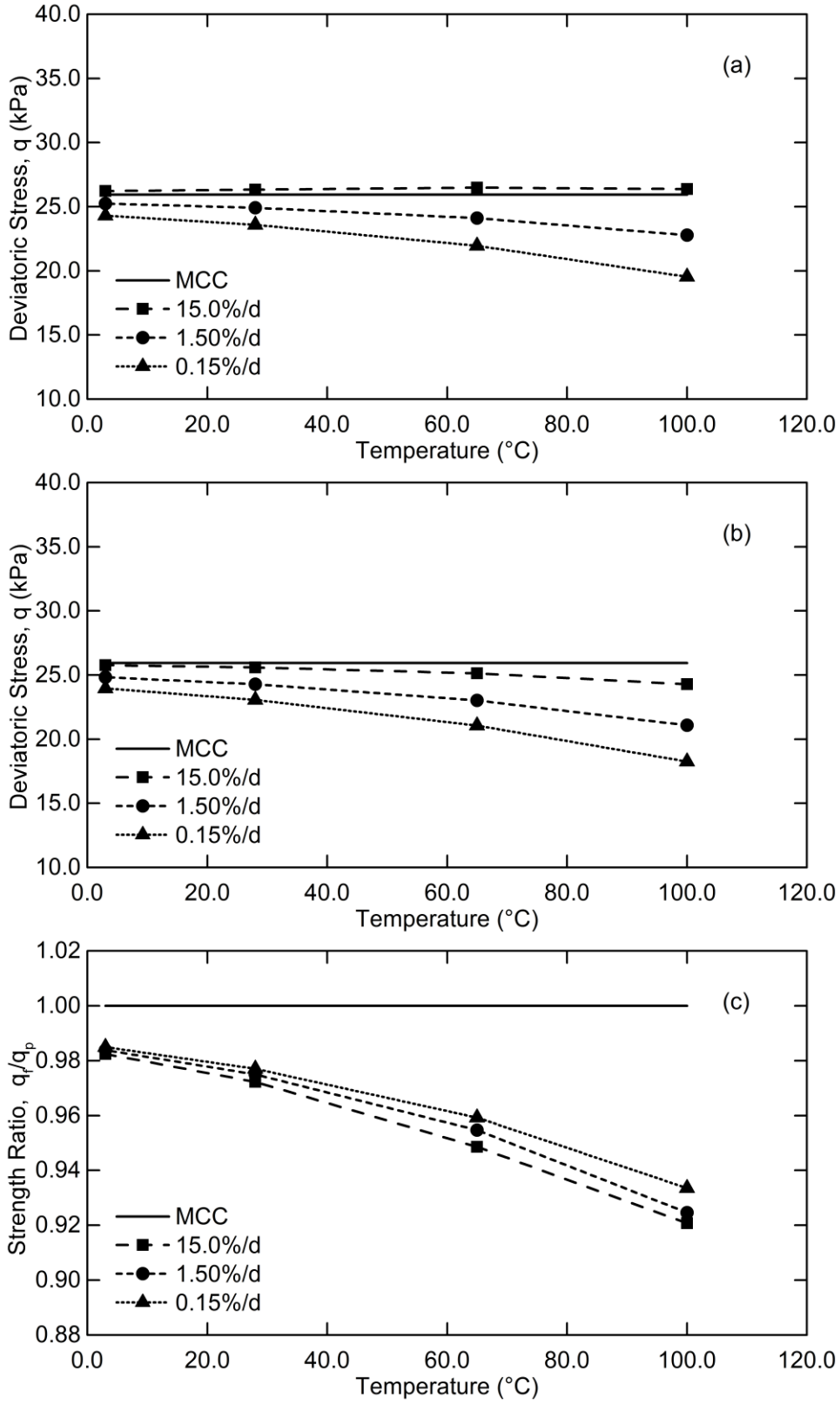

Figure 6.4: CIŪ LOC deviator stress at (a) Peak, (b) EOT, (c) Ratio of EOT/Peak

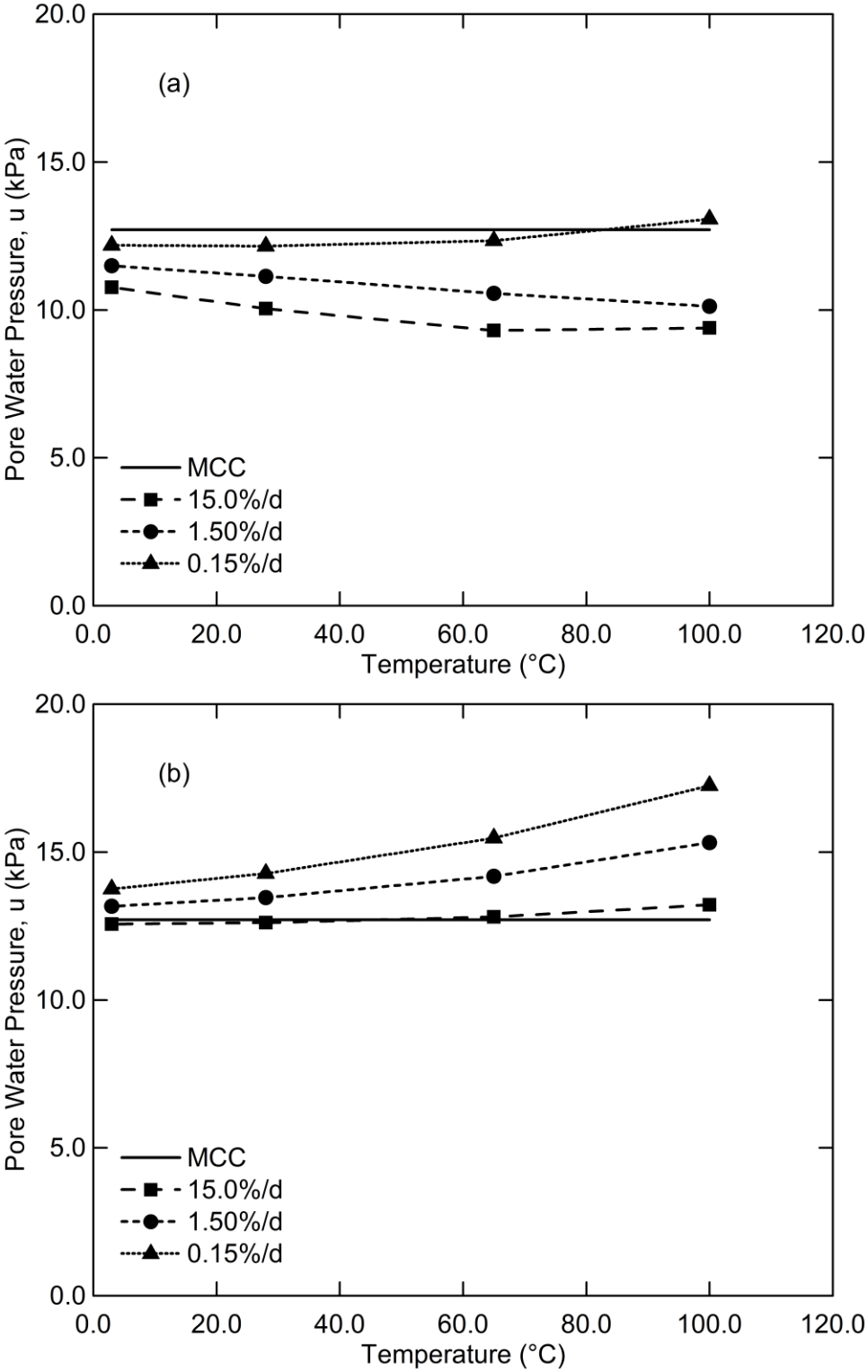

Figure 6.5: CIŪ LOC pore water pressures at (a) Peak, (b) EOT

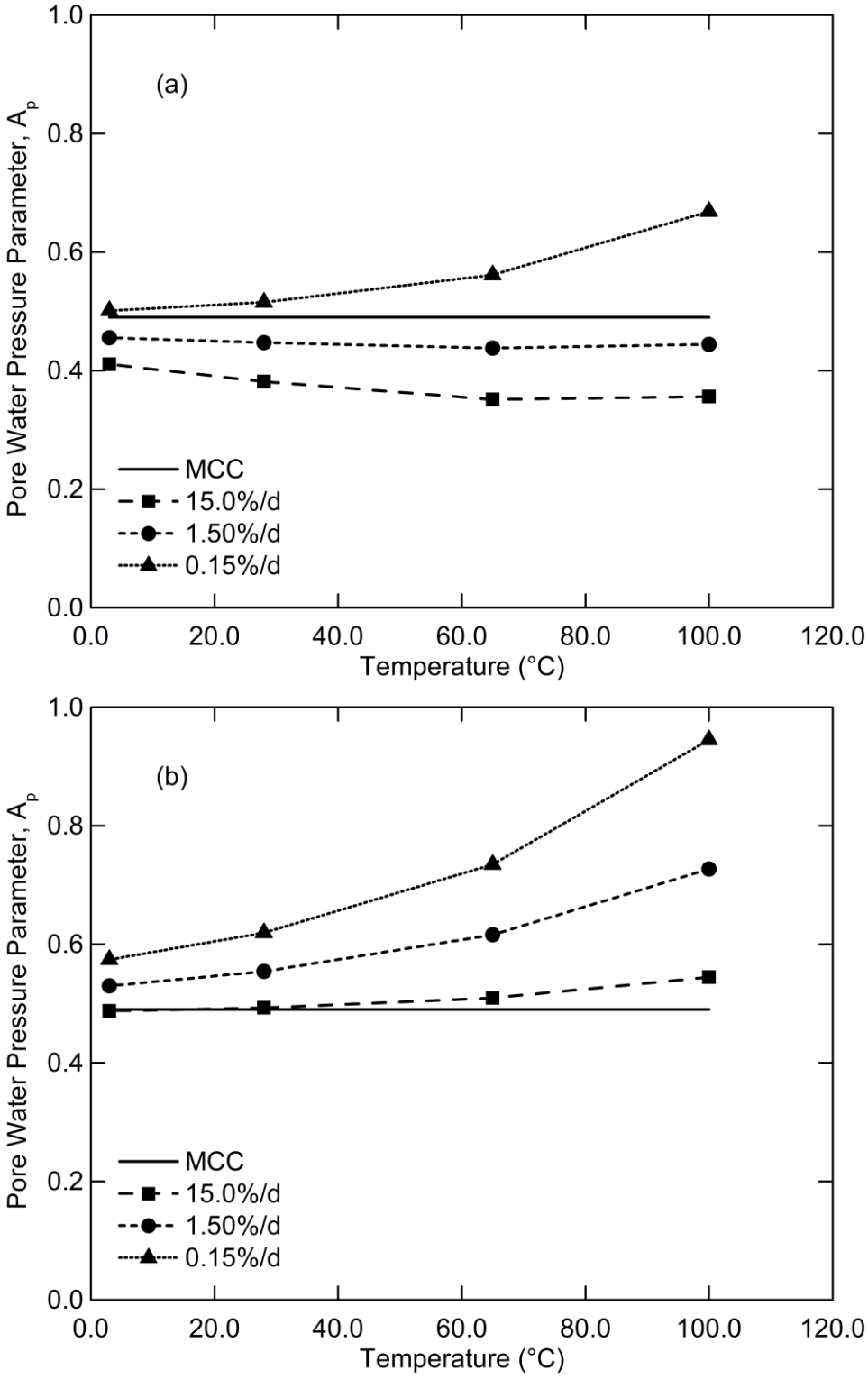

Figure 6.6: CIŪ LOC pore water pressure parameter, A at (a) Peak, (b) EOT

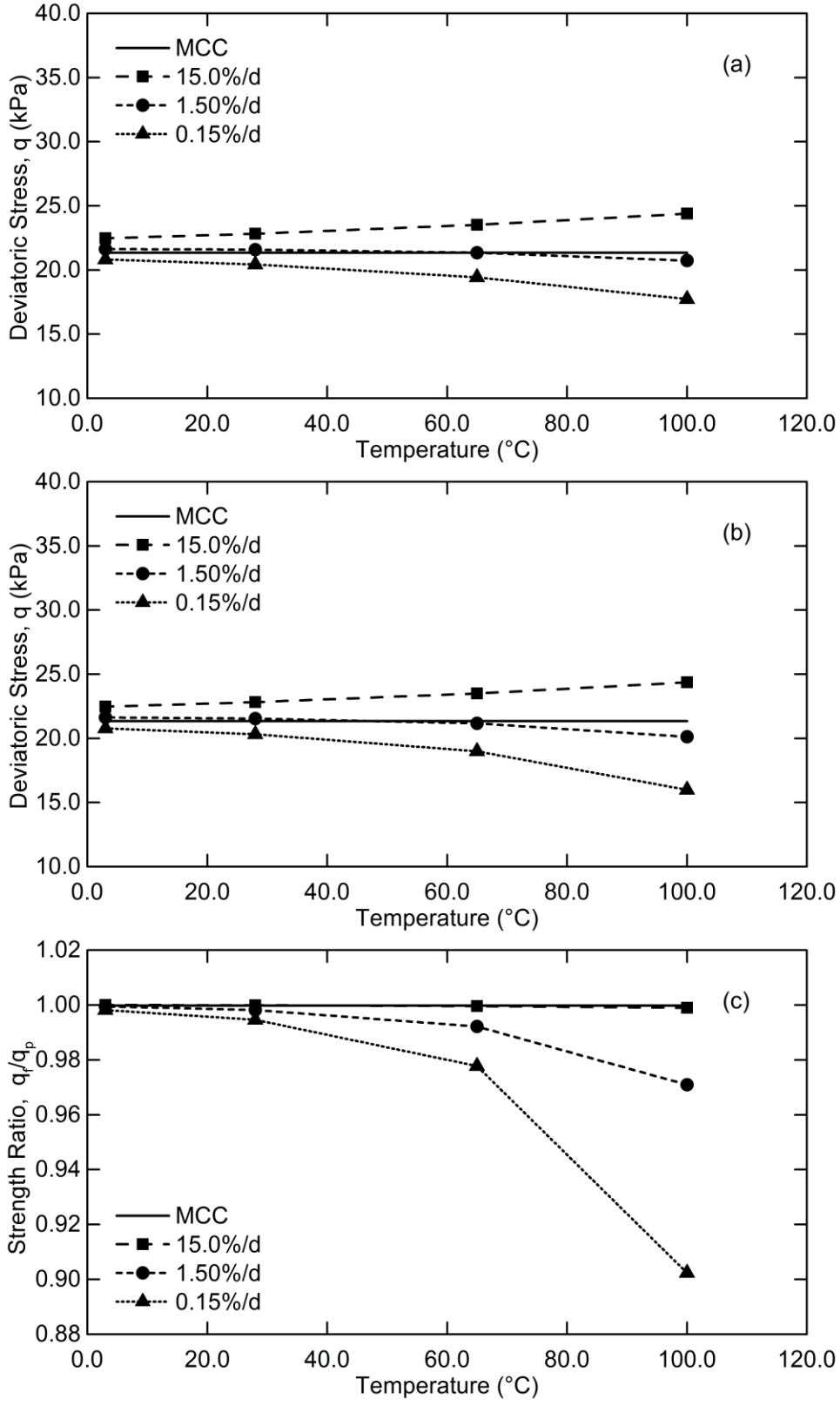

Figure 6.7: CIŪ HOC deviator stress at (a) Peak, (b) EOT, (c) Ratio of EOT/Peak

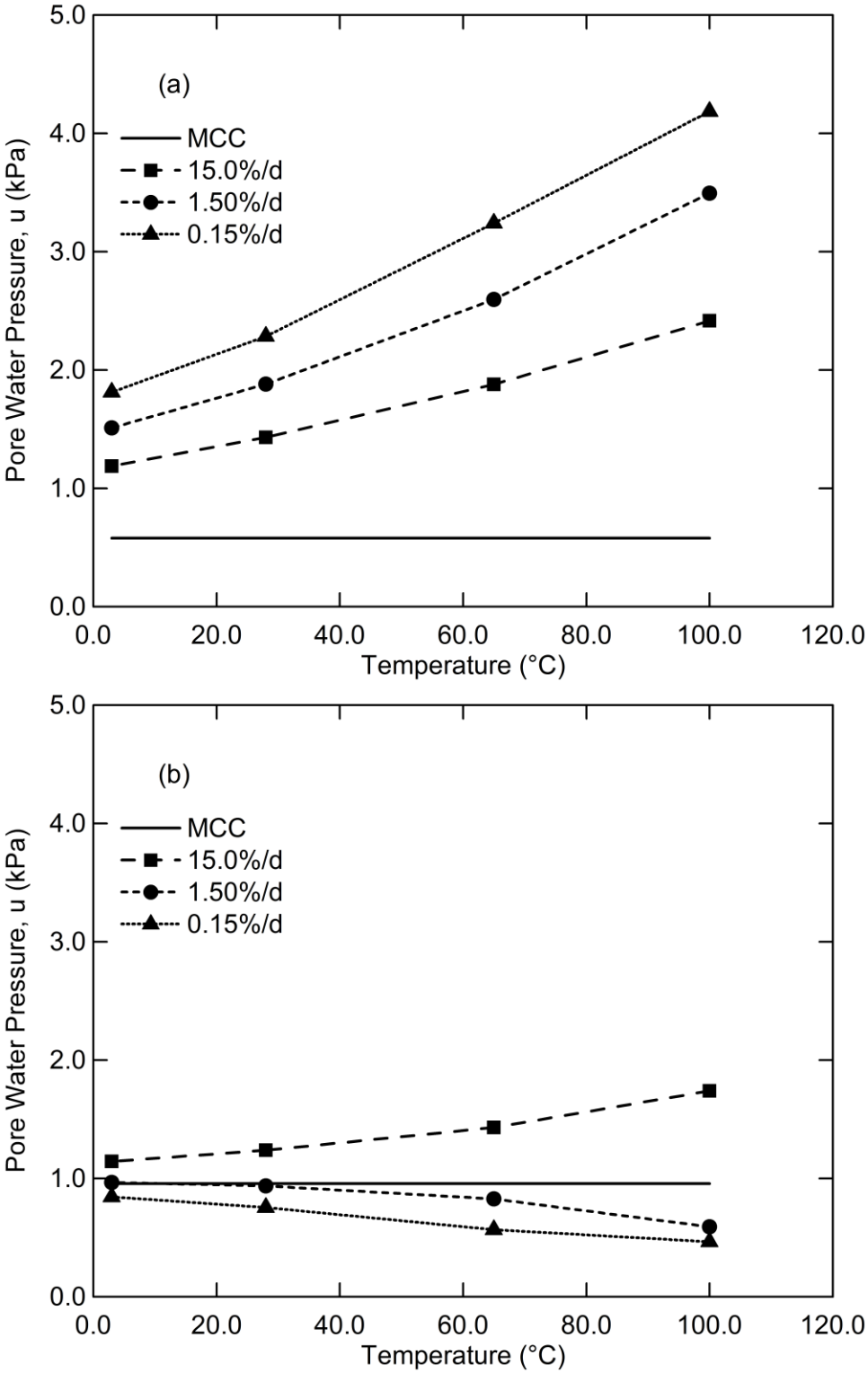

Figure 6.8: CIŪ HOC pore water pressures at (a) Peak, (b) EOT

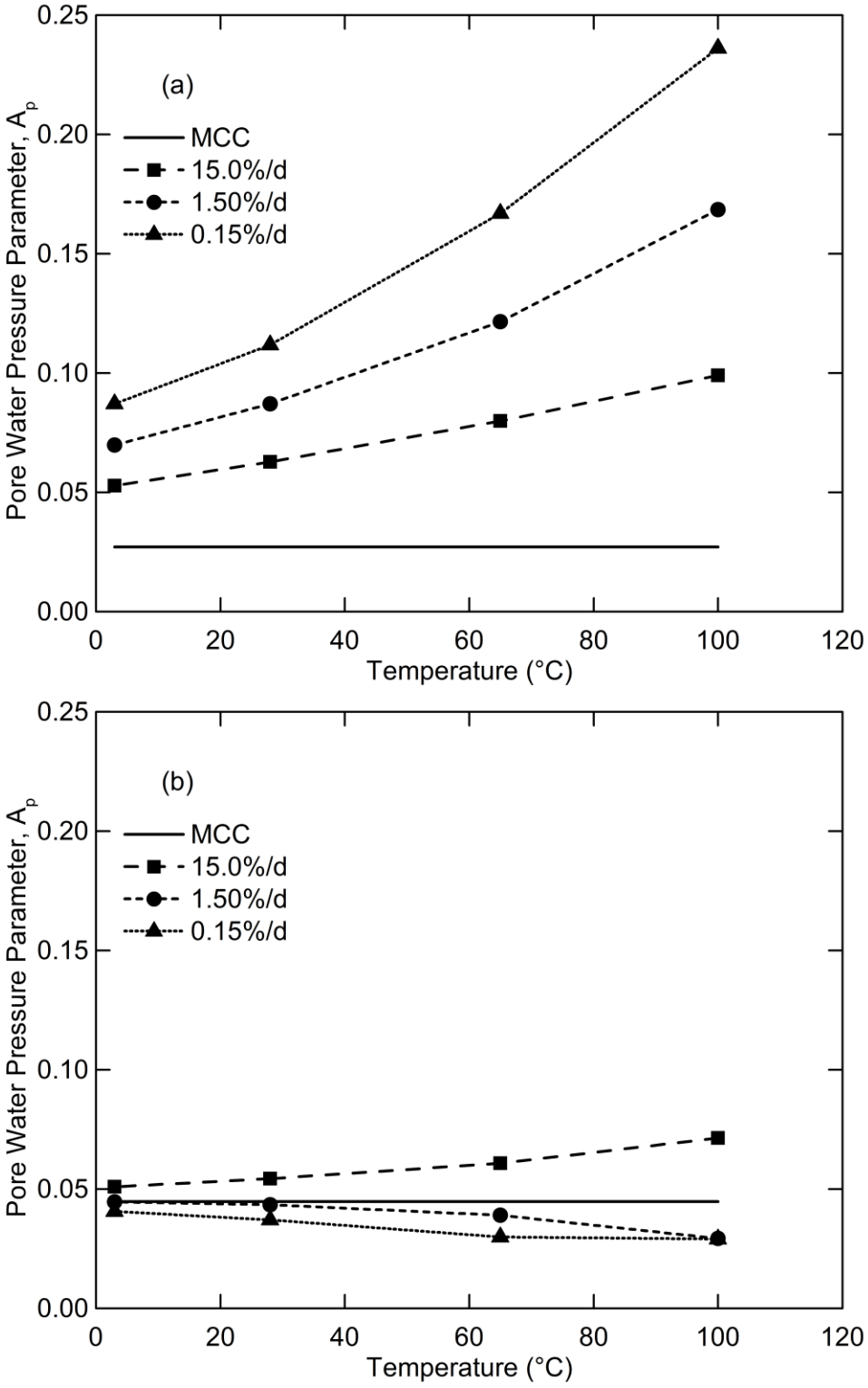

Figure 6.9: CIŪ HOC pore water pressure parameter, A at (a) Peak, (b) EOT

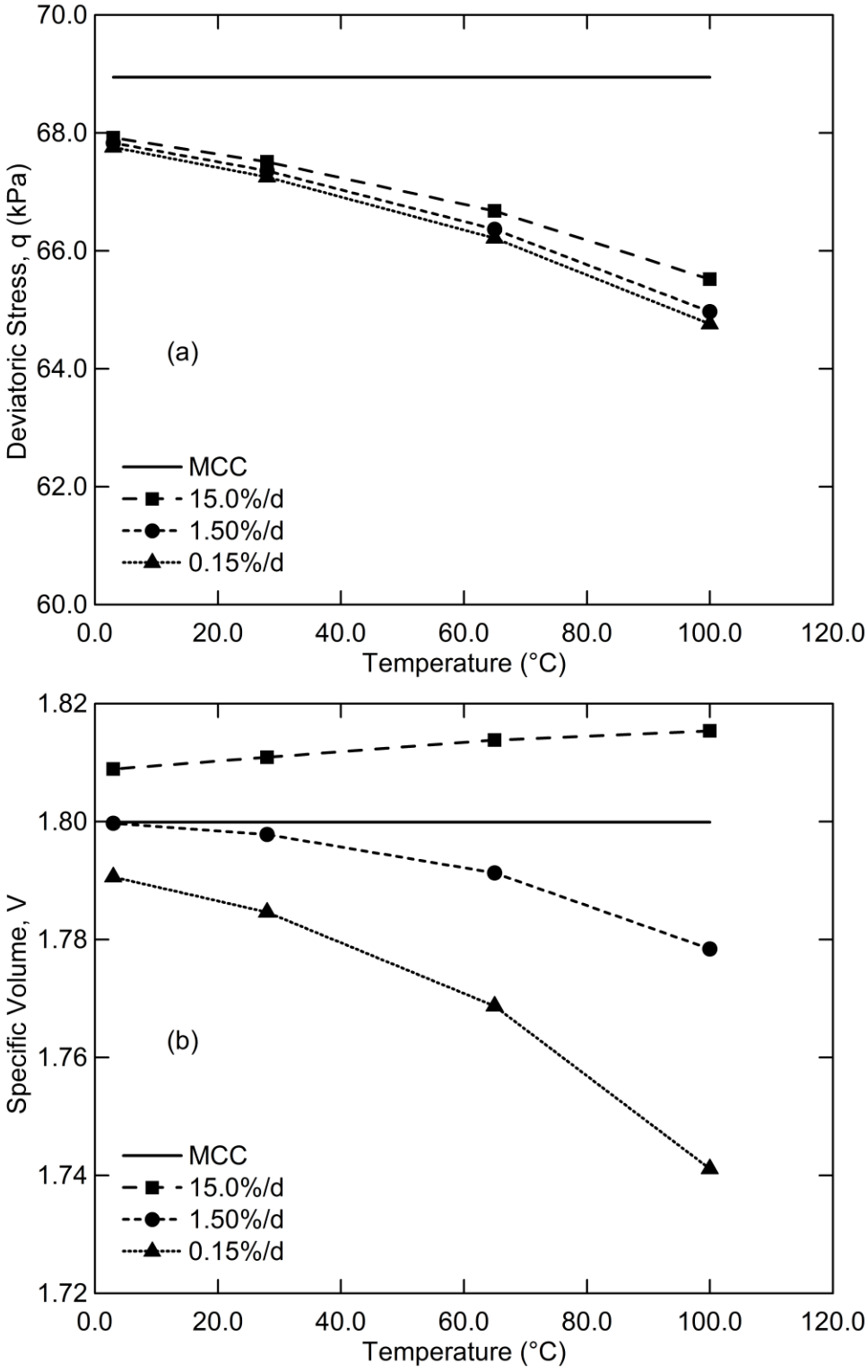

Figure 6.10: CID NC at the EOT for (a) deviator stress and (b) specific volume

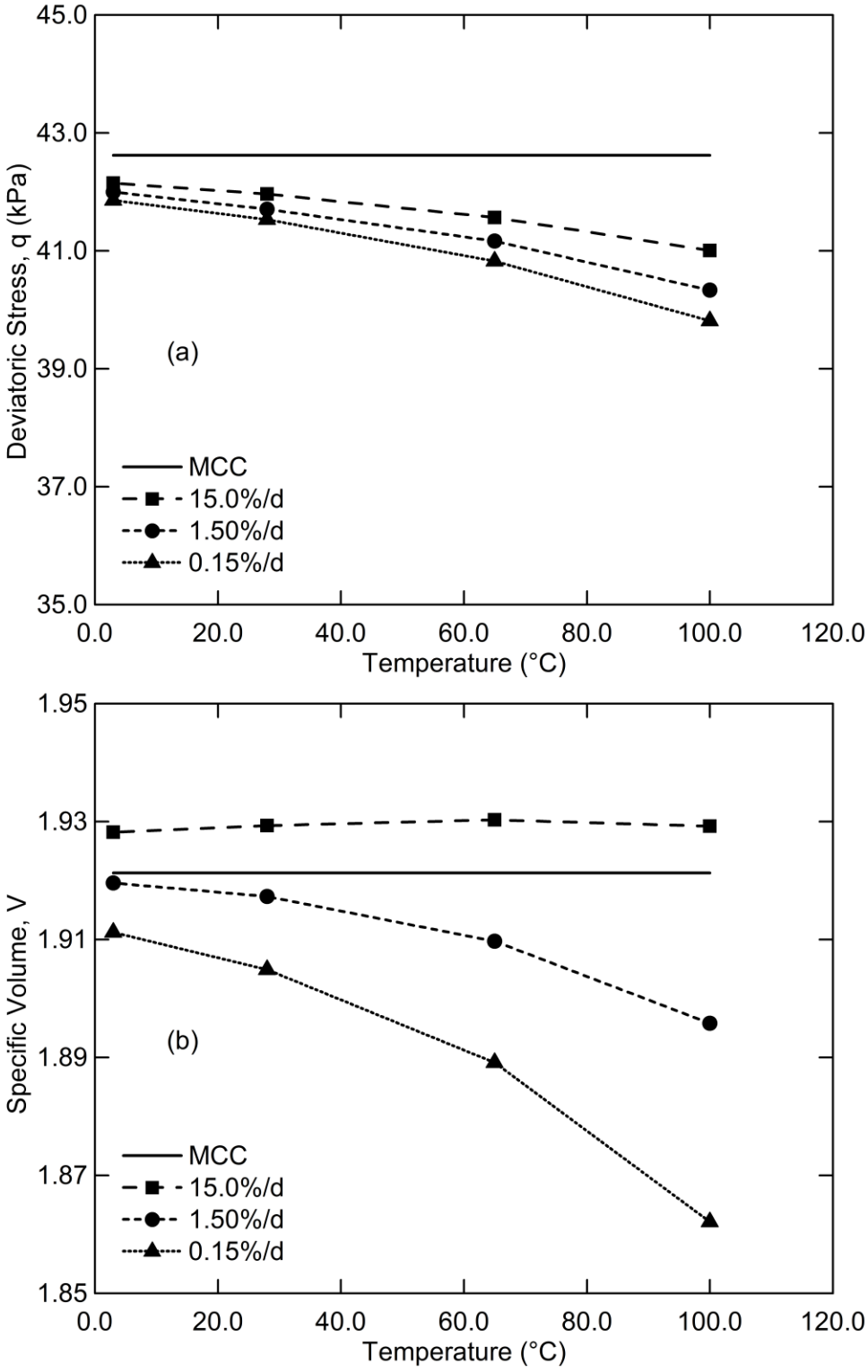

Figure 6.11: CID LOC at the EOT for (a) deviator stress and (b) specific volume

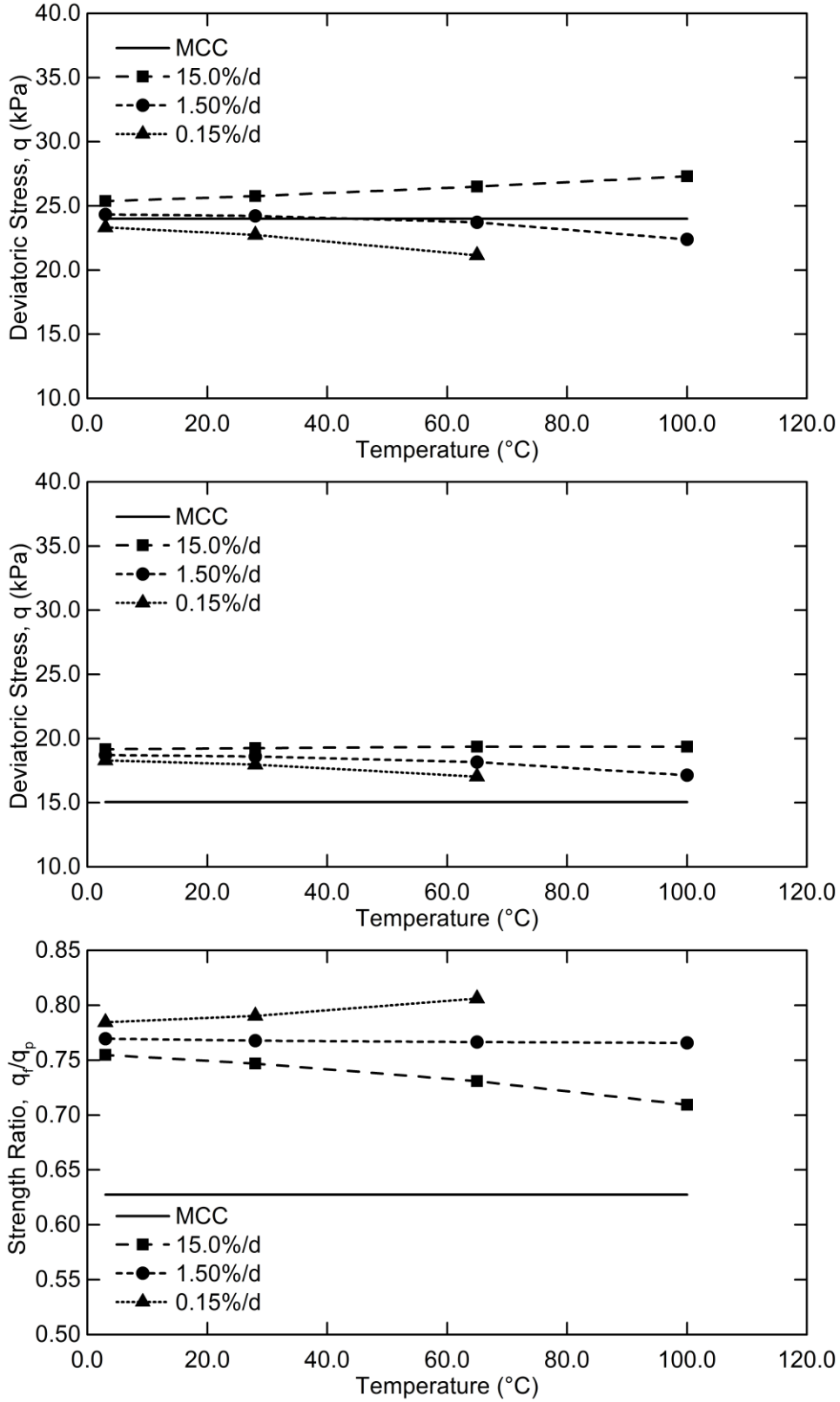

Figure 6.12: CID HOC deviator stress at (a) Peak, (b) EOT, (c) Ratio of EOT/Peak

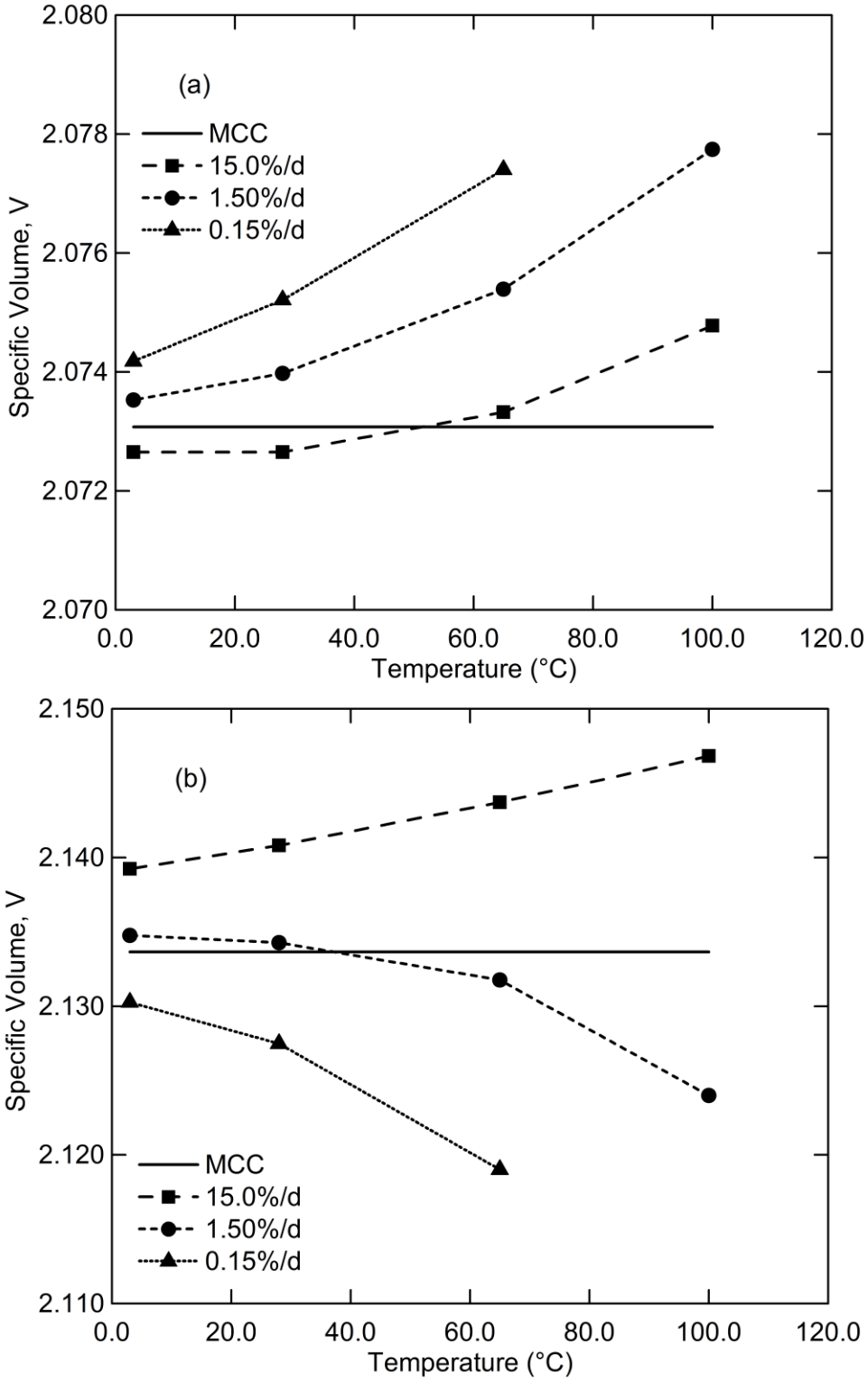

Figure 6.13: CID HOC specific volume, V at (a) Peak, (b) EOT

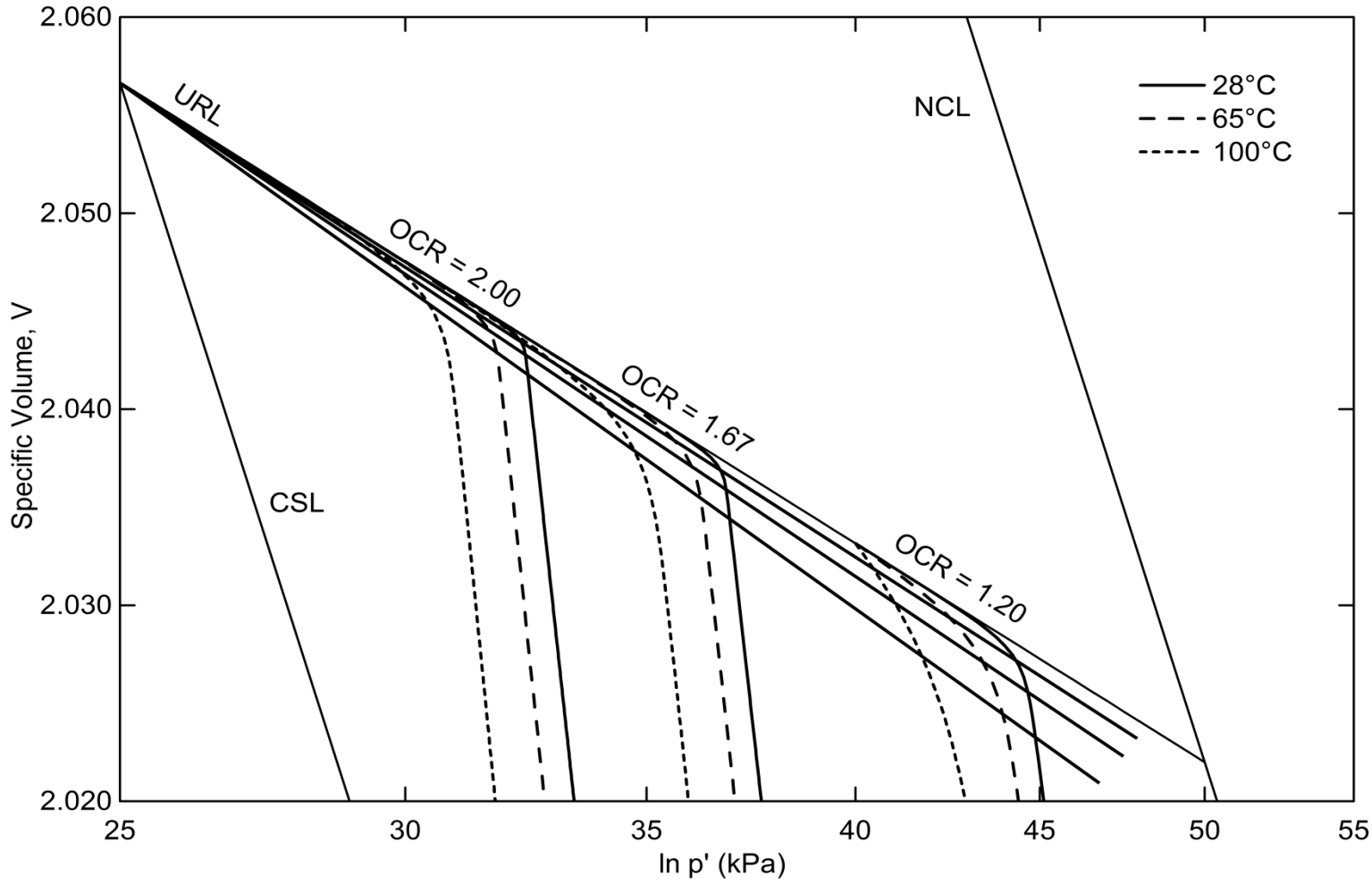

Figure 6.14: CID LOC tests at OCRs 1.20, 1.67, 2.00 illustrating an interpretation of κ(T)

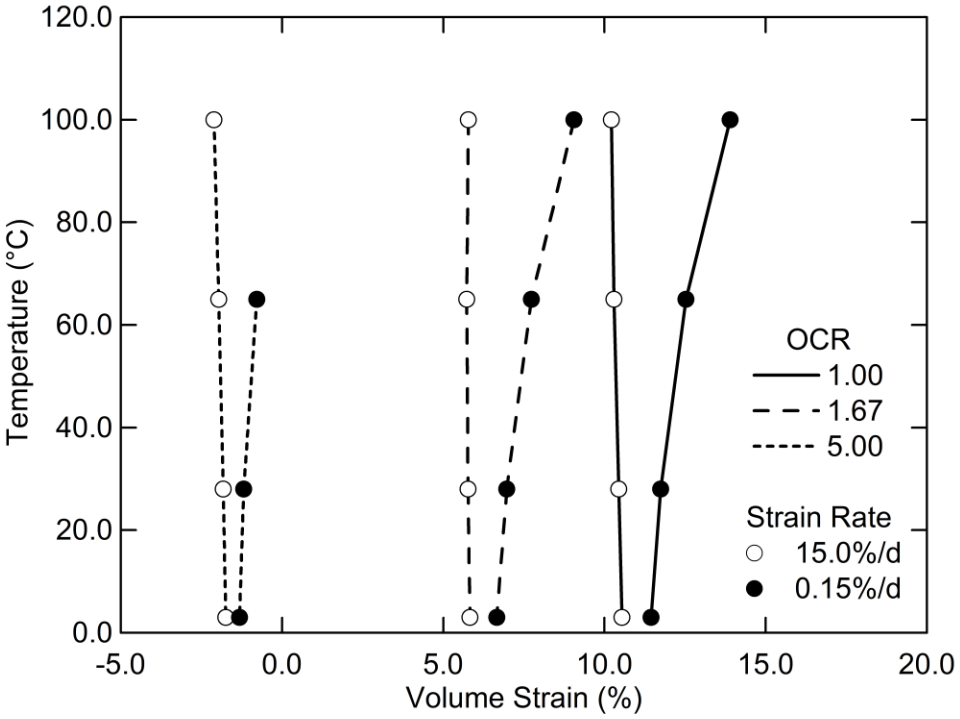

Figure 6.15: Temperature vs. Volumetric Strain for various OCRs

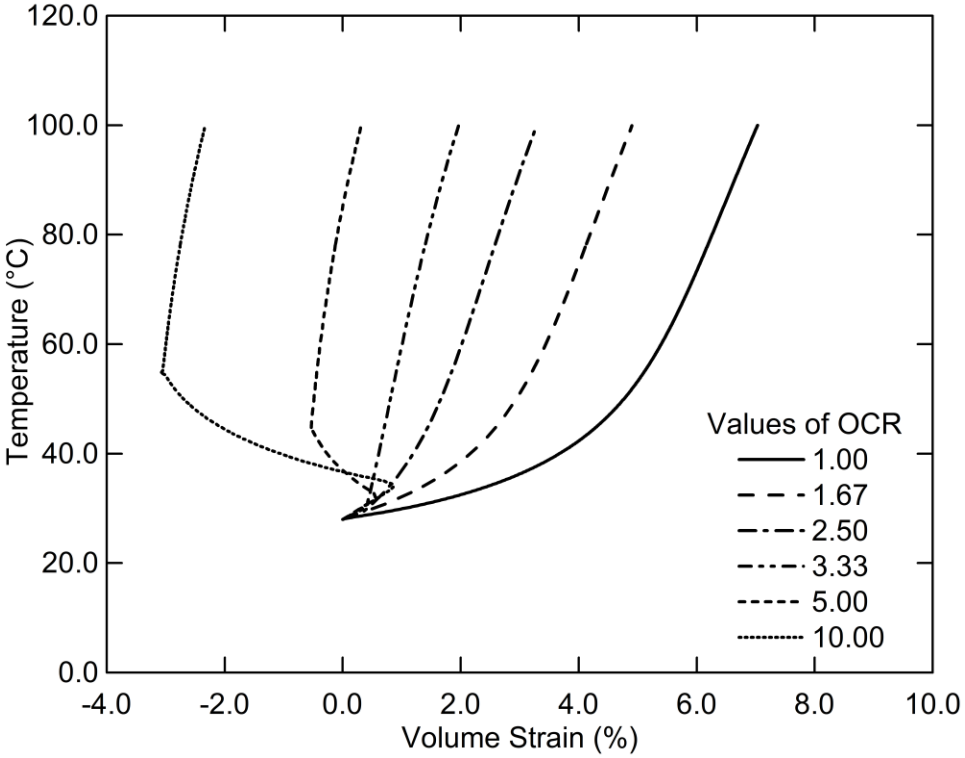

Figure 6.16: Temperature vs. Volumetric Strain for various OCRs during CID Shearing with temperature increase

Chapter 7: Closure

7.1 Summary

The purpose of this research was to gain an understanding into relationships between time, temperature, and load-deformation behaviour in clay soils subject to heating and mechanical loading. This thesis project has examined the two hypotheses presented in Chapter 1. The first hypothesis explored if field thermistors provide useful data for developing a thermal numerical model capable of simulating and predicting temperatures in geotechnical structures. The second hypothesis examined whether the concepts of thermoplasticity and viscoplasticity could be combined into an encompassing elastic thermo-viscoplastic (ETVP) model using a semi-empirical framework.

Fulfillment of the first hypothesis was discussed in Chapters 3 and 4. Values of thermal conductivity were measured in the laboratory using a thermal needle probe and were reported in Chapter 3 for three field sites. Results from this testing were shown to be in good agreement with values from empirical methods available in research literature. These values of thermal conductivity were then used for thermal numerical modeling in Chapter 4 for two of the three sites. Modeling of the third site was not part of the author's program. The thermal numerical modeling using TEMP/W was intended to: (1) explore the effects of various boundary conditions; (2) gain insight as to how changes in temperatures affect geotechnical structures; and (3) determine if these models can be used as predictive tools. It was identified that thermal numerical models are useful tools for

their intended application but do not provide information on changes in stress-strain behaviour as temperatures change. This led to the development of the ETVP model.

Fulfillment of the second hypothesis was discussed in Chapters 5 and 6. Chapter 5 explored and combined the concepts of thermoplasticity and viscoplasticity in an encompassing ETVP spreadsheet model. The effect of temperature was applied to the viscoplastic formulation developed by Kelln (2007) as both a linear and exponential relationship between secondary compression (creep) and temperature. A sensitivity analysis was used to measure the response of the model. In Chapter 6, the response of the model was analyzed quantitatively and then validated qualitatively against published laboratory data.

7.2 Conclusions

The following conclusions can be made.

(1) Thermal conductivities should be determined through laboratory experiments. Thermal conductivity tests using a non-steady state thermal probe are quick and relatively inexpensive to perform. Results should be compared to the many empirical methods established in the literature. Differences between measurements on natural specimens and empirical estimations can then be examined further, if necessary, since the empirical methods do not fully account for the wide range of composition at which natural soil can exist (e.g. mixtures of sand, silt, gravel, clay).

(2) The quality of supporting field data impacts the quality of the thermal numerical model that can be developed. This is evident in the field data obtained from both of the sites that were modeled. The thermistors at PR391 have 'smooth' transitions

between successive thermistors along the cable whereas the older thermistors used in the foundations for the transmission towers gave highly irregular readings. The quality of data also relates to the duration and frequency over which data were collected. This is noticeable in the modeling of PR391 for the thermistors around a depth of 8.0 m at the mid-slope of the embankment (Figure 4.17). If measurements were taken less frequently or for a shorter duration, the gradual temperature increase at this location may have been missed.

(3) The application of the surface boundary condition using a sine function to temperature data and assumed n-Factors improved the results of thermal numerical modeling. For the most part, it was seen in Chapter 4 that the application of a sine function to measured air temperatures produced better predicted ground temperatures compared with those produced using 'raw' climate data.

(4) Once developed and calibrated, thermal numerical models are useful tools for simulating and predicting temperatures in geotechnical structures. This supports the first hypothesis stated in Chapter 1. Chapter 4 presented thermal numerical models for two field sites. It showed that the models simulate measured temperatures well and can therefore be used to predict temperatures.

(5) Thermoplasticity and viscoplasticity have been successfully combined into an encompassing elastic thermo-viscoplastic (ETVP) model. This supports the second hypothesis. The ETVP model was developed using an established viscoplastic strain rate formulation and applied assumed relationships between secondary compression and temperature. The model was validated qualitatively against published laboratory data.

7.3 Recommendations for future work

Based on the conclusions from this research program, the following recommendations for can be made future work:

(1) The thermal numerical model developed for PR391 needs to be redeveloped to clarify the assumptions made in the model. That is, certain assumptions regarding constant temperature boundary conditions (specifically at the assumed depth of mean zero annual amplitude and geothermal gradient) and model geometry (specifically the assumed boundary between the gravel fill and underlying soil) need to be re-examined. The most recent exploration program in late 2012 drilled directly beneath the centre and crest of the embankment; installed additional instruments; and acquired new information regarding boundary conditions.

(2) The ETVP model requires a rigorous validation. The model has so far only been validated qualitatively against published laboratory data. The author recommends this further validation as follows:

   (a) Relationships between the secondary compression coefficient and temperature need to be clarified. The linear and exponential relationships used this project have been arbitrarily defined. A laboratory program designed to test secondary compression at various elevated (and potentially sub-zero) temperatures using oedometers would help determine the nature of this relationship. The oedometers would need to be modified to accommodate a temperature-controlled cell that would still allow the specimens to remain saturated. Alternatively, triaxial cells may be modified to accommodate changes in temperature and pressure and to accommodate 1D experiments. The author

notes that this would require attention to phase-change relationships (below 0.0°C or above 100.0°C). That is, a new laboratory program would better define the $\psi = \psi(T)$ relationship.

(b) The ETVP model should be applied in field applications involving time- and temperature-dependent conditions. The ETVP model can be used to simulate numerous problems involving different temperatures and rates of mechanical loading on various geotechnical structures.

(3) The ETVP model should be incorporated into commercially available software as a user-defined function to further test the functionality of the model. An add-in function developed by Kelln (2007) exists for the EVP model in the GeoStudio software suite. It is reasonable to state that the defined $\psi = \psi(T)$ relationship can be implemented in a similar way, although it would require coding in a computer language associated with the software.

References

Adachi, T., and Oka, F. 1982. Constitutive equations for normally consolidated clays based on elasto-viscoplasticity. Soils and Foundations, **22**(4): 57-70.

Alfaro, MC, Batenipour, H, Graham, J, Kurz, DR and Ng, TNS 2009, 'Highway embankments on degrading and degraded permafrost', *17th International Conference on Soil Mechanics and Geotechnical Engineering - The Academia and Practice of Geotechnical Engineering*, Alexandria, Egypt.

Andersland, Orlando B. and B. Ladanyi. *Frozen Ground Engineering*. 2nd Edition. New Jersey, USA: John Wiley & Sons, Inc., 2004.

Batenipour, H. 2012, 'Understanding the Performance of Highway embankments on Degraded Permafrost' PhD Thesis, University of Manitoba, Winnipeg, MB, Canada.

Batenipour, H, Alfaro, MC, Graham, J and Kalynuk, K. 2011, 'Deformations of a highway embankment on degraded permafrost', *14th Pan-American Conference on Soil Mechanics and Geotechnical Engineering and 64th Canadian Geotechnical Conference*, Toronto, ON.

Batenipour, H, Kurz, D, Alfaro, MC and Graham, J. 2009*a*, 'Effect of Temperature on the 1-D Behaviour of Plastic Clay', *62nd Canadian Geotechnical Conference and 10th Joint CGS/IAH-CNC Groundwater Conference.*, Halifax NS.

Batenipour, H, Kurz, D, Alfaro, MC, Graham, J and Ng, TNS. 2009*b*, 'Highway Embankment on Degrading Permafrost', *14th Conference on Cold Regions Engineering*, Duluth, MN, USA.

Batenipour, H., Kurz, D., Alfaro, M., Graham, J., and Kalynuk, K. 2010, 'Results from an instrumented highway embankment on degraded permafrost', *63rd Canadian Geotechnical Conference and 6th Canadian Permafrost Conference*, Calgary, AB.

Bjerrum, L. 1967. Engineering geology of Norwegian normally consolidated marine clays as related to settlements of buildings, 7th Rankine Lecture. Géotechnique, **17**(2): 81-118.

Bolton, M.D., and Whittle, R.W. 1999. A non-linear elastic/perfectly plastic analysis for plane strain undrained expansion tests. Géotechnique, **49**(1): 133-141.

Brown, RJE. 1967, 'Permafrost in Canada', Geological Survey Map 124A, first edition, Canada.

Brown, RJE 1997, 'Disturbance and recovery of permafrost terrain', in *Disturbance and Recovery in Arctic Lands: An Ecological Perspective*, Kluwer Academic Publishers, Dordrecht, The Netherlands.

Burghinoli, A., Desideri, A., and Miliziano, S. 2000. A laboratory study on the thermomechanical behaviour of clayey soils. Canadian Geotechnical Journal, **37**: 764-780.

Canadian Centre for Climate Modelling and Analysis. 3rd Generation Coupled Global Climate Model (CGCM3.1/T47 IPCC SRES A2 Scenario Data). 2007. University of Victoria. Retrieved May 2012: http://www.cccma.ec.gc.ca/data/cgcm3/cgcm3_t47_sresa2.shtml

Campanella, R.G., and Mitchell, J.K. 1968. Influence of temperature variations on soil behaviour. Journal of the Soil Mechanics and Foundations Division. ASCE, **94**(3): 709-734.

Chen, W.F., and Baladi, G.Y. 1985. Soil plasticity theory and implementation. Elsevier, Amsterdam, Netherlands. 231pp.

Clayton, C.R.I., Heymann, G., 2001. Stiffness of geomaterials at very small strains. Géotechnique 51, 245–255.

Côté, Jean and Konrad, Jean-Marie. 2005a. Thermal Conductivity of base-course materials. Canadian Geotechnical Journal, **42**: 61-78.

Côté, Jean and Konrad, Jean-Marie. 2005b. A generalized thermal conductivity model for soils and construction materials. Canadian Geotechnical Journal, **42**: 443-458.

Côté, J., and Konrad, J.-M. 2006. Granular protection design to minimize differential icing on insulated pavements. Canadian Geotechnical Journal, **43**: 260-272.

Côté, J., and Konrad, J.-M. 2007. Indirect methods to assess the solid particle thermal conductivity of Quebec marine clays. Canadian Geotechnical Journal, **44**: 1117-1127.

Crilly, T.N. 1996. Unload-reload tests on saturated illite specimens at elevated temperature. M.Sc. thesis, University of Manitoba, Winnipeg, Manitoba.

Demars, K.R., and Charles, R.D. 1982. Soil volume changes induced by temperature cycling. Canadian Geotechnical Journal, **19**: 188-194.

Department of the Army and Air Force USA. 1988. *Arctic and Subarctic Construction – Calculation Methods for Determination of Depths of Freeze and Thaw in Soils*, Technical Manual TM 5-852-6/AFR 88-19, Volume 6. Washington D.C.: U.S. Government Printing Office.

Duncan, J.M. and Chang, C.-Y. 1970. Nonlinear analysis of stress and strain in soils. Journal of the Soil Mechanics and Foundations Division. ASCE, **96**(5): 1629-1653.

Environment Canada. Historic Data: Thompson A Station. Environment Canada. Retrieved April 2012: http://www.climate.weatheroffice.ec.gc.ca/climateData/canada_e.html.

Environment Canada. Historic Data: Gillam A Station. Environment Canada. Retrieved August 2008: http://www.climate.weatheroffice.ec.gc.ca/climateData/canada_e.html.

Eriksson, L.G. 1989. Temperature effects on consolidation properties of sulphide clays. *In* Proceedings of the 12th International Conference on Soil Mechanics and Foundation Engineering, Rio de Janeiro, A.A. Balkema, Rotterdam, Netherlands. Vol. 3, pp. 2087-2090.

Farouki, O. T. *Thermal Properties of Soils*. Series on Rock and Soil Mechanics. vol. 11. Clausthal-Zellerfeld, Germany. Trans Tech Publications. 1986.

Forest Products Laboratory. 1999. Wood handbook—Wood as an engineering material. Gen. Tech. Rep. FPL–GTR–113. Madison, WI: U.S. Department of Agriculture, Forest Service, Forest Products Laboratory. 463 p.

Fox, Patrick J., and Edil, Tuncer B. 1996. Effects of stress and temperature on secondary compression of peat. Canadian Geotechnical Journal, **33**: 405-415.

Gens, A., and Potts, D.M., 1988. Critical state models in computational geomechanics. Engineering Computations, Volume 5. pp.178-197.

GEO-SLOPE International Ltd. 2010, *Thermal Modeling with TEMP/W 2007 An Engineering Methodology*, Fourth Edition. GEO-SLOPE International Ltd., Calgary, Alberta, Canada.

Gnanendran, C.T., Manivannan, G., and Lo S.-C.R. 2006. Influence of using a creep, rate, or an elastoplastic model for predicting the behaviour of embankments on soft soils. Canadian Geotechnical Journal, **43**: 134-154.

Graham, J., and Houlsby, G.T. 1983. Anisotropic elasticity of a natural clay. Géotechnique, **33**(2): 165-180.

Graham, J., Crooks, J.H.A., and Bell, A.L. 1983. Time effects on the stress-strain behaviour of natural soft clays. Géotechnique, **33**(3): 327-340.

Graham, J., Noonan, M.L., and Lew, K.V. 1983. Yield states and stress–strain relationships in a natural plastic clay. Canadian Geotechnical Journal, **20**: 502–516.

Graham, J., Tanaka, N., Crilly, T., Alfaro, M. 2001. Modified Cam-clay modelling of temperature effects in clay. Canadian Geotechnical Journal, **38**: 608-621.

Graham, J., Chandler, N.A., Dixon, D.A., Roach, P.J., To, T. and Wan, A.W.L. 1996. The buffer/container experiment. Vol. 4. Results, synthesis, issues. Atomic Energy of Canada Limited Report AECL-11746 and CANDU Owners Group Report COG-97-46-I. 282pp.

Harlan, R.L., and Nixon, J.F. 1978. Ground thermal regime. Chapter 3 in *Geotechnical Engineering for Cold Regions*, ed. O.B. Andersland and D.M. Anderson. New York: McGraw-Hill, pp. 103-63.

Hinchberger, S.D., and Qu, G. 2009. Viscoplastic constitutive approach for rate-sensitive structured clays. Canadian Geotechnical Journal, **46**: 609-626.

Hinchberger, S.D., and Rowe, R.K. 1998. Modelling the rate sensitive characteristics of the Gloucester foundation soil. Canadian Geotechnical Journal, **35**: 769–789.

Hinchberger, S.D., and Rowe, R.K. 2005. Evaluation of the predictive ability of two elastic visco-plastic constitutive equations. Canadian Geotechnical Journal, **42**: 1675–1694.

Horvath, John S. *Geofoam Geosynthentic*. New York, USA, Horvath Engineering, P.C., 1995.

Houston S.L., Houston, W.N. and Williams, N.D. 1985. Thermo-mechanical behavior of seafloor sediments. Journal of Geotechnical Engineering, ASCE, **111**: 1249–1263.

Hueckel, T. 1997. Chemo-plasticity of clays subjected to stress and flow of a single contaminant. International Journal for Numerical and Analytical Methods in Geomechanics, **21**: 43-72.

Hueckel, T., and Baldi, G. 1990. Thermoplasticity of saturated clays: experimental constitutive study. Journal of Geotechnical Engineering, ASCE, **116**: 1778–1796.

Hueckel, T., and Borsetto, M. 1990. Thermoplasticity of saturated soils and shales: constitutive equations. Journal of Geotechnical Engineering, ASCE, **116**: 1765–1777.

Hueckel, T., and Pellegrini, R. 1991. Thermoplastic modelling of undrained failure of saturated clay due to heating. Soils and Foundations, **31**(3): 11-16.

Hueckel, T., and Pellegrini, R. 1992. Effective stress and water pressure in saturated clays during heating–cooling cycles. Canadian Geotechnical Journal, **29**: 1095–1102.

Hukseflux Thermal Sensors. *TP08 Small Size Non-Steady-State Probe for Thermal Conductivity Measurement.* User Manual. Version 0607. Delft, The Netherlands, 2001, pp. 43.

IPCC, 2007: Climate Change 2007: Synthesis Report. Contribution of Working Groups I, II, III to the Fourth Assessment Report of the Intergovernmental Panel on Climate Change [Core Writing Team, Pachauri, RK and Reisinger, A (eds.)]. IPCC, Geneva, Switzerland, 104pp.

Jardine, R.J., Gens, A., Hight, D.W., Coop, M.R., 2004. Developments in understanding soil behaviour. Keynote Address, Advances in Geotech. Eng., Proc. Skempton Memorial Conf., Telford, London UK, 103-207.

Johansen, O. 1975, 'Thermal Conductivity of Soils', PhD Thesis, CRREL draft translation 637, Trondheim, Norway.

Kabbaj, M., Tavenas, F., and Leroueil, S. 1988. In situ and laboratory stress-strain relationship. Géotechnique, **38**: 83-100.

Kelln, C.G. 2007. An elastic-viscoplastic constitutive model for soil. Ph.D. thesis. Queen's University Belfast, Belfast, Northern Ireland, UK.

Kelln, C.G., Sharma, J., and Hughes, D. 2008*a*. A finite element solution scheme for an elastic-viscoplastic soil model. Computers and Geotechnics, **35**(4): 524-536.

Kelln, C.G., Sharma, J., Hughes, D., and Graham, J. 2008*b*. An improved elastic-viscoplastic soil model. Canadian Geotechnical Journal, **45**: 1356-1376.

Kelln, C.G., Sharma, J., Hughes, D., and Graham, J. 2009. Finite element analysis of an embankment on soft estuarine deposit using an elastic-viscoplastic soil model. Canadian Geotechnical Journal, **46**: 357-368.

Kersten, M.S. 1949. *Laboratory Research for the Determination of the Thermal Properties of Soil.* ACFEL Technical Report 23, AD71256. (Also: Thermal properties of soils. University of Minnesota Engineering Experiment Station Bulletin No. 28.)

Kondner, R.L. 1963. Hyperbolic stress-strain response: cohesive soils. Journal of the Soil Mechanics and Foundations Division. ASCE, **89**(1): 115-143.

Kurz, D, Alfaro, M, and Bannister, K. 2009, Thermal Numerical Modeling of Transmission Tower Foundations in Northern Manitoba', *62nd Canadian Geotechnical Conference & 10th Joint CGS/IAH-CNC Groundwater Conference*, Halifax, NS.

Kurz, D, Alfaro, M, Bartley G, and Graham, J. 2012*a*, Thermal Conductivity of clay and peat samples from Northern Manitoba', *65th Canadian Geotechnical Conference*, Winnipeg, MB.

Kurz, D, Alfaro, M, Graham, J, and Batenipour, H. 2012*b*, Thermal Modeling of an Instrumented Highway Embankment on Degraded Permafrost', *65th Canadian Geotechnical Conference*, Winnipeg, Manitoba.

Kurz, David, M. Alfaro, and D. Polyzois. 2008. Numerical Simulation of the Performance of Foundation Insulation for Transmission Line Towers in Northern Manitoba. Technical Report for Manitoba Hydro Research and Development Program. Department of Civil Engineering: University of Manitoba.

Kutter, B.L., and Sathialingam, N. 1992. Elastic-viscoplastic modelling of the rate dependent behaviour of clays. Géotechnique, **42**(3): 427-441.

Ladd, C.C., Foott, R., Ishihara, K., Schlosser, F., and Poulos, H.J. 1977. Stress-defomation and strength characteristics. *In* Proceedings of the 9th International Conference on Soil Mechanics and Foundation Engineering, Tokyo, Japan. pp.421-494.

Laloui, L. and Francois, B. 2009. ACMEG-T: Soil Thermoplasticity Model. Journal of Engineering Mechanics. ASCE, **135**(9): 932-944.

Laloui, L., Leroueil, S., and Chalindar, S. 2008. Modelling the combined effect of strain rate and temperature on one-dimensional compression of soils. Canadian Geotechnical Journal, **45**: 1765-1777.

Leroueil, S., Kabbaj, M., Tavenas, F., and Bouchard, R. 1985. Stress-strain-strain rate relation for the compressibility of sensitive natural clays. Géotechnique, **35**(2): 159-180.

Leroueil, S & Marques, MES 1996, 'Importance of strain rate and temperature effects in geotechnical engineering', in TC Sheahan, VN Kaliakin (eds.), *Measurement and modeling time dependent soil behabiour, Geotechnical Special Publication,* ASCE, Reston, Va.

Li, A.L. and Rowe, R.K. 2007. Effects of viscous behavior of geosynthetic reinforcement and foundation soils on the performance of reinforced embankments. Geotextiles and Geomembranes, **26**: 317-334.

Lingnau, B.E. 1993. Consolidated undrained triaxial behaviour of a sand-bentonite mixture at elevated temperature. Ph.D. thesis, University of Manitoba, Winnipeg, Manitoba.

Lingnau, B.E., Graham, J., and Tanaka, N. 1995. A behavioural model for sand-bentonite at elevated temperatures. 10th PanAmerican Conference on Soil Mechanics and Foundations Engineering, **1**, 252-263. Guadalajara, Mexico, October 1995.

Lingnau, B.E., Graham, J., Yarechewski, D., Tanaka, N., and Gray, M.N. 1996. Effects of temperature on strength and compressibility of sand-bentonite buffer. Engineering Geology **41**: 103-115.

Mesri, G. 1973. Coefficient of secondary compression. Journal of the Soil Mechanics and Foundations Division. ASCE, **99**(1): 123-137.

Mesri, G., and Godlewski, P. M. 1977. Time- and stress- compressibility interrelationship. Journal of Geotechnical and Geoenvironmental Engineering. ASCE, **103**(5): 417–430.

Mesri, G., and Choi, Y.K. 1979. Strain rate behaviour of Saint-Jean Vianney clay: Discussion. Canadian Geotechnical Journal, **16**: 831-834.

Mesri, G., and Choi, Y.K. 1985. The uniqueness of end-of-primary (EOP) void ratio effective stress relationship. *In* Proceedings of the 11th International Conference on Soil Mechanics and Foundation Engineering, San Francisco, United States of America. pp. 587-590.

Mesri, G. and Vardhanabhuti, B. 2005. Secondary compression. Journal of Geotechnical and Geoenvironmental Engineering. ASCE, **131**(3): 398-401.

Mitchell, J.K. and Soga, K. 2005, *Fundamentals of Soil Behavior*, 3rd Edition, John Wiley & Sons.

Modaressi, H. and Laloui, L. 1994. Thermodynamical approach for CamClay-family models with Roscoe-type dilatancy rules. International Journal for Numerical and Analytical Methods in Geomechanics, **18**: 133-138.

Modaressi, H. and Laloui, L. 1997. A thermo-viscoplastic constitutive model for clays. International Journal for Numerical and Analytical Methods in Geomechanics, **21**: 313-335.

Oka, F., Higo, Y., Kim, Y.-S., Imura, Y., and Kimoto, S. 2004. Thermo-hydro-mechanically coupled finite element analysis of clay by an elasto-thermo-viscoplastic model. COMPUTATIONAL MECHANICS, WCCM VI in conjunction with APCOM'04, Sept. 5-10, 2004, Beijing, China, Tsinghua University Press & Springer-Verlag. 11pp.

Olszak, W., and Perzyna, P. 1964. On elastic/visco-plastic soils. *In* International Union of Theoretical and Applied Mechanics (IUTAM) Symposium on Rheology and Soil Mechanics. *Edited by* J. Kravtchenko and P.M. Sirieys. Berlin, New York. 1966. Springer-Verlag, Vol.Grenoble, France, p. 47.

Olzsak, W., and Perzyna, P. 1969. On thermal effects in viscoplasticity. Journal of Applied Mathematics and Physics, **20**(5): 676-680.

Perić, D., Shah, B.R., and Onyango, M.A. 2006. Analytical solutions for a three-invariant original Cam clay model. The Electronic Journal of Geotechnical Engineering, **11(**C), 16pp.

Perzyna, P. 1963. The constitutive equations for rate sensitive plastic materials. Quarterly of Applied Mathematics, **20**(4): 321-332.

Perzyna, P. 1966. Fundamental problems in viscoplasticity. Advances in Applied Mechanics. Academic Press, New York. **9**: 243-377.

Perzyna, P. 2005. The thermodynamical theory of elasto-viscoplasticity. Engineering Transactions, Polish Academy of Sciences, Institute of Fundamental Technological Research, **53**(3): 235-316.

Pietruszczak, S. and Niu, X. 1992. Numerical evaluation of bearing capacity of a foundation in strain softening soil. Computers and Geotechnics, **13**: 187-198.

Prager, W. (1959). *Introduction to plasticity*. Addison-Wesley, Reading, Massachusetts. 148pp.

Roscoe, K.H., and Burland, J.B. 1968. On the generalized stress-strain behaviour of wet clay. *In* Engineering plasticity. Cambridge University Press, New York. pp. 535-609.

Roscoe, K.H., and Schofield, A.N. 1963. Mechanical behaviour of an idealised 'wet clay'. *In* Proceeding of the 2nd European Conference on Soil Mechanics and Foundation Engineering. Weisbaden, Vol.1, pp. 47-54.

Roscoe, K.H., Schofield, A.N., and Thurairajah, A. 1963. Yielding of clays in states wetter than critical. Géotechnique, **13**(2): 210-240.

Roscoe, K.H., Schofield, A.N., and Wroth, C.P. 1958. On the yielding of soils. Géotechnique, **8**(1): 22-53.

Schofield, A.N., and Wroth, C.P. (1968). *Critical State Soil Mechanics*. McGraw-Hill, New York.

Staudzs, A. "Design considerations of the Radisson-Churchill 138 kV transmission line." Presented at Canadian Electrical Association Spring Meeting, Toronto, Ontario. 1986.

Tamagnini, R. 2004. An extended Cam-clay model for unsaturated soils with hydraulic hysteresis. Géotechnique, **54**(3): 223-228.

Tanaka, N. 1995. Thermal elastic plastic behaviour and modelling of saturated clays. Ph.D. thesis, University of Manitoba, Winnipeg, Manitoba.

Tanaka, N., Graham, J., and Crilly, T. 1995. Behaviour of reconstituted illite at different temperatures. *In* Proceedings of the International Workshop on Hydro-Thermo-Mechanics of Engineered Clay Barriers and Geological Barriers, Montreal, Canada, July 1995. 32pp.

Tanaka, N., Graham, J., and Crilly, T.N. 1997. Stress–strain behaviour of reconstituted illitic clay at different temperatures. Engineering Geology, **47**: 339–350.

Tanaka, N., Graham, J., and Lingnau, B.E. 1995*a*. A thermal elastic plastic model based on Modified Cam Clay. *In* Proceedings of the 10th PanAmerican Conference on Soil Mechanics and Foundations Engineering, Guadalajara, Mexico, October 1995. Vol. 1, pp. 252–263.

Tanaka, N., Graham, J., and Lingnau, B.E. 1995*b*. A thermal elastic plastic model based on Modified Cam Clay. *In* Proceedings of the 10th PanAmerican Conference on Soil Mechanics and Foundations Engineering, Guadalajara, Mexico, October 1995. Vol. 1, pp. 534–546.

Tavenas, F., Leroueil, S., La Rochelle, P., and Roy, M. 1978. Creep behaviour of an undisturbed lightly overconsolidated clay. Canadian Geotechnical Journal, **15**: 402-423.

Towhata, I., Kuntiwattanaku, P., Seko I., and Ohishi, K. 1993. Volume change of clays induced by heating as observed in consolidation tests. Soils and Foundations, **33**(4): 170-183.

Wijeweera, H., and Joshi, R.C. 1991. Creep behavior of fine-grained frozen soils. Canadian Geotechnical Journal, 28: 489-502.

Wheeler, S.J. and Sivakumar, V. 1995. An elasto-plastic critical stat framework for unsaturated soil. Géotechnique, **45**(1): 35-53.

Wood, D.M. 1990. Soil Behaviour and Critical State Soil Mechanics. Cambridge University Press, Cambridge.

Yarechewski, D.S. 1993. Constant mean effective stress tests on sand bentonite specimens at elevated temperature. M.Sc. thesis, University of Manitoba, Winnipeg, Manitoba.

Yashima, A., Leroueil, S., Oka, F., and Guntoro, I. 1998. Modelling temperature and strain rate dependent behavior of clays: one dimensional consolidation. Soils and Foundations, **38**(2): 63-73.

Yin, J.H. 1990. Constitutive modelling of time-dependent stress-strain behaviour of soils. Ph.D. thesis, University of Manitoba, Winnipeg, Manitoba.

Yin, J.H., Clark, J.I., Graham, J., and Paulin, M. 1993. Analysis of one-dimensional consolidation in clays applying a new elastic visco-plastic model. *In* Proceedings of the International Conference on Soft Soil Engineering, Guangzhou, China, November 1993. 6pp.

Yin, J.H., Clark, J.I., Graham, J. 1995. Creep behaviour of a soft natural soil and elastic visco-plastic modelling. *In* Proceedings of the 10th Asian Regional Conference on Soil Mechanics and Foundations, Beijing, China, August 1995. 8pp.

Yin, J.H., and Graham, J. 1989. Viscous-elastic-plastic modelling of one-dimensional time-dependent stress-strain behaviour of clays. Canadian Geotechnical Journal, **26**: 199-209.

Yin, J.H., and Graham, J. 1994. Equivalent times and one-dimensional elastic viscoplastic modelling of time-dependent stress-strain behaviour of clays. Canadian Geotechnical Journal, **31**: 42-52.

Yin, J.H., and Graham, J. 1999. Elastic viscoplastic modelling of the time-dependent stress-strain behaviour of soils. Canadian Geotechnical Journal, **36**(4): 736-745.

Yin, J.H., and Zhu, J.G. 1999. Measured and predicted time-dependent stress-strain behaviour of Hong Kong marine deposits. Canadian Geotechnical Journal, **36**: 760-766.

Yin, J.H., Zhu, J.G., and Graham, J. 2002. A new elastic viscoplastic model for time-dependent behaviour of normally and overconsolidated clays: theory and verification. Canadian Geotechnical Journal, **39**: 157-173.

Zhou, Y., Rajapakse, R.K.N.D., and Graham, J. 1998*a*. Coupled consolidation of a porous medium with a cylindrical or spherical cavity. International Journal for Numerical and Analytical Methods in Geomechanics, **22**: 449-475.

Zhou, Y., Rajapakse, R.K.N.D., and Graham, J. 1998*b*. Coupled thermoporoelastic model with thermo-osmosis and thermal-filtration. International Journal of Solids and Structures, **35**: 4659-4683.

Zhou, Y., Rajapakse, R.K.N.D., and Graham, J. 1998*c*. Modeling of coupled hygro-thermo-mechanics of unsaturated soil with volume change. *In* Proceedings of the International Workshop on Key Issues in Waste Isolation Research, Barcelona, Spain, December 1998. 20pp.

Zienkiewicz, O.C., and Cormeau, I.C. 1974. Visco-plasticity—plasticity and creep in elastic solids—a unified numerical solution approach. International Journal for Numerical Methods in Engineering, **8**: 821-845.

Appendix I

This thesis contains the electronic files relevant to the respective chapters in this thesis. These files have been made available on a DVD left with Dr. Marolo Alfaro at the University of Manitoba.

Typically, these files are spreadsheets with formulas, vast quantities of raw data that would be unreasonable to print, or the thermal numerical models that simply cannot be printed. The folders on the DVD contain the following files:

Chapter 3:

- The program and wiring diagram for the thermal probe
- A Microsoft Excel spreadsheet of relevant raw data and plots for each material

Chapter 4:

- Thermal numerical models for PR391 road embankment (GeoStudio files)
- Thermal numerical models for the Transmission tower foundations (GeoStudio files)
- A Microsoft Excel spreadsheet containing field data for the Transmission tower foundations
- Microsoft Excel spreadsheets containing calculations for material properties used in modeling
- Microsoft Excel spreadsheets containing compiled results for all models for all dates simulated

Chapter 5:

- The ETVP model (isothermal) in a Microsoft Excel spreadsheet
- Spreadsheets containing all data for all cases of the sensitivity analysis for simulated CI$\bar{U}$ and CID tests (over 540 figures in Microsoft Excel)
- The second ETVP model (non-isothermal) in a Microsoft Excel spreadsheet allowing temperature change during shearing
- A Microsoft Word document containing all relevant formulas in the ETVP model